STRUCTURAL CONNECTIVITY AND TASK-EVOKED DYNAMICS OF THE DEFAULT MODE NETWORK

by

DANA MARIE MASTROVITO

A dissertation submitted to the School of Graduate Studies

Rutgers, The State University of New Jersey

In partial fulfillment of the requirements for the degree of

Doctor of Philosophy Graduate Program in Behavioral and Neural Sciences

Written under the direction of Professor Stephen José Hanson

And approved by

_____

_____

_____

_____

_____

_____

Newark, New Jersey

October, 2018

ABSTRACT OF THE DISSERTATION

Structural Connectivity and Task-evoked Dynamics of the Default Mode Network

by DANA MARIE MASTROVITO

Dissertation director: Prof. Stephen Hanson

The default mode network (DMN) is a structurally interconnected network of brain regions defined collectively by their high level of intrinsic activity at "rest" and relative decrease in activity while performing a range of cognitive tasks. The functional role of the network's intrinsic activity, as well as the significance of its task-evoked attenuation is unknown. However, aberrations in DMN activity are implicated in many disorders including Alzheimers, depression, autism, and schizophrenia, suggesting it may have a fundamental role in healthy brain function. Using diffusion imaging, I trace the large-scale anatomical connections of the network through the basal ganglia and thalamus, illustrating that the core regions of the network form a distributed cortico-striatal-thalamic circuit. Using Markov chain models of functional MRI, I explore the temporal dynamics of each region of the network during task execution and and present evidence suggesting the DMN may orchestrate switching between bottom up and top down processing in the brain through its connections to the basal ganglia. Subcomponents of the network in parietal cortex may support bottom-up processing while anterior portions in medial prefrontal cortex facilitate top-down. Finally, I classify resting-state data from patients with autism and schizophrenia and find that changes in DMN activity are potential biomarkers for distinguishing between the two disorders.

Acknowledgements

This thesis is dedicated to my loving brother who has always been there for me with encouragement and generosity, and to my friend Robert Assini for sharing his wit and knowledge of the basal ganglia during our fire escape journal club meetings.

This research was supported in part by the National Science Foundation Graduate Research Fellowship under Grant No. DGE-1313667.

Preface

Chapter V has been published in NeuroImage: Clinical (Mastrovito et al., 2018).

Table of Contents

List of Tables

List of Illustrations

List of Abbreviations

ABIDE	Autism Brian Imaging Data Exchange
ADHD	attention-deficit hyperactivity disorder
ADMN	anterior default mode network
ADOS	autism diagnostic observation schedule
ARD	automatic relevance detection
ASD	autism spectrum disorder
AV	anterior ventral nucleus of the thalamus
AD	anterior dorsal nucleus of the thalamus
AM	anterior medial nucleus of the thalamus
BA	Brodmann area
BEDPOSTX	Bayesian estimation of diffusion parameters obtained using sampling techniques – crossing
BG	basal ganglia
BOLD	blood oxygenation-level dependent
CaMKIIα	Calmodulin-dependent protein kinase II
CBF	cerebral blood volume
CBV	cerebral blood flow
$CMRO_2$	metabolic rate of oxygen consumption
COBRE	Center for Biomedical Research Excellence
CST	cortico-striatal-thalamic
DMN	default mode network

DOF	degrees of freedom
DSI	diffusion spectrum imaging
DTI	diffusion tensor imaging
DTM	diffusion tensor model
DSM	Diagnostic and Statistical Manual of Mental Disorders
ECN	executive control network
FEF	frontal eye field
PET	positron emission tomography
fMRI	functional magnetic resonance imaging
fODF	fiber orientation density function
FPR	false positive rate
FSL	fMRI software library
FWHM	full width half max
GLM	general linear model
HCP	Human Connectome Project
ITI	inter-trial interval
LD	lateral dorsal nucleus of the thalamus
LFP	local field potential
LP	lateral posterior nucleus of the thalamus
MCMC	Markov chain Monte Carlo
MD	medial dorsal nucleus of the thalamus
MRI	magnetic resonance imaging

MUA	multi-unit activity
PCC	posterior cingulate cortex
PDMN	posterior default mode network
PG	parietal area “G” of von Economo and Koskinas (1925)
PMC	posterior medial cortex
PROBTRACKX	probabilistic tracking with crossing fibers
RFE	recursive feature elimination
ROC	receiver operator curve
ROI	region of interest
SCP	slow cortical potential
SEM	structural equation model
SNR	signal to noise ratio
STS	superior temporal sulcus
SVM	support vector machine
SZ	schizophrenia
TE	time to echo
TF	temporal area “F” of von Economo and Koskinas (1925)
TH	temporal area “G” of von Economo and Koskinas (1925)
TL	temporal area “L” of von Economo and Koskinas (1925)
TPO	tempero-parieto-occipital
TPR	true positive rate
TR	time to repetition

VA	ventral anterior nucleus of the thalamus
VL	ventral lateral nucleus of the thalamus
vmPFC	ventral medial prefrontal cortex

CHAPTER I

INTRODUCTION

1.1 Significance

Changes in neural energy consumption due to cognitive demands are only about 5% of that at baseline levels (Raichle & Mintun, 2006; Sokoloff et al., 1955). Therefore, most of the what the brain does is ongoing and spontaneous. Spontaneous brain activity, is associated with fluctuations in large-scale functional networks of the brain. Understanding the default mode network (DMN) is necessary for understanding the nature of intrinsic brain activity, because the DMN is the only network more active at baseline than in response to cognitive demands. In addition, disfunction in the DMN is associated with a wide array of neuropsychiatric disorders. Therefore, the functional role of the DMN may be fundamental to healthy brain function.

In this thesis, I aimed to further our understanding of the role of the DMN in healthy brain function by characterizing its anatomical connections and utilizing exploratory techniques to characterize task-evoked changes in DMN activity. The work also furthers our appreciation of the relationship between functional networks and large-scale anatomical structure of neural circuits through subcortical structures.

1.2 Overview of the Introduction

Section 1.3 covers the theoretical underpinnings of magnetic resonance imaging (MRI) and its use in cognitive neuroscience research. Subsections describe the principles of generating contrast in MRI (1.3.1), and in functional MRI specifically (1.3.2), modeling the hemodynamic response function (HRF) (1.3.3) and the neuronal basis of blood-oxygen-level-dependent (BOLD) signal. Leading to the definition of the DMN, Sections 1.3.5 and 1.3.6 introduce the use of task-based fMRI in identifying brain regions that respond to experimental manipulations (activation) and the meaning and interpretation of negative BOLD signal (deactivation). Section 1.3.7 introduces the use of resting-state fMRI in the study of functional brain networks.

In Section 1.4 I review the extant literature on the DMN in some detail. In Section 1.4.1 I begin by describing the discovery of the DMN. The subsequent subsections describe the current state of knowledge on the role of the DMN in cognitive tasks (1.4.2) and its intrinsic activity measured in resting-state fMRI (1.4.3). As the function of the DMN is not known, insight into its role in cognition comes from research characterizing its activity across brain states (1.4.4), over the course of development (1.4.5), in relation to neuropsychiatric disorders (1.4.6), and in other species (1.4.7). In Section 1.4.8 I provide a synthesis on the anatomical connections of individual regions of the DMN from the macaque tracing literature. Dividing the DMN into its anterior and posterior constituents, subsections detail the anatomical connections of six core regions of the DMN. In section 1.4.8.4, I discuss large-scale circuits through subcortical structures known as cortico-striatal-thalamic (STC) circuits and hypothesize on the

DMNs possible connections through such a circuit. Finally, in section 1.4.9, I summarize the current theories of the functional role of the DMN. Section 1.5 provides an overview of the subsequent chapters.

1.3 Magnetic Resonance Imaging

1.3.1 Mechanism of Contrast

Magnetic resonance imaging is a noninvasive technology that is used to produce detailed anatomical images of the brain. A natural property of all biological tissues is magnetic susceptibility which means that the tissue will become magnetized when placed in a magnetic field. MRI makes use of this property using a strong static magnetic field to align protons in the tissue. Larmor resonance frequency describes the relationship between precession frequency of the proton spins and magnetic field strength. Tissue alignment is then perturbed by some angle (flip angle) out of the plane by a series of radio frequency pulses (pulse sequence). The protons spin out of equilibrium and gradually relax back to an equilibrium state aligned with the static magnetic field via two independent relaxation processes each with their own time constant, called spin-lattice (T_1) and spin-spin (T_2) relaxation. Spin-lattice relaxation time (T_1) refers to the time till return to equilibrium in the direction of the static magnetic field. Spin-spin relaxation time (T_2) refers to the relaxation out of the plane of the main magnetic field which is always shorter than T1 relaxation time. The time it takes for the perturbed protons to return to equilibrium depends on the rotational properties of the molecules in the tissue. Different tissues have different relaxation times. The amount of signal measured depends

on the density of aligned protons in the tissue. Contrast in the MR image results from differences in the aligned proton density at tissue boundaries. For example, fluids have long T_1 (1500-2000ms) whereas fat has short T_1 (100-150ms). Therefore, differences in tissue proton density, T_1 and T_2 relaxation properties make up the basis of contrast in all MR images. Pulse sequences can be designed to accentuate different tissue types by varying the time between pulses that perturb alignment (time to repetition (TR) between successive pulses) and the time between measurements (time to echo (TE) between pulse and measurement). Pulse sequences with different combinations of flip angle, TR and TE are used to emphasize the effects of T_1 or T_2 relaxation times for different imaging purposes. Structural MRI images are typically T_1 weighted images in which tissues with long T_1 relaxation times appear dark and tissues with short T_1 relaxation times (fat/lipid) are bright. However, the signal alone is insufficient to produce an image because there is no way to assign signal to the area in 3d space where it originated. Spatial localization of the MR signal requires the use of 3 additional orthogonal linear gradient magnetic fields (x,y,z) measured in mTm^{-1} (millitesla per meter) which influence the resonant frequency of the spins along the gradient. An RF pulse applied at a given frequency will result in a resonant magnetic signal, which can be detected using a receiver tuned to the same frequency (Hopf, 1985). Gradients are normally applied transiently so frequency measurements can be used to distinguish between signals at different positions in three dimensional space. The 3d image is created by exciting and sampling with different pulse frequencies and phases, measuring the spectrum of the object being imaged. This process is known as k-space sampling and results in a matrix of spatial frequencies.

Each point in k-space is a spatial frequency component. The data are then Fourier transformed to produce a final image (McRobbie et al., 2017).

1.3.2 Functional Magnetic Resonance Imaging

Functional Magnetic Resonance Imaging (fMRI) is a technique that is used to detect metabolic changes over time associated with brain activity rather than static images of brain structure. It is based on a series of T_2 weighted images that make use of changes in magnetic susceptibility resulting from activity-dependent changes in blood oxygenation. Changes in magnetic susceptibility occur because deoxygenated blood is paramagnetic, giving it a stronger magnetic susceptibility than oxygenated blood. Local changes in magnetic susceptibility result in local field inhomogeneities. The most common pulse sequences used to collect fMRI images are sensitive to field inhomogeneities that can shorten spin-spin relaxation times (T_2^*) and therefore contain the effects of both T_2 and T_2^* relaxation. A process called neurovascular coupling describes the relationship between neuronal activity and associated changes in cerebral blood flow (CBF). Oxygen use by active cells temporarily increases the amount of local deoxyhemoglobin, inducing dephasing, which shortens T_2^* and results in a decrease in signal intensity. Then the surrounding neurovasculature responds by increasing blood flow to the region, delivering an excess of oxygenated blood which results in an increase in signal intensity. Therefore, increases in neuronal activity are detectable, because of the neurovascular response it produces, which is called the hemodynamic response. The resulting activity-dependent changes in signal intensity are referred to as blood-oxygen-

level dependent (BOLD) signal (Huettal, 2010). A complex relationship between transient and baseline levels of cellular activity, CBF, cerebral blood volume (CBV), and the local metabolic rate of oxygen consumption ($CMRO_2$) underly the BOLD signal. Simplified models of neurovascular coupling, described in the following section, are used to draw inferences about changes in neural activity.

1.3.3 Model of the Hemodynamic Response Function

Because fMRI relies on BOLD signal as an indirect measure of cellular activity, hemodynamic models are of critical importance to the interpretation of fMRI studies. Models of the hemodynamic response must explain the process of neurovascular coupling linking changes in cellular activity with changes in CBF, CBV and changes in $CMRO_2$ as well as describe the resulting transient dynamics in local deoxyhemoglobin concentration that underlie the BOLD signal. The mechanics of steady state increases in CBF and CBV have been determined empirically to follow a power law function (Grubb et al., 1974) of the form:

$$v = f^{\alpha} \quad (1)$$

where α is a approximately 0.4 and:

v = CBV normalized to baseline

f = CBF normalized to baseline

In response to increases in neural activity, relaxation of the smooth muscles of arterioles allow for increases in both CBF and CBV. The relationship between changes in CBF and changes in cerebral rate of oxygen consumption is approximately linear with changes in CBF roughly 2-3 times that of $CMRO_2$ (Davis et al., 1998; Hoge et al., 1999; Kastrup et al., 2002; Marrett & Gjedde, 1997; Seitz & Roland, 1992). Local oxygen concentration depends on changes in CBF, $CMRO_2$ and the fractional rate of oxygen extraction E.

$$CMRO_2 = E \cdot C_a \cdot CBF \tag{2}$$

where:

C_a is the arterial oxygen concentration

E is the net oxygen extraction fraction

Equation (2) expresses the empirical relationship between transient cellular activity, CBF and the fractional rate of oxygen extraction from the blood known as neurovascular coupling. Increases in neural activity lead to increases in oxygen and glucose consumption, followed by an increase in CBF. Oxygen consumption increases much less than CBF, leading to a net increase in the amount of oxygen present. This oversupply of oxygen due to the mismatch between CBF and oxygen consumption is the basis of the BOLD signal. Whether vascular responses to neuronal activity are the result of a passive diffusion process (Attwell & Iadecola, 2002), an active process mediated by neurotransmitters and astrocytes (Harder et al., 1998; Pellerin & Magistretti, 2004) or

some combination of mechanisms (Attwell & Iadecola, 2002; Lauritzen, 2005; Uludag et al., 2004) is an ongoing topic of research. For the purpose of BOLD data, the model must also account for the effects of transient changes in magnetic susceptibility. The MR signal (S) is believed to have an exponential dependence on TE.

$$S = S_{max} e^{-TE \cdot T_2^*} \tag{3}$$

Where S_{max} is the maximum expected signal intensity if TE = 0. T_2^* is assumed to include the effects of both T_2 and T_2^* relaxation. Experiments indicate that changes in magnetic susceptibility can be modeled as a linear function of the local concentration of deoxyhemoglobin and that this quantity in turn can be expressed in terms of the change in the oxygen extraction fraction E.

$$\frac{\Delta S}{S_0} \approx A[\,1 - \frac{V}{V_0}(\frac{E}{E_0})^{\beta}\,] \tag{4}$$

Where A = 0.079 is an experimentally determined constant that depends on TE (Davis et al., 1998), β is ~ 1.5. V_0 ~ 3% represent baseline levels of veinous volume and and E_0 baseline levels of oxygen extraction. Equation (4) is biophysical model that describes the expected change in BOLD signal with a change in blood flow, but does not model the temporal dynamics of the BOLD signal. BOLD signal exhibits an initial dip due to the initial increase in deoxyhemoglobin (Ernst & Henning, 1994; Hu et al., 1997; Menon et al., 1995; Devor et al., 2003), followed by a signal increase that lags behind increased

neural activity by about 1-2 seconds for brief stimuli (Bandettini et al., 1992), reaches a plateau after 4-10 seconds (Buxton et al., 1998) for sustained stimulus, and then gradually returns to baseline. The BOLD signals has been found to exhibit temporal nonlinearities including a refractory period that may last up to 30 seconds (Frahm et al., 1996; Kruger et al., 1996) and the response to repeated stimulation does not add linearly (Birn et al., 2001; Boynton et al., 1996; Friston et al., 1998). These observed transient BOLD dynamics have been described using the Balloon model (Buxton et al., 1998) in which veinous flow dynamics are described as flow f(t) in and out of a flexible balloon (Figure 1.1). The hemodynamic response is defined by time dependent functions of blood volume v(t) and amount of deoxyhemoglobin q(t).

$$\frac{dq}{dt} = \frac{1}{\tau_{MTT}}\left[f(t)\frac{E(t)}{E_0} - \frac{q(t)}{v(t)} f_{out}(v,t)\right] \tag{5}$$

$$\frac{dv}{dt} = \frac{1}{\tau_{MTT}}\left[f(t) - f_{out}(v,t)\right] \tag{6}$$

$$f_{out}(v) = v^{\frac{1}{\alpha}} + \tau \frac{dv}{dt} \tag{7}$$

where:

E_0 is the resting value of oxygen extraction ~ 0.4, τ_{MTT} is the mean transit time through the vein at rest, based on a cerebral blood flow of 60 ml min^{-1} 100 ml^{-1} of tissue ~ 3s and V_0 is the resting volume fraction 0.03 (Buxton et al., 2004)

To account for the undershoot of the BOLD signal after stimulus, the Balloon model proposes an uncoupling of the CBV and CBF dynamics based on the observation that CBV returned to baseline more slowly than CBF (Mandeville et al., 1998). The following equation allows for the possibility of transient independent changes in blood flow that relax back to a new steady state power law relationship after some time constant τ. This model with a time constant $\tau > 0$ predicts the observed late undershoot response. However, it has not been conclusively demonstrated that independent blood volume and blood flow dynamics are the true mechanistic explanation for the observed late BOLD signal undershoot. Blood flow, however, is a measurable quantity using MRI techniques. It has therefore been proposed that changes in blood flow be measured directly with fMRI using MRI sequences for arterial spin labeling, which provide a quantitative measurement of cerebral blood flow using magnetically labeled arterial blood as an endogenous tracer. However this is not yet a common practice in fMRI studies. It is important to note that each model expression depends on a baseline level of blood volume and oxygen metabolism that may differ significantly across brain regions. Studies of oxidative metabolism using arterial spin labeling found that baseline levels of blood flow vary significantly across the cortex (Davis et al., 1998). Based on our current understanding of the relationships between BOLD signal and CBF changes, regional heterogeneity in CBF indicates that the magnitude of functionally induced changes will also vary across regions. Differences in the temporal response of the hemodynamic response across brain regions have also been identified (Miezin et al., 2000; Chang et al., 2008).

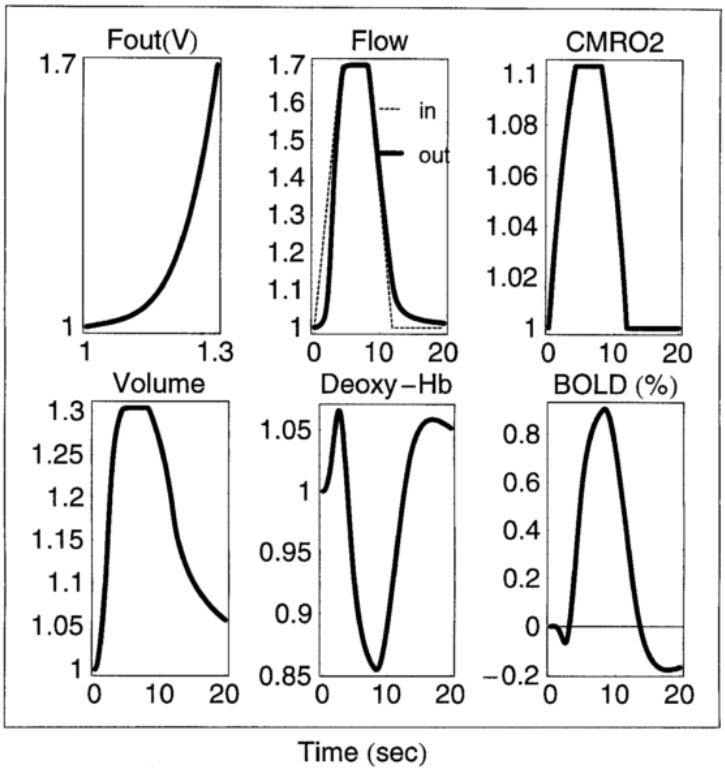

Figure 1.1 Balloon Model of the Hemodynamic Response Function

From " Dynamics of Blood Flow and Oxygenation Changes During Brain Activation: the Balloon Model," by R.B. Buxton, E.C. Wong, L.R. Frank, 1998, *Magnetic Resonance in Medicine : Official Journal of the Society of Magnetic Resonance in Medicine / Society of Magnetic Resonance in Medicine*, 39(6), p. 859. Copyright 1998 by the International Society for Magnetic Resonance in Medicine.

1.3.4 Neuronal Basis of the BOLD signal

Many aspects of neuronal function contribute to cellular metabolism, including the maintenance of membrane potentials, processing synaptic inputs, and cellular firing. However, synaptic activity accounts for the largest share, up to 80% of the brain's energy

usage, due to the metabolic demands of neurotransmitter cycling (Shulman, 2001; Shulman, 2004) and membrane potential maintenance. The relationship between BOLD signal and cellular events has been characterized using simultaneous measurements of fMRI and extracellular recordings. Extracellular recordings measure the summed action potentials and synaptic voltages from hundreds of neurons (Lorente deNo', 1947; Bishop & O'Leary, 1942) depending on the size and placement of the extracellular electrodes. Filtering this signal with a high-pass filter yields so-called multi-unit activity (MUA), containing the high frequency spiking behavior of nearby cells. Low-pass filtering produces a waveform that reflects the local field potential (LFP) which reflects the population average of lower frequency electrical synaptic activity (Ajmone-Marsan, 1965; Fromm & Bond, 1964) and membrane oscillations (Bullock, 1997). Simultaneous measurements of local field potentials and multi-unit spiking activity in combination with BOLD revealed that LFPs have the highest correspondence to BOLD signal (Hyder et al., 2002; Smith et al., 2002a; Logothetis et al., 2001). That is, in instances when MUA and LFP were in disagreement, the LFP predicted 7.6% more variance than the MUA (Logothetis et al., 2001). This suggests that BOLD signal reflects synaptic rather than firing activity (Lauritzen & Gold, 2003; Logothetis, 2002; Logothetis et al., 2001; Lauritzen, 2001). This finding has significant implications for the interpretation of fMRI studies as BOLD signal may reflect the combined effects of sub-threshold modulatory influences, excitatory or inhibitory synaptic activity.

LFPs are generally studied within specific band limited frequency ranges: slow cortical potentials (SCP) < 1 Hz; delta 1–4 Hz, theta 4– 8 Hz, alpha 8–12 Hz, beta 12–24

Hz, and gamma >24 Hz. A survey of the literature does not suggest a 1:1 correspondence between BOLD signal and any specific frequency band. All LFP bands explain some portion of the BOLD variance (Goense & Logotthetis, 2008; Scheeringa et al., 2011). However, oscillations in the SCP and gamma band have been the focus of much of this research. SCPs are believed to represent fluctuations in cortical excitability (Birbaumer et al., 1990) and gamma band activity is believed to underlie binding of features of cognitive processes across brain regions. SCPs modulate gamma band fluctuations (Leopold et al., 2003) such that gamma band power is dependent on the phase of the SCP. This is known as cross-frequency or phase-amplitude coupling. Cross frequency coupling has been proposed as a mechanism for neuronal communication, whereby fluctuations in excitability create temporal windows for communication (Pulvermüller, 1995; Fries, 2005; Fries, 2009). Accordingly, fluctuations in BOLD signal were found to be positively correlated with gamma and modulated by SCPs (Scheeringa et al., 2011; Koch et al., 2012). SCPs have a similar correlation structure to the BOLD signal across waking states, slow wave sleep and rapid eye movement sleep (REM) (He et al., 2008). In contrast, correspondence between BOLD signal and gamma band activity was found in waking states and REM sleep but was absent from SWS (Nir et al., 2008), which was attributed to gamma oscillations' purported role in conscious experience (Rodriguez et al., 1999). BOLD signal is correlated with increased gamma associated with sensory stimulation in both humans (Nir et al., 2007) and non-human primates (Niessing et al., 2005; Goense & Logothetis, 2008) as well as spontaneous gamma-band activity (Hutchinson et al., 2015). Therefore, while the relationship between BOLD and cellular

function is a complex one, BOLD signal appears to capture important aspects of increased synaptic activity and coherent brain activity across regions related to sensory and cognitive processing.

1.3.5 Task-Based fMRI

Task-based fMRI experiments are used to infer the cognitive functions associated with brain regions. Over the last decade, fMRI has been used to study a wide range of cognitive tasks, including but not limited to, visual perception, language, memory, and social cognition. Prior to the use of fMRI, lesion studies had already yielded insights into regional functional specialization in the brain (Broca, 1861; Wernicke, 1874; Scoville & Milner, 1957). However, fMRI gave researchers the ability to design specialized tasks to probe and differentiate the functional roles that different brain regions play in higher order cognitive abilities as well as to infer networks of regions that activate together. Experimental designs in fMRI have relied on the assumption that neural activity associated with an experimental manipulation results in increases in cellular activity relative to some control condition. Based on the concept of pure insertion, experimental manipulations are assumed to evoke linearly increasing activity above that of the control condition. Under these assumptions, the choice of a baseline condition is one of critical importance. A common control condition is the so-called rest condition, where subjects are asked to keep their eyes open and fixate on a white crosshair at the center of a dark screen. Other studies have created carefully constructed control conditions designed to isolate the cognitive function of interest, but still rely on the

assumption of linear signal increase relative to that control condition. Linear models are generally employed to identify regions who's brain activity increases in response to task demands and subsequently thresholded to reduce the chance of finding brain activation by chance. As detailed in section 1.3.3, the BOLD signal is delayed from increased neural activity by several seconds and exhibits nonlinearities associated with events occurring within this period resulting in limited temporal resolution. Therefore, experimental manipulations are often presented in experimental blocks of 30 seconds or more interspersed with rest periods to allow the BOLD signal to return to baseline (Maus et al., 2012). The hemodynamic response function can be thought of as a temporal point spread function which smooths and delays the neural correlates of sensory processing. Therefore, resulting correlations between evoked changes in neuronal activity and measured hemodynamics will be both displaced and broadened in time. To detect the brain activity of interest an HRF is convolved with the experimental design. In practice, biophysical models of neural and hemodynamic processes are not generally used for analysis of fMRI data. A commonly used hemodynamic model is the double gamma function, a lagged positive function with full width at half maximum of about 4 seconds, and a small, delayed, inverted gamma, to model the late undershoot. Analysis proceeds in a univariate matter such that each image voxel is treated as an independent variable. The null hypothesis is that there are no significant activations that correlate with experimental manipulations (Friston, 1991; Worsley, 1992) . For example, the linear model in the case of an experimental design with a single condition would be:

$$y_i(t) = \beta_i \cdot x(t) + b_i + e_i(t) \quad (8)$$

where x(t) is the HRF convolved experimental design, b_i is an average value during a control condition, and $e_i(t)$ is error. The calculated amplitude of β_i from the linear model provides an estimate of the relative strength of the relationship between BOLD signal in voxel i and the experimental design. BOLD signal is also known to have significant spatial autocorrelation reducing the true degrees of freedom. Spatial autocorrelation is taken into consideration when determining the statistical significance of the β_i values (Woolrich et al., 2005).

As pointed out in section 1.3.3 the hemodynamic response can vary significantly across brain regions. As a result, the choice of HRF when modeling fMRI data can have a significant impact on the analysis (Lindquist et al., 2009). Differences in latency estimates between the true HRF and the standard double-Gamma HRF lead to false negatives, while differences in HRF peak width between the model and data lead to smaller magnitude estimates (Handwerker et al., 2004). In addition, the assumption of pure insertion is that cognitive processes do not interact. Subtraction of brain activity evoked in one condition from another is only valid if this assumption holds. However, there is much evidence to indicate that cognitive processes do interact (Sidtis et al., 1999). Spontaneous activity measured in resting-state interacts with task-evoked activity (He, 2013; Northoff et al., 2010) in a behaviorally relevant manner (Friston et al., 1996; Weissman et al., 2006; Boly et al., 2007; Mennes et al., 2010). Task-evoked activity can also impact subsequent regional interactions measured at rest (Lewis et al., 2009; Albert

et al., 2009). These observations strongly suggest the use of more sophisticated analysis techniques such as multivariate pattern analysis or state space models which allow characterization of the spatiotemporal dynamics of the BOLD signal (Mastrovito, 2013).

1.3.6 Negative BOLD Signal

Negative BOLD signal, sometimes called deactivations, refer to task-evoked decreases in BOLD signal intensity when compared to a resting condition, or resulting from a contrast or subtraction performed between two experimental conditions of interest. Negative BOLD signal therefore refers to a relatively lower signal in one condition vs. another. Like activations, deactivations are dependent on the choice of baseline condition (Fransson et al., 1999). Negative BOLD signal is often detected by inverting the design matrix described in section 1.3.5 in order to find regions whose signal decreases relative to the baseline condition. The mechanisms that underlie negative BOLD responses are unclear. There are several possible explanations for such decreases. Negative BOLD could reflect passive shunting of oxygen rich blood to adjacent areas whose cellular activity has increased, the so-called vascular steal effect (Logothetis et al., 2001). This explanation is based on the idea that steady blood supply to active tissue necessitates decreases in blood flow to inactive areas. However, there is evidence that the circulatory system can support large changes in demands by increasing cardiac output (Plum, 1968; Posner, 1969) and blood flow in the brain can also be increased by reducing vascular resistance (Reivich, 1964). Passive shunting is more likely to be a localized effect whereas decreases in BOLD signal are often identified far from the regions of increased

signal (Shulman et al., 1997). Decreased BOLD signal could also be the result of active neural processes including active inhibition or decreases in excitatory input. Coupling spiking activity and LFP measurements with fMRI in monkey visual cortex, negative BOLD signal was associated with decreases in corresponding cellular firing rates when visual stimuli were outside of the cell's receptive fields (Shmuel et al., 2006). The correspondence of time courses of negative BOLD relative to decreases in neuronal activity suggested that negative BOLD signal could not be attributed to passive decreases in cerebral blood flow to the area. Another study combining optical imaging with multiunit spike activity during hindlimb stimulation in the rat, also found that decreases in hemodynamic signal were associated with decreases in spiking activity (Yin et al., 2011). Targeting specific calmodulin-dependent protein kinase II (CaMKIIα) excitatory neurons in rat primary motor cortex, a more recent study pairing optogenetics with high field fMRI found positive evoked BOLD signals in both the region of stimulation as well as in their thalamic targets (Lee et al., 2010). The same study found that optically driving inhibitory parvalbumin-positive cells gave rise to a region of negative BOLD signal surrounding a positive BOLD signal consistent with the properties of lateral inhibition. However, in regions that have a large number of inhibitory neurons, such as is the case in structures within the basal ganglia, it is possible for increases in BOLD signal (likely associated with increased GABAergic synaptic activity) to be associated with decreases in cellular firing rate. One recent study in rats combining electrophysiological measures with high field fMRI found such a dissociation between BOLD and multiunit activity in the caudate and putamen during whisker stimulation (Mishra et al., 2011).

Overall, the evidence suggests that negative BOLD signal results from active processes resulting in decreases in cellular firing rate.

1.3.7 Resting-state fMRI

Task-based studies obscure the fact that most of the what the brain does is ongoing and spontaneous. Changes in neural energy consumption due to cognitive demands are only about 5% of that at baseline levels (Raichle & Mintun, 2006; Sokoloff et al., 1955). Therefore, task-related increases in BOLD signal represent only a small fraction of the brain's activity. Constant neural activity is required to monitor all bodily functions, maintain homeostasis, and continually process sensory and interoceptive information. fMRI in the absence of a task, called resting-state fMRI, measures synchronous ongoing activity in the brain. Coherent brain activity in the absence of an explicit experimental manipulation was first discovered in the sensory motor system (Biswal et al., 1995). This result was replicated in other functionally defined networks (Fox & Raichle, 2007; Cordes et al., 2000) including those supporting auditory, visual (Lowe et al., 1998) and language processes (Hampson et al., 2002). This lead to the idea that intrinsic brain activity could be an avenue for studying brain networks without the potential confounds of specific task demands. Approaches for analysis of resting-state data include seed-based approaches (Biswal et al., 1995), independent component analysis (Beckmann et al., 2005), graph methods (Power et al., 2011; Behrens et al., 2012; Bullmore & Sporns, 2009), clustering algorithms (Lee et al., 2012; Golland et al., 2008; Cordes et al., 2002), multivariate pattern classifiers (Zhong et al., 2017; Anderson

et al., 2011) and functional connectivity (correlation) (Yeo et al., 2011). Using these techniques the entire cortex of the brain has been parceled into a map of constituent networks with patterns of activity that are preserved across scanning sessions and across subjects (Shehzad et al., 2009; Chen et al., 2008) despite the unconstrained nature of the measured activity. Studies have indicated that there are likely between 10 and 15 major brain networks (Shirer et al., 2012; Smith et al., 2012; Damoiseaux et al., 2006; De Luca et al., 2006; Beckmann et al., 2005). In addition to a sensory motor network, identified networks include those that support visual processing, attention (ventral and dorsal networks), executive function, auditory processing, memory and language. Although functional connectivity can be detected between brain regions in the absence of direct anatomical connections (Honey et al., 2009), the observed patterns of functional connectivity are consistent with large-scale structural connections between brain areas (Meier et al., 2016; Honey et al., 2010; Skudlarski et al., 2008). Anatomical connectivity alone can account for up to 15% of the variance in functional connectivity in resting-state scans (Messe' et al., 2014). Over development, the organization of resting-state activity into functional networks has been shown to mature in conjunction with white matter fiber tracts (Hagmann et al., 2010; Olesen et al., 2003). Therefore, ongoing brain activity measured in the resting-state contains information about the intrinsic network-level organization of the brain. There is evidence that this activity may represent a larger set of spatio-temporal patterns of activity from which task-evoked activity is sampled (Luczak et al., 2009). For example, variance in metabolic activity decreases from resting levels during explicit task engagement (He et al., 2013) and functional connectivity during task

performance is primarily shaped by intrinsic architecture (Greicius et al., 2003; Cole et al., 2014; Chu et al., 2012). In addition, there is a large and growing body of literature showing that resting-state fMRI in combination with multivariate pattern analysis and machine learning techniques can distinguish aberrant patterns of brain activity associated with a large number of neurologic and psychiatric disorders (Mastrovito et al., 2018; Nielsen et al., 2013; Cecchi et al., 2009).

1.4 The Default Mode Network

1.4.1 Discovery of the Default Mode Network

The overwhelming majority of cognitive neuroscience studies report only the set of regions that exhibit task-evoked activations. They do not generally report regions exhibiting task-evoked decreases in BOLD signal. The first study to examine task-evoked decreases, analyzed a series of nine positron emission tomography (PET) experiments. The experiments included one color/motion/shape discrimination task, three visual search tasks varying color, form, eccentricity and motion, one spatial attention task, two language tasks varying reading vs verb-generation, and a task involving recall of word lists (Shulman, 1997a). A set of brain regions were found to exhibit task-evoked decreases in metabolic activity across all nine of these tasks relative to a passive resting-state condition (Shulman, 1997b). Shulman identified these regions as posterior cingulate cortex (PCC) (Brodmann area (BA) 31), precuneus (BA 7), bilateral inferior parietal cortex (BA 40), left dorsolateral frontal cortex (BA 8), left lateral inferior frontal cortex (BA 10/47), left inferior temporal gyrus (BA 20), medial

frontal cortex (BAs 8, 9, 10, 32), as well as the right amygdala. Shulman noted that these decreases did not appear to be related to vascular steal effect since decreases were not accompanied by increases in neighboring regions and also occurred in the absence of a common set of increases across tasks. However, it was not clear from this study whether signal decreases reflected task-evoked inhibitory processes, such as those that might suppress task-irrelevant sensory information, or the cessation of ongoing processes in the passive condition. In order to discriminate between these two possibilities, Raichle et al., compared the blood oxygen extraction fraction (OEF) (a ratio of oxygen usage relative to oxygen delivery via blood flow) in these regions in a passive condition to hemispheric average OEF values (Raichle et al., 2001). The OEF is relatively uniform throughout the brain at rest (Lebrun-Grandie et al., 1983, Raichle et al., 2001), and accordingly their analysis failed to find any regions with OEF values significantly below hemispheric averages (which would have signified activations relative to the mean). This result, suggests that these regions were not activated at rest, but rather exhibit a high level of baseline activity. They concluded that there was "an organized, baseline **default mode** of brain function that is suspended during specific goal directed behaviors". As as result, this network became known as the Default Mode Network (DMN).

1.4.2 DMN in task-based fMRI

Since the discovery of the DMN, studies using both PET and BOLD measurements have consistently reported deactivation in DMN regions across a wide variety of task conditions (Mazoyer et al., 2001; Laird et al., 2009). Some found

increased deactivation in DMN regions associated with increased task difficulty (Harrison et al., 2011) and with better task performance (Weissman et al., 2006 ; Boly et al., 2007; Kelly et al., 2008; Minzenberg et al., 2011; Sala-Llonch et al., 2012; Douw et al., 2016). High baseline activity in the DMN in combination with the behavioral relevance of task-evoked deactivation has been interpreted as an indication that task-evoked deactivation in the network is related to cessation of internal rumination required to redirect attentional resources. However, the evidence on the relationship between DMN deactivation and task difficulty and performance is far from conclusive. In Shulman's initial discovery of task-evoked deactivation, he noted that decreases were not influenced by changes in difficulty in either visual processing or language tasks (Shulman et al., 1997b). It has also been noted that strong correlation within the DMN remains even during task-associated deactivation (Greicius et al., 2003; Greicius & Menon, 2004). Increased connectivity between the posterior cingulate and the superior frontal gyrus was shown to result in faster reaction times in motor tasks (Vatansever et al., 2015). BOLD signal measured during task performance in the DMN contains task-specific patterns that can be used to distinguish task conditions (Crittenden et al., 2015). Furthermore, not all experimental paradigms evoke decreases in DMN regions. Task-evoked increases in the DMN have been reported for tasks involving autobiographical memory (Cabeza, 2004), self-referential processing (Gusnard et al., 2001; Buckner & Carroll, 2007; Andrews-Hanna et al., 2010b), theory of mind (Amodio & Frith, 2006; Carrington & Bailey, 2009), semantic processing (Binder, 2009), task-switching (Crittenden et al., 2015), planning for the future (Baker et al., 1996; Spreng et al., 2010),

working memory (Andreasen et al., 1995), and action monitoring (Luu et al., 2000) (for reviews, see Buckner et al., 2008; Spreng et al., 2009). A comparison has been made between this collection of activities that evoke activations in the DMN and cognitive functions likely to make up stream of consciousness or daydreaming occurring in resting state.

1.4.3 DMN during Resting-state fMRI

Studies of resting-state functional connectivity universally find a coherent set of brain regions corresponding to the DMN. The DMN network is so prominent that it is found no matter the analysis technique applied whether whole-brain functional connectivity, seed-based analysis (Greicius, 2003), PCA/ICA (Beckmann et al., 2014), or clustering analysis (Golland et al., 2008). Studies of cerebral blood flow, measured using arterial spin labeling (Chen et al., 2015), found that blood flow was significantly higher in DMN regions both during rest (Zou et al., 2009) and during task performance (Pfefferbaum et al., 2011). Patterns of functional connectivity in the resting-state reflect, in large part, the underlying pattern of structural connectivity through commissural, associative, and projection fibers (Skudlarski et al., 2008). As such it constitutes the large-scale intrinsic pathways of the brain which closely resemble those measured during task manipulations (Greicius et al., 2003; Cole et al., 2014). It is believed that the intrinsic pattern of temporal activity in the DMN is negatively correlated with a network corresponding to a combination of parts of the executive control (Greicius et al., 2003; Fair et al., 2007, Seeley et al., 2007) and dorsal attention networks (Corbetta & Shulman,

2002, Fox et al., 2006), called the task-positive network (TPN). However this relationship is controversial because of an applied preprocessing technique that is known to induce negative correlations (Fox et al., 2009). An electrophysiological study in cats found anticorrelations between the two networks occurred only 20% of the time (Popa et al., 2009), suggesting a relationship with both cooperation and antagonism. A resting-state study using self-report of mind-wandering found that the process of mind wandering recruited the DMN as well as the executive control network (Christoff et al., 2009). Using a group temporal ICA to divide resting-state data into spatial patterns with independent time courses, several patterns ("temporal functional modes" (TFMs)) contained DMN network regions. In one pattern, DMN is anticorrelated with the task positive network and in another it is not (Smith et al., 2012). A more recent study found that each region of the DMN had a functional connectivity gradient with regions in the attention network that strengthened over the course of development (Anderson et al., 2011). Some have suggested that anticorrelation between the two networks is mediated by competition between them for cognitive and metabolic resources (Fox et al., 2005; Kelly et al., 2008) based on a balance between internally and externally directed attention (Golland et al., 2008; Salomon et al., 2014). Other have suggested that the relationship between the two networks is mediated by the anterior insula (Sridharan et al., 2008). Variability in the strength of the anticorrelation between the two networks was found to be behaviorally relevant, with stronger anticorrelation related to less variation in reaction time (Kelly et al., 2008). However, correlation between the two networks has been reported during tasks that evoke activation rather than deactivation in the DMN, calling

into question the intrinsic nature of anticorrelation between them.

The DMN is sometimes partitioned into two main subdivisions dividing the anterior and posterior halves of the network based on resting-state temporal dynamics (Damoiseax et al., 2006). Posterior parts of the DMN are more strongly correlated with the hippocampal gyrus and lateral parietal cortex and more negatively correlated with the task positive network than anterior parts of the network (Greicius et al., 2003; Yu et al., 2011). Dissociation between anterior and posterior DMN has also been reported in their responses to modulation via serotonin (Hahn et al., 2012). The division between spontaneous patterns of functional connectivity in anterior and posterior parts of the network suggests that the DMN does not function as a single unit. Anterior and posterior regions likely have different dynamic interactions with other networks related to differences in their anatomical connections (Vogt et al., 1979) as well as their role in cognition. In addition, there is some evidence for further subdivision of the medial posterior cingulate and precuneus, separating limbic and associative cognitive networks (Cavanna & Trimble, 2006; Parvizi et al., 2006; Vogt et al., 2006; Laird et al., 2009; Yu et al., 2011; Leech et al., 2012).

1.4.4 DMN across brain states

Spontaneous brain activity with spatiotemporal patterns similar to those measured in the resting state persist across levels of conscious awareness, (Hobson & Pace-Schott, 2002), in sleep (Fukunaga et al., 2006; Larson-Prior et al., 2009), and under anesthesia (He et al., 2008; Breshears et al., 2010; Liu et al., 2015). Coherent

fluctuations in the DMN persist with loss of consciousness (Greicius et al., 2008) and are present even in a vegetative state; their absence has come to define brain death (Boly et al., 2009). As sleep stages progress (S1 – S2 - SWS), several changes occur in the functional connectivity patterns of the DMN. Functional connectivity between PCC and and parahippocampal gyrus is present in SWS but is decreased in early sleep stages (Sämann et al., 2010). The anticorrelated activity in DMN and task positive network becomes uncorrelated during S2 and SWS (Sämann et al., 2010). Most pronounced is a reduction in the strength of connectivity between the PCC and ventral medial prefrontal cortex (vmPFC) (Greicius et al., 2008; Horovitz et al., 2009; Sämann et al., 2011) as sleep stages progress. A reduction in functional connectivity between anterior and posterior DMN begins with sleep pressure (Sämann et al., 2010; De Havas et al., 2012), and sees its largest decrease with transition from wakefulness into the early stages of sleep as conscious awareness is lost. Therefore, it has been suggested that coupling between anterior and posterior DMN regions, may support conscious awareness (He & Raichle, 2009). However, significant functional connectivity between anterior and posterior DMN persist through SWS and under anesthesia which suggest that coherent DMN activity may also support fundamental aspects of homeostatic maintenance unrelated to self-awareness or conscious thought (Buckner et al., 2008; Horovitz et al., 2008).

1.4.5 DMN Throughout Development

Functional connectivity of the DMN changes in a behaviorally relevant manner across the human lifespan. At birth, the DMN does not appear to be a coherent network (Gao et al., 2009). However, by one to two years of age the DMN becomes spatially similar to that observed in adults (Gao et al., 2009). The anterior part of the DMN is a region of the brain that develops more slowly than other brain areas (Huttenlocker & Dabholkar, 1997; Johnson, 2001), experiencing high growth rates later in development between the ages of 5 and 11 (Sowell et al., 2004) and is one of the last brain regions to myelinate (von Bonin, 1950). As such, functional connectivity patterns of the DMN continue to change over the course of development. The DMN is still only weakly functionally connected before adolescence (Fair et al., 2008), especially connectivity between anterior and posterior DMN regions. During adolescence, functional connectivity between anterior and posterior DMN strengthens. At the same time, network segregation becomes more pronounced in the form of decreased connectivity between networks (Fair et al., 2007; Anderson et al., 2011; Sherman et al., 2014). These changes correspond to developmental increases in both within and between network white matter tracts and is correlated with IQ (Uddin et al., 2011; Sherman et al., 2014). However, in addition to the maturation of structural connectivity, some have suggested that it is the coactivation of these regions over time that increases their connectivity strength in a Hebbian manner (Bi & Poo, 1999). The adult pattern of DMN functional connectivity is characterized by strong connectivity within the DMN and smoothly varying gradients of connectivity between each node of the DMN and those of the TPN,

ranging from weak negative correlation to positive correlation (Anderson et al., 2011). This organization is proposed as a mechanism for balancing activity between the DMN and the TPN. In coordination with age-related cognitive decline, connections between anterior and posterior parts of the DMN are disrupted (Andrews-Hanna et al., 2007; Damoiseax et al., 2008). Therefore, as children mature and develop the ability to perform cognitive tasks, such as episodic memory formation/retrieval and theory of mind, connectivity within the DMN continues to strengthen. Cognitive decline is associated with decreases in connectivity between the same brain regions within the DMN. The developmental trajectory of DMN connectivity suggests that coherent DMN activity is necessary for healthy brain development and that the development of brain maturation involves a balancing of activity across networks (Supekar et al., 2009).

1.4.6 DMN in Disease

Changes in connectivity of the DMN have been associated with a wide range of neurological and neuropsychiatric disorders (for reviews see Buckner et al., 2008; Anticevic et al., 2012; Roberto et al., 2016) including depression (Sheline et al., 2009; Posner et al., 2016), obsessive-compulsive disorder (Beucke et al., 2014; Gonçalves et al., 2017), ADHD (Liddle et al., 2011; Sun et al., 2012), bipolar disorder (Liu et al., 2012; Wang et al., 2016;), schizophrenia (Bluhm et al., 2007; Harrison et al., 2007), autism (Assaf et al., 2010; Washington et al., 2014), Alzheimer's (Greicius et al., 2004; Wang et al., 2007a; Buckner et al., 2008), post-traumatic stress disorder (Daniels et al., 2010; Lanius et al., 2010), and even Parkinson's disease (Van Eimeren et al., 2009; Zhang et al.,

2015). In addition, disease specific treatments restore normal DMN functional connectivity patterns (Mayberg et al., 2005; Delaveau et al., 2010; Lorenzi et al., 2011). Despite the variation in disease etiologies and symptoms across these disorders, studies find disruption in DMN functional connectivity that correlate with disease severity. Of course, DMN connectivity is differentially altered across these disorders. For example, in depression, increases in DMN functional connectivity are associated with the tendency for negative rumination (Zhu et al., 2012). In contrast, decreases in DMN connectivity are associated with severity of cognitive impairment and memory disruption in Alzheimer's (Hafkemeijer et al., 2012). The literature on the role of the DMN in each of these disorders is vast and outside the scope of this brief introduction. There is however, a growing understanding that a common feature over a spectrum of neurological disorders is an imbalance in excitatory and inhibitory influences across brain networks (Yizhar et al., 2011; Anticevic et al., 2017; Foss-Feig et al., 2017; Tatti, 2017). Dysfunction at many levels of organization, from the synaptic to large-scale structural connectivity can lead to such imbalances. Variations on the pathways that lead to excitatory/inhibitory imbalances may explain the spectrum of resulting behavioral phenotypes, but may also explain the DMNs ubiquitous involvement across so many different disorders. The DMN is consistently described in opposition to the TPN and tuning in the pattern of this relationship continues to mature over the course of brain development (Anderson et al., 2011). In addition, the DMN, and particularly the precuneus and PCC are structural hubs connecting many other brain regions (Hagmann et al., 2008; Segall et al., 2012). Therefore, any regional or network-level imbalance in

excitatory and inhibitory influences is likely to impact DMN functional connectivity.

1.4.7 DMN in other species

The DMN consists of regions that have undergone significant expansion in humans, particularly those in medial prefrontal cortex (BAs 10 and 32) (Ongür & Price, 2000). In addition, BA 32 is believed to have no homologue in monkeys (Brodmann, 1909). However, in spite of the extensive evolutionary expansion of association cortex, a well-organized intrinsically coherent network resembling the human DMN has been identified in other species. In the resting-state, a set of regions centered on the posterior cingulate was identified in the macaque using group ICA (Hutchison et al., 2011), but did not include any medial prefrontal structures. Several seed-based resting-state studies did identify networks linking monkey PCC with prefrontal cortex (Vincent et al., 2007; Rilling et al., 2007). However, given the differences in prefrontal anatomy, the identified prefrontal regions tended to be more lateral than those generally associated with the human DMN including dorsolateral prefrontal cortex (Margulies et al., 2009). Task-associated deactivations in macaques are also similar to those identified in human studies (Mantini et al., 2011), but also included more lateral prefrontal areas (BAs 9/46d and 8b) and may not include lateral parietal areas (Hayden et al., 2009). However, unlike in humans, in macaques, the dorsal striatum, rather than DMN regions exhibit the greatest blood flow during rest (Kojima et al., 2009). Intriguingly, resting-state networks similar to the human DMN have also been identified in mice (Stafford et al., 2014), rats (Lu et al., 2007; Upadhyay et al., 2011) and cats (Popa et al., 2009). The existence of a default-

mode-like network in species such as mice raises some questions about the function of this network, as it is not known whether the DMN in other species supports cognitive functions such as social/emotional processing and autobiographical memories. Theory of mind abilities are generally thought to be unique to humans, however there is some evidence that macaques do possess limited theory of mind abilities (Drayton et al., 2016). Comparative anatomical studies of humans and macaque monkeys suggest a high degree of similarity in overall cytoarchitecture (Petrides & Pandya, 1999; Ongür & Price, 2000; Jbabdi et al., 2013), functional and anatomical connections. Therefore, a survey of the tract-tracing literature in macaques will provide a foundation for an anatomical understanding of the information processing of each region of the DMN.

1.4.8 DMN Anatomy

While there are variations across studies in the extent of the cortical regions included in the DMN, there is however agreement on the core regions that make up the network. The core of the network is made up of a cluster of regions in medial prefrontal cortex and a cluster of regions in posterior medial cortex (PMC). The anterior portion of the network in medial prefrontal cortex includes BA area 10 medial and BA 32 pregenual. The posterior part of the network includes the posterior cingulate (BA 23 and BA 31), the precuneus (BA 7m) and lateral parietal cortex (BA39). As the hippocampus is not always included in the network and is understood to have a role in spatial navigation and long-term memory unrelated to purported DMN function, I have not included it here. In this section the anatomical connections of core DMN brain regions

will be explored from the tract tracing literature in macaque monkeys. There is broad organizational similarity across species in the anatomical organization of cortical areas and their connections (Jbabdi et al., 2013; Ongür & Price, 2000). However, the cortex has been subdivided architectonically by a number of investigators and there is considerable disagreement regarding the boundaries of its subdivisions (Brodmann, 1909; Walker, 1940; Vogt et al., 1987). These differential classifications have been taken into consideration as best as possible in compiling a comprehensive account of the cortical and subcortical projections of each of the core DMN regions. In addition, the tract tracing literature suffers from overlap in injection sites across Brodmann areas and uncertain homologues in humans (Carmichael et al., 1994). Many studies are focused on regional connections to or from a given area and/or do not report interhemispheric projections, making whole-brain summaries for each Brodmann area difficult. Nonetheless, it provides a strong starting point for understanding the organization of afferents and efferents into these core regions which cannot be ascertained from noninvasive techniques in humans.

1.4.8.1 DMN Regions of the Medial Prefrontal Cortex

1.4.8.1.1 Brodmann Area 10 medial

In humans, BA 10 is larger relative to the rest of the brain than it is in non-human primates, and it has more connections to higher-order association areas (Semendeferi et al., 2001). From this observation it has been suggested that this part of the cortex became highly specialized during human evolution. BA 10 medial is granular cortex (Carmichael

& Price, 1994) that makes up the most ventral medial portion of the frontal cortex and also some portion of the medial orbital cortex. The medial portion of BA10 (BA10m) is part of a network of medial prefrontal structures that are tightly interconnected and have a distinct pattern of connectivity to other cortical and subcortical structures compared to that of the surrounding orbital and lateral prefrontal areas (Carmichael & Price, 1996; Ongür & Price, 2000). They provide cortical output to visceromotor structures in the hypothalamus and are connected to the nucleus accumbens and ventromedial caudate and putamen in addition to having strong connections throughout the cingulate gyrus. While abstract representation of all sensory modalities are present in the lateral network, there is little evidence for sensory input directly to the medial network (Carmichael & Price, 1996). However, bidirectional connections through BA 13, BA1 2, BA 9 and BA 46 connect the medial network with the orbital and lateral prefrontal cortex. Three main groups of efferent fibers emanate from medial prefrontal structures: a lateral group through the extreme capsule targets auditory and multi-sensory regions in superior temporal cortex, and ventral insula, 2) a medial group of bidirectional association fibers through the cingulate fasciculus targets anterior and posterior cingulate, and 3) fibers that connect prefrontal cortex with the temporopolar regions, the hippocampal gyrus and ventrolateral part of basal nucleus of amygdala through the uncinate fasciculus (Petrides & Pandya, 2007). In addition, subcortical fibers from the medial prefrontal network enter the external capsule and terminate in the head and body of the caudate and rostral part of the putamen, dorsomedial and caudal parts of the mediodorsal (MD), intralaminar and pulvinar nucleus of the thalamus, and include minor projections to the hypothalamus.

1.4.8.1.2 Brodmann Area 32

BA 32 makes up the most ventral part of the anterior cingulate and also a subgenual portion just inferior to the anterior part of the genus of the corpus callosum. BA 32 is agranular cortex cytoarchitecturally distinct from other regions of the cingulate (Pandya et al., 1981) and BA 10m (Carmichael & Price, 1994). It has bidirectional connections with BAs 24 and 25 in the anterior cingulate and BA 23 in posterior cingulate (Parvizi et al., 2006). However, its pattern of afferent and efferent connections are more similar to other regions of the ventral medial prefrontal cortex than adjacent anterior cingulate BA 24 (Pandya et al., 1981). It projects to medial prefrontal regions BAs 8, 9 and 10, lateral BAs 6, 8, 9, 10 and 46 and orbitofrontal BAs 11-14 (Pandya et al., 1981; Pandya et al., 1991; Petrides & Pandya, 2007). Fibers projecting medially from BA 32 terminate in the opposite hemisphere through the genus of the corpus callosum and to BA 24 and BA 23. Laterally projecting fibers project to the head and body of the caudate and dorsomedial nucleus of the thalamus through the internal capsule. Another group of fibers through the external capsule terminate in the ventromedial putamen and the shell of the nucleus accumbens (Haber et al., 1995). Via the extreme capsule and uncinate fasciculus, fibers reach the amygdala, ventral anterior superior temporal gyrus (BA 22, TS1, and TS2) as well as TPO (BA 39) of the superior temporal sulcus (Pandya et al., 1981;Vogt & Pandya, 1987; Pandya et al., 1991; Petrides & Pandya, 2007).

1.4.8.2 DMN regions of the posterior medial cortex

Like the anterior part of the network, the posterior regions of the DMN are also part of a group of tightly interconnected regions sometimes called the PMC including posterior cingulate regions BA 23, BA 31, and BA 7 medial in the precuneus (Parvizi et al., 2006). These regions share connections to BAs in the anterior cingulate, mid-dorsolateral prefrontal cortex (BA 46), area PG (macaque homologue of human inferior parietal lobule), posterior area of tempero-parieto-occipital (TPO) junction BAs 39/40, the caudate, and extensive connections with the thalamus. Thalamic projections from each region of the PMC reach all parts of the dorsal associative nuclei of the thalamus from the anterior to posterior extent including anterior ventral (AV), anterior dorsal (AD), anterior medial (AM), superficial lateral dorsal (LD), dorsal tip of ventral lateral (VL) and ventral anterior (VA), lateral posterior (LP) and lateral pulvinar (Parvizi et al., 2006). However, these connections are not all reciprocal, a fact that has led some to speculate PMC connections to the thalamus contribute a modulatory influence (Sherman, 2001). Projections to the striatum span the entire head and body of the caudate (Parvizi et al., 2006) and include contralateral areas of both the caudate and putamen. PMC is generally connected to associative cortex with few connections to primary sensory, primary motor cortex and sensory thalamic nuclei. Outside of their shared connectivity patterns and strong interconnectivity, each region has distinct connections suggesting unique functional roles. Connections to PMC and the DMN in general exclude primary sensory and motor regions as well as primary sensory thalamic nuclei.

1.4.8.2.1 Brodmann Area 23

Based on patterns of connections and cytoarchitectural attributes, BA 23 is sometimes subdivided into 3 ventrodorsal subregions(a-c). BA 23c distinguishes itself from BA 23a,b with connections to sensorimotor areas BA 3, 4, 6 and secondary somatosensory cortex BA 40 (Parvizi et al., 2006). BA 23 receives input from the insula (Vogt & Pandya, 1987) and has bidirectional connections to BA 24 in anterior cingulate and retrosplenial cortex BAs 29/30 (Parvizi et al., 2006). In prefrontal cortex, BA 23 has reciprocal connections to BAs 9, 10, 11,14 and 46 (Vogt & Pandya, 1987). BA 23 is heavily connected to parietal cortical regions including the inferior parietal lobule (BA 39), TPO (BA 39), and is also connected to visual association cortex BA 19. In the temporal lobe, BA 23 has bidirectional connections to the STS, TF, TH and entorhinal cortex (Vogt & Pandya, 1987; Kobayashi & Amaral, 2003; Parvizi et al., 2006). The principle thalamic input to BA 23 is from the AM nucleus and is topographically organized (Vogt et al., 1987), with more inferior BA 23a receiving input mainly from the central core of the nucleus. Thalamic afferents also come from the AV, AD, AM, LD, intralaminar and pulvinar regions of the thalamus (Vogt et al., 1987; Parvizi et al., 2006). BA 23 projects to the head and body of the dorsal caudate and has sparse projections to the putamen.

1.4.8.2.2 Brodmann Area 31

BA 31 is situated dorsal to BA 23 in the posterior cingulate and is a major hub of regional connectivity in the brain. It is connected to all regions of the cingulate, superior

and inferior parietal lobules, the frontal pole, temporal cortex, and the basal forebrain. In the frontal cortex, it has reciprocal connections with BAs 10, 9/46 (Vogt & Pandya, 1987), and premotor BA 6. In temporal cortex, it receives projections from TL and TH in the parahippocampal region (Vogt & Pandya, 1987), and the STS (Vogt & Pandya, 1987) and entorhinal cortex. In parietal cortex, BA 31 receives dense projections from BAs 39, 40 and 7 (Vogt & Pandya, 1987) and projects back to BA 39. Similar to the patterns of thalamic connectivity in BA 23, BA 31 has extensive projections to the thalamus extending through AV, AD, AM, LD, VL, VA, LP and the lateral pulvinar. BA 31 receives projections from more thalamic nuclei than other PMC regions including projections from AV, AM, anterior intralaminar, VL, MD, LP, and anterior, lateral, and medial pulvinar, but far more from posterior than anterior nuclei. As is the case for other PMC regions, striatal projections from BA 31 reach the dorsal part of the head and body of the caudate and hav sparse projections to the putamen (Vogt et al., 1987).

1.4.8.2.3 Brodmann Area 7m Precuneus (PGm)

Dorsal to BA 31 in the precuneus, is medial BA 7 (BA 7m) also referred to as PGm in the macaque literature (Von Economo & Koskinas, 1925). In the frontal cortex, BA 7m is bidirectionally connected to both ipsilateral and contralateral dorsal premotor and supplementary motor cortex (BA 6) and the FEF (BA 8) (Petrides & Pandya, 1984; Cavada & Goldman-Rakic, 1989; Parvizi et al., 2006). BA 7m is not connected to BA 32 in the anterior cingulate (Parvizi et al., 2006) nor insular cortex (Leichnetz, 2001). It is however it is reciprocally connected with BAs 23 and 31 and retrosplenial cortex

(Cavada & Goldman-Rakic, 1989) in the posterior cingulate (Leichnetz, 2001; Parvizi et al., 2006). BA 7m may also project to premotor regions of BA 24 in the cingulate gryus (Petrides & Pandya, 1984; Parvizi et al., 2006). In parietal cortex, it has bidirectional connections to the medial intraparietal sulcus and superior parietal lobule (BA 7 lateral) and BA 39/40 (Cavada & Goldman-Rakic, 1989; Pandya & Seltzer, 1982; Leichnetz, 2001; Parvizi et al., 2006). It has reciprocal thalamic projections with VL, MD, LP, AV, and intralaminar nuclei as well as the pulvinar (Leichnetz, 2001; Parvizi et al., 2006). It projects to the basal forebrain (Leichnetz, 2001), dorsolateral caudate and putamen with denser connections to the putamen than other PMC regions (Leichnetz, 2001; Parvizi et al., 2006). In the temporal lobe, BA 7m is interconnected with the STS and BA 22 (Cavada & Goldman-Rakic, 1989; Leichnetz, 2001) and has sparse connections within the hippocampal formation (Cavada & Goldman-Rakic. 1989; Parvizi et al., 2006).

1.4.8.2.4 BA 39 Inferior Parietal Lobule or PG

Located in the inferior parietal lobule, BA 39 is more laterally located than the rest of the core DMN regions and has connections to lateral prefrontal cortex not seen in other core regions of the DMN. Cytoarchitecturally, it appears to be part of the same structure as BA 7m (Brodmann, 1909), sometimes referred to as BA 7a (Pandya & Seltzer, 1982). It shares, reciprocal connections with all of the PMC regions (BA 23, BA 31, BA 7m, BA 29 and 30) (Mesulam et al., 1977; Cavada & Goldman-Rakic, 1989; Parvizi et al., 2006). It has bidirectional connections with both ipsilateral and contralateral FEF (BA 8) and BA 46 in dorsolateral prefrontal cortex (Mesulam et al., 1977; Petrides & Pandya, 1984). It is reciprocally connected to BA 24 in the cingulate

gyrus, BA 19 in occipital cortex (Mesulam et al., 1977; Cavada & Goldman-Rakic, 1989) as well as the parahippocampal region and STS (Cavada & Goldman-Rakic, 1989; Mesulam et al., 1977). Its thalamic projections are also similar to that of BA 7m, with connections to the pulvinar, LP (Weber & Yin, 1984) , and intralaminar nuclei (Mesulam et al., 1977; Weber & Yin, 1984). However, unlike BA 7m, BA 39 has substantial projections to VP medial nuclei (Yeterian & Pandya, 1985) as well as the supragenicular (Weber & Yin, 1984) and the dorsal reticular nuclei (Yeterian & Pandya, 1985). In addition, BA 39 projects to both the caudate and putamen (Weber & Yin, 1984; Yeterian & Pandya, 1985).

1.4.8.3 Summary DMN Anatomy

PDMN regions have connections to visual and somatosensory association and premotor cortical regions that are not shared by the ADMN. ADMN receives input from few if any regions associated with sensory-motor processing and has connections to more limbic structures such as the amygdala, which are not shared by the posterior part of the network. In addition, anterior and posterior parts of the DMN differ in their subcortical connections. Although both anterior and posterior DMN regions are connected to midline and intralaminar thalamic nuclei, posterior DMN regions also have connections throughout the anterior and lateral thalamic nuclei (Vogt et al., 1979). In addition, the macaque literature suggest that BAs 10 and 32 in the ADMN are connected to PDMN cingulate regions in BA 23 and 31. Interestingly, the tract tracing literature in macaques suggest that BAs 7m and 39 are exclusively connected to lateral prefrontal areas rather

than the medial anterior structures that are part of the DMN.

1.4.8.4 DMN and Cortical-Striatal-Thalamic circuits

Current understanding of the large scale organization of circuits in the brain posits that at least five functionally distinct parallel circuits link cortex, basal ganglia and thalamus. The currently proposed circuits include a motor circuit originating in supplementary motor region, an occulomotor circuit originating in the FEF, two associative prefrontal circuits originating in dorsolateral prefrontal and lateral orbital cortex, and a circuit with unknown function originating in the anterior cingulate cortex (Alexander, 1986). Each is believed to be a partially closed-loop segregated circuit, originating in cortex, converging onto non-overlapping regions within striatal structures (caudate, putamen, and ventral striatum), projecting from the basal ganglia to circuit-specific targets in the thalamus and returning to the cortical region from which it originated. Each circuit is thought to receive input from multiple interconnected functionally related cortical areas whose inputs are progressively integrated through basal ganglia structures. Each circuit involves excitatory cortical projections to the striatum which proceed through inhibitory GABA-mediated direct and indirect pathways through the basal ganglia (Alexander & Crutchner, 1990). The two pathways are believed to differentially modulate their thalamic targets, balancing and selecting excitatory and inhibitory responses to their targets. Interaction between segregated circuits also occurs at the level of the basal ganglia where inputs from individual circuits are also relayed to associative cortex (Joel & Weiner, 1994), suggesting that behavior is dependent on complex interactions between cortex and cortico–basal ganglia networks (Haber, 2016).

Disruption of any one of these circuits results in a variety of cognitive and neuropsychiatric disorders (Cummings, 1993; Mega & Cummings, 1994; Tekin & Cummings, 2002 ; Price & Drevets, 2009) and similar neuropsychiatric symptoms may arise from damage or disruption at different levels within or between circuits.

As noted in the previous section, both anterior and posterior portions of the DMN project to different areas of the striatum (Draganski et al., 2008; Haber, 2016). In addition, they have bidirectional connections with different thalamic nuclei. Anterior DMN is connected to midline thalamic nuclei and posterior DMN is connected to lateral and anterior nuclei (Vogt et al., 1979). This suggests that anterior and posterior DMN may be part of separate circuits through the thalamus (Parvizi et al., 2006) and therefore that they may participate in more than one CST circuit. The posterior DMN is structurally interconnected with cortical occulomotor structures and may therefore contribute to the occulomotor circuit. The associative and limbic circuits through the basal ganglia are less well characterized than that of the motor and occulomotor circuits. The contribution of projections of anterior DMN regions in ventral medial prefrontal cortex (BA 10 and BA 32) is not explicit in the currently defined circuits. However, given the projections of BA 10 and BA 32 through the striatum, they may contribute to one or both of the associative circuits, the limbic circuit and/or may be part of an additional as of yet undefined circuit. It is likely that an understanding of these non-motor CST circuits is necessary to elucidate the true functional role of the DMN in cognition, its functional relationship with the TPN, as well as the changes in DMN activity associated with a wide range of disorders.

1.4.9 Function of the DMN

The functional role played by the DMN in cognition is not well understood. Several theories regarding its functional role have been proposed. One theory is based on inferences drawn from the set of experimental paradigms that evoke increases rather than decreases in BOLD signal within the network. Experimental paradigms involving processing social or emotion stimuli (Spreng et al., 2009, Kelley et al., 2002, Mitchell et al., 2006), making moral judgements (Greene et al., 2016a), thinking about oneself (Gusnard & Raichle, 2001) or the mental state of others (theory of mind) (Fletcher et al., 1995; Rilling et al., 2004; Amodio & Frith, 2006), envisioning or planning for the future (Okuda et al., 2003, Szpunar et al., 2007, Gilbert et al., 2007, Addis et al., 2007, Botzung et al., 2008, D'Argembeau et al., 2008), and autobiographical recollection (Andreasen et al., 1995) all evoke increases in BOLD signal within the network. These studies collectively suggest that the cognitive role of the DMN is related to self-referential and related social cognitive processing (Buckner & Carroll, 2007). Additional evidence for this view comes in part from lesion studies of prefrontal cortex. Patients with lesions in medial prefrontal brain regions may suffer changes in personality and exhibit inappropriate social behavior (Bechara et al., 1994, Damasio & VanHoesen, 1983) and deficits in the ability to carry out plans. Furthermore, the role of vmPFC in emotional regulation is underscored by clinical research indicating increased activity in vmPFC associated with anxiety disorders (Simpson et al., 2001) and depression. The role of the DMN in autobiographical memory is bolstered by the observation that BOLD signal in the hippocampus is temporally correlated with that of spontaneous DMN brain activity.

In addition, medial posterior parts of the network have been associated with recollection (Vincent et al., 2006). One study identified diurnal variation in functional connectivity between PCC/precuneus and the hippocampal formation, present in the evening and absent in the morning after sleep (Shannon et al., 2013). However, in the absence of any explicit social, self-referential or memory-related experimental task, in resting-state, the DMN is known to exhibit a high level of baseline activity. Based on the tasks known to cause increases in DMN activity, one possible explanation is that typical of stream of consciousness during rest, may involve thinking about oneself, planning for the future, remembering the past or thinking about events with social or emotional relevance. Therefore, spontaneous BOLD signal in the DMN may correspond with the kind of cognitive tasks carried out spontaneously in resting conditions. If so, one possible explanation for commonly observed task-evoked decreases in the DMN is the need to divert attention away from internal rumination in order to direct attention towards external stimuli. From this perspective, decreases in DMN activity are interpreted as evidence that the DMN does not participate in tasks that require externally directed focus. Others have suggested that at rest, in addition to supporting internally directed thoughts, the DMN may subserve a broad unfocused attention on the environment, scanning the periphery for salient stimuli. An fMRI study designed to test this hypothesis found that the DMN responds to visual stimuli when presented in peripheral vision, particularly when their appearance is unpredictable (Hahn et al., 2007). Anatomical considerations alone suggest a role for posterior DMN regions in visual attention as BAs 7m and 39 are both connected to cortical areas associated with higher order visual processing in the

dorsal stream (Ghatan et al., 1995, Hahn et al., 2007). Bilateral lesions that extend across posterior parietal cortex can induce Balint's syndrome (Mesulam, 2000), a form of tunnel vision in which patients can only perceive a small portion of the visual world and often fail to notice the appearance of objects outside the immediate focus of attention. These observations suggests that task-associated deactivations in the DMN occur because attention has been narrowed from that of broad unfocused exploration to focus on a specific cognitive task (He et al., 2013). Combining evidence from the set of tasks that evoke increases in the DMN and observations of the network's likely role in perception of salient visual stimuli, the most parsimonious of the currently proposed functions of the DMN suggests its role as a sensory-visceromotor link (Raichle, 2015) that functions to pair experience with appropriate behavioral and emotional responses (Ongür & Price, 2000). In this view, the DMN, far from being disengaged during externally focused tasks, plays a role integrating external awareness and experience with the moods and autobiographical relevance of the self in order to influence behavior. If so, task-evoked decreases in the DMN observed in fMRI experimental paradigms must be evaluated more cautiously. If the DMN does play such a role, the temporal dynamics of activity in the network should reflect both the bottom up processing of sensory stimuli and top-down modulatory signals that influence behavior. In addition to mapping the anatomical connections of the core DMN regions in humans, the temporal dynamics of the DMN in response to a variety of task demands are a focus of this thesis.

1.5 Summary

The core regions of the DMN are midline cortical structures in vmPFC and PMC. Anterior and posterior parts of the network have different connectivity profiles in macaques suggesting that different parts of the network play a different role in DMN function. The DMN has a high baseline level of activity in the absence of externally focused attention. This activity is attenuated while performing a wide range of cognitive tasks. The functional significance of task-evoked deactivation in the DMN is not known. However, certain tasks, such as those requiring self-referential thinking, do not evoke decreases in the DMN. As the function of the DMN is not well understood, a detailed accounting of its anatomical connections and the temporal evolution of its activity during task performance may yield insights into its function.

1.6 Overview of the Data Chapters

In the previous sections I have synthesized the tracing literature in macaques to detail the anatomical connections of each region of the DMN. DMN regions, particularly those in vmPFC, are significantly larger in humans and may not have homologues in monkeys. Therefore in Chapter III, I detail the connections of each region of the DMN in humans using diffusion spectrum imaging data. I characterize differences in connectivity profiles of anterior and posterior portions of the network and emphasize the connections of the network as a whole through the basal ganglia and thalamus.

Chapter IV focuses on task-evoked activity in the DMN. It begins with a careful accounting of the regions that exhibit task-evoked decreases in activity across several

experimental paradigms. The temporal evolution of activity in the DMN is then explored in the context of three paradigms that purportedly evoke different responses in the DMN (increase, decrease, no change).

In Chapter V, I explore the role of the DMN in autism spectrum disorder (ASD) and schizophrenia (SZ). Using a supervised machine learning technique, I identify changes in connectivity, particularly in the DMN, that distinguish ASD and SZ patients from healthy controls as well as from each other.

CHAPTER II

GENERAL METHODS

2.1 Human Connectome Project Data

Data used for this work was collected by the Human Connectome Project (HCP) (http://www.humanconnectome.org) with the exception of patient population data detailed in chapter V. The HCP is a consortium led by Washington University, University of Minnesota, and Oxford University with the aim to map large-scale human brain circuitry in order to decipher the neural pathways underlying healthy brain function and behavior. In pursuit of this goal they have collected both structural (T1) and functional MRI ($T2^{*}$), Diffusion tensor imaging (DTI) and magneto-electroencephalography (MEG) data from 1200 healthy adults between the ages of 22 and 35 (Sotiropoulos et al., 2013; Van Essen et al., 2014). MEG and high-temporal resolution MRI data were collected in resting state and for 7 different task paradigms. Tasks include 1) an emotion processing task in which subjects were asked to judge the similarity of faces that were either angry or fearful (Hariri et al., 2002) , 2) a gambling task in which subjects played a card guessing game in order to win or lose money (Delgado et al., 2000), 3) a language processing task with alternating blocks of audibly presented stories and arithmetic problems followed by a forced choice question (Binder et al., 2011), 4) a motor task where subjects were asked to tap fingers, toes, and move their tongues (Bucker et al., 2011), 5) a relational task in which subjects were asked to find the feature that varied across one set of objects (shape or texture) and determine if the same

feature varied across a second set of objects (Smith et al., 2007), 6) a social cognition/theory of mind task in which subjects were asked to judge the mental interaction of objects that either interacted in a socially evocative manner or moved randomly in short video clips (Casetelli et al., 2000; Wheatley et al., 2007), and 7) a working-memory n-back task (Barch et al., 2013; Van Essen et al., 2013). The data set included four 15 minute resting state scans (eyes open). Functional MRI data were collected with a spatial resolution of 2 mm isotropic voxels and a TR of .72 seconds using a multiband factor of 8. A subset of the HCP data used for this work was based on the 27 subjects who had completed the entire battery of MRI and MEG experiments as of January 1, 2015 from the 800 subject release. Three left-handed subjects were later excluded for analysis in order not to confound results based on differences in lateralization associated with handedness. The remaining 24 subjects included 17 females, and 8 males. Two subjects were between the ages of 22-25, 12 between the ages of 26 and 30 and 11 between the ages of 31 and 35. Data for the remaining 24 subjects was used in Chapters III and IV.

2.2 Region of Interest Definition Anatomical Brain Atlas

For ease of comparison with animal literature and to include both cortical and subcortical regions of interest (ROIs), we opted to use a brain atlas based on the Brodmann areas. The atlas chosen is called the Human Brainnetome Atlas (Fan et al., 2016). It consist of 246 regions (210 cortical and 36 subcortical regions). Regions of the Brainnetome atlas are defined by their structural similarity as well as similarity of connectivity patterns. It is based on an initial automated gyral-based parcellation

Desikan-Killany atlas (Desikan et al., 2006) followed by a clustering over similarity of structural connectivity determined through DTI probabilistic tract-tracing. Naming of regions was based on similarity of the resulting parcellation to other atlases based on cytoarchitecture, myelnation maps and receptor based architectonic parcellations. However, in order to allow for analysis based on circuitry through the direct and indirect pathways of the basal ganglia, pallidal ROIs from the Brainnetome atlas were replaced with those of a recently created probabilistic BG atlas (Keuken & Forstman, 2015). From the BG atlas ROIs for bilateral internal and external globus pallidus, as well as the subthalamic nucleus and substantia nigra were added to those of the Brainnetome atlas for a total of 252 ROIs. A set of putative DMN regions were identified within the Brainnetome atlas with the use of a separately generated functional atlas, the willard atlas. The willard atlas contains 14 functional networks (Richiardi & Altmann, 2015) defined by multimodal independent component analysis combining resting state fMRI and post mortem gene expression. Brainnetome regions overlapping with the "ventral" and "dorsal" default mode networks as defined in the willard atlas included bilateral Brainnetome regions: BA 10m (medial), BA 32p (pregenual), BA 7m (medial), BA 39rv (rostroventral), BA 31, and BA 23d (dorsal). These ROIs were used for all analysis in chapters III and IV. A table of the combined regions and their coordinates in MNI space can be found in Table 2.1.

CHAPTER III

ANATOMICAL CONNECTIONS OF THE HUMAN DMN

3.1 Introduction

The relationship between structure and function in the brain is observed across all scales from the protein-level, through the level of the synapse, and microcircuit, as well as the entire brain. At the network level, evidence for the relationship between the structural connections between brain areas and their function comes from many sources. From developmental neuroscience, we know that network level activity resembling the functional networks of adults emerges in concert with the development of the structural connections between brain regions (Casey et al., 2005). For example, in a longitudinal study of axonal myelination and axonal thickness in children between the ages of 8 and 18, reading ability was found to correlate with white matter development in the left temporal lobe (Nagy et al., 2004). Multimodal approaches combining structural and functional imaging, have shown that loss of function is often associated with decreases in white matter integrity. Disruption of the structural connections between brain areas is associated with psychiatric and cognitive disorders including including Alzheimer's (Scheltens et al., 1992), schizophrenia (Davis et al., 2003), and autism (Barnea-Goraly et al., 2004; Wolff et al., 2012). The degree of structural connectivity between brain regions is also known to be a strong predictor of functional connectivity (Vincent et al., , 2007; Greicius et al., 2009; Honey et al., 2009; Margulies et al., 2009; Kelly et al., 2010; Messe' et al., 2014). Furthermore, insights into the functional role played by a region can

be gained by identifying its afferents and efferents. For example, if a brain region receives input from primary sensory regions, it likely has a role in processing low-level sensory information. If a region receives inputs from multiple sensory modalities, it is likely involved in integrating sensory information. This relationship between structure and function at the regional level underlies recent studies of connectomics with the goal of mapping the large-scale structural connections of the brain.

White matter tracts in the brain are divided into three main categories: projection pathways, commissural pathways and association pathways. Projection pathways contain both ascending and descending fibers connecting the cortex to subcortical structures. Association pathways connect cortical regions within a hemisphere along the anterior to posterior axis of the brain. The commissural pathways consist of fibers that connect brain regions across hemispheres and includes the corpus callosum, the largest fiber tract in the brain. The DMN consists of several medial brain areas that are situated along both the main association pathway in the cingulum and the main commissural pathway, the corpus callosum. Anterior DMN regions in vmPFC sit just anteriorly to the genu of the corpus callosum and the posterior regions at the splenium of the corpus callosum. Medial anterior and posterior regions of the DMN are connected to each other through the association fibers of the cingulum. Therefore, the midline regions of the DMN are robustly connected to each other through major white matter tracts. As such, it is has been found that the DMN has the strongest relationship between structural and functional connectivity amongst the identified functional networks (Horn et al., 2104). In addition, several studies of whole-brain structural connectivity have concluded that DMN regions,

particularly those in medial parietal cortex, are part of a set of structural hubs through which many regions may connect mono or polysynaptically (Hagmann et al., 2008; Gong et al., 2009). Each region, however, has its own profile of connections which should yield insights into the functional role of each region in the network. Most of the literature on structural connectivity has been carried out using tract-tracing techniques in animals. Comparative anatomical studies indicate that general organizational principles are conserved across humans and non-human primates (Uylings & van Eden, 1991; Jbabdi et al., 2013). In chapter I, I detailed the anatomical connectivity of the key nodes of the DMN from the tract-tracing literature in macaque monkeys. There are, however, anatomical differences in human brains relative to macaques. The DMN comprises regions that are known to have undergone extensive evolutionary changes especially in prefrontal cortex (Semendeferi et al., 2001). Furthermore, it is not clear that all vmPFC structures have homologues in non-human primates. Therefore, it is not certain that primate tract-tracing studies in these regions accurately reflect the connectivity of these regions in humans. One recent study directly compared structural connectivity in vmPFC in humans and macaques and found broad agreement in the organization of white matter tracts but did not address connections at the level of individual Brodmann areas that may or may not have homologues (Jbabdi et al., 2013).

Five parallel cortico-striatal-thalamic (CST) circuits have been proposed: motor circuit, occulomotor, dorsolateral prefrontal, lateral orbitofrontal, and anterior cingulate (Alexander, 1986). Except for the motor circuit, each of the proposed circuits contain regions that are part of the DMN, especially BA 10, BA 32 and BA 7. This led me to

hypothesize that the DMN may participate in one or more of these large-scale circuits. Surprisingly, there are few if any studies characterizing the brain-wide structural connections of functional networks. Therefore, in this chapter I will characterize the structural connectivity of each DMN brain region in humans using diffusion spectrum imaging and probabilistic tractography. Emphasizing tracts that run through the basal ganglia and thalamus, I show that the core regions of the DMN form a distributed (CST) circuit. Differences in the connectivity of anterior regions in ventral medial prefrontal cortex and posterior regions of the network in the posterior cingulate and lateral parietal cortex are also highlighted.

3.1.1 Principles of Diffusion Imaging

Water diffusion in white matter tracts and other tissues of the body is anisotropic, meaning that water molecules do not diffuse equally in all directions (Hansen, 1971). Water diffusion is restricted in the direction perpendicular to the axon. This feature is exploited in diffusion tensor imaging (DTI) which makes use of the fact that the direction of maximal diffusivity is parallel to the direction of the axonal fiber where diffusion occurs faster. Contrast in diffusion weighted images is created in the same way as in fMRI and therefore includes effects of both T_1 and T_2 contrast. Diffusion weighted images are created by adding additional magnetic field gradients to standard MRI sequences. As in standard MR imaging, gradients are applied once to dephase and again to counteract dephasing (rephasing). In the case where no diffusion has occurred, the effects of the applied gradients will be cancelled out. Displacement of molecules due to

diffusion occurring in the time between gradient applications results in attenuation of signal that is dependent on the magnitude of the applied gradient, its duration, and the time between dephasing and rephasing gradient applications. Changes in image intensity due to diffusion provide a quantitative measure of the extent of diffusion anisotropy and its predominant direction within a voxel. Analysis of diffusion weighted images generally involves two steps. The first being a voxel-level local estimation of anisotropy and a second step that traces through the resulting voxel-level vectors to estimate 3-d tracts through the brain, a process called tractography or tract tracing. Generally, the diameter of axon bundles traced in tractography are on the order of 1mm whereas individual axon fibers are on the order of 1-30 um (Mori, 2002). Therefore, on average white matter voxels may contain between 30-1000 fibers. The signal measured within a voxel is indicative of the averaged diffusion properties of water molecules and fibers within them. As a result, reconstructed pathways are often interpretable as major fiber tracts in the brain. Tractography has shown reasonable agreement with ex vivo studies in non-human primates and humans posthumously (Behrens et al., 2003). However diffusion tensor models fail to accurately identify tracts with large curvatures or tracts that cross one-another. Fiber bundles that are oriented in a single direction pose less difficulty, but many voxels contain fibers that cross. In voxels containing two crossing fibers, the average diffusion signal results in an apparent principal direction intermediate to the fiber orientations, and therefore not in the direction of either fiber (Basser et al., 2000). The diffusion tensor model will therefore result in misidentified fiber directions, with larger discrepancies associated with larger crossing angles. More accurate estimates

of fiber direction may be obtained by achieving better angular resolution in diffusion weighted images. This can be achieved by acquiring measurements at several gradient intensity (b or shell) values and in multiple gradient directions. So-called multi-shell approaches demonstrate greater sensitivity in detecting fiber crossings than single shell schemes (Wedeen et al., 2008). Diffusion spectrum imaging (DSI) or Q-ball imaging is a multi-shell imaging technique that employs the same pulsed gradient spin echo used to obtain diffusion weighted images, but results in diffusion displacement distributions rather than a single measurement of the diffusion tensor in each voxel (King et al., 1994). Spin displacement profiles, or diffusion spectrums, are obtained via Fourier transform of Q-space in a manner analogous to Fourier transform of k-space in T_1 or T_2 weighted MR images. Spectrum imaging techniques estimate a probability distribution of diffusion direction at each voxel, with broad probability distributions reflecting increased uncertainty. The diffusion spectrum of a voxel containing crossing fibers will exhibit multiple discrete peaks, with each peak directed towards a component fiber group. In this way spectrum imaging can resolve crossing fibers that cannot be resolved using a diffusion tensor model. Probabilistic tractography is then performed by drawing samples from the diffusion distribution within a seed voxel to generate streamlines across voxels building a probabilistic connectivity distribution. Thousands of samples are drawn in each seed and the density of streamline samples reflects the probability of connection with other seed voxels. The combination of DSI and probabilistic tractography reduce model errors and more accurately identify fiber tracts than simpler models that assume a single primary direction of diffusion (Jbabdi et al., 2012).

3.2 Methods

3.2.1 Data

Diffusion spectrum data was obtained from the HCP database for the same subjects as for the functional MRI data detailed in Chapter II Section 2.2.1. As the main goal of the HCP is to map macroscopic connections in the human brain and its variability in healthy adults, considerable effort was put into optimizing the scanning parameters for diffusion data (Ugurbil et al., 2013). After sampling the parameter space, the best trade-off between angular contrast and SNR was found when all shells were below b = 3500 s/mm^2 (Sotiropoulos et al., 2013). It was further determined that three shells were better for resolving three way fibre crossings than two shells while having almost identical performance in detecting two-way crossings. Therefore, HCP DSI data was collected using three shells (b = 1000, 2000, and 3000 s/mm^2) each with 192 data points in 90 gradient directions (Jones, 2004). Six b=0 acquisitions were also acquired (three pairs in each of 2 phase encoding directions). The scanning protocol resulted in a diffusion resolution of 1.25 mm isotropic voxels with 111 slices (TR 5520 ms; TE 89.5 ms, FOV 210x180).

3.2.2 Data Preprocessing

The data was obtained in a preprocessed form from the HCP database. The preprocessing pipeline executed by the HCP includes normalization of b_0 image intensity across runs, and corrections for EPI distortions, eddy-current-induced distortions, subject motion, and gradient-nonlinearities (Glasser et al., 2013). Large amplitude gradient

fields and rapid gradient switching are required for diffusion spectrum MR sequences. The required gradients result in image distortion due to gradient induced eddy currents. The HCP scheme for correction of EPI and eddy-current induced distortions is based on manipulation of acquisitions so that the distortion manifests differently in different images (Andersson et al., 2003). Two phase-encoding direction-reversed images for each diffusion direction are acquired. Reversing the phase encoding direction flips the sign of the susceptibility-induced distortions. Knowledge of distortion in complimentary diffusion image pairs is used to invert a generative model to simultaneously correct for motion, susceptibility and eddy current distortions (Andersson & Sotiropoulos, 2015; 2016). Image pairs are then combined into a single distortion-corrected image, as implemented in FSL's (Smith et al., 2004) eddy (Anderson et al., 2012; Anderson & Sotiropoulos, 2015; 2106; Jesper et al., 2016) and topup (Andersson et al., 2003) algorithms. A gradient nonlinearity correction warp field is then calculated to remove spatial distortion (Jovichich et al., 2006) in b_0 images. Structural images for each subject are registered to the gradient nonlinearity corrected mean b_0 image using rigid body six degrees of freedom (DOF) boundary-based registration (Greve & Fischl, 2009). Eddy corrected diffusion data is then registered to the structural volume for each subject according to both the gradient nonlinearity correction and the b_0 to T_1 registration transform.

3.2.3 Fiber Orientation Estimation

A common model-based approach to fiber orientation estimation is the so-called ball and stick model (Behrens et al., 2003b). In this model, the diffusion within a voxel is assumed to be comprised of two types of compartments: a non-oriented tissue that gives rise to an isotropic diffusion signal, and an oriented fiber component with an anisotropic diffusion signal. The approach is to model the diffusion signal attenuation u_i for each gradient intensity value b_i as a 3D gaussian distribution (Behrens et al., 2003b) along a gradient direction r_i

$$u_i = S_0((1-f)\exp(b_i d) + f\exp(-b_i d\, r_i^T R\, AR^T r)) \quad (1)$$

where d is diffusivity, S_0 is the diffusion signal with no applied gradients, f is the fraction of the signal contributed to by anisotropic diffusion within the voxel corresponding to a single fiber and RAR^T is the corresponding tensor along the fiber direction. The first term represents the isotropic partial volume and the second term the anisotropic partial volume. The parameters of interest are the tensor eigenvalues and the angles between them that describe the direction of the fiber. Bayesian estimation of the parameters of this model to the signal at each voxel generates a fiber orientation density function (fODF) for each voxel as well as a measure of its uncertainty. Additional fibers j are added to the partial volume model as a sum over fiber compartments f_j within the voxel:

$$u_i = S_0((1-\sum_{j=1}^{N} f_j)\exp(b_i d) + \sum_{j=1}^{N} f_j \exp(-b_i d\, r_i^T R_j\, AR_j^T r_i)) \quad (2)$$

The partial volume model of the diffusion signal within each voxel is the sum of an isotropic signal and the weighted sum of signals from a set of fibers with different orientations. However, at b values above 1500 s/mm^2 however, diffusive decay is no longer mono-exponential (Niendorf et al., 1996). Therefore, when multi-shell imaging is used, simply adding additional terms for additional fiber directions leads to erroneous results. Approaches that attempt to explicitly model the divergence from a single exponential term can lead to model overfitting (Jbabdi et al., 2012) and false positive connections. Therefore, an extension of this model for the estimation of additional fiber directions treats the diffusion coefficients within a voxel as a continuous (gamma) distribution (Jbabdi et al., 2012). Parameterizing the distribution allows an analytic expression to be formulated for the (fODF) and requires the addition of only one parameter to the mono-exponential model, avoiding overfitting. This algorithm is implemented in the Bayesian estimation of diffusion parameters obtained using sampling techniques for crossing fibers (BEDPOSTX) algorithm, part of the fMRI software library (FSL). It runs Markov Chain Monte Carlo (MCMC) sampling to build distributions on diffusion parameters at each voxel. Automatic relevance determination (ARD) or shrinkage priors (MacKay, 1995; Friston, 2003; Woolrich & Smith, 2001) are used for assessing the most appropriate number of fiber orientations at each voxel (Behrens et al., 2007). ARD does not fit a separate model for different numbers of fibers and compare them. Instead it fits a single model with parameters for multiple fiber orientations. When there is little evidence that additional directions are present within a voxel, the corresponding estimate of parameter variance will be very small and the parameter

estimate will be forced to zero. ARD is used on the partial volume parameters for all additional fiber orientations beyond the first one. BEDPOSTX algorithm was applied to the preprocessed HCP data to estimate fiber orientation densities and their uncertainties using this framework and a Rician noise model (Jbabdi et al., 2012; Sotiropoulos et al., 2013).

3.2.4 Probabilistic Tractography

After generating voxel-wise probability density functions, a global connectivity model is inferred by spatially propagating the local fiber orientation information obtained through the BEDPOSTX procedure (Behrens et al., 2003b; Parker & Alexander, 2003). A probabilistic streamline tractography procedure was used called probabilistic tracking with crossing fibers (PROBTRACKX), also part of the FSL package (Behrens et al., 2007; Behrens et al., 2003b). Tracing proceeds from a seed location along a direction sampled from the posterior probability distributions resulting from the previous voxel-level analysis and continues through neighboring voxels by choosing samples whose orientation is closest to that of the preceding one in the streamline. This procedure is repeated at each seed regions drawing many samples in order to create a probability distribution on the connection between n seed regions and n target regions. The resulting nxn matrix will contain the number of streamlines that have started from one seed region and passed through any target ROIs. The number of streamlines that passed though target regions are then counted and divided by the total number of samples drawn to compute a probability. This generates a spatial probability distribution function on

connectivity between each seed region and all target brain regions given the local probability distributions. In this way, structural connectivity matrices are obtained using a seeding strategy. Probabilistic tractography was performed using all 252 Brodmann area ROIs as described in Section 2.2 as seeds and targets. The algorithm was run using the following parameters: 5000 samples were drawn from each voxel within a seed region, a curvature threshold of .2 excludes tracts with a sharp curvature in a single step (corresponding to the cosine of the allowable angle between two steps ~+-80 degrees); 2000 steps per sample with a .5 mm step length; volume fraction threshold of .01 for inclusion of more than one fibre orientation, loop checks were performed on paths and no minimum distance threshold. Results at three different thresholds 1%, 5%, and 10% were compared against connectivity reported in the macaque literature. Based on this comparison, a 5% thresholding (250 of 5000 seeds) was chosen. A seed region was considered to be connected to a target region if any voxel within the target exceeded this threshold. Binary group-level connectivity matrices were created from single subject matrices with the added requirement that connections be present in at least half (12/24) of the subjects. These matrices were used to generate group-level whole-brain connectivity profiles for each DMN region. Group-level matrices containing the mean number of streamlines reaching target ROIs were generated using the same criteria, as a de-facto measure of connection strength. The resulting group-level binary connection matrices were visualized using BrainNet Viewer (Xia et al., 2013). In addition, visualizations of the reconstructed tracts were created for qualitative assessment of patterns of connectivity. Since tractography traces through fODFs, of which there is no group-level

estimate, fiber tract visualizations are performed at the single subject level. Therefore, a euclidean distance measure between the group connectivity matrix and each individual subject was calculated to identify the subject whose individual structural connectivity was most similar to the group connectivity matrix. This subject was chosen to generate visualizations of tracts through DMN regions. For these visualizations, a deterministic fiber tracking algorithm (Yeh et al., 2013) was used to trace through the results of the BEDPOSTX reconstruction allowing for 2 fibers of different orientation within a voxel. A random seeding procedure was used covering the whole brain with an anisotropy threshold of 0.12, angular threshold of 65 degrees, and step size of 0.1 mm. The fiber trajectories were smoothed by averaging the propagation direction with 40% of the previous direction. A total of 200,000 tracts were calculated. DMN ROIs were transformed via a non-linear transformation to warp them from MNI standard space to the subject's diffusion space. Visualizations of the tracts passing through the DMN ROIs were then created using using trackVis (Wang et al., 2007b).

In addition to the methodological considerations described above, there are many other caveats to the interpretation of DTI data. Even using data with high angular resolution suffers from difficulties tracing fibers through the grey matter white matter boundary particularly from cortical areas within sulci (Reveley et al. 2015). Because diffusion is equally likely in any direction along a fiber, the direction of axonal projection cannot be determined and therefore afferents and efferents cannot be inferred. Synapses are much smaller than diffusion imaging resolution, therefore connectivity results are typically based on the assumption that a connection is made if a fiber passes through a

structure without direct evidence or ability to discern the type of cells being synapsed. The number of fiber tracts between regions is not the only indicator of connection strength as factors such as the firing properties of the post-synaptic cells and arrangement of incoming synapses also play an important role in determining the strength of regional connections. Errors in fiber orientation estimation can propagate along the the length of a tract and therefore longer tracts have greater possibility for both false positives and false negatives. With these caveats in mind, diffusion imaging also allows unprecedented insight into the large scale organization of the brain and the connectivity of functional networks.

3.2.5 Comparing Connections of ADMN and PDMN

Comparisons of connections in different lobes of the brain and different thalamic nuclei were made to summarize differences in connectivity profiles of anterior and posterior portions of the DMN. Using single subject binary connectivity matrices, regional connections between anterior and posterior DMN regions were compared. Number of streamlines for each region and subject were calculated and normalized by the number of right/left lateralized ROIs in anterior (4) and posterior (8) portions of the network. Connections between DMN brain areas and ROIs in 24 regional subdivisions based on lobe and gyri from the Brainnetome atlas (described in Section 2.2) were then compared via t-test.

3.3 Results

Overall, the connectivity patterns of the DMN regions are similar to those detailed in macaques in Section 1.4.8, including in regions of significant evolutionary changes in ventral medial prefrontal cortex. With the exception of lateral parietal cortex BA 39, all of the DMN regions are strongly interconnected. However the connections of individual regions differ significantly, especially between anterior and posterior parts of the network. Both portions of the network have extensive connections through subcortical structures in the striatum and thalamus although they project to different areas within those structures. Differences in connectivity in anterior and posterior portions of the network are also consistent with the animal literature. The following sections first detail the connections of each DMN region in anterior and posterior DMN. Then, the differences in connectivity between the anterior and posterior portions of the network are considered. The chapter concludes with a discussion of DMN region projections through the basal ganglia and thalamus. Tables of connections for each region sorted by their connection strength are provided in the Appendix.

3.3.1 Connections of the Anterior Default Mode Network

3.3.1.1 Brodmann Area 10 medial

As shown in Figure 3.1, BA 10 medial (m) projects strongly and ipsilaterally through the cingulum bundle to medial posterior parts of the network, BAs 31, 23, and 7m and to secondary somatosensory cortex BA 5. While, connections to posterior cingulate and medial parietal regions are mostly ipsilateral, it is strongly connected through the genu of the corpus callosum to contralateral regions in frontal cortex

including BAs 10m, 14, 32p, 8 (FEF), and 9m. It has connections to the ventral insula and hippocampus and parahippocampal gyrus. Its striatal projections intersect both the head and body of the caudate as well as the nucleus accumbens. Streamlines from BA 10m intersect all subdivisions of the thalamus except sensory thalamus. It does not appear to have direct connections with BA39, typically considered part of the DMN. Table B1 lists all connections of BA 10m ordered by de-facto connection strength (number of streamlines) and averaged over left and right lateralized regions.

3.3.1.2 Brodmann Area 32 pregenual

In comparison to BA 10m, BA32 pregenual (p) has a more circumscribed pattern of almost exclusively ipsilateral connections through the cingulum (Figure 3.2). It has connections with most regions within and anterior to the cingulate gyrus including BAs 32 subgenual (sg), 9m, 8, 6, 24, 23, 31, and 7m. A large number of fibers connect it to the nucleus accumbens but not to other striatal regions nor the thalamus. Also absent are connections to regions in the temporal and occipital lobes. See Table B2 for a list of all connections of BA 32p.

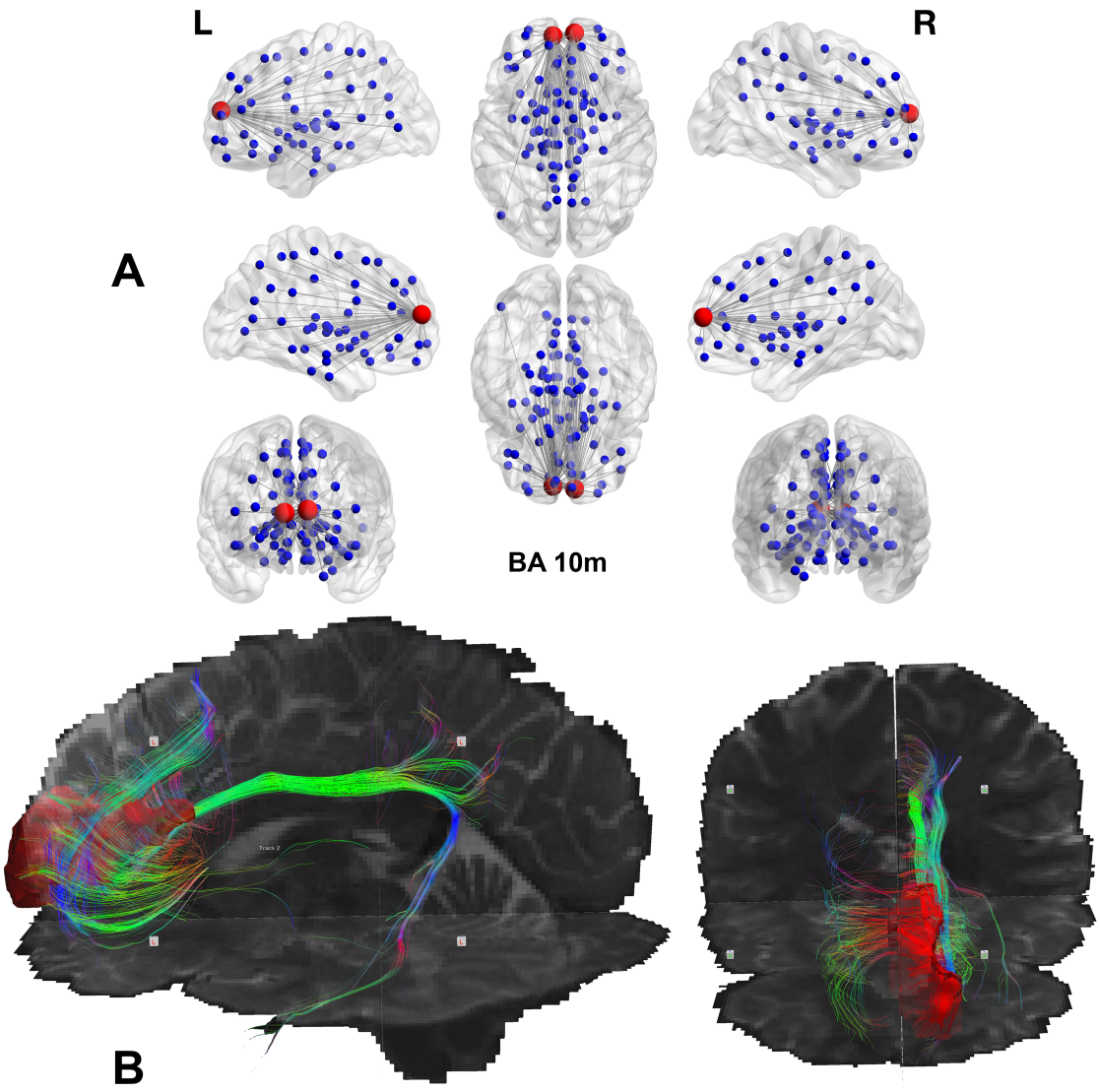

Figure 3.1 Anatomical Connections of BA 10 Medial

A. Group-level connectivity for BA 10m (red). **B.** Side and front views of single subject tractography for left hemisphere BA 10m (red), illustrating ipsilateral fibers projecting to subcortical regions, projections through the cingulum and contralateral connections in prefrontal cortex through the genu of the corpus callosum. The color-coding of

tractography pathways was based on a standard red-green-blue code for each pathway (red for right-left, blue for dorsal-ventral and green for anterior-posterior).

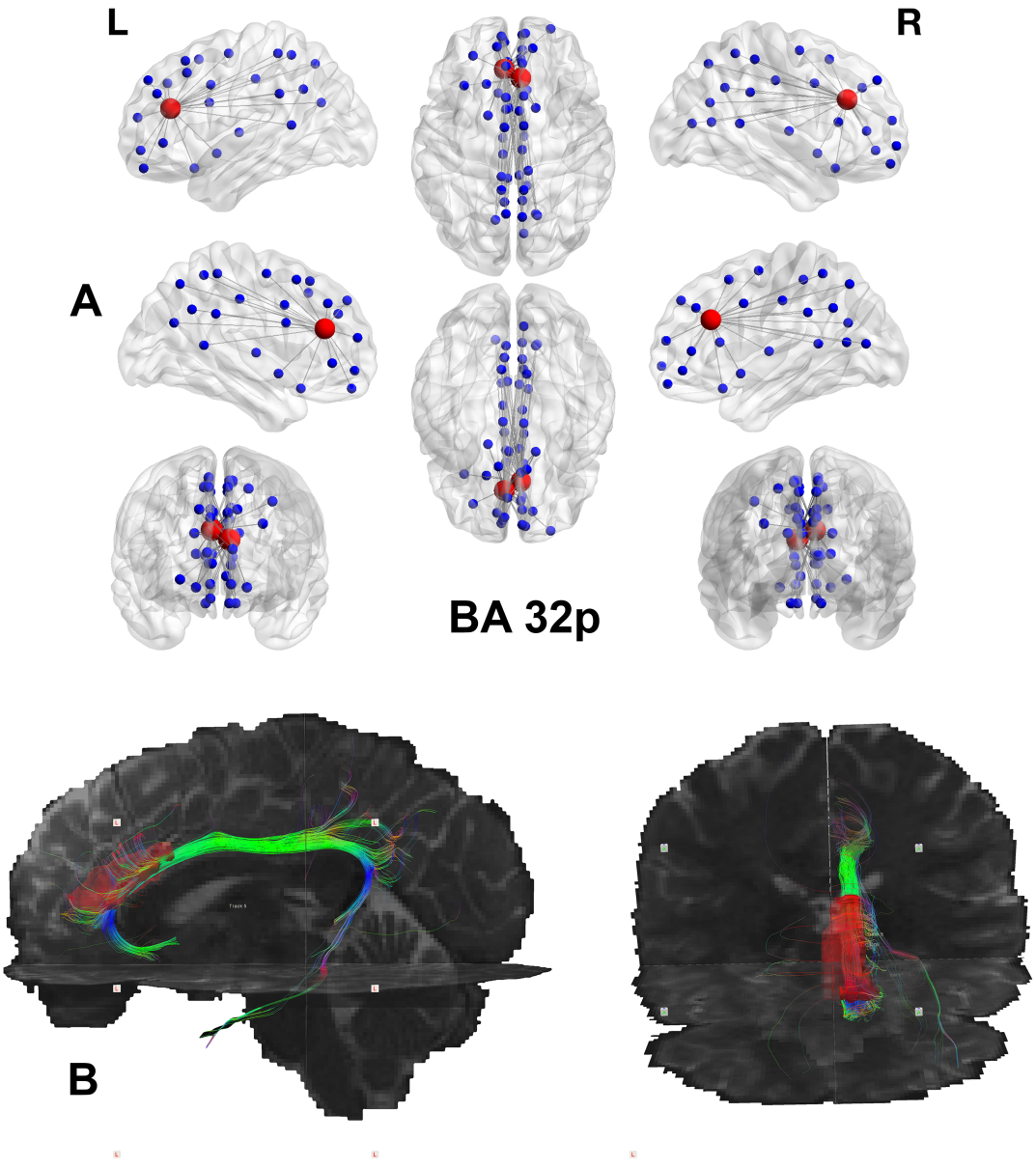

Figure 3.2 Anatomical Connections of BA 32 Pregenual

A. Group-level connectivity for BA 32p (red). **B.** Side and front views of single subject tractography for left hemisphere BA 32p (red). BA 32p has almost exclusively ipsilateral connections through the cingulum. Tractography pathways coded red for right-left, blue for dorsal-ventral and green for anterior-posterior.

3.3.2 Connections of the Posterior Default Mode Network

3.3.2.1 Connections of Posterior Parietal Cortex - BA 23 dorsal

BA 23 dorsal (d) in the posterior cingulate has connections to all other parts of the posterior DMN both ipsilaterally and contralaterally through the isthmus of the corpus callosum (Figure 3.3). Through the cingulum bundle, it is connected ipsilaterally with anterior regions of the DMN as well as regions within and superior to the cingulate gyrus including BAs 32 sg, 24, 5, 8m, and 9m. It is also connected with neighboring cortical regions in cuneal cortex BAs: 7rostral (r), 7 postcentral (pc) and 7 caudal (c), parietal-occipital sulcus as well as primary motor and somatosensory cortex including BAs 1, 2, 3 and medial portions of BA 4. It has both ipsilateral and contralateral connections with the insula and temporal regions including the hippocampus, parahippocampal gyrus and superior and inferior temporal gyrus (BAs 22 and 20). It projects to the dorsal caudate, dorsal lateral putamen and nucleus accumbens and has connections with thalamic subdivisions associated with temporal, occipital, posterior-parietal, sensory, premotor, medial and lateral prefrontal cortex (Table B3).

3.3.2.2 Connections of Posterior Parietal Cortex - BA 31

Situated just dorsal to BA23d in the posterior cingulate, BA 31 is connected ipsilaterally to all other regions of the DMN (Figure 3.4) and contralaterally to posterior DMN regions. Like area 23d, BA31 is also connected ipsilaterally through the cingulum to regions within and on the anterior border of the cingulate gyrus including BAs 5, 7, 8, 9, 24, 32sg as well as primary somatosensory cortex BAs 1, 2, 3 and primary motor cortex. It has connections with area 9 lateral (l) in lateral prefrontal cortex, the insula and neighboring regions in cuneal cortex, and parietooccipital sulcus. It has both ipsilateral and contralateral connections to all parts of the striatum and all major subdivisions of thalamic nuclei except premotor thalamus (Table B4). There is some disagreement between the group-level connectivity matrix and the single-subject tracts for BA 31. The single-subject results show connections throughout the ipsilateral temporal lobe that are not present in the group-level connectivity matrices. Connections between BA 31 and temporal regions have been identified in the macaque literature (Section 1.4.8.2.2). However, these connections can be seen when using a lower connectivity threshold of about 1%. Given the probabilistic nature of the tractography algorithm, it is possible that a lower threshold is required for hub regions such as BA31.

3.3.2.3 Connections of the Precuneus - BA 7m

Located in the medial superior parietal lobule, BA 7m is connected bilaterally to other posterior DMN regions and ipsilaterally to the anterior DMN via the cingulum (Figure 3.5). Along the cingulum, tracts reach medial BAs 5 ,6, 8, and 9, and primary

sensory cortex. It has extensive connections in the ipsilateral temporal lobe and more extensive connections in occipital cortex than BAs 23 or 31. In the striatum, it projects to the dorsal caudate, ventral and dorsal putamen, and nucleus accumbens. Its thalamic connections include nuclei associated with sensory, premotor, occipital, temporal, posterior parietal, and lateral prefrontal regions (Table B5).

3.3.2.4 Connections of BA 39 rostrovental

BA 39 rostroventral (rv), located more laterally in superior parietal cortex than the rest of the posterior DMN regions, has a connectivity profile unlike any of the other DMN regions (Figure 3.6). Its projections are much more laterally focused with extensive connections throughout the temporal lobe. It has connections with the caudal hippocampus as well as the insula and lateral prefrontal cortex including BAs 5l, 6l, 8l, 10l, 44 and the inferior frontal junction (IFJ). Furthermore, it does not share connections through the cingulum to the anterior portions of the network. It projects to a more restricted area of the striatum, having connections with the nucleus accumbens dorsal and ventral putamen, but not the caudate nucleus. It is also connected with more lateral and inferior portions of the thalamus having connections only with nuclei associated with posterior parietal, sensory and and temporal cortex (Table B6).

3.3.3 DMN Structural Connections Summary

Fibers that pass through the DMN were found to pass through 62% of the Brodmann areas in the Brainnetome atlas outside the network itself. Anterior and

posterior regions of the DMN are connected to one another through the association fibers of the cingulum, but each has a local connectivity profile that shifts gradually across the network as you go from anterior to posterior regions (Figure 3.7). Connections through ADMN are concentrated medially in prefrontal cortex, subcortical areas and throughout the cingulate gyrus. The anterior portion of the DMN, BAs 32p and 10m are highly interconnected with one another both ipsilaterally and contralaterally through the genu of the corpus callosum. They are both connected to ipsilateral regions throughout the cingulate gyrus through the cingulum. Tracts did not appear to connect ADMN regions with the amygdala or temporal cortex through the uncinate fasciculus. Connections to frontal cortex through the uncinate fasciculus appear to be restricted to regions more ventral in orbital prefrontal cortex and regions more lateral than BA 10m. Therefore, if DMN connections through the uncinate fasciculus do exist, BA 11 must also be considered part of the network. Alternatively, ADMN may have connections to temporal cortex indirectly through the PDMN regions. Ipsilaterally, PDMN regions are tightly interconnected with ADMN regions through the cingulum, with the exception of BA 39. PDMN has significantly more connections to hippocampal regions as well as regions throughout the temporal lobe, regions associated with visual processing and regions in precentral and postcentral gyrus associated with sensory-motor processing (Figure 3.7). As you move more dorsally through the medial posterior DMN regions, there are more occipital connections and connections with more inferior regions of temporal cortex. The connections of BA 39 are quite different than those of the rest of the network as it does not appear to have connections through the cingulum bundle. Instead, it has has

extensive projections in the temporal lobe and to some areas of lateral prefrontal cortex that are not associated with the DMN. Anterior and posterior DMN regions project to the striatum especially the caudate and nucleus accumbens, and PDMN also has connections to the putamen. Differences between ADMN and PDMN can also be seen in their thalamic connections (Figure 3.8). ADMN has the strongest connection to the medial thalamus generally associated with prefrontal cortical regions and the thalamic subregion associated with premotor cortices. PDMN has a connections throughout most of the thalamic subregions. PDMN tracts enter the thalamus at its medial posterior and lateral posterior extent, with a subset of those fibers continuing through the center of anterior thalamus through its entire anterior to posterior extent.

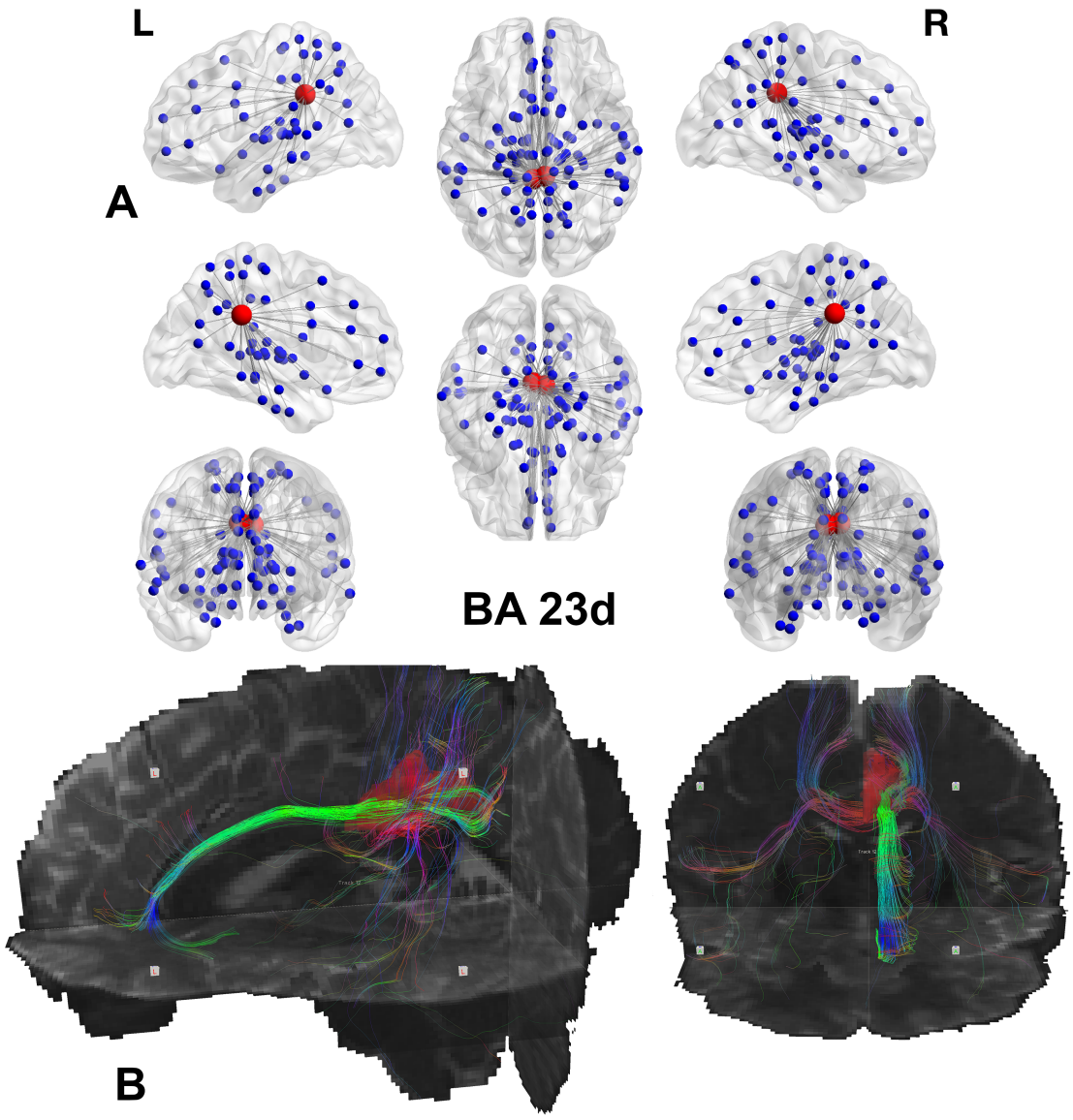

Figure 3.3 Anatomical Connections of BA 23 Dorsal

A. Group-level connectivity for BA 23d (red). **B.** Side and front views of single subject tractography for left hemisphere BA 23d (red). BA 23d has ipsilateral and contralateral connections with DMN regions in the posterior cingulate and the hippocampal and parahippocampal regions through the cingulum and ipsilateral connections to regions

throughout and anterior to mid and anterior cingulate. Tractography pathways coded red for right-left, blue for dorsal-ventral and green for anterior-posterior.

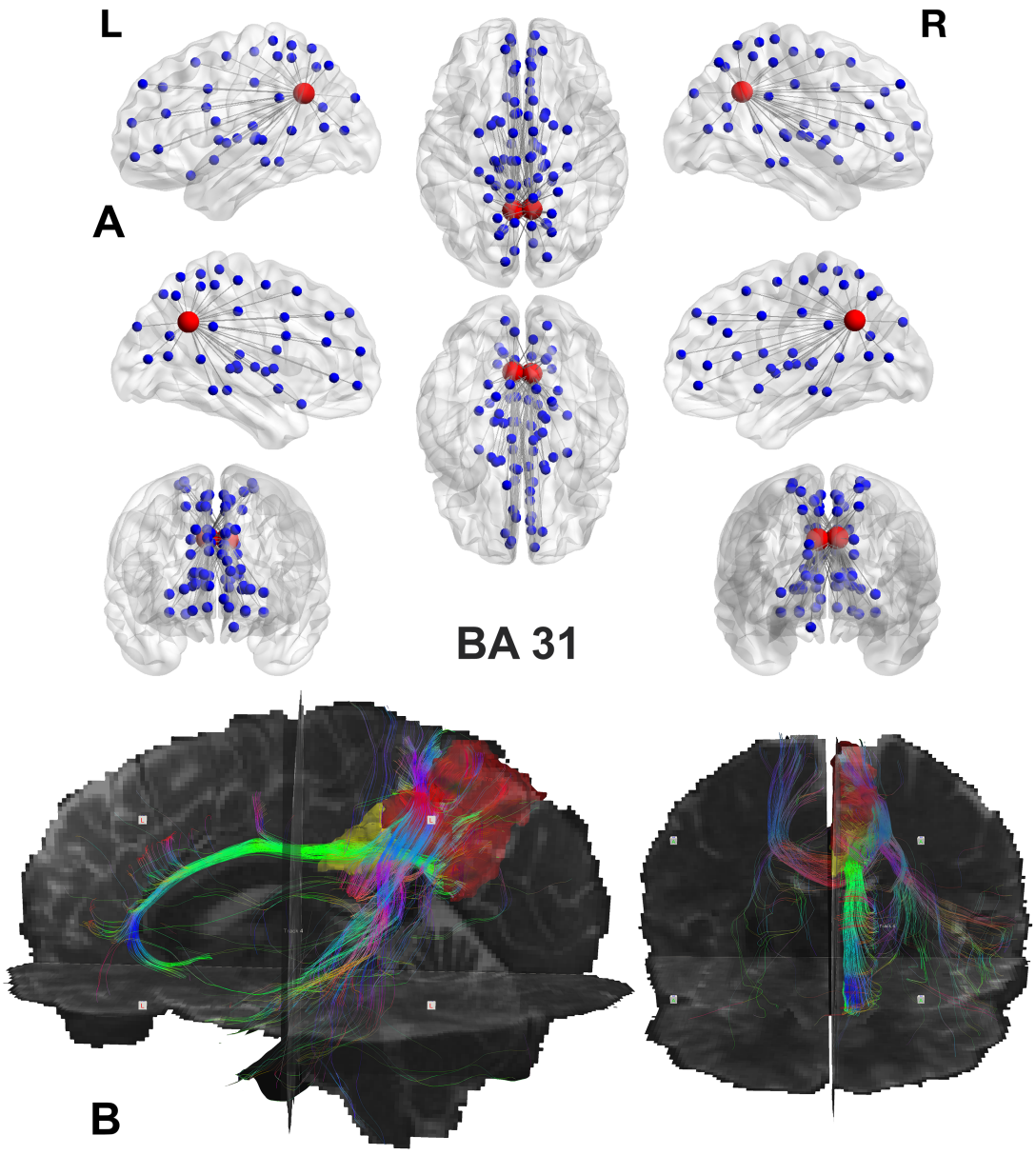

Figure 3.4 Anatomical Connections of BA 31

A. Group-level connectivity for BA 31 (red). **B.** Side and front views of single subject tractography for left hemisphere BA 31 (red). BA 31 has ipsilateral and contralateral connections with DMN regions in the medial posterior cingulate. It has ipsilateral connections to anterior DMN regions, regions throughout the cingulate gyrus and the hippocampus and extensive connections through the temporal lobe. Tractography pathways coded red for right-left, blue for dorsal-ventral and green for anterior-posterior.

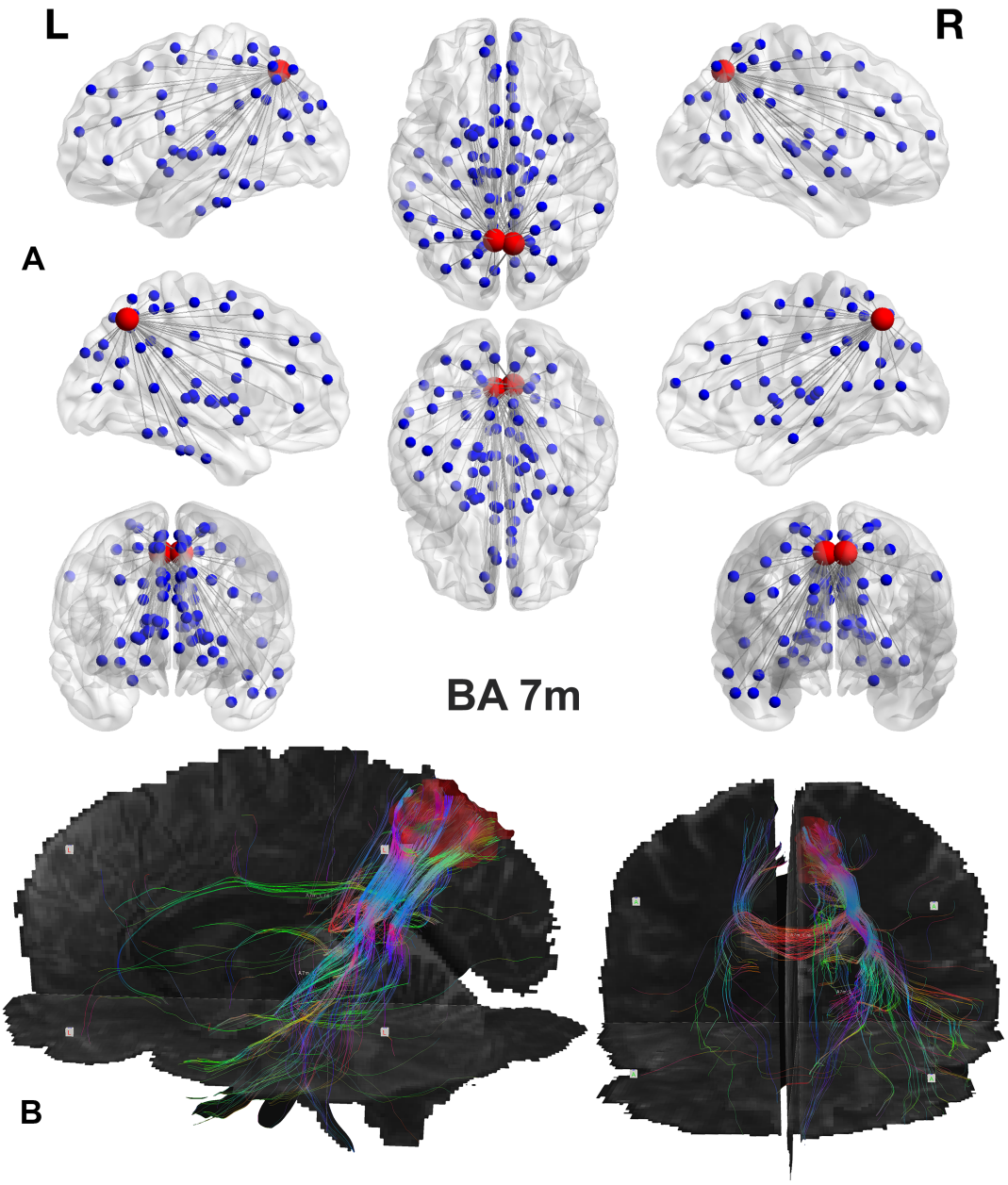

Figure 3.5 Anatomical Connections of BA 7 Medial

A. Group-level connectivity for BA 7m (red). **B.** Side and front views of single subject tractography for left hemisphere BA 7m (red). BA 7m has ipsilateral and contralateral connections with DMN regions in the posterior cingulate and connections ipsilaterally

within the temporal lobe and occipital cortex. Tractography pathways coded red for right-left, blue for dorsal-ventral and green for anterior-posterior.

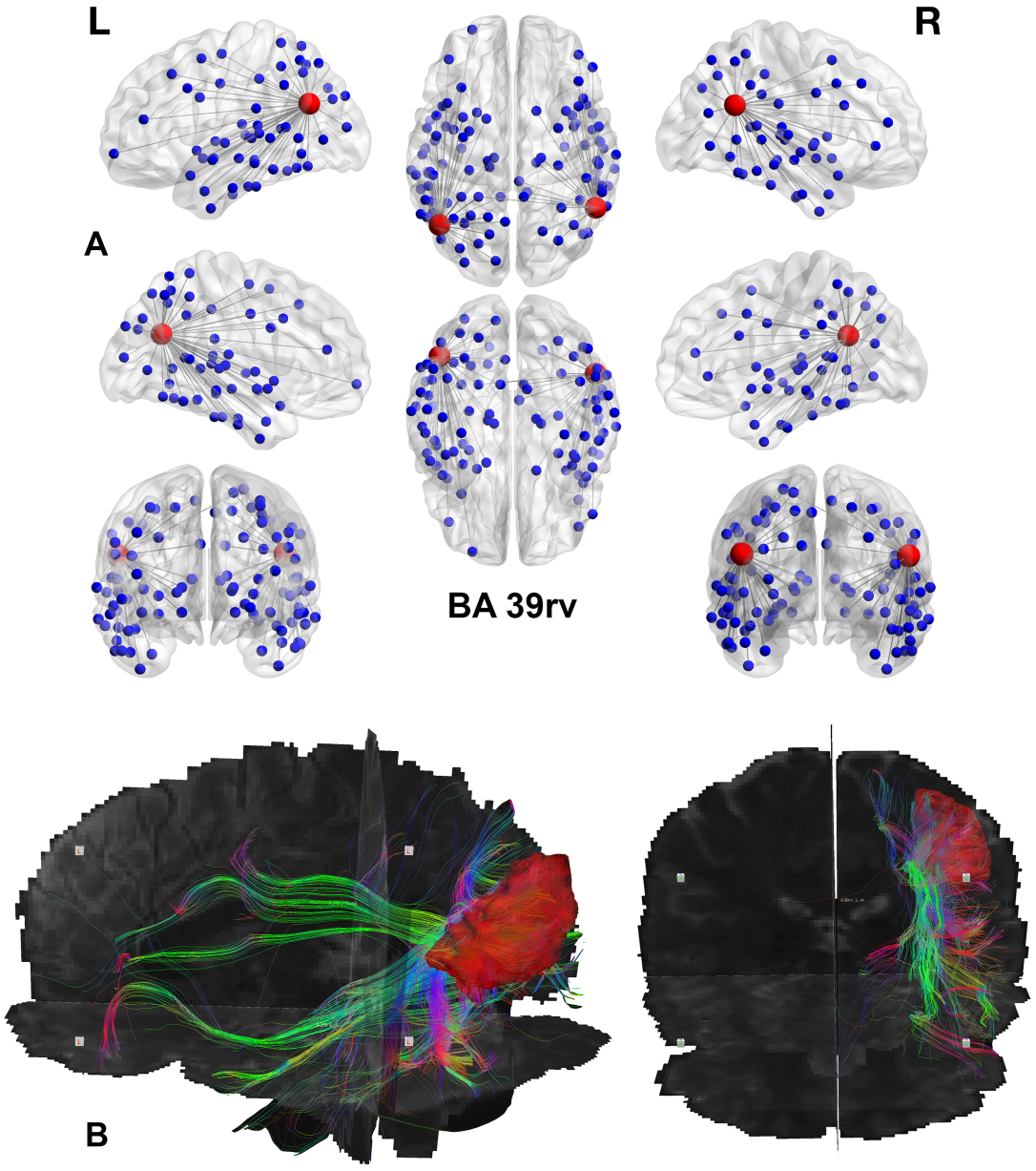

Figure 3.6 Anatomical Connections of BA 39 Rostroventral

A. Group-level connectivity for BA 39rv (red). **B.** Side and front views of single

subject tractography for left hemisphere BA 39rv (red). BA 39rv has connections mostly in ipsilateral temporal lobe and lateral prefrontal areas and does not have connections through the cingulum bundle to ADMN regions. Tractography pathways coded red for right-left, blue for dorsal-ventral and green for anterior-posterior.

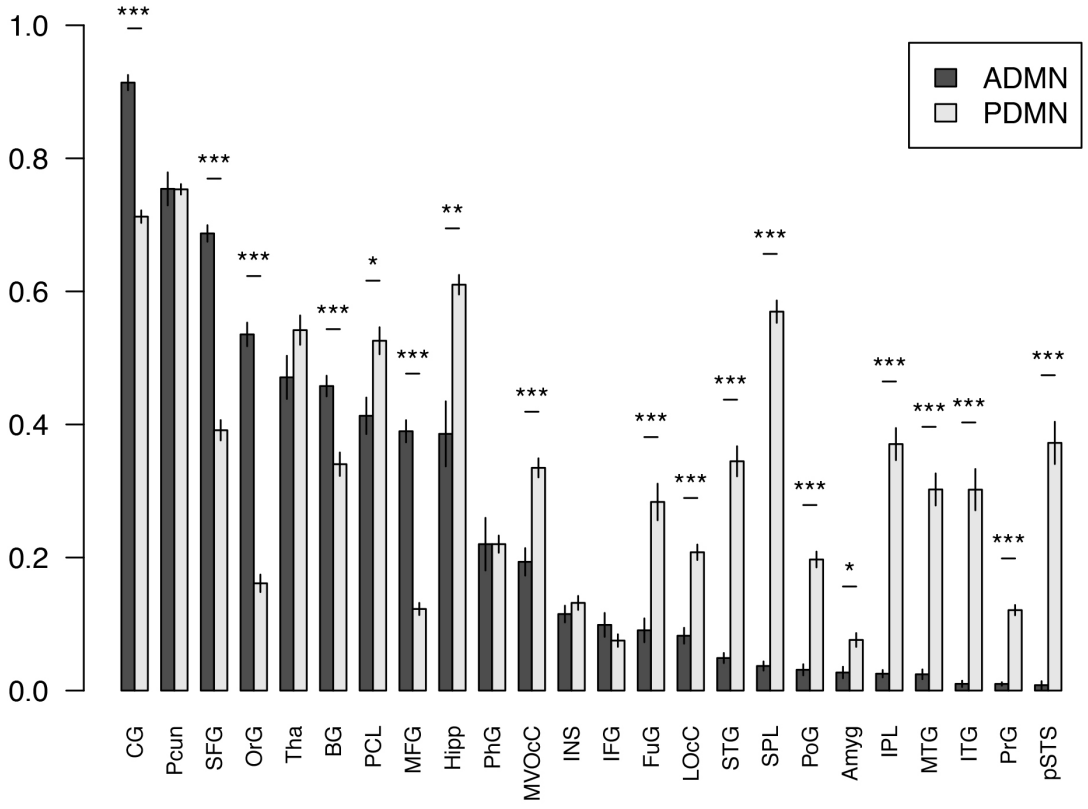

Figure 3.7 Regional Connections of the Anterior vs. Posterior DMN

Anterior and posterior DMN connections through the Brainnetome atlas across subjects normalized by the number of areas in each cortical region so that a value of 1 indicates a mean across subjects where all DMN regions are connected to all cortical subregions. Regional connection frequency is sorted by their association with ADMN, illustrating a dissociation between ADMN and PDMN connections. PDMN has more extensive

connections to temporal, parietal and occipital cortex while ADMN has more connections in the superior frontal, medial frontal and orbital gyrus. CG = cingulate gyrus, SFG = superior frontal gyrus, Pcun = precuneus, OrG = orbital gyrus, BG = basal ganglia, MFG = middle frontal gyrus, Tha = thalamus, Hipp = hippocampus, PCL = paracentral lobule, MVOcC = medio-ventral occipital cortex, PhG = parahippocampal gyrus, Amyg = amygdala, INS = insula, STG = superior temporal gyrus, FuG = fusiform gyrus, IFG = inferior frontal gyrus, LocC = lateral occipital cortex, SPL = superior parietal lobule, ITG = inferior temporal gyrus, MTG = medial temporal gyurs, IPL = inferior parietal lobule, PrG = precentral gyrus, pSTS = posterior superior temporal sulcus, PoG = postcentral gyrus. *** indicates significance at $p < .001$, * significance at $p < .05$ corrected, error bars indicate standard error.

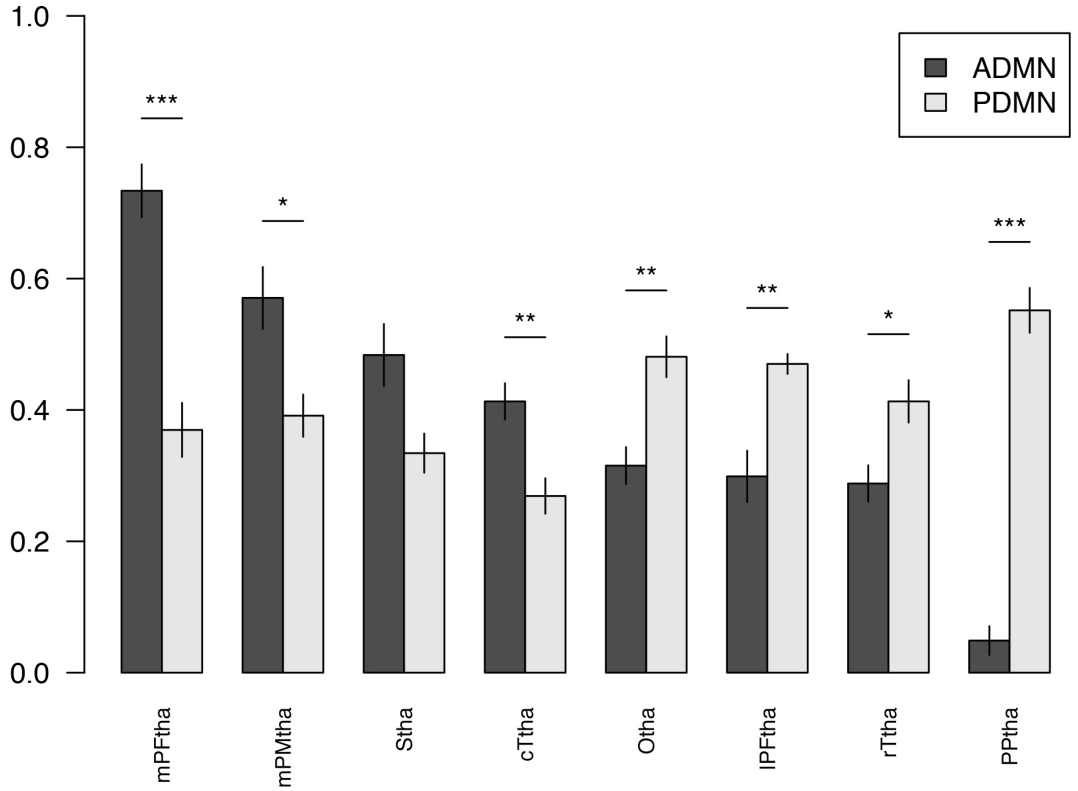

Figure 3.8 ADMN and PDMN Thalamic Connections

Anterior and posterior DMN connections through the thalamic subregions of the Brainnetome atlas across subjects sorted by connection frequency in the ADMN. A dissociation between ADMN and PDMN connections in thalamic regions is apparent. PDMN has connections throughout a greater extent of the thalamus while ADMN has greater connections to thalamic subregions associated with prefrontal and premotor cortices. A value of 1 indicates a mean across subjects where all DMN regions are connected to the thalamic subregion. *** indicates significance at $p < .001$, ** $p<.01$ and * $p<.05$ corrected, error bars indicate standard error.

3.3.4 Cortico-Striatal-Thalamic Circuit of the DMN

Both anterior and posterior regions of the DMN have connections with the striatum and thalamus. However, the two parts of the network appear to project to different areas within these structures. Anterior parts of the DMN appear to project to both medial and lateral regions of the head of the caudate and anterior nucleus accumbens. Posterior parts of the network project to the tail of the caudate and to the posterior parts of the putamen and nucleus accumbens (Figure 3.9). ADMN has connections with the anterior medial thalamus while posterior regions have fibers that approach the thalamus from its posterior extent and continue anteriorly through most of the thalamic subregions. Therefore, ADMN and PDMN connect to the striatum and thalamus from opposite ends forming a circuit in the sagittal plane through the basal ganglia and thalamus ipsilaterally. Contralateral connections through the striatum and thalamus form a second loop also in the sagittal plane that circumscribes the ipsilateral one (Figure 3.10). In the ipsilateral circuit, cingulum fibers from the PDMN pass through ADMN regions and continue into the anterior ventral caudate and nucleus accumbens. Contralaterally, PDMN regions appear to have connections to the same areas of the basal ganglia and thalamus as it does ipsilaterally. ADMN also has connections through contralateral striatal regions. It does not appear to have direct connections to contralateral thalamic regions, though such connections may occur downstream of its basal ganglia connections. Tracts that go through anterior and posterior regions of the network in one hemisphere are connected to striatal and thalamic nuclei in the contralateral hemisphere. Therefore, a contralateral circuit circumscribes the ipsilateral

circuit (Figure 3.11A). Assuming that striatal connections are unidirectional and that there are likely reciprocal connections between the thalamus and each DMN region, Figure 3.11B diagrams the proposed CST circuit through the DMN.

Cortical maps of connections to the basal ganglia and thalamus indicate that projections from regions with similar functionality cluster into distinct regions within these subcortical structures (Choi et al. 2012; Metzeger et al., 2013; Haber & McFarland, 2001; Haber, 2016; Choi et al. 2017). Based on tract tracing studies, five CST circuits have previously been proposed (Alexander, 1986). Two prefrontal circuits, one originating in dorsolateral prefrontal cortex, and one originating in lateral orbitofrontal cortex, an occulomotor circuit and a circuit with unknown function originating in the anterior cingulate gyrus were described. It is possible that the CST circuit through the DMN participates in or subsumes one or more of these circuits, particularly the occulomotor and anterior cingulate circuits. The occulomotor circuit is believed to originate in the frontal eye field (BA 8) and is proposed to include projections from BAs 9, 10 and 7 (Yeterian & VanHoesen, 1978, Selemon & Goldman-Rakic, 1985) to the body of the caudate and the ventral anterior and mediodorsal regions of the thalamus. My results suggest that only BA 10m has direct connections to lateral portions of BA 8 (FEF), but all of the other medial DMN structures have connections with BAs 8m, 7 and 9l as well as the caudate nucleus and the anterior subregions of the thalamus. Therefore, there is considerable overlap in the DMN circuit and the proposed occulomotor circuit. The anterior cingulate circuit is described as having projections from BA 24 in anterior cingulate, the hippocampus, amygdala, entorhinal cortex and regions throughout the

temporal lobe to the nucleus accumbens and mediodorsal portion of the thalamus. While BA 24 is not part of the DMN, the circuit through which the DMN connects to the striatum and thalamus projects heavily through the entire cingulate gyrus. In addition, the hippocampus and entorhinal cortex are connected to DMN regions and are often considered to be part of the DMN. Therefore, it may be that the DMN CST circuit is an amalgamation of two of the proposed circuits through the striatum and thalamus. The other two prefrontal circuits were described as dorsolateral and lateral orbitofrontal circuits. The orbitofrontal circuit is said to originate in BAs 9 and 10 in orbitofrontal cortex and also includes BA 7 in posterior-parietal cortex with projections throughout the caudate. Thus it is conceivable that the CST circuit described here through DMN structures may have some overlap with all but the motor circuit.

Projections through the basal ganglia are organized into two main pathways called the direct and indirect pathways generally believed to have opposing roles in motor function. The direct pathway through the basal ganglia proceeds from the striatum directly to the globus pallidus internal (GPi) and substantia nigra pars reticulata (SNr). The indirect pathway proceeds from the striatum to the GPi via the globus pallidus external (GPe) and subthalamic nucleus (STN) (Haber, 2016). Activation of the direct pathway acts to release thalamic regions from inhibition, while activation of the indirect pathway increases inhibition of thalamic nuclei. The two pathways are believed to cooperate by releasing from inhibition cell assemblies related to desired movement, while inhibiting unwanted movement. The role of the two pathways in cognitive function is less well understood. As the two pathways have opposing roles, understanding the

relationship of functional networks that may compete with one another through these subcortical structures is of particular interest. However, it is not possible to disambiguate the two pathways using diffusion imaging, because many of the fibers that synapse in the GPi reach the GPi by first passing through the GPe. However, it is worth noting that connections from sensory motor cortex have a relatively vertical trajectory through the GP so that the majority of fibers that traverse the internal segment pass first through the external segment. Fibers originating in frontal and parietal cortex, however, appeared to pass through the external segment at an oblique angle such that they do not always pass through the GPi. Further study is required to determine the veracity of this observation and, if true, its functional significance. Nevertheless, the anatomical connections of the DMN appear to form a CST circuit that may subsume several of the previously proposed CST circuits. This result also raises the possibility that other functional networks identified in the functional MRI literature may each be involved in parallel CST circuits.

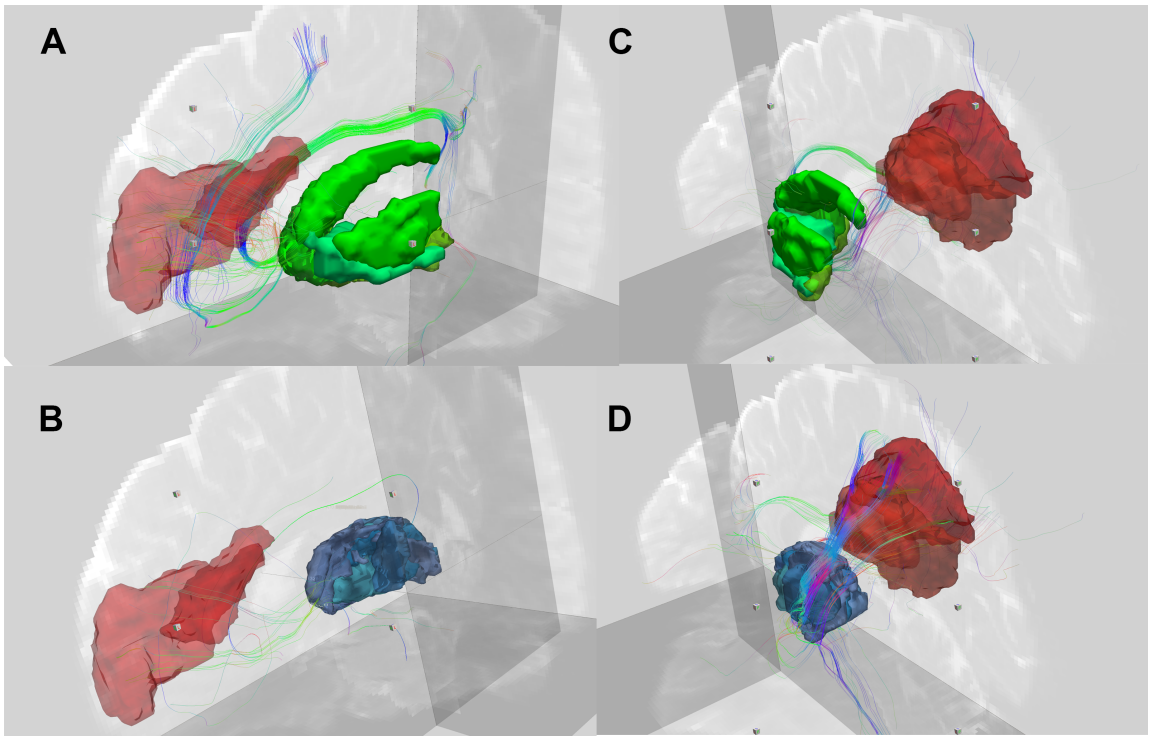

Figure 3.9 Thalamic and Striatal Connections of the DMN

A. ADMN connections to the striatum. **B.** ADMN connections to the thalamus.

C. PDMN connections to the striatum. **D.** PDM connections to the thalamus.

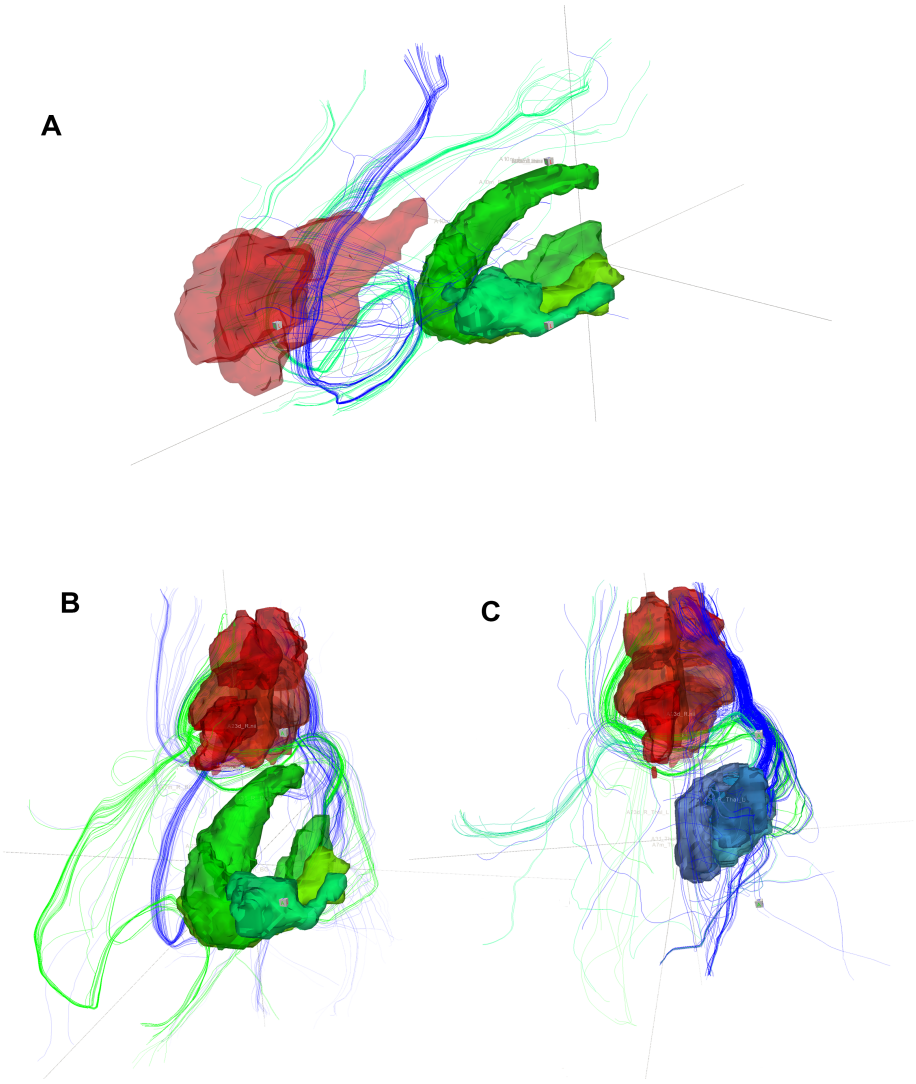

Figure 3.10 Ipsilateral and Contralateral DMN connections to Striatum and Thalamus

A. ADMN tracts through the striatum. **B.** PDMN tracts through the striatum. **C.** PDMN thalamic tracts. Crosshairs indicate the midline of the brain. Blue tracts indicate ipsilateral connections, green tracts indicate connections from contralateral DMN regions.

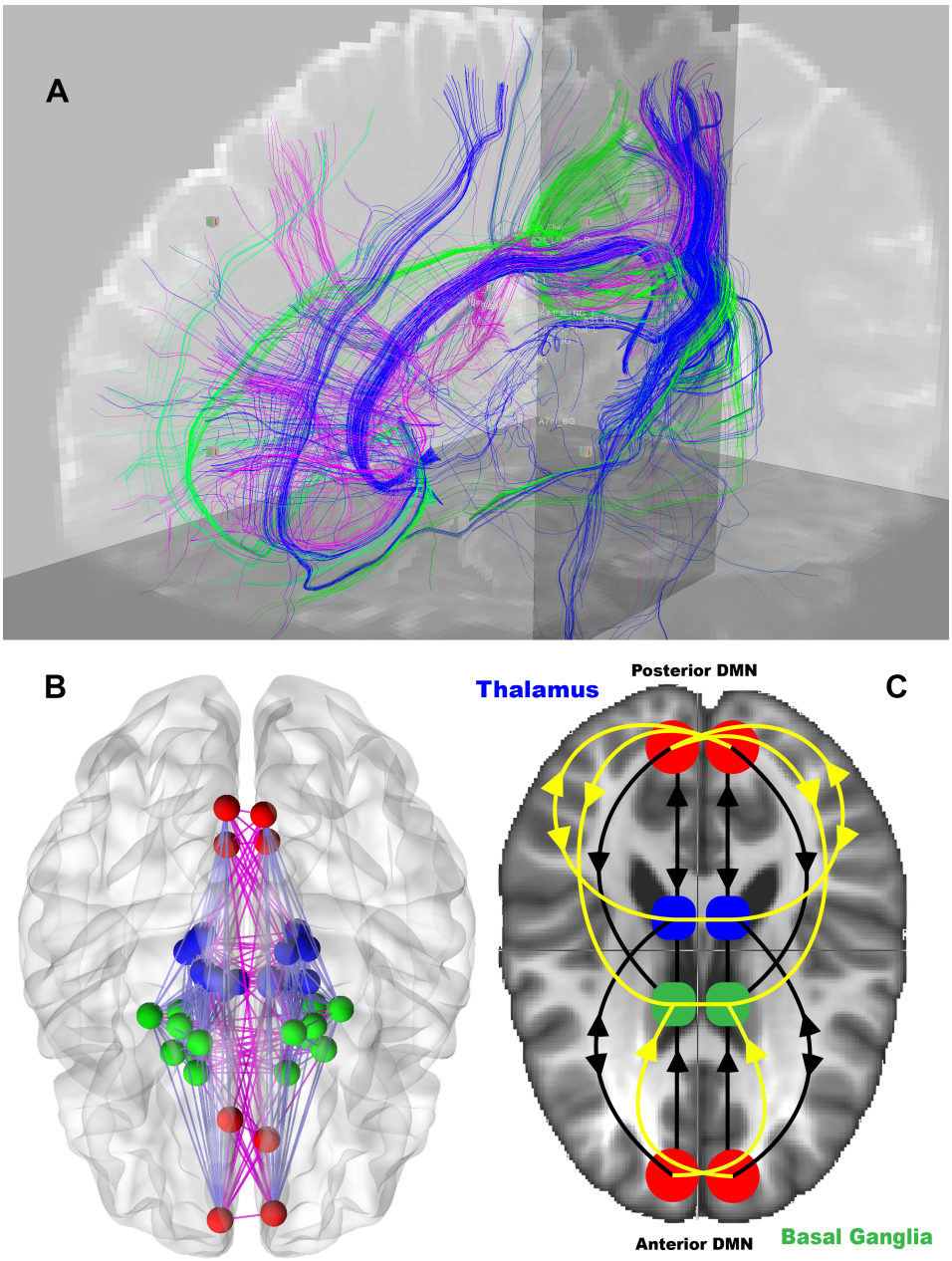

Figure 3.11 Cortical Striatal Thalamic Circuit of the DMN

A. Blue tracts show ipsilateral circuit on the left side. Green and purple lines show contralateral circuit with connections from left DMN regions in purple and right DMN regions in green. **B.** Group level connection matrix of DMN connections with striatum

and thalamus. **C.** Diagram of the ipsilateral and contralateral cortical striatal thalamic circuits through the DMN. Black lines indicate ipsilateral connections. Yellow lines indicate contralateral connections.

CHAPTER IV
DMN TASK-EVOKED DYNAMICS

4.1 Introduction

Task-based fMRI studies have identified networks that support a wide range of cognitive abilities (Cabeza & Nyberg, 2000). Regions associated with attention and executive control exhibit task-evoked increases in BOLD signal and are known collectively as the fronto-parietal control network or the task positive network (TPN) (Shulman et al., 1997; Niendam et al., 2012). Task-evoked increases in the TPN are often coincident with decreases in signal within the DMN (Golland et al., 2008; Spreng et al., 2010), although the functional significance of this relationship is not yet known. The consistency of DMN deactivations across disparate experimental paradigms suggests that DMN deactivation has a more general purpose in the context of externally directed focus. Many studies report a correlation between task-evoked suppression of DMN activity and task accuracy (Weissman et al., 2006; Kelly et al., 2008; Esterman et al., 2013). Therefore it is thought that a reduction in DMN activity is required to successfully redirect attention away from internal rumination towards the external environment (Buckner et al., 2008). Others have suggested that decreased activity in the DMN may act to reduce brain activity in regions supporting task-irrelevant functions (Anticevic et al., 2013). A negative relationship between the DMN and TPN has also been observed in spontaneous BOLD fluctuations measured in the resting state (Fox et al., 2005). This observation led to the view that there is an intrinsic antagonism between the two networks. However, some have attributed negative correlation between the DMN and

TPN during rest to an artifact caused by the use of global signal regression in preprocessing (Dixon et al., 2016). Additionally, it has been shown that coordinated activity in the DMN and TPN can be evoked by certain cognitive tasks (Spreng et al., 2010; Gerlach et al., 2011), demonstrating that the two networks are not necessarily antagonistic. Several studies have suggested that interaction between the TPN and DMN is mediated by the anterior insula (dIa) (Menon & Uddin, 2010; Sridharan et al., 2008), which is believed to play a role in task switching. However, the mechanism underlying the interaction between the TPN and DMN is unknown.

Inference about the interaction between brain regions requires characterizing their concurrent changes in activity over time. However, the most commonly used fMRI analysis techniques provide no information about dynamic changes in activity. General linear models typically employed for the analysis of task-based fMRI provide only a static picture of voxels whose activity is significantly correlated with the time course of experimental manipulation. In block design fMRI studies, the time course of the experiment is modeled by blocks of on-off periods. On periods represent experimental epochs consisting of multiple trials. Each trial typically includes several distinct operations including processing visual stimuli, any number of cognitive computations, and choosing a response. The rational for block designs in task-based fMRI is based on the lagging temporal response of the HRF, but the successful use of event-related designs (Friston et al., 1997; Buckner et al., 1998; Amaro & Barker, 2006) suggests that BOLD signal contains fluctuations related to events on smaller time scales (Mechelli et al., 2003). Another commonly used technique for analysis of MRI data is functional

connectivity. Functional connectivity is more commonly applied to resting-state fMRI. It measures the correlation between regions, but provides only a static snapshot of the pattern of these relationships over time. Several approaches have been developed for the purpose of studying temporal dynamics in MRI time series. One simple approach, sliding window correlation, bins the time series into small segments and measures the correlation over successive bins (Hutchison et al., 2013). Sliding window correlations may not accurately reflect changes in the covariance structure between brain regions over time, as changes in signal variance across windows are often accounted for. More critically, if the DMN and TPN are negatively correlated both during the execution of explicit cognitive tasks as well as during periods of rest (Cole et al., 2014; Hansen et al., 2014), brain activity related to behavioral changes may not be reflected in functional connectivity analysis. Another approach for studying temporal dynamics is effective connectivity. Effective connectivity analyses such as Bayesian network analysis (Spirtes et al., 2000, Ramsey et al., 2011), granger causality (Brovelli et al., 2004) and dynamic causal modeling (Friston et al., 2003), describe the direction of influence between brain regions in addition to the strength of their functional relationships. However, these approaches cannot disambiguate whether task-evoked decreases in the DMN result from decreases in excitatory input, increases in inhibitory input, or a specific pattern of activity across functionally connected regions.

Recent neurophysiological studies have demonstrated transient changes in neural activity in response to external task demands corresponding to sequential bottom-up and top-down flow of information (Siegel et al., 2015). Transient task-evoked activity has

also been identified using fMRI where it has been shown that while some regions exhibit sustained increases over task blocks, others, such as in the occipito-parietal junction, exhibit only transient increases in activity during task transitions (Gonzalez-Castillo et al., 2012). Therefore, characterizing the temporal dynamics of changes in BOLD signal across trials may provide insights into the functional role of the DMN. In this chapter, I present the results of a series of exploratory analyses designed to describe the dynamics of task-evoked activity in the DMN. The work is based on the assumption that task-evoked changes in activity in the DMN are dependent on changes in brain regions that provide input to the network and makes use of the anatomical connectivity described in Chapter II. I show that DMN regions do not exhibit sustained suppression of activity during experimental epochs and do not function as a unit. Rather, each region of the DMN exhibits unique task-specific fluctuations. Time courses of DMN activity appear to be related to trial responses. Using an approach that combines clustering analysis and Markov chain models, I show that for each task, there is a predictable progression through successive patterns of activity across brain regions. The anterior and posterior part of the network often act independently of one another and frequently demonstrate opposing changes in signal intensity. During task performance, the most common configuration of activity has above baseline activity in parietal regions, and below baseline activity in DMN regions in the prefrontal cortex and cingulate. This pattern appears to be reversed for motor-related tasks. Periods of time when the ADMN and PDMN are correlated appear to be associated with specific changes in BG and thalamic activity. Based on these observations, I speculate on a functional role for the DMN in

directing the flow of top-down and bottom up influences during task performance.

4.2 Methods

4.2.1 Data

The HCP data set included seven task paradigms, with two runs each. A subset of these tasks included rest epochs interspersed with task epochs in a block design. As the definition of deactivation implies a comparison to a baseline condition, usually a rest condition, only paradigms that included resting epochs were used. These were the working memory, gambling, motor, relational, and social cognition tasks. Of these tasks, three were chosen for more detailed analysis because of their differential engagement of the DMN, exhibiting task-evoked increases, decreases, and no significant change in activity. These are the social cognition, relational processing and motor tasks respectively. The social cognition paradigm is a theory of mind task. Theory of mind is a cognitive ability that is believed to engage the DMN and to evoke increases in DMN activity (Fletcher et al., 1995). The Relational task involves visual information processing. Visual processing tasks were among the first shown to evoke decreases in DMN activity (Shulman, 1997b). Motor tasks do not evoke increases or decreases in the DMN (Allison et al., 2000; Liu et al., 2011). The details of each of these tasks has previously been described elsewhere and will be briefly described here (Barch et al., 2013a).

In the gambling task, participants play a card guessing game to win or lose money (Delgado et al., 2000). On each trial participants are asked to guess the number on a card

marked with a "?" and respond if they think the number is more or less than 5. After participant response, the number on the card is revealed with either a green up arrow indicated a $1 reward, a red down arrow indicating $.50 loss or the number 5 indicating no monetary reward or loss. The "?" is presented for up to 1500 ms or until the participant responds. Feedback is displayed for 1000 ms. The task is presented in blocks of eight trials with a 1000 ms inter-trial interval (ITI). Blocks were either mostly reward, or mostly loss. Reward blocks had six reward trials with two randomly interleaved loss or neutral trials. Loss blocks had six loss trials with two randomly interleaved reward or neutral trials. In each of two runs, there were two reward blocks, two loss blocks and four 15 second fixation blocks.

The social cognition task is based on videos developed for the purpose of studying theory of mind (Castelli et al., 2000; Wheatley et al., 2007). In 20 second video clips, geometric figures (squares, circles, and triangles) move either randomly on the screen or in a manner suggesting social interaction. After each video, participants judged wether the objects interacted with each other or moved randomly. Each of two task runs had five video blocks (two mental and three random in one run, three mental and two random in the other run) and five fixation blocks (15 seconds each).

The working memory task consisted of separate blocks of trials for objects of four different types: places, tools, faces, and body parts. For each object type, half of the trials were 2-back memory trials and the other half were 0-back memory trials. A cue indicating the trial type was displayed for 2500 ms prior to each block. Each of two runs consisted of four 15 second fixation blocks and eight 25 second blocks each with ten

25000 ms trials. On each trial the stimulus was presented for two seconds followed by a 500 ms ITI.

The relational task is a visual information processing paradigm involving stimuli with different shapes and textures (Smith et al., 2007). In each trial, participants are presented with two pairs of objects, one at the top of the screen and one at the bottom of the screen. In the relational condition, subjects first decide whether the pair at the top of the screen differs in shape or texture and then decide whether the bottom pair differs along the same dimension (shape or texture) as the top pair. In a matching condition, subjects are presented with one pair at the top of the screen and a single image at the bottom of the screen. A cue with the word "shape" or "texture" in the middle of the screen instructs subjects to decide if the image at the bottom of the screen matches either image at the top of the screen on that dimension. In the relational condition, the stimuli are presented for 3500 ms with a 500ms ITI, with four trials per block. In the matching condition, the stimuli are presented for 2800 ms, with a 400 ms ITI and 5 trials per block. In each of two runs there are three 18 second relational blocks, three 18 second matching blocks and three 16 second fixation blocks.

The motor task was adapted from previous motor MRI experiments (Yeo et al., 2011) involving movement of the hands, feet, and tongue. Participants are presented with a visual cue instructing them to tap the fingers of their left or right hands, squeeze their left or right toes, or move their tongues. Each movement block lasted 12 seconds, preceded by a three second cue. In each of the two runs, there are ten blocks, two of tongue movements, four of hand movements (two right and two left), four of foot

movements (two right and two left) and two 15 second fixation blocks. All 24 subjects included in this analysis were right handed and in all but the motor paradigm, subject responses were made with a button box using their right hands.

4.2.2 Data Preprocessing

Functional MRI data from the HCP was acquired after preprocessing with their minimal preprocessing pipeline (Glasser et al., 2013). Custom design of the HCP Siemens Skyra scanner required a customized correction for gradient nonlinearities which was performed using the gradient_nonlin_unwarp package of FreeSurfer (Jovicich et al., 2006). The pipeline corrects for motion by frame realignment using six degrees of freedom (DOF) linear image registration tool (FLIRT) registration to a single band reference image with greater anatomical contrast. FSL topup (Andersson et al., 2003) algorithm is used to estimate the distortion due to B_0 field inhomogeneities in the phase encoding direction. Transformations for registration and distortion correction (gradient nonlinearity distortion, motion correction and EPI distortion) are concatenated and applied in a single transform with spline interpolation. The resulting images are in 2 mm MNI space. Next, data is corrected for receive and transmit bias using field maps estimated from the distortion-corrected single band reference image. Data is then masked and normalized to a 4D whole brain mean of 10,000. Following these preprocessing steps, mean time series were extracted for each of the 252 ROIs in the combined Brainnetome (Fan et al., 2016) and basal ganglia atlases (Keuken & Forstman, 2015) (Chapter II 2.2) and detrended to remove linear trends in the time series.

4.2.3 General Linear Modeling

Functional imaging studies often do not report deactivations in their results. Others report deactivations in regions associated with the DMN without including the specific coordinates of the regions that were identified. Since the definition of the DMN is tied so closely to task-evoked deactivation, general linear modeling (GLM) analysis was used to identify the regions that deactivated across HCP experimental paradigms. All linear modeling was run using FSL's FEAT (http://fsl.fmrib.ox.ac.uk/fsl/fslwiki/ Smith et al., 2004). First, voxel-wise multiple regression of experimental block designs was performed at the single subject level. This analysis included pre-whitening (Woolrich et al., 2001), spatial smoothing using a Gaussian kernel of 4 mm full width half max (FWHM) and high pass temporal filtering with a cutoff of 200 seconds. Activation map Z statistic images were created for single subjects with an initial cluster threshold of $Z > 3.29$ and corrected cluster significance threshold of $p < 0.05$ (Worsley, 2003). For each paradigm, GLM results for each of two runs were combined for individual subjects using a fixed effects model. This resulted in an average activation map for each subject and condition of each experimental paradigm, as well as average deactivation maps over those conditions. For each paradigm, group level analysis was then carried out using a mixed-effects model (FLAME1) (Beckmann et al., 2003; Woolrich et al., 2004). Percent signal change for each subject and task was calculated using FSL's featquery for voxels in the group level average activation and deactivation masks. Finally, a higher level analysis using a mixed effects model was used for group-level deactivation maps across paradigms. The resulting group-level Z statistic map, with

corrected cluster significance threshold of $p < 0.05$, was indicative of regions that on average exhibit decreases in BOLD signal during task epochs across all four task conditions. Next the Brodmann areas associated with the final group-level Z statistic map were determined. To do this a binary mask of the Z statistic map was created and multiplied by the Brainnetome atlas. Any non-zero voxels in the resulting image are indicative of deactivated regions.

4.2.4 PeriStimulus Plots

In neurophysiological studies, peristimulus histograms are often used to visualize changes in neuronal firing rate in relation to an external event or stimulus. Analogously in fMRI, peristimulus plots can be used to visualize task-evoked changes in BOLD signal and qualitatively characterize the dynamics of task-evoked BOLD signal. On average, the DMN exhibits decreases in BOLD signal over experimental epochs containing some number of trials. However, the dynamics of signal change in these regions over experimental trials is unknown. To explore these dynamics, visualizations of peristimulus activity in each of the DMN regions were created. First, mean time series for each ROI of the Brodmann atlas and basal ganglia (Section 2.2) atlas were calculated for each subject and task. Then, TRs associated with trials of a single experimental condition were identified using the experimental block design convolved with a canonical double gamma HRF function identical to that used in the GLM analysis. For each subject and ROI, average signal during rest epochs was used as a baseline. For ease of comparison to GLM results, ROI time series were centered on this value and normalized

by their standard deviation over the entire scan. Across subjects, the resulting time series in each region of the DMN was averaged over task-associated experimental blocks. To account for different block lengths without discarding data, each trial was linearly interpolated to match the number of time points of the longest trial. Similarly, an average across subjects was calculated over the task-activated regions identified through the GLM analysis. This created a single time series for each task condition representing the dynamics associated with task-activated regions, which exhibit sustained signal increase over experimental blocks. In addition, a special button press ROI was created using data from the social cognition paradigm. The social cognition contained separate video watching epochs and response epochs such that response periods could be modeled separately. The group-level activation map for the response condition was used to identify voxels in the motor cortex associated with the button press response. These voxels were used to create an average time series across subjects of the BOLD activity associated with button press for each experimental paradigm and for the contralateral motor cortex. Peristimulus plots for each paradigm were created by averaging data over task epochs for 24 subjects with two runs each: relational task = 144 blocks; mental condition of the social cognition paradigm = 120 blocks. For the motor paradigm, separate peristimulus plots were created for both the left and right hand conditions, with 96 blocks each.

4.2.5 Structural Equation Modeling

Functional connectivity can exist in the absence of direct or monosynaptic connections. Nonetheless, the strength and spatial pattern of functional connectivity is constrained by anatomical structure. Therefore, structural connectivity was used to define an anatomically constrained structural equation model (SEM) (de Marco et al., 2007). The model was used to estimate the strength of the functional relationships between connected regions. The BOLD signal of each region R at time t was defined as a linear function of the BOLD signal in structurally connected regions at time t-1.

$$\begin{bmatrix} R_1(t) \\ R_2(t) \\ R_3(t) \\ \vdots \\ R_n(t) \end{bmatrix} = \begin{bmatrix} \beta_{11} & 0 & \beta_{12} & \dots & \beta_{1n} \\ 0 & \beta_{23} & \beta_{24} & \dots & \beta_{2n} \\ 0 & \beta_{33} & 0 & \dots & 0 \\ \vdots & \vdots & \vdots & \vdots & \vdots \\ \beta_{n1} & \beta_{n2} & 0 & \dots & \beta_{nn} \end{bmatrix} \begin{bmatrix} R_1(t-1) \\ R_2(t-1) \\ R_3(t-1) \\ \vdots \\ R_n(t-1) \end{bmatrix} \quad (1)$$

The model contained an equation for each region of the DMN as well as each region with structural connections to the DMN, resulting in a system of 200 equations with 1500 parameters (β coefficients, intercepts and error terms). The system of linear equations was solved for β coefficients using a weighted least squares method (Browne, 1984) and data from a resting-state scan using the R systemfit package (Henningsen & Hamann, 2007). To solve the system for β coefficients, resting-state data (1200 TRs per subject) was normalized (Z-scored) by subject and the data for 5 subjects was concatenated resulting in 6000 samples. A bootstrap procedure solved the system of equations 100 times using the concatenated resting-state time-series for 5 randomly sampled subjects at

a time. Coefficients significant at the $p < .01$ level were included in the final model. To test the solution, mean values of the coefficients over bootstrap solutions (Efron & Tibshirani, 1993; Hoyle, 1995) were used to predict the time series of a second resting-state scan (Cudeck et al., 1991). Regional time series in the second scan were normalized for each subject. The value of the first time point of the second scan was used as t_0 in the model. The rest of the time series (t_1-1200) for each region was then predicted by the model. Mean correlation across subjects between the predicted and observed values were used a measure of goodness-of-fit. Regions with significant β coefficients were included in the Markov model of task-based state transitions (Section 4.26).

4.2.6 Finite Markov Chain Model

A Markov chain describes a stochastic process characterized by the Markov property, which states that future behavior of the process depends only on its current state. A Markov chain model can describe dynamic changes in patterns of brain activity across many brain regions with the simplifying assumption that future states can be predicted based solely on the current pattern of activity. For example, it is known that activation of the TPN during experimental epochs is often coincident with decreases in signal in the DMN. This configuration of brain activity, including both task-evoked increases and decreases, could be considered a single state in a finite Markov chain model. States for this model were based on the signal intensity of 120 ROIs in the DMN, BG, thalamus, insula and regions with functional influence on the DMN (Section 4.2.5).

To define the state space of the model, BOLD signal from each region was normalized (Z-scored) for each subject. Then, a moving average was calculated using a window of size five TRs. The window was advanced in increments of two TRs along the time series of each region, for each subject. This has the effect of smoothing and downsampling the time series. Downsampled time series for each of (n = 24) subjects were computed individually. This results in an array of intensity values of 120 regions at each of m time points for each subject. These values were then concatenated to form a superset of size (n*m) x 120. The euclidean distance between each of the (n*m) vectors was then calculated. The elements of the resulting matrix contain the distances between the patterns of intensity values at every five TR bin. Wards hierarchical agglomerative clustering was then performed on the distance matrix to factor the data into 20 empirically determined "states". The choice of the number of states is somewhat arbitrary, but was chosen to maximize the amount of variance accounted for while minimizing the number of states containing a disproportionately large or small (less than 1%) number of time points. These 20 states then form a finite state space (X) from which the probability of transition between states can be calculated. Assuming a first order Markov process, a state transition table can be generated indicating the likelihood of transition to state x_j given that the currently occupied state is x_i.

$$P\ (X_{t+1} = x \mid X_t = x_n) \qquad (2)$$

Empirical probabilities are calculated across subjects as the number of times a transition

from state x_i to state x_j occurs relative to the number of times state x_i is occupied. States can be characterized in terms of their association with particular conditions (rest or task) within an experimental paradigm. In addition, detailed information about the pattern of brain activity across ROIs in each state can be retrieved. Thus the model provides a means to explore the temporal dynamics of changes in DMN activity in relation to other functionally connected brain areas.

4.2.7 Validating Markov Chain Models

To validate the results of the clustering analysis several steps were taken. The first was to verify that the clusters identified show state transitions that correspond to the experimental design. This was done visually using a raster plot of states over time. In addition, the clustering solutions were tested for an interaction between state and scan condition (rest vs. task). An interaction would indicate that a state was more prevalent in rest or task condition. However, each subject's data may contain a different number of task and rest bins. Therefore, the proportion of states in each condition was calculated as the number bins in each state in each condition divided by the number of bins in that condition (state or rest). To determine whether certain states are preferentially associated with task or rest conditions, the proportion of states in each condition were compared using a repeated measures two-way ANOVA with two within-factors (condition and state). This was done separately for each experimental paradigm.

The second test made use of random permutations of the time series for each subject. If the clustering identifies specific states that are associated with task rather than rest

conditions, this association should disappear if the temporal order of the time series is disrupted. Therefore, a random permutation of the time points for each subject was prepared and the clustering was repeated. Finally, the clustering solution was used to predict the states of the second run of each experimental paradigm. Linear discriminant analysis (Ripley, 1996; Venables et al., 2002) was used to create a classifier based on the clustering solution. States of the second run of each paradigm were predicted by the classifier based on their downsampled time series. The resulting predictions could then be compared to the experimental model (block design) of the second scan.

4.3 Results

4.3.1 GLM Task-evoked Deactivation

Linear modeling was employed to identify brain regions that exhibit task-evoked decreases in signal relative to a resting condition in response to multiple task conditions. The group-level deactivation map, included all DMN regions in the medial prefrontal cortex and cingulate gyrus : BA 10m, BA 32p, BA 23d, BA 31 (Figure 4.1). However, only three voxels were significant in BA 7m and deactivations in BA 39rv were found only in the left hemisphere. Task-evoked deactivation was also found in left lateralized hippocampus and parahippocampal gyrus. In addition to regions typically associated with the DMN, many other regions also showed significant task-evoked deactivations (Table 4.2). Among them are some regions of the left dorsolateral prefrontal cortex and bilateral insular cortex more typically associated with the TPN. Regions of both the pre and post central gyrus, particularly in the right hemisphere also exhibited task-evoked

decreases as did voxels in the nucleus accumbens and ventral caudate. Task-evoked deactivations, therefore, extend beyond the DMN. They include regions of motor cortex bilaterally, although more extensive in the motor cortex ipsilateral to the dominant hand (the motor cortex associated with the unused hand).

Percent signal change between task and rest epochs was calculated using FSL's featquery tool. This allowed a comparison of the magnitude of signal change in DMN regions relative to task-activated regions. For each paradigm, mean, and max percent signal change was calculated for voxels in the task-specific group-level activation and deactivation masks (Table 4.1) (24 subjects * 2 scans each = 48 scans per paradigm). For all experimental paradigms, mean and max percent signal change in deactivating regions was significantly smaller ($p << .001$) than changes in task-activated regions. Therefore, relative to its high level of baseline activity, task-evoked changes in the DMN are smaller and less variable than those in task-activated brain regions.

	Percent Change			
Task	**DMN**		**Task Activated Regions**	
	mean	max	mean	max
Relational	-0.46% +- 0.20	3.00% +- 1.47	0.73% +- 0.19	17.26% +- 4.73
Social	-0.37% +- 0.19	1.37% +- 0.74	0.65% +- 0.23	16.75% +- 4.99
Gambling	-0.35% +- 0.18	2.40% +- 1.48	0.49% +- 0.22	10.20% +- 3.81
WM	-0.42% +- 0.31	2.11% +- 1.38	0.65% +- 0.24	13.20% +- 4.12

Table 4.1 Percent Signal Change

Percent signal change in task activated regions (red) and in task deactivated regions (blue) at the single subject level and their standard deviation across subjects. Across all tasks, percent signal decreases evoked in the DMN from that baseline are small relative to evoked increases in task-activated regions.

Relational:	mean t (47) = 33.39, p << .001; max t (47) = 21.35, p << .001
Social:	mean t (47) = 25.59, p << .001; max t (47) = 21.89, p << .001
Gambling:	mean t (47) = 27.15, p << .001; max t (47) = 14.50, p << .001
Working Memory:	mean t (47) = 31.44, p << .001; max t (47) = 20.50, p << .001

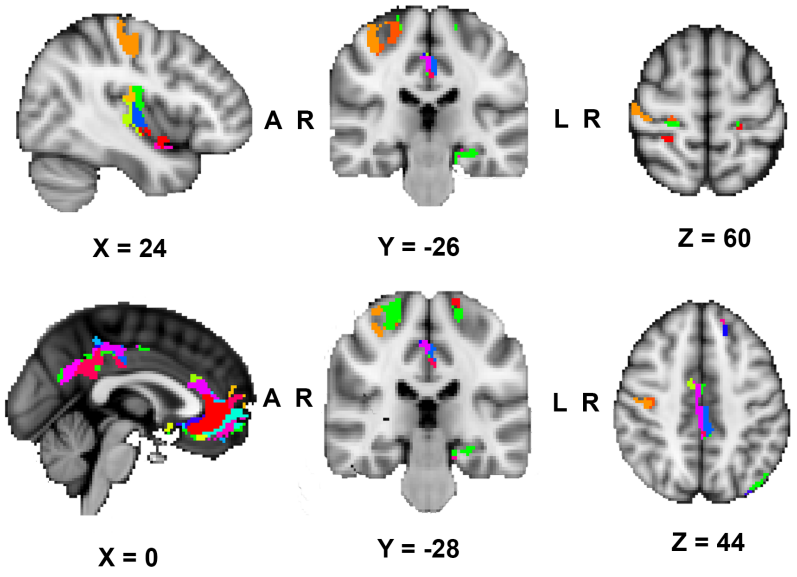

Figure 4.1 Task-Evoked Deactivation Beyond the DMN

A. Decreases in BOLD signal evoked across the HCP relational, social, gambling and working memory paradigms. Each color represents a different BA in the Brainnetome atlas; coordinates in MNI 2mm space. In addition to regions typically associated with the DMN, BOLD decreases were evoked in bilateral sensory motor cortex and the striatum.

Gryus	Region	L			R			# Voxels		Description
		X	Y	Z	X	Y	Z	L	R	
Superior Frontal	BA 8dl	-20	36	44				39		dorsolateral area 8
	BA 9l	-18	48	40				9		lateral area 9
	BA 6m				6	-2	46		17	medial area 6
	BA 10m	-8	60	10	2	60	8	270	87	medial area 10
Middle Frontal	BA 8vl	-24	34	38				2		ventrolateral area 8
	BA 10l	-16	66	0				3		lateral area10
Orbital	BA 14m	-8	54	-4	4	50	-4	405	563	medial area 14
	BA 11m	-6	56	-12	2	60	-8	26	34	medial area 11
	BA 13	-6	24	-10	2	22	-12	113	50	area 13
Precentral	BA 4ul	-22	-26	66	30	-20	56	19	86	area 4(upper limb region)
	BA 4t				18	-24	66		5	area 4(trunk region)
	BA 4tl	-60	0	12	56	2	10	34	43	area 4(tongue and larynx region)
Paracentral Lobule	BA 1_2_3ll	47	-34	52	4	-26	50	6	3	area1/2/3 (lower limb region)
	BA 4ll				0	-16	50		9	area 4 (lower limb region)
Superior Temporal	TE1_0_TE1_2	-50	-6	-2	46	-6	0	49	229	TE1.0 and TE1.2
	BA 38l	-44	2	-12	42	6	-14	6	30	lateral area 38
	BA 22r	-54	-6	-10				93		rostral area 22
Middle Temporal	BA 21r	-64	-6	-16				14		rostral area 21
	aSTS	-58	-6	-12	50	-2	-8	231	1	anterior superior temporal sulcus
Para-hippocampal	BA 35_36c	-18	-28	-16				4		caudal area 35/36
	TL	-26	-30	-14				3		area TL (lateral posterior parahippocampal gyrus)
	BA 28_34	-20	-22	-18				19		area 28/34 (EC entorhinal cortex)
	TH	-16	-32	-10				17		area TH (medial PPHC)
Superior Parietal Lobule	BA 7pc				24	-36	66		43	postcentral area 7
Inferior Parietal Lobule	BA 39c	-38	-78	44				12		caudal area 39(PGp)
	BA 39rd	-46	-70	48				2		rostrodorsal area 39(Hip3)
	BA 40c	-50	-64	48				1		caudal area 40(PFm)
	BA 39rv	-46	-70	40				109		rostroventral area 39(PGa)
	BA 40rv				40	-18	20		30	rostroventral area 40(PFop)
Precuneus	BA 7m	-4	-70	40				3		medial area 7(PEp)
	BA 5m	-4	-38	50	-2	-38	52	22	6	medial area 5(PEm)
	dmPOS	-12	-62	26	8	-58	24	454	169	dorsomedial parietooccipital sulcus(PEr)
	BA 31	-8	-52	32	6	-50	34	411	301	area 31 (Lc1)
Postcentral Gyrus	BA 1_2_3ulhf				40	-18	56		226	area 1/2/3(upper limb head and face region)
	BA 1_2_3tonla	-50	-10	16	44	-6	16	30	155	area 1/2/3(tongue and larynx region)
	BA 2				52	-16	58		11	area 2
	BA 1_2_3tru	-22	-28	68	22	-28	66	19	85	area1/2/3(trunk region)
Insular Gyrus	G	-42	-24	6	38	-14	8	24	111	hypergranular insula
	vld_vlg	-42	-2	-8	40	2	-8	48	45	ventral dysgranular and granular insula
	dlg	-42	-14	20	38	-10	16	4	42	dorsal granular insula
	dld	-38	8	14				25		dorsal dysgranular insula
Cingulate Gyrus	BA 23d	-6	-40	34	2	-42	34	328	160	dorsal area 23
	BA 24rv	-6	32	6	2	30	2	10	163	rostroventral area 24
	BA 32p	-4	36	18	0	32	26	61	21	pregenual area 32
	BA 23v	-8	-50	14	6	-46	16	85	73	ventral area 23
	BA 24cd	-2	-6	46	4	0	44	6	6	caudodorsal area 24
	BA 23c	-6	-28	44	0	-20	46	105	99	caudal area 23
	BA 32sg	-6	40	0	2	42	4	596	199	subgenual area 32
MedioVentral Occipital Cortex	vmPOS	-10	-72	30	8	-64	28	28	6	ventromedial parietooccipital sulcus
Hippocampus	rHipp	-24	-16	-14				49		rostral hippocampus
	cHipp	-28	-22	-12				63		caudal hippocampus
Basal Ganglia	vCa	-12	12	4	10	12	-4	30	10	ventral caudate
	GPe	-16	8	-4				1		globus pallidus external
	NAC	-10	12	-6	4	12	-4	42	51	nucleus accumbens

Table 4.2 Brodmann Areas Exhibiting Task-evoked Deactivation

Brodmann areas exhibiting task-evoked decreases across the HCP relational, social, gambling and working memory paradigms. Coordinates in MNI space represent the central voxel of the deactivated region.

4.3.2 DMN Peristimulus Dynamics

Task-activated brain regions exhibit a sustained increase in BOLD signal across a block of experimental trials. Peristimulus plots for each region of the DMN were created in order visualize the dynamics of DMN activity during experimental epochs. Peristimulus activity in voxels of the button-press ROI and its contralateral counterpart are included as a reference for activity related to task response. Across all tasks, it is readily apparent that activity in the DMN is not simply an inverse of the activity in task-activated brain regions. DMN activity does not exhibit sustained suppression of activity across experimental blocks. Instead, each region of the DMN has a unique and task-specific time course that corresponds with experimental trials.

4.3.2.1 ADMN Peristimulus Activity

In the relational paradigm, activity in BA 10m exhibits oscillatory behavior that corresponds to the timing of within-block trials (Figure 4.3). Clearly activity in these regions is not simply suppressed over task epochs. Changes in signal intensity in left and right BA 10m were significantly related to the time course of individual trails (Pearson r = -.43 and -.46 respectively, $p < .05$). The time course suggests that task-evoked activity in this region is initially suppressed, but begins to increase before the end of the trial, at or about the time of peak activity in the task-related brain regions. In the social paradigm, where there is only one trial in each block, the relationship between activity in ADMN regions and the trial response is more readily apparent (Figure 4.2). Temporal dynamics of BA 32p in the anterior cingulate cortex of the right hemisphere, resembles that of the

motor cortex of the dominant hand, the left motor cortex. All ADMN regions exhibited significant increases in signal intensity during task response (BA 10m left $t(23) = 15.47$, $p < .001$; BA 10m right $t(23)= 9.15$, $p < .001$; BA32p left $t(23) = 4.46$, $p < .001$; BA 32p right $t(23) = 5.09$, $p < .001$). The motor paradigm included periods of right hand and left hand movements. During right hand movements, the temporal dynamics of BOLD signal in BA 32p in the right hemisphere closely resembles that of the left motor cortex (Figure 4.5). The resemblance switches during left hand trials to that of the right motor cortex (Figure 4.4). Therefore activity in right lateralized BA 32p appears to consistently fluctuate with that of the motor cortex of the actively engaged hand. Unlike in the relational and social cognition tasks, activity in BA 10m remains above baseline during right and left hand movements in the motor paradigm.

4.3.2.2 PDMN Peristimulus Activity

In the social cognition paradigm, there is a clear distinction between the activity in BAs 39rv and 7m, and the rest of the DMN (Figure 4.2). These PDMN regions exhibit task-evoked increases with similar time courses to the task-activated brain regions while regions in the posterior cingulate increase during task response (BA 23 left $t(23) = 5.4$, $p < .001$; BA 23 right $t(23) = 4.9$, $p < .001$; BA 31 left $t(23) = 17.69$, $p < .001$; BA 31 right $t(23) = 11.49$, $p < .001$) . However, only BA 7m exhibited task-evoked increases in the relational paradigm (Figure 4.3). In this paradigm, regions in the PCC and lateral parietal cortex showed a significant association with the time course of individual trials (Pearson r left lateralized BA 31 $r = -.42$, BA 39rv left side $r= -.46$, BA 39rv right side $r = -.44$,

$p < .05$). All p values FDR corrected for multiple comparisons. In contrast, both regions exhibited task-evoked decreases in the motor paradigm (Figures 4.4 and 4.5). The time courses of peristimulus activity in the posterior cingulate gyrus (BAs 23d and 31) resemble that of the motor cortex of the motionless hand in all experimental paradigms.

4.3.2.3 Peristimulus Summary

Peristimulus activity in DMN regions is consistent with the GLM results. Across cognitive paradigms the GLM finds task-evoked decreases in the ADMN and in the posterior cingulate cortex (PCC), but not in BA 7m. The peristimulus activity in BA 7m shows sustained increases in activity in both the social and relational paradigms. Also consistent, the GLM fails to find deactivations during motor performance. Peristimulus activity during left and right hand conditions of the motor task show above baseline activity for all regions of the DMN. However, while the GLM analysis indicates a pattern of evoked decreases independent of the experimental paradigm, the peristimulus visualization makes clear that the DMN response is task-specific. The visualizations suggest that task-evoked activity in medial parietal cortex opposes that in the cingulate and medial prefrontal cortex. The cognitive paradigms (social and relational) evoked a sustained increase in parietal cortex while the ADMN exhibited trial-associated fluctuations resembling those of trial responses. The motor paradigm evoked the opposite pattern of activity with sustained increases in ADMN and suppressed activity in BA 7m.

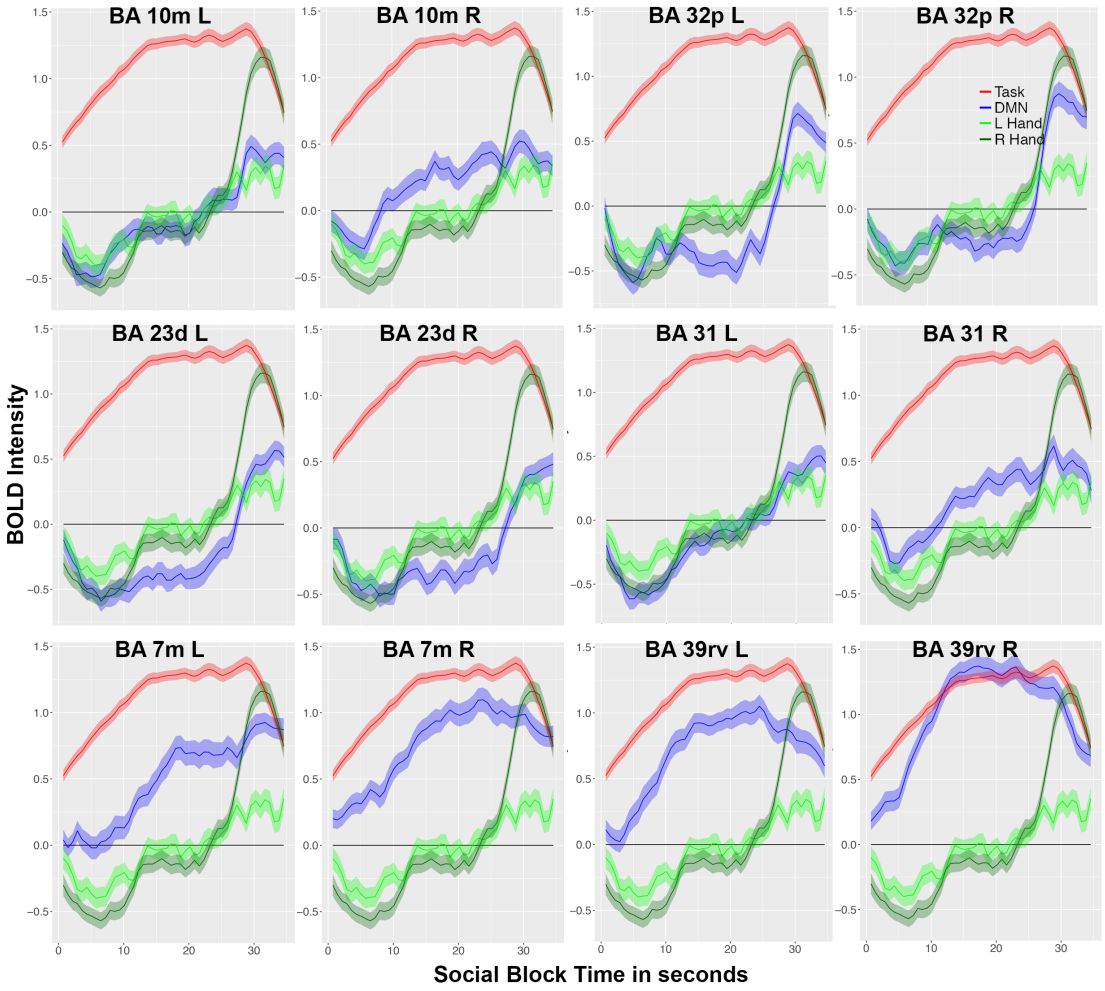

Figure 4.2 Social Cognition DMN Peristimulus Evoked Activity

The social cognition task is a theory of mind manipulation in which subjects watch short video clips of animated geometric shapes from which a social relationship can be inferred. An experimental block contained a single trial. Peristimulus time courses represent the mean and standard error across 24 subjects of 120 trials of the social (not random) condition. Each panel shows a different DMN region (blue) against identical traces of the task-activated regions (red) and signal associated with left hand (light green)

and right hand (dark green). The right hand trace (R Hand) represents the signal from the left motor cortex associated with movement of the right hand during the trial response. Qualitatively, there is a clear distinction in the evoked responses from each region of the DMN. Dynamics of bilateral regions BA 7m and 39rv exhibit sustained increases over the trial while activity in the rest of the DMN has a time course that resembles trial response.

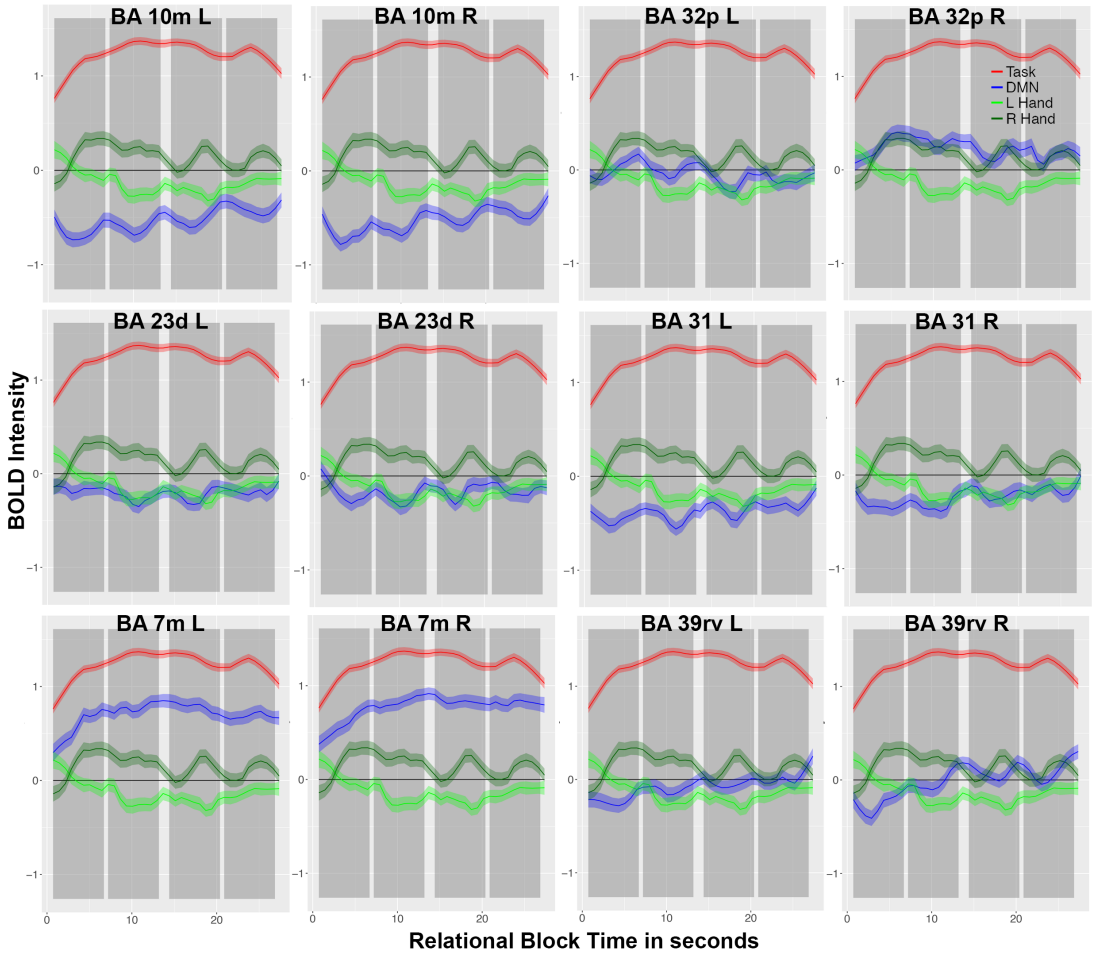

Figure 4.3 Relational Task DMN Peristimulus Evoked Activity

The peristimulus is produced as the mean and standard error across 24 subjects over 144 experimental blocks of the relational condition which contains 4 trials per block (vertical grey bars). Task-activated brain regions (red) identified from group level GLM analysis exhibit sustained increases in BOLD signal across trials, but also have fluctuations in signal intensity that appear to correspond to individual trials. It is readily ascertained that all regions of the DMN (blue) have fluctuations that correspond to the 4 trials. In addition, it can be seen that each region of the DMN has a unique task-evoked pattern of activity. Areas in the posterior cingulate, particularly BA 23d, have time courses that appear to align with the motor cortex associated with the non-dominant (left) hand (light green). BA 32 in the right hemisphere, has a time course resembling that of the dominant (right) hand (dark green) used to make a button press at the end of each trial. Time courses of task regions (red) and hands (green) are identical in each plot.

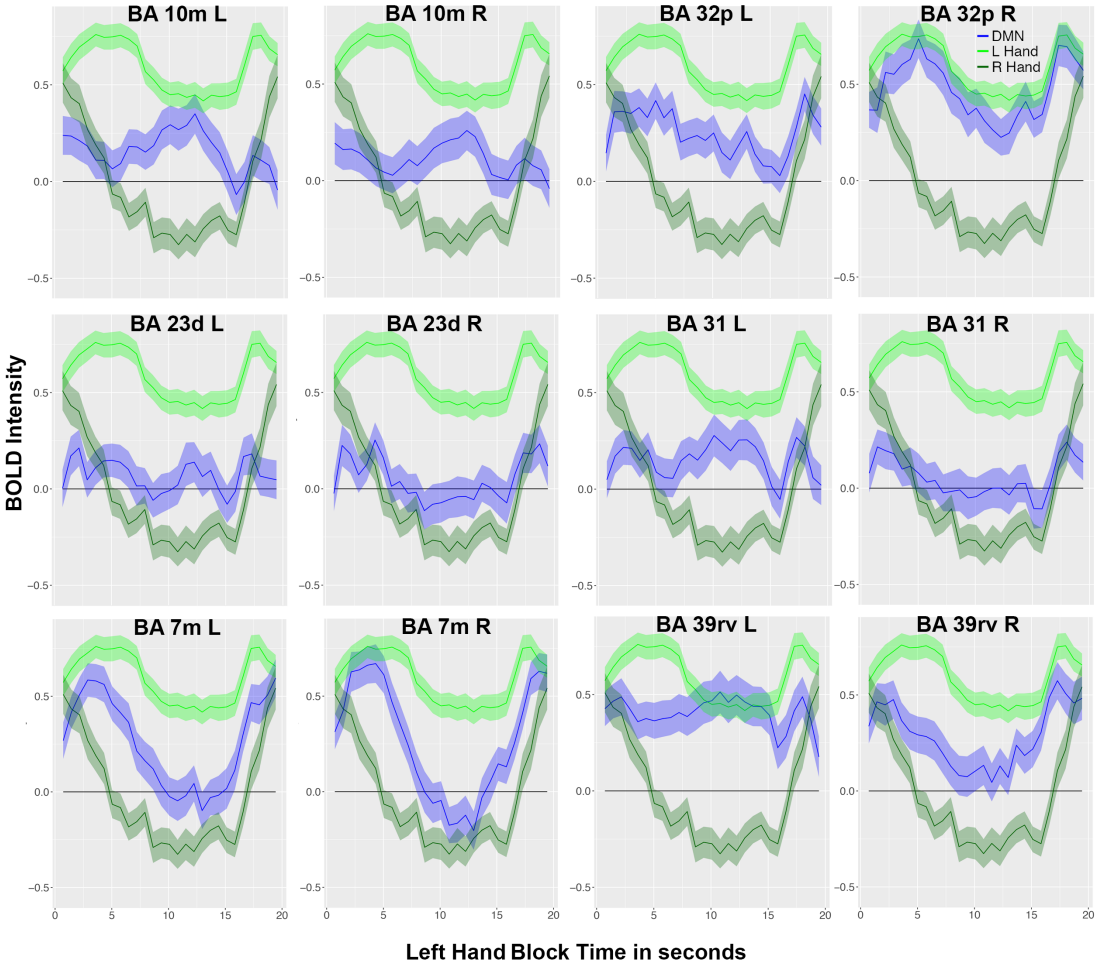

Figure 4.4 Motor Task Left Hand Condition DMN Evoked Activity

Peristimulus mean and standard error across 24 subjects over 96 blocks, consisting of a three second cue and a 12 second block in which subjects tap the fingers of their left hand. The pattern of DMN (blue) activity in the motor condition differs substantially from that in the non-motor paradigms. The temporal dynamics of BA 32p in the right hemisphere appears to correspond to that of the active left hand (light green). BA 10m exhibits task-evoked increases while BA 7m is suppressed. Right lateralized regions of the posterior cingulate (BAs 23d and 31) resemble that of the right (dark green)

motionless hand.

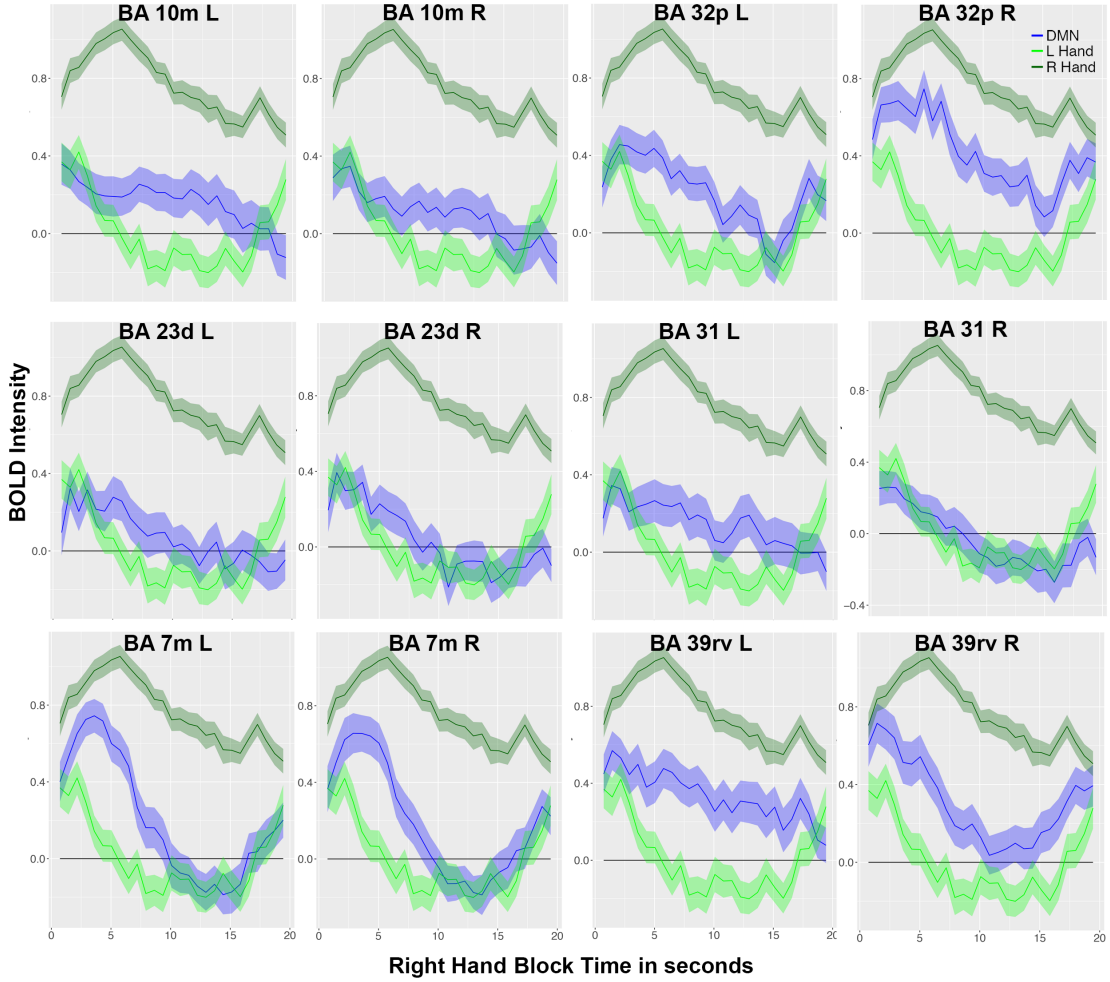

Figure 4.5 Motor Task Right Hand Condition DMN Evoked Activity

Peristimulus mean and standard error across 24 subjects over 96 blocks consisting of a three second cue and a 12 second block in which subjects tap the fingers of their right hand. The temporal dynamics of BA 32p in the right hemisphere appears to correspond to that of the active right hand (dark green). Activity in BA 7m is suppressed. Right lateralized regions of the posterior cingulate (BAs 23d and 31) resemble that of the left

(light green) motionless hand.

4.3.3 DMN Functional Influences

The strength of functional influences on the DMN were estimated using an atomically constrained structural equation model in which the observed signals at time t are modeled as a linear function of BOLD signal in structurally connected regions at time t – 1. Coefficients representing the strength of regional influences were determined by simultaneously solving the set of linear equations in the model. After removing non-significant coefficients, the model was used to predict the time series of a second resting-state scan. The correlation between the predicted and measured time series (1200 TRs) was used as a measure of the goodness-of-fit of the model. Mean correlations for all regions of the DMN (Figure 4.6) were significant ($t(1198) = 19.99$; $p < .01$ corrected), and the distribution of coefficients show good agreement over bootstrap solutions (ADMN Figure 4.7; PDMN Figure 4.8).

The TPN and DMN are believed to have an antagonistic relationship. If true, TPN regions would be expected to have negative coefficients in the SEM. The results, however, show a complex mixture of both positive and negative coefficients for TPN regions. The sum over mean coefficients for functional connections to the ADMN and PDMN are shown in Figures 4.9 and 4.10. Generally, the strongest positive influence on any region of the DMN comes from other regions of the DMN. However, several within-network negative interactions were identified. In the ADMN these were BA 32p R → BA 10m L and BA 10m R → BA 32 R. In the PDMN, BA 23d L → BA 7m R.

Although structural connections to thalamic and insular regions were included in the model, their coefficients were not significant.

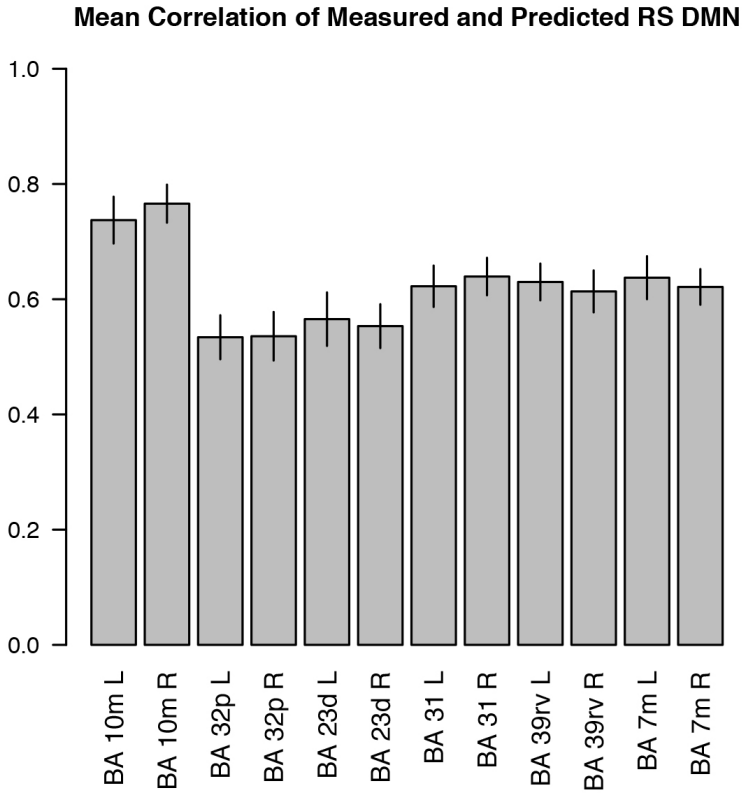

Figure 4.6 Linear System Solution Predicts Resting State Time series

A SEM was used to predict BOLD in a second resting-state time series with 1200 TRs. Each bar indicates the mean and standard error of correlations between predicted and measured time series for each subject.

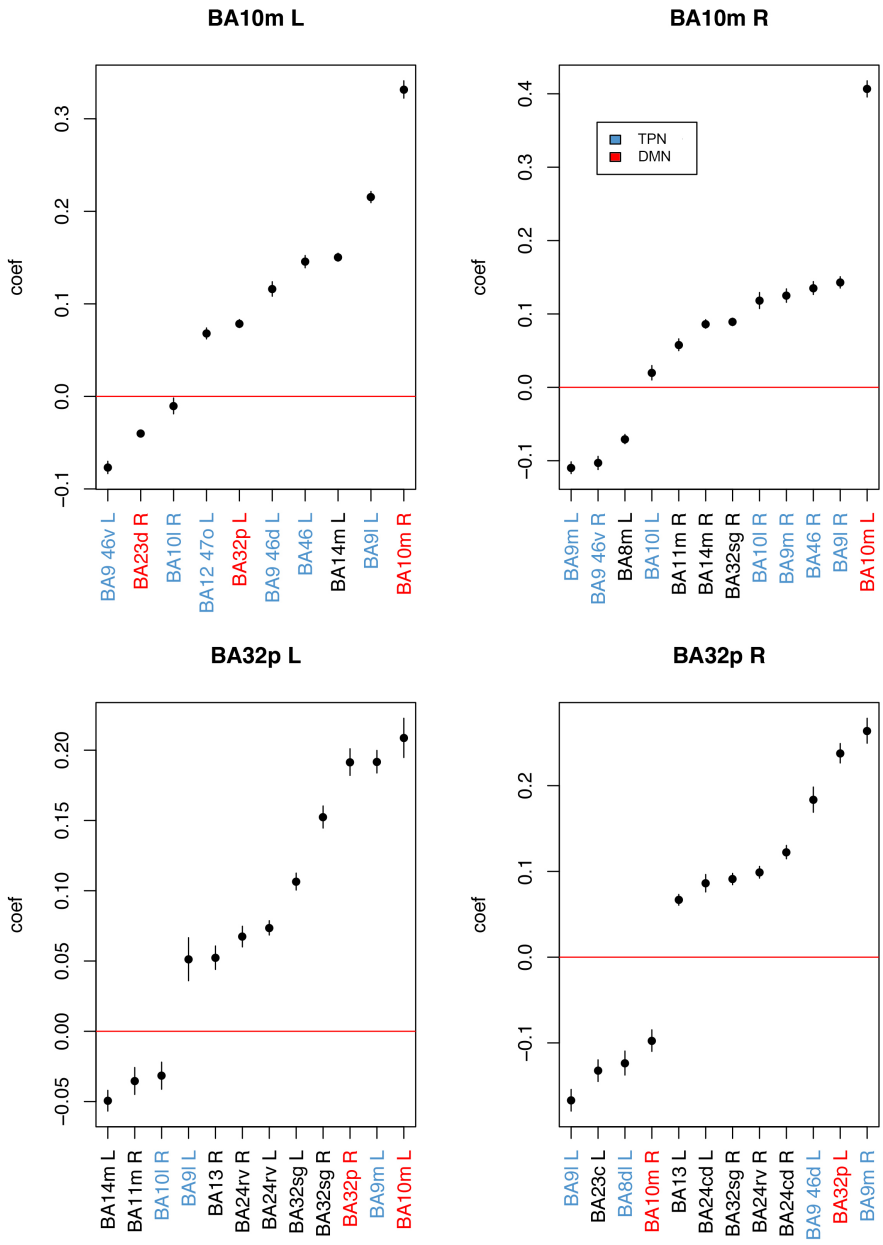

Figure 4.7 ADMN Coefficients of Functionally Connected Regions

Coefficient values over 100 bootstrap solutions of the anatomically based SEM defined by structural connections identified from DTI analysis in Chapter III. Coefficient

magnitudes (mean and standard error) are sorted from lowest to highest and show good agreement over bootstrap solutions.

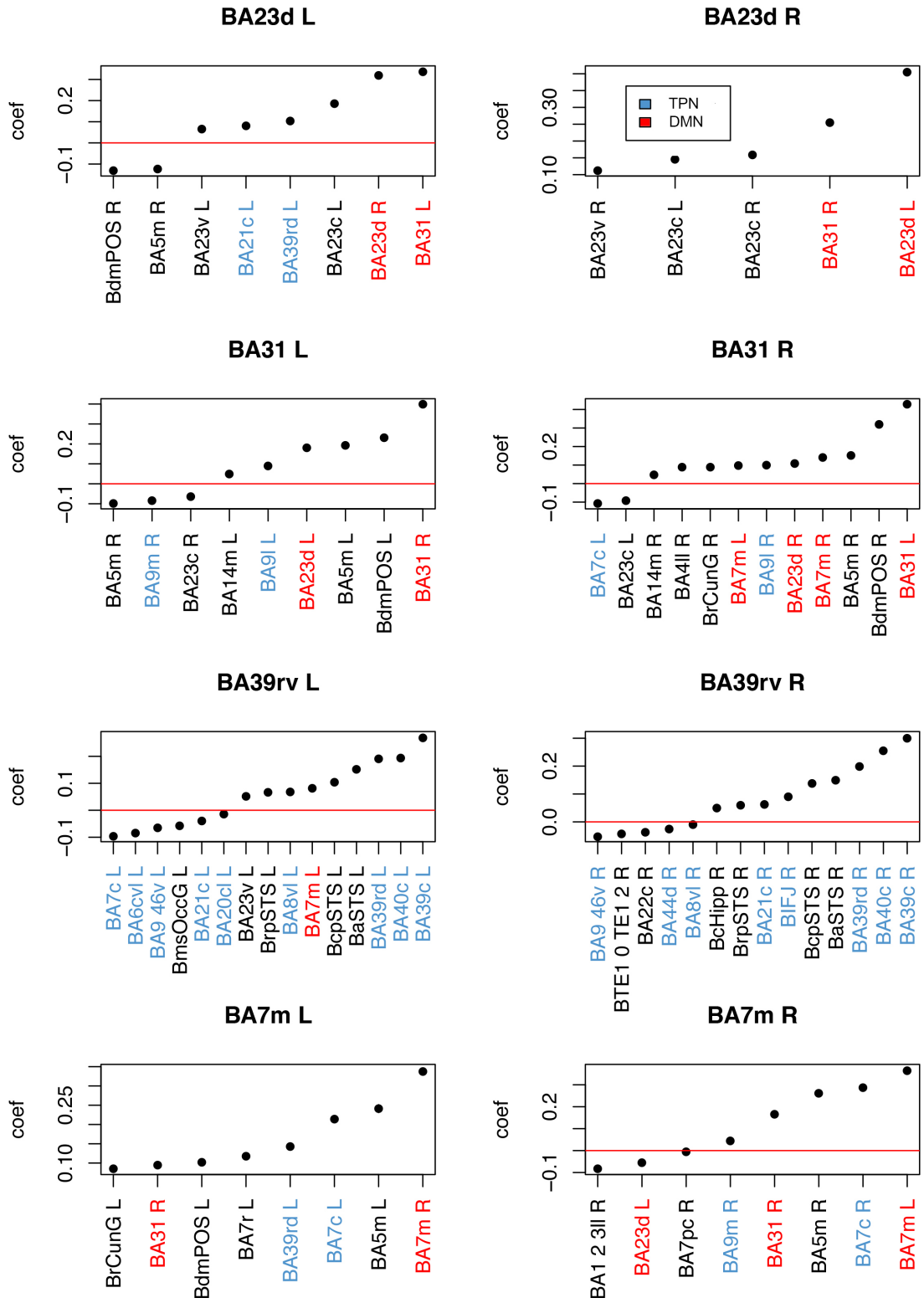
BA23d L
coef
−0.1
0.2
BdmPOS R
BA5m R
BA23v L
BA21c L
BA39rd L
BA23c L
BA23d R
BA31 L
BA23d R
coef
0.10
0.30
TPN
DMN
BA23v R
BA23c L
BA23c R
BA31 R
BA23d L
BA31 L
coef
−0.1
0.2
BA5m R
BA9m R
BA23c R
BA14m L
BA9l L
BA23d L
BA5m L
BdmPOS L
BA31 R
BA31 R
coef
−0.1
0.2
BA7c L
BA23c L
BA14m R
BA4ll R
BrCunG R
BA7m L
BA9l R
BA23d R
BA7m R
BA5m R
BdmPOS R
BA31 L
BA39rv L
coef
−0.1
0.1
BA7c L
BA6cvl L
BA9 46v L
BmsOccG L
BA21c L
BA20cl L
BA23v L
BrpSTS L
BA8vl L
BA7m L
BcpSTS L
BaSTS L
BA39rd L
BA40c L
BA39c L
BA39rv R
coef
0.0
0.2
BA9 46v R
BTE1 0 TE1 2 R
BA22c R
BA44d R
BA8vl R
BcHipp R
BrpSTS R
BA21c R
BIFJ R
BcpSTS R
BaSTS R
BA39rd R
BA40c R
BA39c R
BA7m L
coef
0.10
0.25
BrCunG L
BA31 R
BdmPOS L
BA7r L
BA39rd L
BA7c L
BA5m L
BA7m R
BA7m R
coef
−0.1
0.2
BA1 2 3ll R
BA23d L
BA7pc R
BA9m R
BA31 R
BA5m R
BA7c R
BA7m L

Figure 4.8 PDMN Coefficients of Functionally Connected Regions

Coefficient values over 100 bootstrap solutions of the anatomically based SEM defined by DTI analysis in Chapter III. Coefficient magnitudes (mean and standard error) are sorted from lowest to highest and show good agreement over bootstrap solutions.

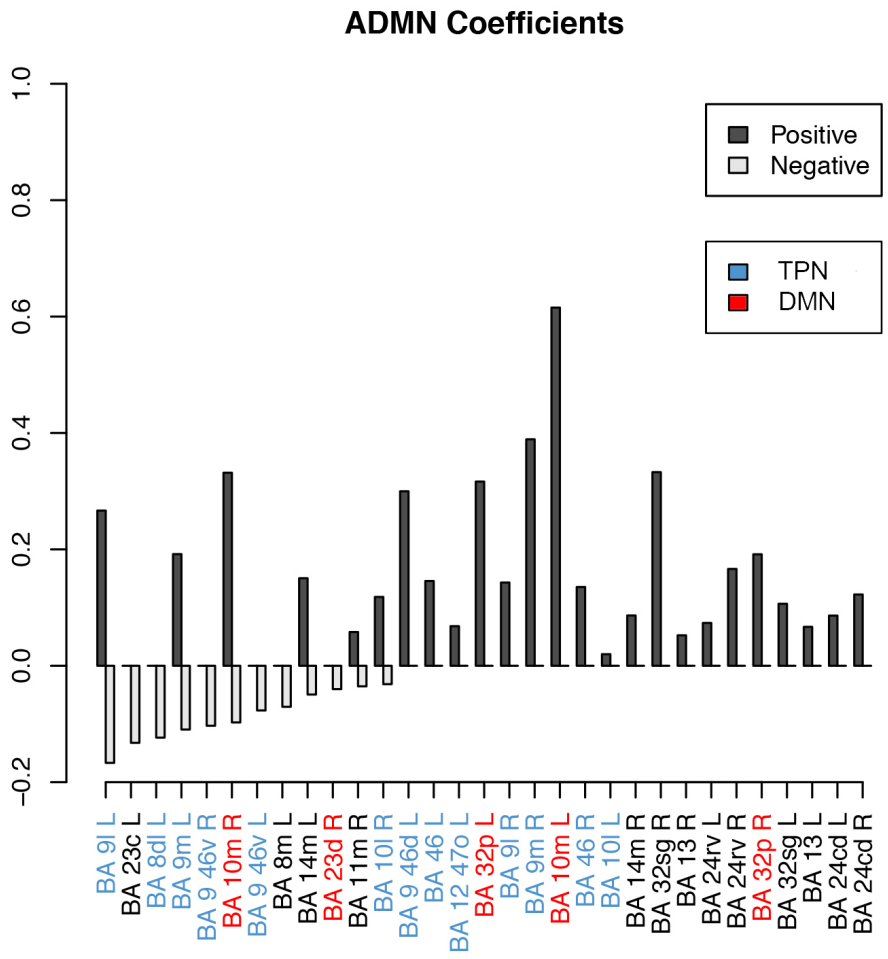

Figure 4.9 ADMN Functional Connectivity

Each bar indicates the sum of the region's influences on the ADMN, with positive and negative coefficients considered separately. Regions that have a negative influence on one component of the DMN may also have a positive influence on other components.

Regions of the TPN have a mixture of positive and negative influences.

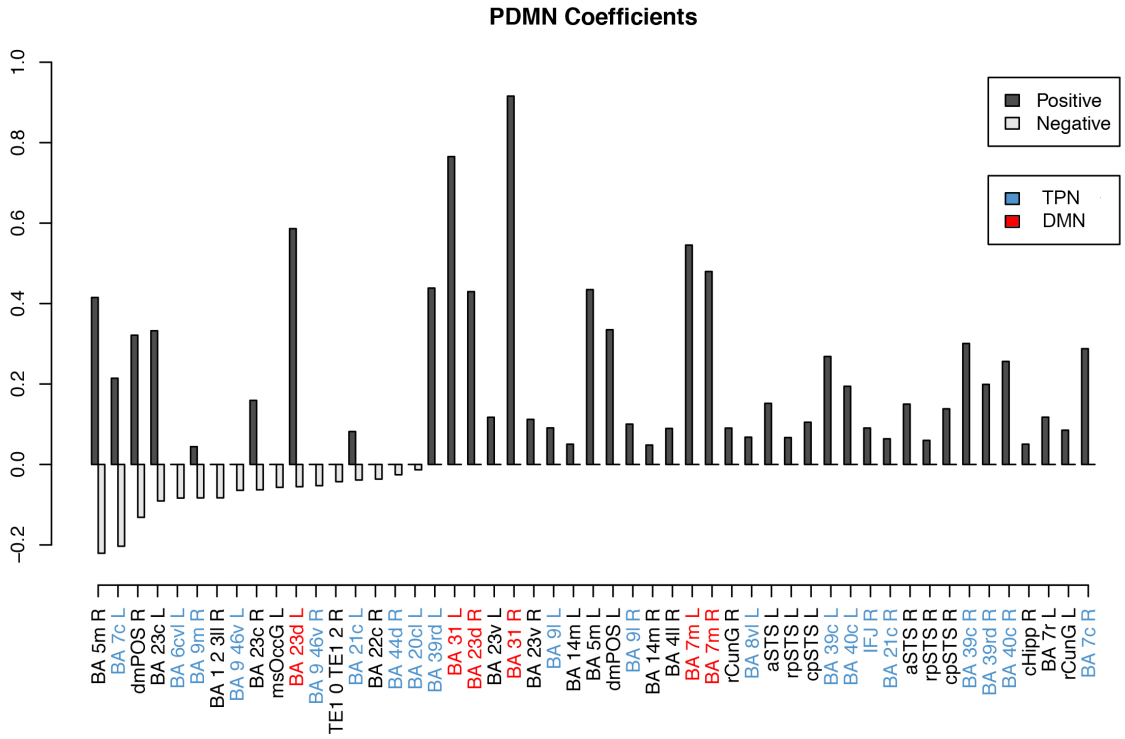

Figure 4.10 PDMN Functional Connectivity

Each bar indicates the sum of the region's influences on the PDMN, with positive and negative coefficients considered separately. Regions that have a negative influence on one component of the DMN may also have a positive influence on other components. As is the case for the ADMN, regions of the TPN have a mixture of positive and negative influences.

4.3.4 Markov Chain Models

Markov chain models with 20 states were created for the relational, social cognition, and motor paradigms. The clustering solutions for each paradigm can be seen in Figures 4.12 A, 4.14 A, and 4.16 A. The amount of variance accounted for by the clustering solution is defined as the ratio of between-cluster variance to the total variance: 64.39% for the relational paradigm, 51.95% for the social cognition paradigm, and 58.79% in the motor task. Several steps were taken to establish that the states identified by the clustering solutions represent behaviorally meaningful transitions. In the relational and social cognition paradigms, raster plots of the temporal progression of states show clear boundaries between task and rest epochs (Figures 4.11A and 4.13A). As expected, state boundaries between rest and task epochs are no longer visible in the cluster solutions generated on randomly permuted time series (Figures 4.11B and 4.13B). As a final validation step, linear discriminant analysis was used to create a linear classifier based on the clustering solution. The classifier was then used to predict the states of the second run of each experimental paradigm. The predicted states successfully reproduce state changes associated with rest and task epochs of the second experimental run (Figures 4.11C and 4.13C). Therefore, the clustering solutions appear to capture dynamics meaningfully related to behavioral changes. Probabilistic state transition tables assuming a first order Markov process were created and are shown in graphical form for each experimental paradigm (Figures 4.12B, 4.14B, 4.16B). To determine whether certain states are preferentially associated with task or rest conditions, a separate repeated measures ANOVA was conducted on the proportion of states in each condition with two

within-factors (condition and state) for each paradigm. In addition to the main effect of state $F(1,19)$, $p< 2e\text{-}16$, the interaction between state and condition was significant for all tasks $F(1,19)$ $p < .0005$. Tukey post hoc tests were carried out to identify the states associated with each condition (Figures 4.12C, 4.14C, 4.16C). For the social cognition and relational paradigms, several states were preferentially occupied during task and rest conditions. The pattern of signal intensities associated with these states are shown in Figures 4.12 D, 4.14 D, 4.16 D ordered by the frequency of their occurrence. These patterns represent the mean intensities for each region over time bins within the clustered state.

The clustering solution of the motor paradigm differed from relational and social cognition in several ways. State transitions at the boundaries of task and rest epochs in the motor paradigm raster plots are not clearly visible, as they are in the relational and social tasks (Figure 4.15). In addition, in the motor paradigm, no states were preferentially associated with task epochs. One state, however, was preferentially related to rest epochs (Figure 4.16C). Note that state numbers have no particular meaning and the same number does not represent the same pattern of activity across experimental paradigms.

Within network activity in the DMN is correlated over time scales of 10s-100s of seconds. However, the patterns of activity identified in the Markov chain model show that transient states exist in which regions of the ADMN and PDMN are negatively correlated. One such state preferentially corresponds to task epochs. The most common pattern of activity associated with non-motor task performance (state 20 in the relational

task and states 17 and 18 in the social cognition task), had below baseline activity in the ADMN and above baseline activity in the PDMN. This pattern is consistent with the peristimulus plots for these paradigms.

The relational and social paradigms both have task-associated states in which the entire DMN is above baseline (state 1 of the relational task and state 11 of the social cognition task). States in which all regions of the DMN exhibit above baseline activity are one of the most striking patterns across all three experimental paradigms. When the ADMN and PDMN simultaneously exhibit above baseline activity, the striatum, thalamus and most functionally connected regions also exhibit above baseline activity, while activity is suppressed in the substantia nigra (state 1 of the relational paradigm (Figure 4.12 D), state 7 of the social paradigm (Figure 4.17) and states 5 and 7 (Figures 4.17 and 4.16 D) of the motor paradigm). States in which all regions of the DMN exhibit below baseline activity have the opposite pattern: increases in the substantia nigra and decreases throughout the striatum, thalamus and most other regions in the model (social state 4 Figure 4.14 D, motor state 10 Figure 4.16 D, and relational state 6 Figure 4.17). In the social cognition raster plot (Figure 4.13 A,C), it can be seen that the latter half of task epochs, corresponding to the task response, is associated with a state in which all regions of the DMN and thalamus are above baseline and activity in the STN and substantia nigra is suppressed. This pattern of activity during task response suggests its interpretation as a release from inhibition as might be expected from direct pathway stimulation. Additionally, there is an apparent relationship between activity in BA 7m and that of the dorsal insula (dIa). The relationship is most prevalent in the relational task, in both task

and rest associated states. Activity in BA 7m frequently opposes that of the rest of the DMN, but is consistently correlated with activity in the dIa.

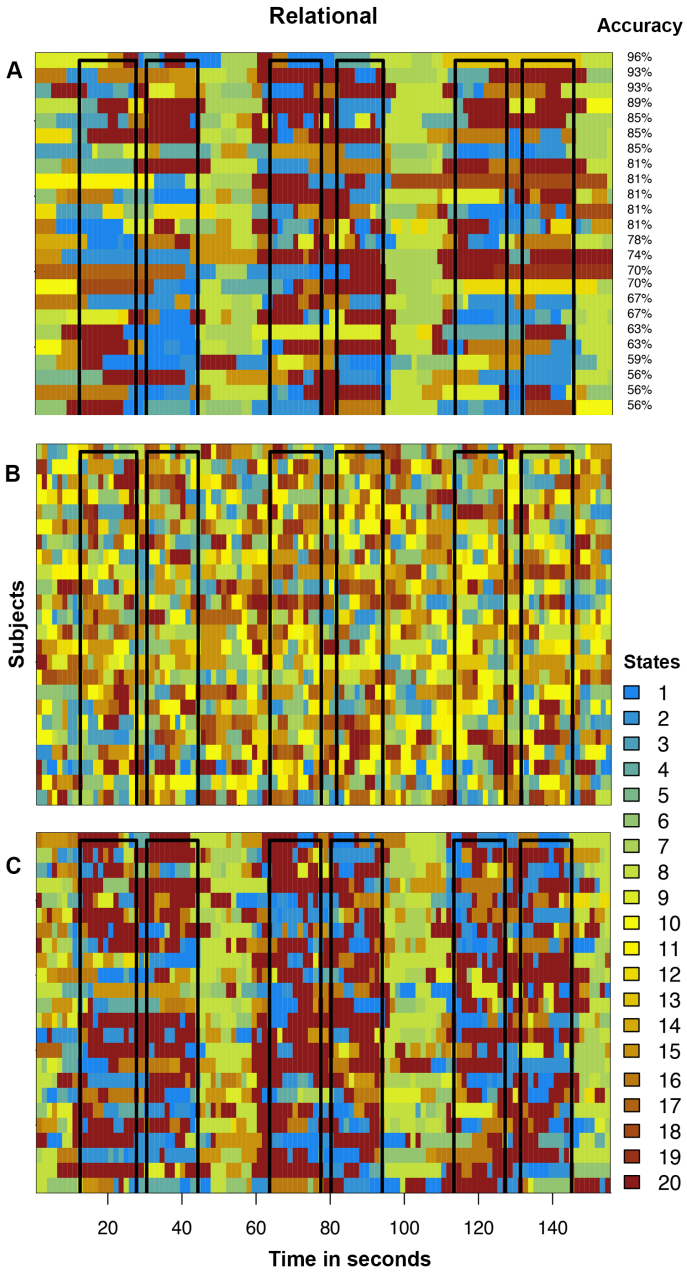

Figure 4.11 Relational Paradigm Cluster Validation

A. Raster plot of empirically determined states of the relational paradigm. Black lines indicate experimental epochs. **B.** Clustering solution of randomly permuted time series. **C.** States predicted by a linear discriminant classifier for a second relational scan on the same subjects.

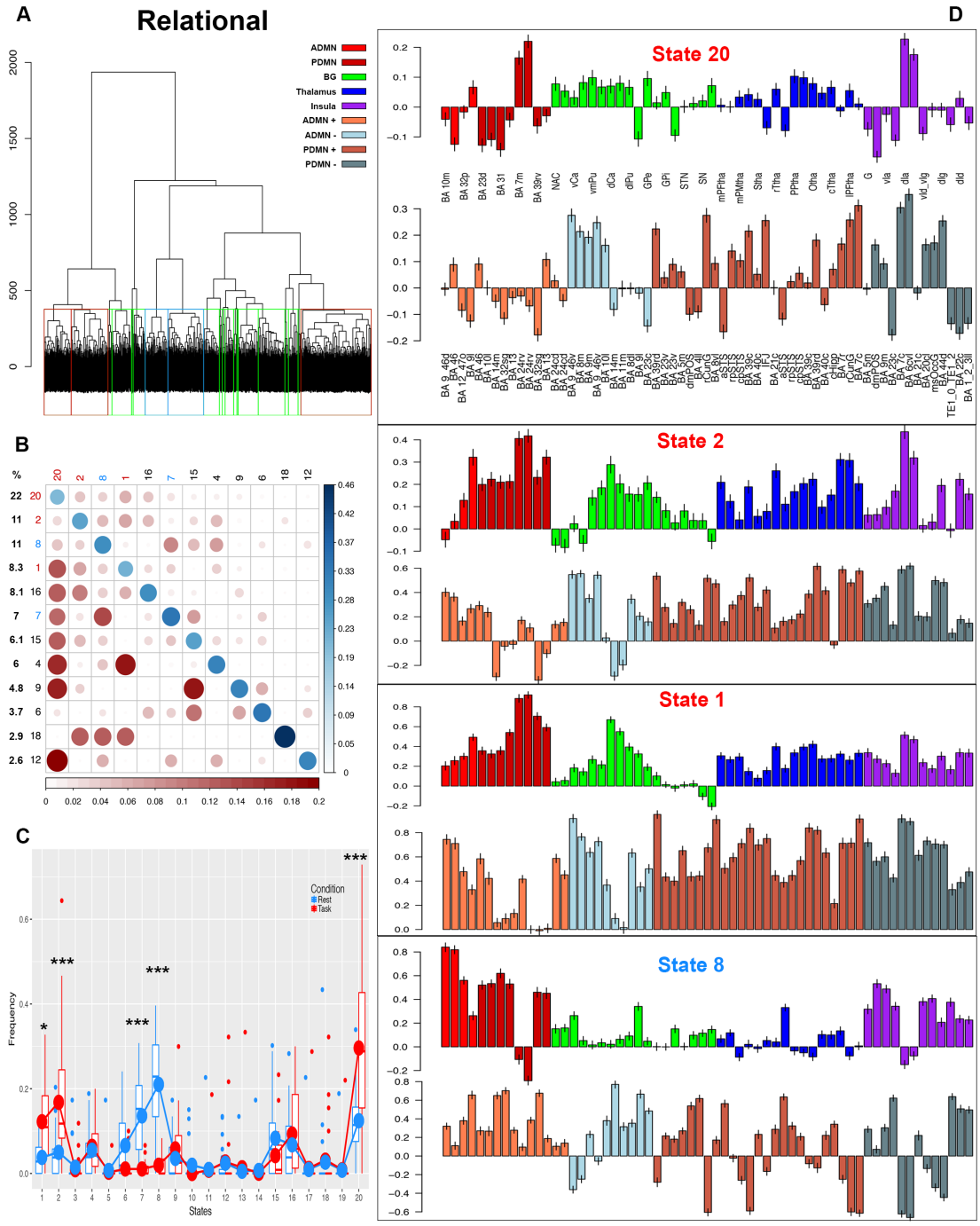

Figure 4.12 Relational Visual Processing Markov Chain Model

A. Twenty state clustering solution. Clusters are indicated by a colored outline: red for

states preferentially associated with task conditions, blue for states preferentially associated with rest conditions, green for states with no preferential association. **B.** State transition probability matrix. States are ordered according to their frequency and colored according to their association with task (red) or rest (blue). The percent of time spent in each state over the scans for all subjects is indicated (left). Each row indicates the probability of transition from the row state to the column state. Probability of remaining in the current state is indicated along the diagonal (blue), while the probability of state transition is indicated in the off diagonal elements (red). **C.** Box-plot indicating the distribution (minimum, first quartile, median, third quartile, maximum) of the proportion of time points in each state as function of the scanning condition (rest or task epoch); * = $p < .05$; ** = $p < .01$; *** = $p < .001$. **D.** The pattern of signal intensities for states associated with task and rest conditions. Each pattern represents the mean and standard error over signal intensities in the state cluster. The top row of each state includes signal intensities for the DMN (red - ordered from anterior to posterior), the BG (green - ordered from input to output nuclei), the thalamus (blue), and the insula (purple). The bottom row shows the signal intensities for regions with structural and functional connections to the DMN. The first half are those with connections to the ADMN; the second half are those with connections to the PDMN. These are colored according to the direction of their functional influence (positive = salmon/dark salmon; negative = light blue/grey). State 1 is a state associated with the task condition in which the DMN has above baseline activity and is associated with above baseline activity in the striatum, thalamus, insula and most functionally regions, but below baseline activity in the

substantia nigra.

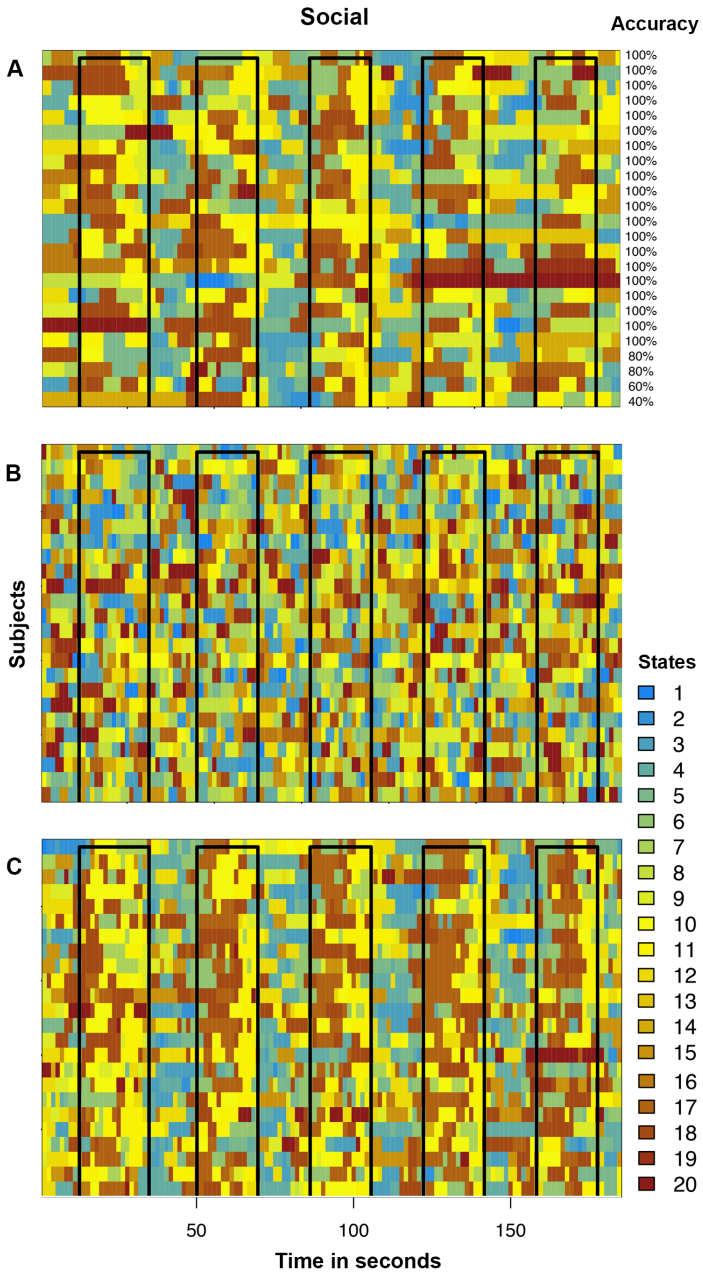

Figure 4.13 Social Paradigm Cluster Validation

A. Raster plot of empirically determined states of the social cognition paradigm. Black lines indicate experimental epochs. **B.** Clustering solution of randomly permuted time

series. **C.** States predicted by a linear discriminant classifier for a second social cognition scan on the same subjects.

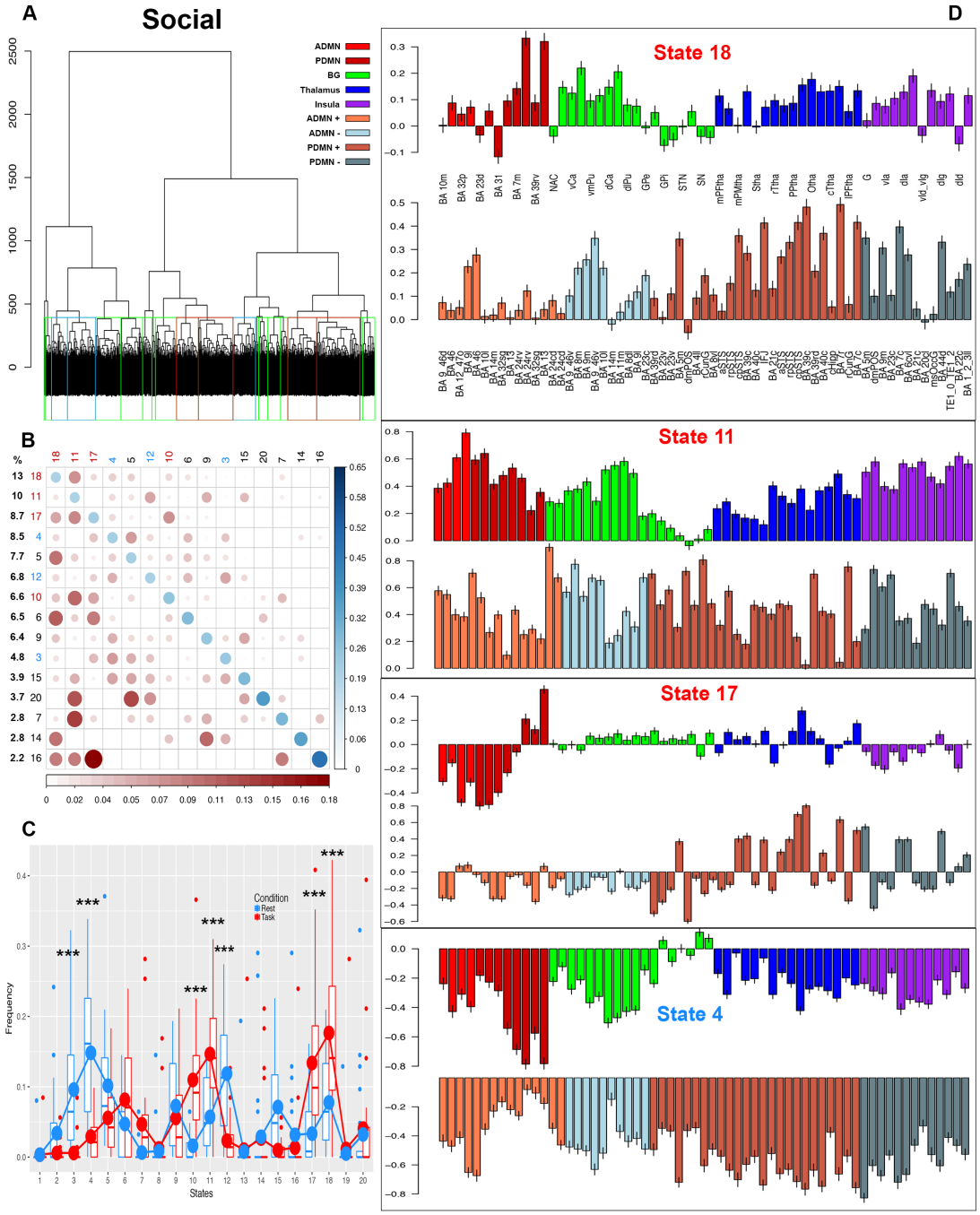

Figure 4.14 Social Cognition Markov Chain Model

A. Twenty state clustering solution. Clusters are indicated by a colored outline: red for states preferentially associated with task conditions, blue for states preferentially associated with rest conditions, green for states with no preferential association. **B.** State transition probability matrix. States are ordered according to their frequency and colored according to their association with task (red) or rest (blue). Each row indicates the probability of transition from the row state to the column state. Probability of remaining in the current state is indicated along the diagonal (blue), while the probability of state transition is indicated in the off diagonal elements (red). **C.** Box-plot indicating the distribution (minimum, first quartile, median, third quartile, maximum) of the proportion of time points in each state as function of the scanning condition (rest or task epoch); *** = $p < .001$. **D.** The pattern of signal intensities for states associated with task and rest conditions. Each pattern represents the mean and standard error over signal intensities in the state cluster. The top row of each state includes signal intensities for the DMN (red - ordered from anterior to posterior), the BG (green - ordered from input to output nuclei), the thalamus (blue), and the insula (purple). The bottom row shows the signal intensities for regions with structural and functional connections to the DMN. The first half are those with connections to the ADMN; the second half are those with connections to the PDMN. These are colored according to the direction of their functional influence (positive = salmon/dark salmon; negative = light blue/grey). State 11 is a state associated with the task condition with above baseline activity in the DMN, striatum, thalamus, insula and most functionally connected regions, and decreased activity in the

substantia nigra and STN. State 4 is a rest condition with an opposite pattern of activity.

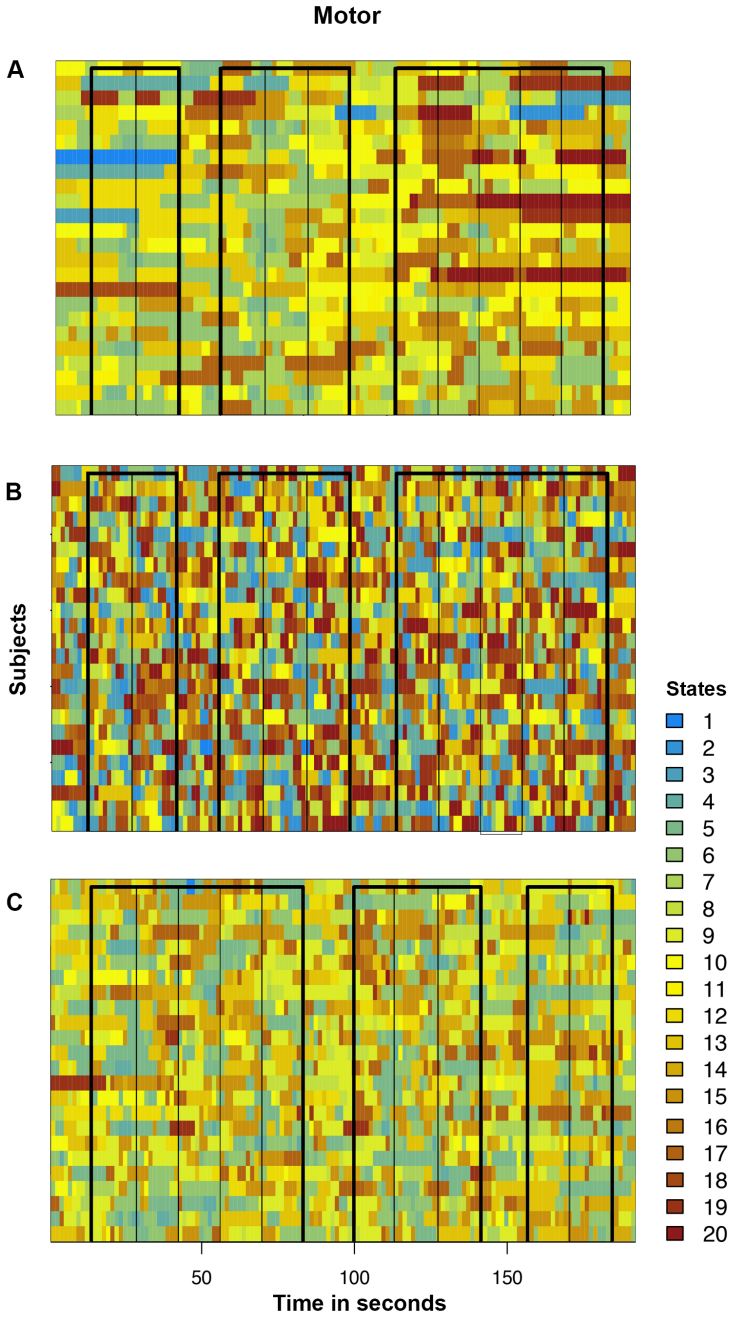

Figure 4.15 Motor Paradigm Cluster Validation

A. Raster plot of empirically determined states of the Motor paradigm. Black lines indicate experimental epochs. **B.** Clustering solution of randomly permuted time series.

C. States predicted by a linear discriminant classifier for a second Motor scan on the same subjects.

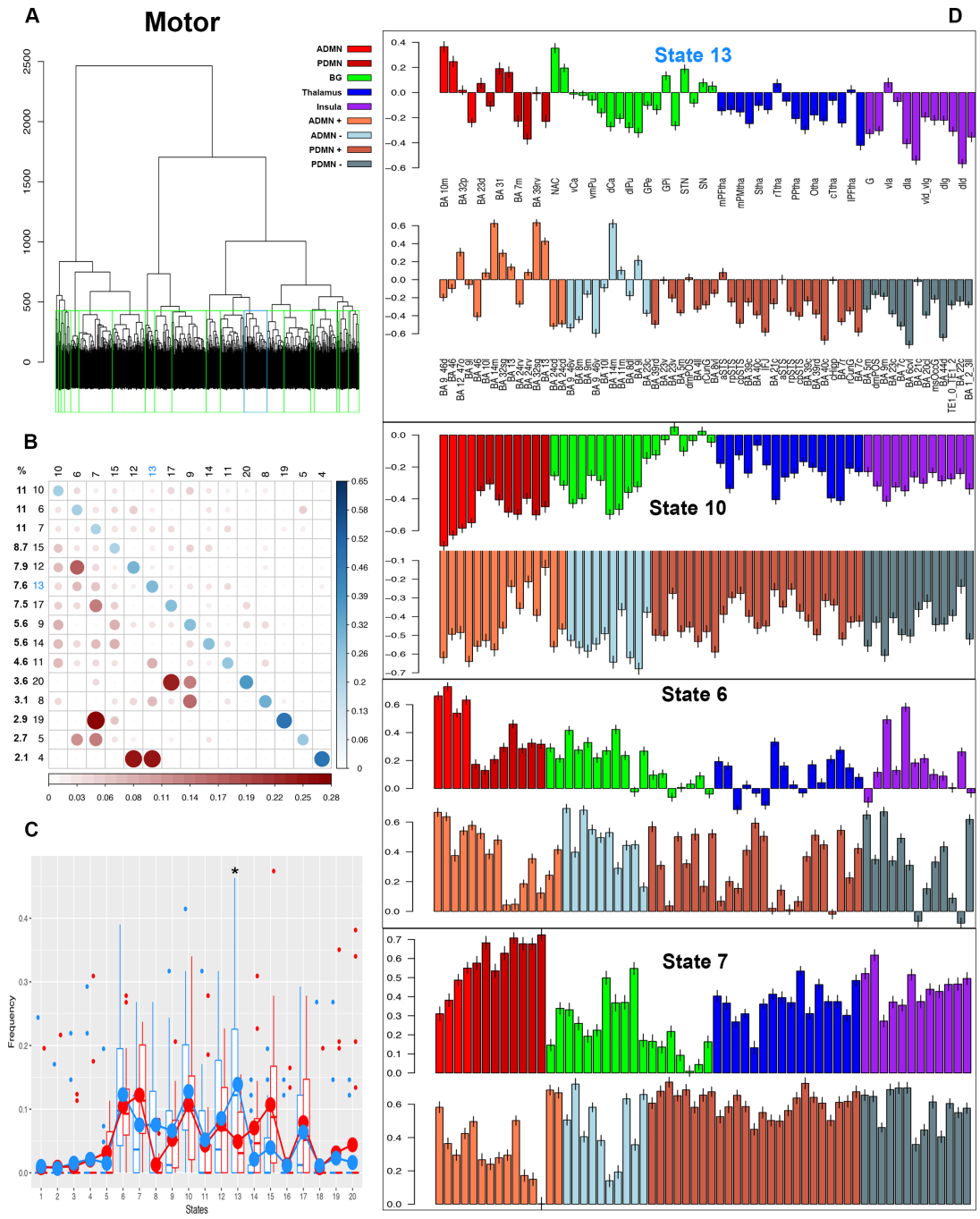

Figure 4.16 Motor Task Markov Chain Model

A. Twenty state clustering solution. Clusters are indicated by a colored outline: red for states preferentially associated with task conditions, blue for states preferentially associated with rest conditions, green for states with no preferential association. **B.** State transition probability matrix. States are ordered according to their frequency and colored according to their association with task (red) or rest (blue). Each row indicates the probability of transition from the row state to the column state. Probability of remaining in the current state is indicated along the diagonal (blue), while the probability of state transition is indicated in the off diagonal elements (red). **C.** Box-plot indicating the distribution (minimum, first quartile, median, third quartile, maximum) of the proportion of time points in each state as function of the scanning condition (rest or task epoch); * = $p < .05$. **D.** The pattern of signal intensities for the state associated with rest conditions and other frequently occupied states. Each pattern represents the mean and standard error over signal intensities in the state cluster. The top row of each state includes signal intensities for the DMN (red - ordered from anterior to posterior), the BG (green - ordered from input to output nuclei), the thalamus (blue), and the insula (purple). The bottom row shows the signal intensities for regions with structural and functional connections to the DMN. The first half are those with connections to the ADMN; the second half are those with connections to the PDMN. These are colored according to the direction of their functional influence (positive = salmon/dark salmon; negative = light blue/grey). No states were preferentially associated with the motor task condition.

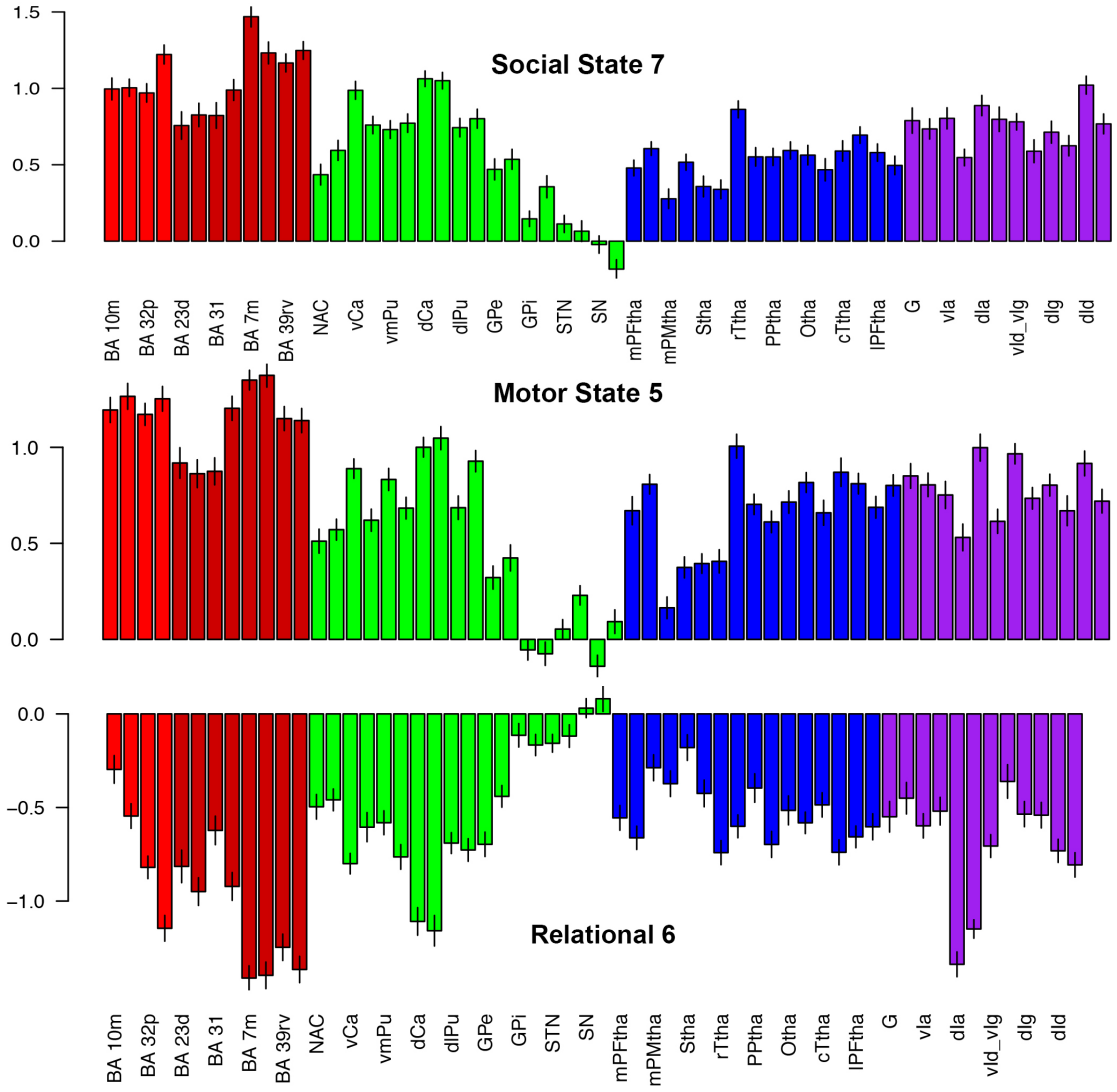

Figure 4.17 DMN Activity and the Thalamus

States with correlated activity in the DMN have a characteristic relationship with activity in the BG and thalamus. Above baseline activity in the DMN is associated with increased thalamic activity and below baseline activity is associated with decreased thalamic activity.

4.4 Discussion

4.4.1 Task Evoked Decreases Across Experimental Paradigms

Task-evoked decreases were identified in a large number of brain areas across four distinct experimental paradigms. All DMN-associated regions detailed in Chapters I and II are amongst the deactivating regions except BA 7m. This result highlights the necessity of anatomical specificity in reporting task-evoked deactivations. That is, while the DMN is visually recognizable in the spatial pattern of deactivated voxels, functional specialization of subcomponents of the network may be revealed by the differences in their task-evoked activity. The hippocampus is a region that is often associated with the DMN and although it has not been a focus of this work, deactivations were identified in both the left hippocampus and parahippocampal gyrus. In addition, BA 14m in the medial orbital frontal cortex and BA 32sg in the ventral anterior cingulate both exhibited task-evoked deactivation. These regions have anatomical connectivity patterns similar to that of BA 10m and BA 32p. Therefore, it's possible these regions should be considered part of the ADMN. However, task-evoked decreases were not restricted to regions within the DMN. Other studies have also reported task-related deactivations outside of the DMN, particularly in the posterior insula (Harrison et al., 2011), a region believed to support somatosensory and interoceptive processing (Eickhoff et al., 2006). The results presented here are consistent with this finding as deactivations were found in the insula bilaterally, but were also found in the nucleus accumbens and ventral caudate. In addition, bilateral areas of sensorimotor cortex also exhibited task-evoked decreases, but were more extensive in the right hemisphere. Since all subjects included in this analysis

were right-handed, deactivations in the right motor cortex correspond to that of the resting hand.

4.4.2 Task-evoked Activity in the DMN

Task-evoked activations are characterized by sustained increase in BOLD signal over blocks of repeated experimental trials. Visualizing the temporal dynamics of task-evoked signal changes in the DMN revealed that deactivations in the DMN are not equal and opposite that of task-activated regions. Rather than a sustained suppression of activity over trials, BOLD signal in all regions of the DMN fluctuates in a task-specific manner. The temporal dynamics of BOLD signal in DMN regions seen in combination with that of the motor cortex, suggest that DMN activity is related to the task response. Other studies have previously reported that activity in the DMN contained task-specific information (Vatansever et al., 2015). However, with the exception of parietal DMN regions, peristimulus time courses suggest a role specifically in trial responses. The clearest indication of DMN participation in task responding is seen in the social cognition peristimulus. With a single trial per block, and a separate epoch associated with task response, the relationship between activity in the DMN and activity associated with the button press response is readily appreciable. It's possible that this relationship could be the result of the DMN's purported role in theory of mind abilities. However, it is important to note that the social cognition paradigm was included in the GLM analysis, which identified regions that deactivate across task paradigms, including the social cognition paradigm. In fact, all core regions of the DMN exhibited task-evoked

deactivations on average during epochs in which subjects watched the socially evocative videos. A GLM contrast of the social (theory of mind) vs random condition implicated regions of the superior, medial, and inferior temporal gyrus, as well as the parahippocampal gyrus and inferior parietal lobule. The core regions of the DMN were not activated by the theory of mind condition. In fact, the role of the DMN as a whole in theory of mind tasks is far from established. Meta-analytic studies of theory of mind literature suggest that the temporal parietal junction may be the only region that is consistently identified across different experimental approaches (Mars et al., 2012; Mahy et al., 2014). Published analysis of the social cognition paradigm from the HCP project also reported task-evoked deactivation in the DMN (Barch et al., 2013b). Therefore, the role of the DMN in theory of mind cognition may depend entirely on the experimental paradigm.

Peristimulus activity also showed that each region of the DMN has unique task-evoked dynamics. Therefore each node of the network likely has a unique role. For example, across all paradigms, the temporal dynamics of BOLD signal in BA 32p, of the right anterior cingulate, mirrored that of the motor response in the left motor cortex associated with button press using the right hand. This is similar to the response in the motor paradigm in the right hand condition when subjects are tapping the fingers of their right hand. When subjects tap their left hand, activity in BA 32p switches to resemble that of the opposite hemisphere, associated with movement of the left hand. The dynamics of DMN regions in the posterior cingulate (BA 31 and BA 23d), resembled that of the unused hand. Consistent with this interpretation, one large-scale, coordinate-based

meta-analysis of DMN function using the BrainMap database, identified the functional domain of the ventral ACC as “action preparation” and found that the PCC had a decreased preference for action (Laird et al., 2009). Unlike the ADMN and PCC, BA 7m, exhibited sustained increases in activity in both the relational and social cognition paradigms. As both tasks involve processing visual stimuli, this is consistent with the region's anatomical connections to visual cortex. It's also consistent with recent studies indicating that portions of the medial parietal cortex become uncorrelated with the DMN and correlated with the TPN during task execution (Leech et al., 2011). However, during both the left hand and right hand conditions of the motor paradigm, activity in BA 7m is suppressed.

The time course of DMN activity suggests a possible role for the DMN in facilitating task responses. Of course the time course of evoked activity in the DMN does not mean it directs or controls motor activity. Understanding the relationship between the DMN and task response will require further research. Nevertheless, some evidence for DMN influence on motor responses was reported in a resting-state study which identified negative relationships between activity in vmPFC and parietal visual spatial regions and between PCC and prefrontal motor circuits. Using granger causality analysis they found that vmPFC and PCC exerted greater influence on anticorrelated regions than the other way around (Uddin et al., 2009). Furthermore, a large body of neurophysiological literature supports the role of the anterior cingulate in voluntary movement including one study that found voluntary movements can be predicted by changes in neural firing rate in the anterior cingulate (Fried et al., 2011). In

combination, the lateralization of deactivation in motor cortex identified through linear modeling, and the similarity of DMN temporal dynamics with that of motor cortex, suggests that the DMN may play a role in top-down control of task responses.

4.4.3 DMN Deactivation – Interactions with the TPN and the Insula

There is growing evidence against the suggestion that DMN deactivation results from increases in the TPN due to their intrinsic opposition. The coefficients of TPN regions in the structural equation model were found to have a mixture of positive and negative influences on the DMN. In addition, empirically derived states across experimental paradigms featured correlated activity in the DMN and TPN regions. This is consistent with other recent work showing that the two networks exhibit periods of coupled activity at rest and during task performance (Spreng et al., 2010; Dixon et al., 2017; Dixon et al., 2018). An alternative hypothesis is that DMN deactivations are mediated by the anterior insula (Sridharan et al., 2008; Menon & Uddin, 2010). A detailed account of the proposed function of the anterior insula posits that it is critically involved in bottom-up detection of salient events and in switching between large-scale networks to facilitate access to attentional resources in response to those events (Menon & Uddin, 2010). The coordinates of the region (Uddin et al., 2011) hypothesized to play this role coincides with the dorsal agranular insula (dIa) of the Brainnetome atlas. Several states in the Markov chain models showed correlated activity between BA 7m and specifically the dIa rather than any other region of the insula. This relationship is most readily appreciated in states in which activity of BA 7m opposes that of the rest of

the DMN. This suggests that the dIa may act cooperatively with regions of the DMN in parietal cortex to detect salient events and elicit state transitions that support bottom-up visual information processing.

4.4.4 DMN Activity and Striato-Thalamic Circuits

Studies of the basal ganglia have identified two main pathways: the direct and indirect pathways (Albin et al., 1989; DeLong, 1990). The canonical understanding of the two pathways has it that the thalamus is released from inhibition through the direct pathway and inhibited through the indirect pathway. Movement is associated with coordinated activity through both pathways (Bolam et al., 2000). However, the basal ganglia's role in cognition more broadly is not understood. In chapter III, I showed that core regions of the DMN have extensive connections through the BG and thalamus forming a large CST circuit. The synaptic organization of DMN connections through the direct and indirect pathways is unknown. However, a recent tracing study generated a brain-wide map of connections through the BG and found synaptic connections through both pathways from both the ventral orbitofrontal cortex and cingulate gyrus (Wall et al. 2013). Although for both regions more direct than indirect pathway synapses were identified. The Markov chain models for all three paradigms identified a reciprocal relationship between DMN activity and striato-thalamic activity. Activity in the thalamus was consistently above baseline in states when both the anterior and posterior DMN were active above baseline. Reciprocally, thalamic activity was consistently below baseline when all regions of the DMN were below baseline. In both of these states, correlated

activity in the DMN and thalamus was coincident with correlated activity in functionally connected brain regions. Transient periods of widespread synchrony have been reported previously (Hutchison et al., 2013b), but here it can be seen that these states are negatively associated with activity in output regions of the BG. The functional significance of these states is uncertain. However, tract-tracing and human neuroimaging studies have shown that both the medial and lateral PFC project to the dorsal caudate where it thought that information is integrated through interconnected CST loops (Joel & Weiner, 1994). Therefore, transient periods of correlated activity in the DMN and TPN may allow for integrating information processed across the two networks resulting in changes in thalamic inhibition. Simultaneous increases in the DMN, TPN, and striatum in combination with increases in thalamic activity are consistent with direct pathway stimulation.

4.4.5 Functional Role of the DMN

The DMN has been characterized as a task negative network as a result of its relative decrease in activity during externally focused attention. However, a certain set of tasks such as planning for the future, remembering the past, and self reflection evoke increases rather than decreases in DMN activity. Therefore it is believed that the DMN supports these cognitive abilities. Motor tasks do not evoke decreases in DMN activity. The prevailing explanation for the continuation of DMN activity during motor tasks is that they lack cognitive difficulty, and therefore do not require cessation of internal rumination. However, there is another important difference between the types of tasks

known to evoke increases rather than decreases in the DMN. Tasks such as planning for the future, or self reflection are self-directed tasks. They do not require bottom-up processing of external (visual) stimuli. Likewise, motor tasks are usually conducted in a self-directed manner, in the sense that subjects move their fingers at their own pace independent of any externally presented stimuli. Therefore, a more parsimonious explanation for the functional role of the DMN might be that it is involved top-down processing. In this view, the network is not really task-negative, but preferentially responds when bottom-up processing is complete. The majority of fMRI experimental paradigms involve visually presented stimuli and participant response via button box. The moment a subject responds typically marks the end of a trial. The end of a trial is associated with rebound in DMN activity. This is true in event-related (Shannon et al., 2006) as well as block design studies. It is presumed that post-trial increases in DMN activity support the resumption of internally directed thoughts associated with mind-wandering in the resting state. However, the temporal dynamics of DMN activity in the relational and social cognition paradigms appears to correspond to the motor-related response at the end of each trial. This suggests that post-trial increases in DMN activity may actively support top-down processing related to trial responses. This explanation also accounts for the existence of DMN activity in other species including rodents which are not believed to engage self-reflection and other cognitive abilities associated with the DMN.

Subcomponents of the DMN may have different functional roles in supporting top-down processing. Peristimulus DMN activity in all three experimental paradigms

showed that parietal regions of the DMN may work in opposition to the ADMN and PCC. During bottom-up processing in the relational and social cognition paradigms, DMN regions of the parietal cortex exhibited increases in activity while activity in the ADMN and PCC was suppressed. This can also be seen in the pattern of activity associated with task epochs in the social and relational Markov chain models. In the self-directed motor paradigm, this pattern is reversed. ADMN is above baseline while BA 7m in medial parietal cortex was suppressed. The time course of activity in PCC consistently resembled that of the motor cortex of the unused hand. It is possible that these regions may play a role in top-down suppression of unwanted motor responses. When activity across the network is cooperative, there are correlated changes in thalamic activity. This state may function as a switch supporting the redirection of attention from endogenous to exogenous stimuli or between bottom-up and top-down modulation of brain activity.

Combining evidence from the set of tasks that evoke increases in the DMN and observations of the network's likely role in perception of salient visual stimuli, the most parsimonious of the currently proposed functions of the DMN suggests its role as a sensory-visceromotor link (Raichle, 2015) that pairs experience with appropriate behavioral and emotional responses (Ongür & Price, 2000). The results of this work are consistent with this explanation. However, the DMN may play an additional role in facilitating the switch between bottom-up processing of sensory information and top-down execution of motor responses, with posterior parietal regions supporting the sensory and the ADMN and PCC visceromotor functions.

4.4.6 Methodological Considerations

A SEM was used to estimate functional influences on the DMN and to select variables for consideration in the Markov chain model. However, interactions between activity in different brain regions are likely non-linear. In addition, the SEM was formulated with a temporal lag of 1 TR. To account for uncertainties in the hemodynamic response within different brain areas, a more sophisticated approach such as blind deconvolution could be employed in the future. A selection of the most influential brain regions and a more complex model may better reflect the functional relationships between the DMN and other cortical regions. However, the model performed well at predicting activity in the DMN in a second resting-state scan and therefore may provide a first order approximation of the strength of regional functional influences.

The hierarchical clustering method captured behaviorally relevant state transitions. A nested hierarchical clustering approach may provide a method to explore dynamic patterns of activity within states associated with task performance in greater detail. In addition, the predictive power of the probabilistic Markov chain modeling approach was not fully exploited in these analyses. Applied to resting-state fMRI data, this approach has potential to yield exciting new insights into the dynamics of intrinsic brain activity.

CHAPTER V

ABERRANT DMN ACTIVITY DISTINGUISHES AUTISM AND SCHIZOPHRENIA

5.1 Introduction

Clinical similarities between schizophrenia (SZ) and autism spectrum disorder (ASD) were recognized even in the earliest descriptions of the two disorders (Kolvin, 1971; Rutter, 1972). The first reported cases of autism were initially thought to be a form of infantile SZ. In fact, the name Autism, which comes from the Greek word "auto" meaning "self", was originally used to describe a lack of interest in social interaction in individuals with schizophrenia (Bleuler, 1951). Later the term became associated with children who exhibited a similar lack of interest in social interaction and the spectrum of disorders we now call ASD. The young age of onset of clinical symptoms and lack of psychosis in ASD were later recognized as the main features that separated SZ from ASD. While they are now recognized as distinct disorders, their shared cognitive symptoms include impairments in social interaction and communication, deficits in processing emotion (Wallace et al., 2011; Brune, 2003; Morrison et al., 1998), theory of mind abilities (Pilowsky et al., 2000), language skills (Magaud et al., 2010) and learning (Titone et al., 2004), and the inability to suppress irrelevant information (Bird et al., 2006; Cutting et al., 1987). There are currently no medical tests available for either disorder. According to the diagnostic guidelines contained in the Diagnostic and Statistical Manual of Mental Disorders (DSM), many patients may qualify as having

either condition (Solomon et al., 2011; Konstantareas et al., 2001). Therefore, there is considerable interest in identifying reliable biomarkers.

Aberrant brain connectivity is strongly implicated in both disorders, as many of the genes implicated in ASD and SZ are involved in developing both long-range projections between brain areas as well as short-range synaptic connections (Crespi et al., 2010). Comparative studies aimed at understanding the genetic etiological relationship between the two disorders have identified some evidence for overlapping etiology and some evidence for diametric etiology (resulting from reciprocal alterations to common risk factors). However, while there is strong evidence for genetic risk factors and heritability, overlapping epigenetic mechanisms are now recognized as potentially playing a vital role in pathogenesis (McCarthy et al., 2014; see Persico et al., 2006, Roth et al., 2009 for reviews in ASD and schizophrenia respectively). The resulting cognitive deficits observed in both disorders are believed to be caused by altered communication between brain areas. However, studies aimed at identifying the regions of altered connectivity have yielded many conflicting results and failed replications. The large majority of such studies have made use of resting-state fMRI because of its ease of collection and the ability to make measurements of large-scale functional connectivity across the brain. Both disorders are associated with decreases in interhemispheric connectivity (SZ:Venkataraman et al., 2012; ASD: Anderson et al., 2011c), particularly in sensory regions and alterations in connectivity between frontal and posterior regions in the parietal lobe and occipital cortex (SZ: Venkataraman et al., 2012; ASD: Cherkassky et al., 2006; Just et al., 2007). Both have been associated with changes in connectivity

within the DMN. However, in some studies, increases rather than decreases in inter-regional functional connectivity are reported and others fail to find significant regional differences (see Anderson, 2014 for review in ASD and Fornito et al., 2012 for SZ). Inconsistencies in study outcomes may reflect methodological differences, and/or differences in patient sub-populations (age, sex, IQ, medication, and/or disease severity and duration), but also highlight the variability in these patient populations and the difficulty of characterizing either disorder by changes in connectivity between any one or two regions.

Where studies of regional changes in connectivity have yielded inconsistent results, studies using whole-brain measures of functional connectivity, in combination with machine learning algorithms, have demonstrated that multivariate patterns of connectivity can successfully distinguish patients from healthy controls (Shen et al., 2010; Anderson et al., 2011a; Du et al., 2012; Nielsen et al., 2013; Castro et al., 2014; Plitt et al., 2015). Using a multivariate classification approach, a recent study aimed at identifying biomarkers specifically for ASD found that application of their ASD model to other disorders was moderately successful in identifying SZ patients from healthy controls, but not those with attention-deficit hyperactivity disorder (ADHD) or major depressive disorder (Yahata et al., 2106). This suggests that common cognitive deficits in the two disorders may be accompanied by common changes in connectivity. Therefore, a comparative study of the changes in functional connectivity between ASD and SZ may identify divergent features that make the two disorders unique, which may aid in the development of disease interventions (Sasson et al., 2011). Both ASD and SZ

have been associated with changes in connectivity in the DMN, however, it is unknown whether differences in aberrant connectivity patterns across disorders can be used to differentiate between them. Therefore, in this chapter I apply supervised machine learning to whole-brain models of effective connectivity for subjects with ASD and SZ. The resulting machine learning models are cross-validated on independent training-naive data sets to determine if they generalize. I identify the most diagnostic features for each disorder and show that changes in effective connectivity, particularly in the DMN, can be used to successfully classify autistic subjects from those diagnosed with schizophrenia.

5.2 Methods

5.2.1 Data

Resting state data for subjects with SZ was archived by the Center for Biomedical Research Excellence (COBRE) and obtained from http://fcon_1000.projects.nitrc.org/indi/retro/cobre.html. The data set included 146 subjects ranging in age between 18 and 65 (72 SZ mean age = 38.17, SD = 13.89, 58 males; and 74 controls mean age = 35.82, SD = 11.58, 51 males). This data set was used to train a support vector machine (SVM) classifier. A separate data set was used as a testing cross validation set. The classifier was never trained on the testing cross validation data sets. Testing data was collected at the Rutgers University Brain Imaging Center as part of another study (not yet published). It included ten subjects ranging in age from 19-54 years old (5 SZ mean age = 42.6, SD = 11.59, 2 males; and 5 controls mean age = 20, SD = 1.22, 2 males) with two resting state scans each.

Resting state data for autistic spectrum disorder subjects was archived by the Autism Brian Imaging Data Exchange (ABIDE) and obtained from http://fcon_1000.projects.nitrc.org/indi/abide. The data set used was the ABIDE I University of Utah School of Medicine (USM) data set. It consisted of 101 subjects between the ages of 8 and 50 (58 ASD 11-50 years old, mean = 22.65, SD = 7.73; and 43 controls 8-39 years old, mean=21.36, SD=7.64). As the COBRE dataset did not include any individuals below 18 years of age, subjects younger than 18 were excluded, resulting in 37 patients (mean age = 26.34, SD = 7.37, 37 males) and 27 controls (mean age = 25.42, SD = 6.28, 27 males). Testing cross validation was performed on the ABIDE II Barrow Neurological Institute (BNI) data set. It consisted of 58 subjects between the ages of 18 and 64 (29 controls age range = 18 – 64, mean age = 39.59, SD = 15.09; and 29 patients age range 18 – 62, mean age = 37.44, SD = 16.09). After removing four 18 year old subjects, the sample consisted of 27 controls (mean age = 39.58; SD = 15.09; 27 males) and 27 patients (mean age = 37.6; SD = 16.09; 27 males). All data was collected in compliance with their relevant institutional review boards.

5.2.2 Preprocessing

Preprocessing steps were carried out using FSL (http://fsl.fmrib.ox.ac.uk/fsl/fslwiki/FSL) and included brain extraction using FSL's BET (Smith, 2002b), motion correction using FSL's MCFLIRT (Jenkinson et al., 2002), and linear registration to the Montreal Neurological Institute (MNI152) 2mm standard (Mazziotta et al., 1995) using FSL's FLIRT (Jenkinson et al., 2001; Jenkinson et al.,

2002). Frame displacement parameters were regressed out of each data set to control for motion.

5.2.3 Region of Interest Selection

A previously generated parcellation based on meta-analysis over a range of tasks identified 264 ROIs of putative functional relevance spanning both cortical and subcortical areas (Power et al., 2011). The resulting atlas was extended to include an additional 19 ROIs in the brainstem, basal forebrain, hippocampus, amygdala, and putamen bilaterally for a total of 283 regions. Each ROI is a 5mm sphere around a voxel of peak significant activity during performance of tasks such as button-pressing, reading, and memory retrieval. For each subject, average time series was extracted for each ROI. Data sets were matched for number of time points to the COBRE SZ data set by randomly selecting a start point that resulted in 120 consecutive scans.

5.2.4 Connectivity Matrix Graph Model Generation

There are several possible approaches to generating connectivity matrices. The simplest and most common is to use thresholded functional connectivity. However, data from patient populations have a higher risk of motion artifacts (Greene et al., 2016b). Even after motion correction and regressing motion parameters, residual motion artifacts can alter correlation coefficients across the brain (Power et al., 2012). Therefore, a Bayesian approach was used to determine effective connectivity between brain areas (Friston, 1994). Because connections are determined probabilistically in Bayesian

models, they are less susceptible to spurious connections resulting from motion artifacts (Hanson et al., 2016). Bayesian network models can be represented as graphical models where variables (ROIs) are depicted as the nodes of the network and directed edges as the interactions between nodes. Connections between ROIs represent probabilistic dependencies among variables quantified by their conditional probability distributions. The network structure expresses the joint probability distribution over all variables. The structure of a Bayesian network model representing the interactions between ROIs over the scan duration is learned from the ROI time series data using a score-based hill-climbing greedy search algorithm as implemented in the R bnlearn package (https://cran.r-project.org/web/packages/bnlearn/index.html). Such algorithms have been benchmarked for use in fMRI data and have demonstrated excellent accuracy and stability (Ramsey et al., 2011) over known network structures. Bayesian information criterion (BIC) scores measure the goodness of fit of the model based on the log-likelihood of the data given the network structure, while simultaneously penalizing the number of parameters in the model.

$$BIC = \ln(n)\,k - 2\ln(\hat{L}) \tag{1}$$

$$\hat{L} = p(x \mid \theta\,, M) \tag{2}$$

$\hat{L}$ = maximized likelihood function of the model M over the observed data x, and parameter values θ

n = number of data points

k = number of parameters to be estimated

As the number of parameters k in the model increases the BIC score also increases; lower BIC scores are considered better models. In this way, the number of parameters in the model is constrained. Edges are added to the model individually and a new BIC score is calculated to determine whether the additional variable improves the fit. The search procedure concludes when the fit is not further improved (the BIC score is not reduced) by inclusion of new edge parameters. The number of ROIs in the feature set was 283, resulting in 80,089 (283x283) possible edges or features. Therefore this is the feature space that is searched during the learning procedure. Once the graph structure is determined, edge weights are calculated as linear regression coefficients, resulting in a weighted connectivity matrix for each subject. These weights were then normalized by subject by z-scoring over the non-zero model edge weights in order to preserve the relationships between variables and to facilitate comparison across subjects and data centers.

5.2.5 Identifying Relevant Discriminatory Features

A linear support vector machine (SVM) was used to classify schizophrenic patients from controls based on each subject's weighted connectivity matrix. An SVM is a supervised multivariate classification method that treats each of the features, or edges,

as a point in a high dimensional space. Training of an SVM results in a set of support vectors (points in multidimensional feature-space) that represent the boundary between classes. Because the support vectors are at the boundary between classes, they are not useful in determining features that are most indicative of each class. Recursive feature elimination (RFE) was used to identify the most predictive features (Guyon et al., 2002; Hanson et al., 2008). The basic principle of RFE is to initially include all edges in the model and to gradually exclude edges, that contribute least to successful discrimination between the two classes. This approach iteratively trains and tests the SVM, discarding the least important features at each iteration until a core set of features remain, having the highest discriminative power. At each iteration, data from the training set is randomly sub-divided into training and testing sets consisting of 10% of the total number of subjects. After training, the least significant 10% of features are removed from the feature set. Feature significance is based on the support vector model coefficients (Krantz et al., 1971). Classification accuracy on the held out 10% of subjects is recorded at each iteration. A bootstrap procedure was implemented that repeats the RFE process 100 times. Accuracies are averaged over the 100 bootstrap samples. The number of features to include in the final model was determined by choosing the number that yielded the highest classification accuracy on average over bootstrap samples. Edge features were sorted according to the frequency (1-100) of their inclusion in the top feature set yielding highest accuracy. The RFE process was done separately and identically for both the SZ and ASD datasets, resulting in a separate set of distinguishing features for each patient population from that of healthy controls. A separate SVM

model for SZ and ASD was then created using these features.

5.2.6 Cross Validation on Independent Data

Independent data sets, from a new cohort of subjects that were collected at different sites were used as testing cross validation sets. The SVM models generated from the features identified through the RFE procedure, were used to predict group membership of the validation data sets. Each of the new data sets underwent identical preprocessing procedures as the original training cohorts. Their weighted edge matrices were used to determine how well the SVM models generalize. Group membership, (ASD vs. control, SZ vs. control), was predicted for these new subjects using the SVM models that were trained on the initial training cohort of subjects. Cross-validation in this way will determine how well the models generalize outside of the patient population on which it was trained and also ensures that classification accuracy is not driven by differences in age, scanning site or other potential cohort or procedural differences in subject groups.

5.2.7 Identifying Common and Disparate Features

To identify common and disparate features, a hybrid control group was created by combining the 27 ASD control subjects from the ASD training set with 27 randomly selected subjects from the control group of the SZ training data set. Using this hybrid group during training controls for differences in the samples that may be present due to different protocols and/or scanning sites. RFE was performed separately for ASD and SZ

against this common control group. Identified features were separated into common and divergent feature sets. Common features were those present in both the SZ and ASD models relative to the common control; divergent features were the remaining SZ and ASD features combined. Features were then divided into non-overlapping functional networks for the purpose of visualization using network definitions from a previously defined functional brain atlas (Richiardi et al., 2015). ROIs were defined as belonging to a given network if they were spatially overlapping with the atlas network mask.

5.3 Results

5.3.1 Discriminative Features

RFE was performed separately on the ASD and SZ training data sets and resulted in: 1) a set of features or edges that were most diagnostic in distinguishing ASD/SZ subjects from healthy controls 2) a model generated by training an SVM on just these features which can then be used to predict the class of a new set of subjects in the validation data sets.

5.3.1.1 ASD Diagnostic Features

The RFE procedure was performed on the ASD training data set to classify ASD subjects from healthy controls. The procedure resulted in maximum average accuracy over 100 bootstrap samples using 4500 features. SVM models for classification of the ASD training set were generated by training an SVM on a range of between 100 and 4500 of the top RFE determined features. Classification accuracy dropped steeply if

fewer than 100 of these diagnostic features were used. In order to determine whether the model generalizes to ASD patients outside of this set, diagnostic accuracy was tested on an independent testing data set. The features were used to predict the identity of subjects in the training-naive ASD validation data set. Receiver operator curves (ROCs) were generated to show classification accuracy on the training-naive dataset as a function of the number of the top features used (Figure 5.1A). An ROC is a visual representation of the sensitivity and specificity of the model. Sensitivity is the ability to correctly identify ASD subjects or the true positive rate (TPR). Specificity is the ability to correctly identify healthy individuals or 1- false positive rate (1-FPR). A perfect model would have 100% sensitivity (TPR = 1) and specificity (FPR = 0). Note that the SVM was never trained on the validation data set. Rather, SVM models generated on the training data set with different numbers of the top features identified through the RFE procedure were used to predict the identity of subjects in the ASD validation set. Over a range between 800 and 1000 of the top RFE-determined features, the models performed well, with accuracies of 83% (75% sensitivity and 89% specificity). Therefore these edges represent the features that are most diagnostic for ASD and generalize across data sets. Diagnostic features are distributed across the brain and across networks, with the largest number of diagnostic features clustering within the default mode, salience, executive control, higher order visual and motor networks (Figure 5.2A).

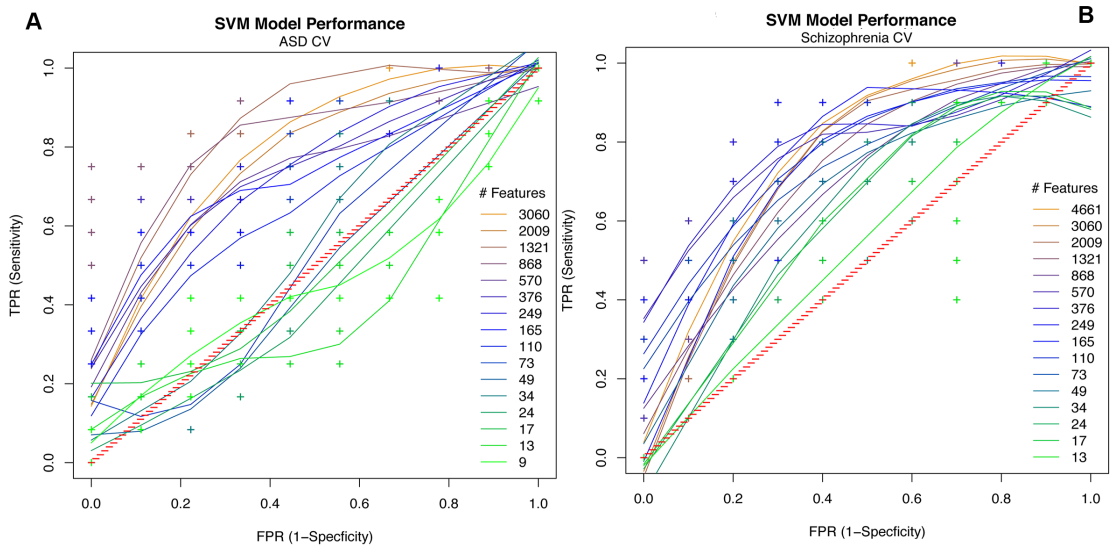

Figure 5.1 Cross-Validation ROCs

A. ASD training-naive test data set as a function of the number of diagnostic features used for prediction. Best model performance: of 83% accuracy (75% sensitivity and 89% specificity) was achieved using between 800 and 1000 of the top RFE-determined features. **B.** SZ training-naive test data set. Best performance was achieved using the top 400-600 RFE features which resulted in 80% accuracy with 80% sensitivity (TPR) and 80% specificity (1-FPR). Diagnostic features were determined by RFE on training data sets. Performance at chance is represented on the red diagonal.

ASD			
Number of Features	Specificity	Sensitivity	Accuracy
9	0.33	0.33	33.00%
13	0.33	0.5	42.00%
17	0.44	0.33	39.00%
24	0.33	0.75	54.00%
34	0.44	0.42	43.00%
49	0.44	0.5	47.00%
73	0.56	0.75	66.00%
110	0.56	0.67	62.00%
165	0.56	0.75	65.00%
249	0.56	0.75	65.00%
376	0.44	0.75	60.00%
570	0.55	0.75	65.00%
868	0.89	0.75	83.00%
1321	0.89	0.75	83.00%
2009	0.78	0.67	73.00%
3060	0.78	58	68.00%

Table 5.1 Specificity and Sensitivity for ASD classification on untrained data.

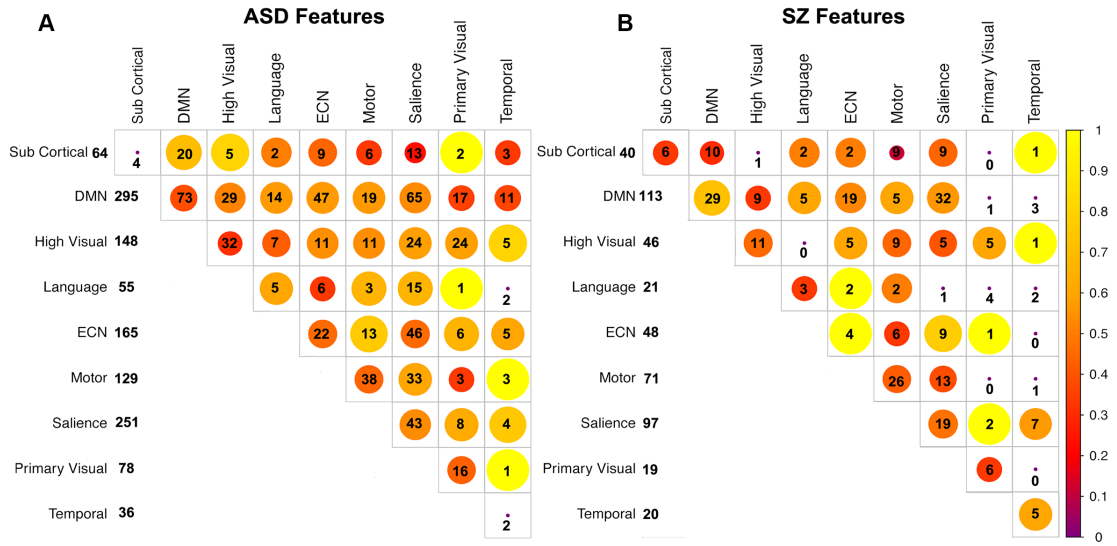

Figure 5.2 Diagnostic Features by network.

Diagonal elements represent within network edges (edges between different regions of the same network). Numbers represent the number of features while the size/colors indicate the ratio of those features that represent increases rather than decreases in connectivity strength relative to controls. Larger circles/yellow colors indicate a greater proportion of connectivity increases and red a greater proportion of decreases. Total number of features per network are indicated in the left column. **A.** In ASD, features cluster within the DMN, salience, ECN, higher order visual and motor networks. **B.** In SZ, features are also clustered in the DMN and salience networks with fewer features in the ECN.

5.3.1.2 Schizophrenia Diagnostic Features

The RFE procedure was performed on the SZ training data set to classify SZ subjects from healthy controls. SVM models using these features on the training set were created by training an SVM on the SZ training data using the top 165-4500 features. These features were then used to predict SZ patients in the training-naive SZ validation set. ROC curves were generated to show the classification performance on the test data set as a function of the number RFE features used (Figure 5.1B). Again, the SVM was never trained on the SZ validation set. Models generated on the training data set with different numbers of the top features identified through the RFE procedure were used to predict the identity of subjects in the SZ testing data set. Fewer features were required to achieve good classification in the SZ test validation data set than in the ASD test validation set. Over a range between 400 and 600 of the top RFE-determined features the models performed very well, achieving accuracy of 80% (80% sensitivity and 80% specificity) on the SZ validation set. These edges are those features that are most diagnostic for SZ across data sets. Diagnostic features had the largest contributions from the DMN, salience network, and sensory-motor cortices (Figure 5.2B).

SZ			
Number of Features	Specificity	Sensitivity	Accuracy
12	0.3	0.4	35.00%
16	0.8	0.2	50.00%
22	0.3	0.7	50.00%
31	0.3	0.8	55.00%
45	0.5	0.8	65.00%
66	0.4	0.8	60.00%
99	0.5	0.7	60.00%
149	0.6	0.8	70.00%
225	0.7	8	75.00%
339	0.7	8	75.00%
514	0.8	0.8	80.00%
782	0.8	6	70.00%
1809	0.7	0.7	70.00%
2754	0.7	0.7	70.00%
4195	0.8	0.8	80.00%
5753	0.8	0.7	75.00%

Table 5.2 Specificity and Sensitivity for SZ Classification on Untrained Data.

5.3.2 Common Features

Approximately 100 features were common to the SVM models for ASD and SZ against the common control group. Common features are the graph model edge weights whose values are diagnostic for both disorders. Common features may not necessarily be increases (or decreases) relative to controls for both disorders. It is possible for a common feature to be indicative of increased connectivity in one disorder and decreased connectivity in the other. However, the overall pattern of connectivity changes in common features across networks are similar for both ASD and SZ, with similar patterns of increases relative to decreases. A small number of features such as those between the salience and ECN networks indicated a greater proportion of increases than decreases for

SZ as compared to ASD subjects. The number of increases relative to decreases in these features are shown for ASD in Figure 5.3A and for SZ in Figure 5.3B. About half of the common features are within-network connectivity differences (changes in connectivity between spatially disparate regions of the same network) shown along the diagonal in Figure 5.3. Common diagnostic features across the disorders are concentrated within the sensory-motor cortex, executive control, salience and default mode networks and were visualized (Figure 5.4) using BrainNet Viewer (http://www.nitrc.org/projects/bnv/) (Xia et al., 2013).

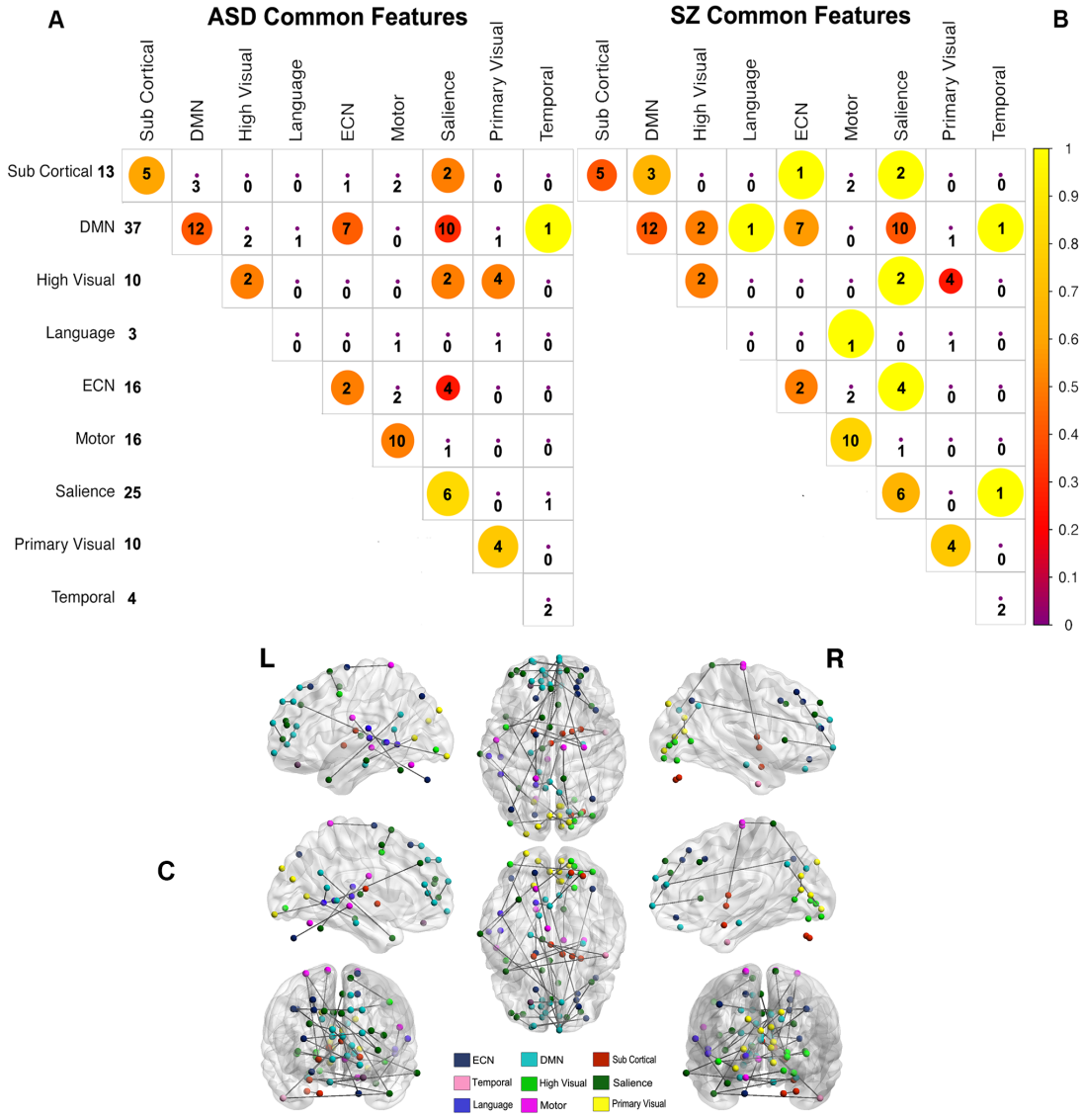

Figure 5.3 Common Features of ASD and SZ

Features common to both the ASD and SZ models relative to the common control group. Diagonal elements represent within network edges between different regions of the same network. Numbers represent the number of features within and between networks while

the size/colors indicate the ratio of those features that represent increases rather than decreases in connectivity strength relative to controls. Larger circles/yellow colors indicate a greater proportion of connectivity increases and red a greater proportion of decreases for **A.** ASD and **B.** SZ. Total number of features per network are indicated in the left column. Overall pattern of connectivity changes in common features across networks are similar for both ASD and SZ. **C.** Common diagnostic features across the disorders are concentrated within the sensory-motor cortex, executive control, salience and default mode networks and cluster in the left hemisphere.

5.3.2.1 Common Features Predict Deficits in ASD Communication

Symptom severity scores for SZ patients were not available in the COBRE and Rutgers data sets. A variety of cognitive assessments were available for ASD patients in the ABIDE dataset. Scores on social and communication deficits were of particular interest since social deficits are common to both ASD and SZ. The average edge weights of ASD patients relative to controls over common features were compared to the autism diagnostic observation schedule (ADOS) (Lord et al., 2000) standardized assessment of social and communicative abilities. Differences in edge weights of the common edges between the two models significantly predicted ADOS social scores, $b = -17.24$, $t(35) = -2.054$, $p < .05$; $R^2 = .11$, $F(1,35) = 4.219$, $p < .05$. Decreased average connectivity strength over the edges common to the ASD and SZ models in the DMN were associated with higher ADOS scores indicative of greater communication deficits.

5.3.3 ASD and SZ Disparate Features

The remaining disparate features between the ASD and SZ models (~1000) represent features found to be diagnostic in either the ASD (Figure 5A) or SZ (Figure 5B) models relative to the common control group, but were not present in both models. The ASD model required a greater number of features to obtain good classification. Both models contain a mixture of increases and decreases in connectivity strength across and within networks. The ASD and SZ models exhibited a large number of non-overlapping features within the DMN and the salience network. However, a much larger proportion of diagnostic features associated with ASD were within-network changes in the DMN as compared to SZ. Features within sensory-motor networks were more prominent in the ASD than SZ model, while changes in the ECN and increases in connectivity in higher level visual processing areas were more prominent in the SZ model. Sections 5.3.1.1 and 5.3.1.2 detail the features identified through the RFE procedure when performed on each of the individual training data sets. These features were compared to those identified by performing the same procedure using the common mixed control group, which consisted of an equal number of control subjects from both data sets. From the initial set of potential features, about half of those identified using RFE on the original training data sets were also identified using the hybrid control group.

5.3.3.1 SVM Discrimination between SZ and ASD Subjects

An SVM was trained using the combined common and distinct features across the

ASD and SZ models to determine wether they could be used to classify ASD from SZ subjects. Patients from the training data sets were successfully classified achieving 98% accuracy with 10-fold cross-validation. These features were then used to predict group membership in ASD and SZ subjects from the validation data sets. Again, the SVM model was trained on the training data sets and the resulting model was used to predict membership in the validation set. As in the other validation procedures, diagnostic accuracy was explored over different numbers of the most significant features. A prediction accuracy of 75% was achieved using 40-50 of these features (Figure 5.6). When examining the edge weights of these features in ASD and SZ patients (Figure 5.7), a striking difference in the pattern of increases and decreases is readily apparent. In the feature set that distinguishes ASD from SZ subjects, ASD is characterized by increases rather than decreases in connectivity strength in nearly all connections between and within networks. While DMN connectivity is prominent in the feature sets for both disorders, the DMN is also the most diagnostic network for distinguishing ASD from SZ. Examining the specific edges involved, SZ exhibited decreased connectivity strength in all DMN connections except those between the posterior cingulate and supplementary motor cortex, and between the precuneus and lateral occipital cortex.

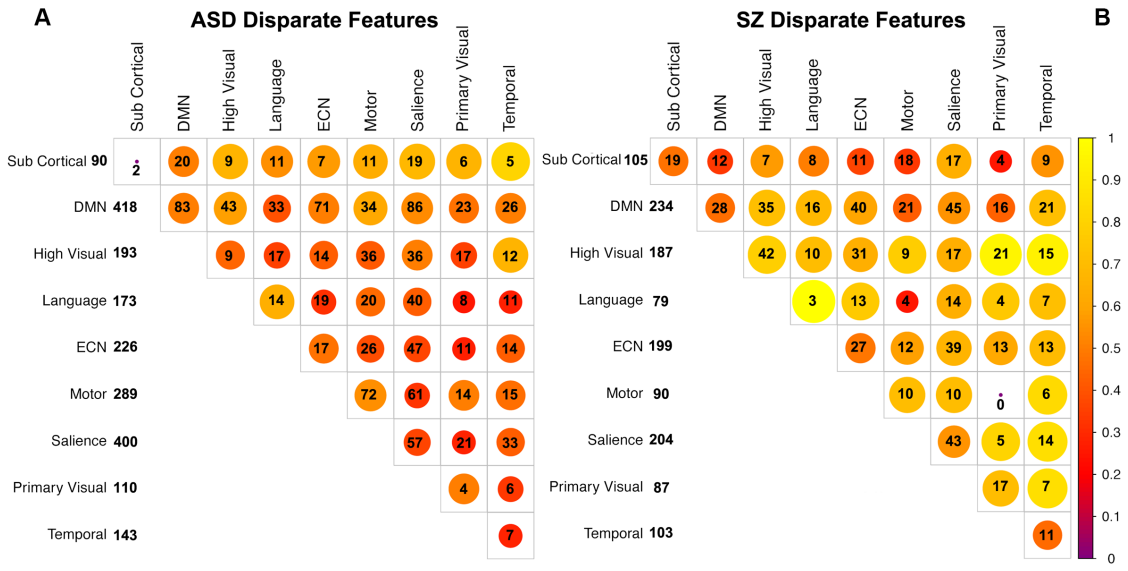

Figure 5.4 Disparate Features of ASD and SZ

Disparate features present in a) ASD model or b) SZ model but not in both models. Connectivity strength differences are relative to healthy individuals in the hybrid control group. Diagonal elements represent within network edges between different regions of the same network. Numbers represent the number of features within or between networks, while color and size indicate the ratio of increases to decreases in connectivity strength for those features relative to controls. Yellow colors indicate a greater proportion of connectivity increases, red a greater proportion of decreases. The DMN and salience networks account for the largest number of features with a mix of increases and decreases in connectivity strength.

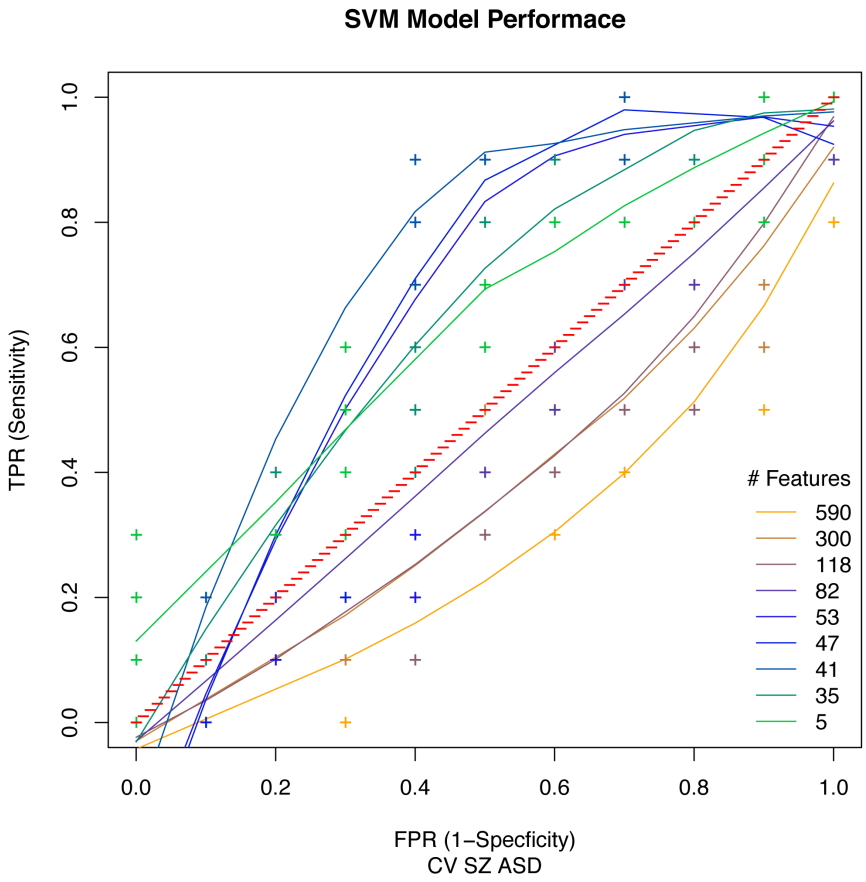

Figure 5.5 Prediction Accuracy ASD of SZ Cross-Validation

ROCs of cross-validation accuracy predicting SZ from ASD patients in the training-naive validation set as a function of the number of diagnostic features used for prediction. Diagnostic features are the combination of the SZ and ASD features when trained against the hybrid control group. Best performance was achieved using the top 40-50 RFE features which resulted in 75% accuracy with 90% sensitivity (TPR) and 60% specificity (1-FPR).

Number of Features	Specificity	Sensitivity	Accuracy
5	0.5	0.6	55.00%
35	0.6	0.6	60.00%
41	0.6	0.9	75.00%
47	0.6	0.9	75.00%
53	0.6	0.7	65.00%
82	0.3	0.7	50.00%
118	0.2	0.6	40.00%
300	0.3	0.5	40.00%
590	0.3	0.4	35.00%

Table 5.3 Prediction Accuracy ASD from SZ Cross-Validation

Specificity and Sensitivity for classification of ASD patients from SZ patients in untrained testing data sets.

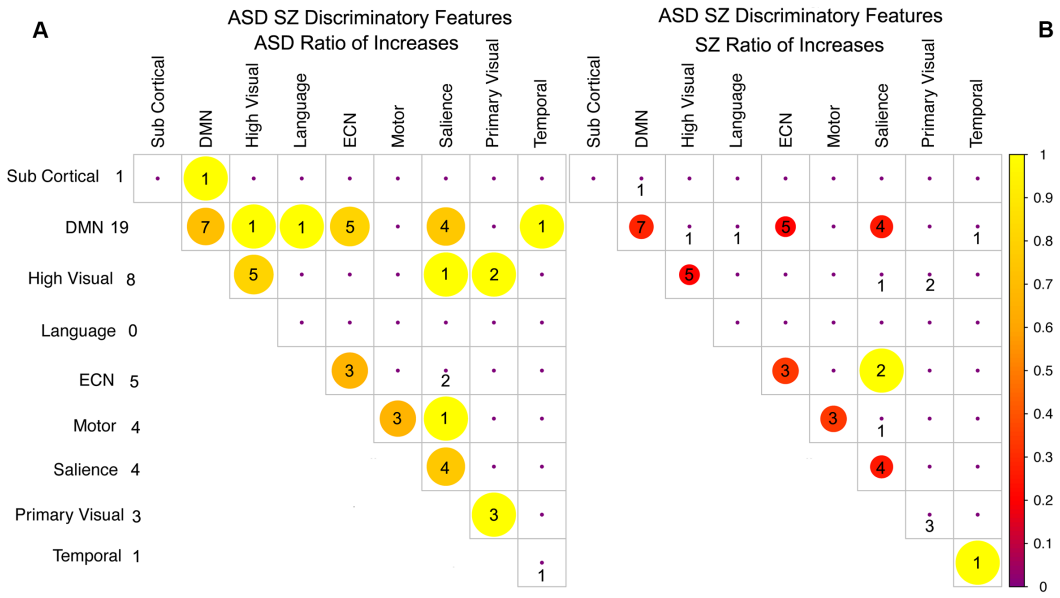

Figure 5.6 DMN Distinguishes ASD from SZ

Features that distinguish ASD from SZ. Diagonal elements represent within network edges between different regions of the same network. **A.** For ASD relative to SZ, the

DMN network accounts for the largest number of features where there are mostly increases in connectivity strength relative to SZ patients. **B.** SZ relative to ASD. Numbers represent the number of features within or between networks, while color and size indicate the ratio of increases to decreases in connectivity strength in those features. Yellow colors indicate a greater proportion of connectivity increases, red a greater proportion of decreases.

5.4 Discussion

From a diagnostic point of view, there is considerable interest in identifying biomarkers for psychiatric disorders such as ASD and SZ. However, there is a recognition that symptoms in many psychiatric disorders lie along a continuum with some degree of overlap across disorders. Despite the similarities between ASD and SZ, particularly in social cognitive deficits and their overlapping etiologies, they are seldom studied comparatively. In their separate literatures, aberrant connectivity has been the focus of study in both ASD and SZ, because it is believed that their cognitive deficits may be caused by the impaired ability to integrate information across functionally distributed brain areas. However, studies of connectivity differences in both ASD and SZ have yielded conflicting results, particularly those that have focused on average connectivity changes between specific brain regions. This highlights the difficulty of using regional connectivity differences between just one or two regions to characterize complex disorders such as ASD and SZ. Even if individual features did reach statistical

significance, this would not be sufficient for use as a biomarker, since there is still considerable overlap in the distributions of regional connectivity strengths between patients and controls. Multivariate pattern analysis, on the other hand, can reliably distinguish patients from healthy controls by identifying a set of features that in combination best describe the deviations from normal connectivity patterns. In addition, this technique makes use of the mixture of increases and decreases in regional connectivity strength to help distinguish groups. In contrast, univariate techniques typically require averaging over regional changes which may account for some of the conflicting results in the literature.

5.4.1 Classification Accuracy

For both SZ and ASD, SVM models were created on an optimized set of diagnostic features identified through a feature elimination procedure. These models were then tested on independent data sets to see if they generalize. The most significant features from each classification set did generalize and yielded good classification accuracies on testing data sets: 83% accuracy on the ASD validation data set and 80% accuracy on the SZ validation data set. Many studies using multivariate classifiers have previously been carried out for both disorders (see Demirci et al., 2008 and Kambeitz et al., 2015 for schizophrenia review; Stevenson et al., 2010 autism). The overwhelming majority of such studies cross-validate their models using a leave one out, leave two out, or 10-fold cross validation scheme. Very few test the generalization of their models on independent data sets. For example, in one recent study of ASD (Ecker et al., 2009) 81%

classification accuracy was achieved using SVM and leave two out cross validation of MRI structural images. They identified differences in grey matter structure in frontal, parietal, and limbic regions as well as the basal ganglia. In another large multi-site study of 964 autistics, 60% accuracy was achieved using functional connectivity and leave one out cross-validation. They identified features in DMN, temporal cortex and the intraparietal sulcus. Similar studies have been carried out in the SZ literature. One such study reported 85% classification accuracy using SVM with 10-fold cross validation on functional connectivity measures (Arbabshirani, 2014). Another study achieved 93% accuracy using Fishers' linear discriminant analysis. Their analysis identified the DMN, temporal and visual regions as the most significant classification features (Du et al., 2012). Testing the classification models on independent data sets over a range of the top diagnostic features showed that the most predictive features for the training data sets, determined based on the SVM model coefficients, generalized to independent training-naive data sets and that validation accuracies decrease as the number of diagnostic features becomes insufficient.

5.4.2 Divergent Features of ASD and SZ

The diagnostic features identified through the RFE procedure were distributed across the brain, which supports the hypothesis that impaired integration of information across distributed brain areas is a hallmark of both ASD and SZ. Both disorders exhibited a large number of changes in connectivity in the DMN and salience networks. However, the two disorders dissociate in terms of the specific pattern of alterations. ASD

showed a greater proportion of within-network changes in the DMN and reduced connectivity between DMN and language areas. In contrast, SZ changes between DMN and language areas were largely increases in connectivity. Diametric changes in connectivity were also identified within the ECN where ASD exhibited largely decreases in connectivity relative to controls and SZ largely increases. The ECN is involved in execution of voluntary control of behavioral responses to salient stimuli and has been identified as a loci of changes in connectivity in SZ (PC et al., 2013; Orellana et al., 2013). It is unclear however whether changes in ECN associated with ASD are a primary cause of dysfunction or the result of dysfunction in lower-level sensory processing (Kenworthy et al., 2008). In fact, a much larger proportion of diagnostic features were found in sensory-motor regions in ASD than were identified in SZ patients. The role of the sensory-motor cortex in social cognition has been studied in the context of the mirror-neuron system, where it is believed that individuals make sense of the actions and emotions of others (Gallese et al., 2004; Oberman et al., 2007). Mirror neurons were originally discovered in the pre-motor cortex of macaque monkeys (Rizzolatti et al., 1996). They are known to fire during goal-oriented motor action, but also in response to observing the same action performed by another individual. Previous studies have indicated dysfunction of the mirror-neuron system in both ASD (Oberman et al., 2005; Enticott, et al., 2012) and SZ (Mehta et al., 2013; Möhring et al., 2015) patients. In addition, the ASD model required more features for accurate classification than were required for SZ subjects. This may be due to the onset of the disorder early during brain development. It has been suggested that early changes in sensory processing of facial

features, for example, lead to changes in the perceived salience of such features and eventually to altered attentional processing and social impairments in ASD (Schultz et al., 2005). Therefore, aberrant function and connectivity early in development may lead to compound changes later in development for higher level skills that are dependent on more elementary or sensory-level function.

5.4.3 Common Features of ASD and SZ

The ability to behave in a context appropriate manner is dependent on recognition of socially relevant sensory information. Accordingly, the overwhelming majority of diagnostic features identified for both ASD and SZ are in the salience and default mode networks. The DMN is believed to be essential to theory of mind abilities (Buckner & Carroll, 2007), while the salience network contributes to a variety of cognitive abilities including communication, social behavior and self-awareness (Menon & Uddin, 2010). Both networks have previously been implicated in a variety of brain disorders including SZ and ASD. For example, in autism is it known that the relative salience of social queues including facial expressions are impaired (Volkmar, 2005). In schizophrenia, misattribution of salience to external and internal stimuli may be a cause of positive symptoms such as hallucinations (Palaniyappan & Liddle, 2012). The DMN is an important part of association cortex. The DMN has connections to supplementary motor areas, frontal eye fields involved in control of visual attention, and reciprocal connections to thalamic nuclei that in-turn connect exclusively with higher association cortices (Cavanna & Trimble, 2006). Many studies have identified the DMN as a collection of

areas that are structural and functional hubs, acting as a common connection point for many other brain areas (Nijhuis et al., 2013; van den Heuvel & Sporns, 2013). The DMN may play a key role in integrating executive control and salience networks, as was reported recently in the context of an n-back working memory task (Liang et al., 2016). As the task load elevated, functional connectivity increased between the salience network and the default mode and executive control networks. Interestingly, there is evidence that the DMN may integrate with salience networks in a graded manner. In a very large study of resting state functional connectivity, smoothly varying gradients of connectivity were found between each region of the DMN and salience network (Anderson et al., 2011b). These connectivity gradients were found to strengthen with maturity. It is possible that aberrant balance between these gradients of connectivity develop as a result of improper pruning and fine tuning over the course of development leading to disfunction. Therefore, the changing interaction of these networks over the course of brain development is one possible explanation for why cognitive deficits similar to those of ASD do not manifest in SZ till early adulthood. A graded response between key networks may also contribute to the spectrum of cognitive deficits observed when this system is compromised.

5.4.4 Discriminating ASD from SZ

A small subset of the common and divergent features that distinguished either ASD or SZ from controls had diagnostic importance for classifying ASD from SZ subjects. This subset was dominated by features in the DMN. The results indicate that,

relative to SZ patients (rather than controls), ASD is associated with stronger connectivity in the DMN, while weaker connectivity was found in SZ patients for the same edges. Positive symptoms associated with SZ, such as hallucinations, are one of the main characteristics that distinguish SZ from ASD. Positive symptoms in SZ are reportedly correlated with increased functional connectivity between the posterior regions of the DMN and the salience network (Bluhm et al., 2007). The features identified in this study are consistent with this and suggest that such increases involve connections specifically between the posterior cingulate and supplementary motor cortex, and between the precuneus and lateral occipital cortex. In addition, some studies have indicated that negative symptoms in SZ, such as impaired social cognition, are associated with decreased connectivity with anterior parts of the DMN in medial prefrontal cortex (Camchong et al., 2011). The diagnostic features identified suggest that SZ subjects have weaker connectivity over specific edges within anterior DMN regions particularly related to connections to the paracingulate. These features successfully classified ASD from SZ subjects in validation data sets, demonstrating that multivariate machine learning techniques can be used to distinguish between disorders even when there is considerable overlap in their symptoms.

5.4.5 Limitations of the current study

The RFE method employed demonstrates that there are characteristic changes in the patterns of resting state connectivity that generalize to patient populations outside of the training sets. A specific challenge to be met in identifying diagnostic biomarkers

from resting state functional connectivity is to find the best set of features to maximize diagnostic capability. The set of ROIs used, while comprehensive in their representative coverage of functional brain areas, nonetheless has sparse coverage over the whole brain. Future work should explore similar analysis using a voxel level approach to determine if there are better features to use for this purpose. Additionally, symptom severity measures were not available for schizophrenic patients, it was not possible to explicitly associate common connectivity differences in ASD and SZ to measures of symptom severity in SZ patients. Finally the sample size of the SZ test data was small. Future studies should explore the the utility of identified features over several data sets for greater certainty of diagnostic utility. However, few studies attempt to validate classifier models on data sets outside of the training set. The SVM models achieved good classification accuracy on this small data set as well as the larger ASD test set, suggesting that the model features are based in disease specific changes in connectivity that may generalize to other patient populations.

5.5 Summary

In summary, common changes in connectivity between ASD and SZ were identified that predict deficits in communication skills in ASD patients. The results suggest that common social cognitive deficits associated with ASD and SZ may be related to changes in connectivity within higher order association cortex in the DMN and salience network. In addition, divergent changes in connectivity were identified, which were successfully used to discriminate between ASD and SZ patients. These features resulted in classification accuracies well above chance performance in training-naive data

sets, suggesting that these models may generalize across patient populations. Relative to healthy individuals, there were more disparate than common features of the two disorders, but only a few features had diagnostic significance in distinguishing the two populations. Relative to SZ patients, the distinguishing features of ASD were increases in connectivity within higher order visual processing areas and the DMN. When disorders exhibit considerable overlap in their symptoms, as is the case in ASD and SZ, comparative studies can yield insights into the changes in connectivity that lead to common deficits.

CONCLUSION

In this thesis I propose an account of DMN function based on the anatomical connections of each region of the network as well as their temporal dynamics in response in to task demands. Unlike DMN regions in vmPFC and the cingulate, parietal DMN regions have connections to visual cortex. I found that these regions increase in activity during visual processing. In contrast, regions of the vmPFC increased in activity after visual stimuli were processed, during task responses, suggesting dynamic changes in DMN activity that correspond to changes in bottom-up and top-down processing. This pattern of evoked activity was consistent across experimental paradigms. An interpretation of DMN function based on top-down and bottom-up modulation provides a parsimonious explanation for the network's high level of baseline activity as well as the collection of tasks known to evoke increases and decreases in DMN activity. The observed patterns of activity in the DMN, TPN, basal ganglia and thalamus, suggest that the transitions between between bottom-up and top-down processing may be accomplished through coordinated signaling between the DMN and TPN through these subcortical structures. The arrangement of DMN projections through the direct and indirect pathways of the basal ganglia may be key in understanding how this transition takes place and may also yield insights into the relationship between DMN disfunction and the wide array of neuropsychiatric disorders with which it is associated.

REFERENCES

Addis, D. R., Wong, A. T., & Schacter, D. L. (2007). Remembering the past and imagining the future: common and distinct neural substrates during event construction and elaboration. *Neuropsychologia*, 45, 1363–77.

Ajmone-Marsan, C. (1965). Electrical activity of the brain: slow waves and neuronal activity. *Isr. J. Med. Sci*. 1,104–17.

Albert, N., Robertson, E., Miall, R. (2009). The resting human brain and motor learning. *Curr Biol,* 19,1023–1027.

Alexander, G. E., Crutcher, M. D. (1990). Functional architecture of basal ganglia circuits: neural substrates of parallel processing. *Trends in Neurosciences*, *13*(7), 266–271. https://doi.org/10.1016/0166-2236(90)90107-L

Alexander, G., Crutcher, M., Delong, M. (1990). Basal ganglia-thalamocortical circuits: Parallel substrates for motor, oculomotor, "prefrontal", and "limbic" functions. *Progress in Brain Research*, *85*, 119–146.

Alexander, G. (1986). Parallel Organization of Functionally Segregated Circuits Linking Basal Ganglia and Cortex. *Annual Review of Neuroscience*, *9*(1), 357–381. https://doi.org/10.1146/annurev.neuro.9.1.357

Allison, J., Meador, K., Loring, D., Figueroa, R., Wright, J. (2000). Functional MRI cerebral activation and deactivation during finger movement. *Neurology*, *54*(1), 135–142.

Amaro, E., Barker, G. J. (2006). Study design in fMRI: Basic principles. *Brain and Cognition*, *60*(3), 220–232. https://doi.org/10.1016/j.bandc.2005.11.009

Amodio, D. M., Frith, C. D. (2006). Meeting of minds: The medial frontal cortex and social cognition. *Nature Reviews Neuroscience*, *7*(4), 268–277. https://doi.org/10.1038/nrn1884

Andersson, J. L. R., & Sotiropoulos, S. N. (2016). An integrated approach to correction for off-resonance effects and subject movement in diffusion MR imaging. *NeuroImage*, *125*, 1063–1078. https://doi.org/10.1016/j.neuroimage.2015.10.019

Andersson, J. L. R., Sotiropoulos, S. N. (2015). Non-parametric representation and prediction of single- and multi-shell diffusion-weighted MRI data using Gaussian processes. *NeuroImage*, *122*, 166–176. https://doi.org/10.1016/j.neuroimage.2015.07.067

Anderson, J. (2014). Cortical Underconnectivity Hypothesis in Autism: Evidence from Functional Connectivity MRI. In Comprehensive Guide to Autism, 671–692.

Andersson, J.L.R., Xu, J., Yacoub, E., Auerbach, E., Moeller, S., Ugurbil, K. (2012). A Comprehensive Gaussian Process Framework for Correcting Distortions and Movements in Diffusion Images. ISMRM, Melbourne, Australia.

Anderson, J. S., Nielsen, J. A., Froehlich, A. L., Dubray, M. B., Druzgal, T. J., Cariello, A. N., … Lainhart, J. E. (2011a). Functional connectivity magnetic resonance imaging classification of autism. *Brain*, *134*(12), 3739–3751. http://doi.org/10.1093/brain/awr263

Anderson, J. S., Ferguson, M. a, Lopez-Larson, M., & Yurgelun-Todd, D. (2011b). Connectivity gradients between the default mode and attention control networks. *Brain Connectivity*, *1*(2), 147–157. https://doi.org/10.1089/brain.2011.0007

Anderson, J. S., Druzgal, T. J., Froehlich, A., Dubray, M. B., Lange, N., Alexander, A. L., Lainhart, J. E. (2011c). Decreased interhemispheric functional connectivity in autism. *Cerebral Cortex*, 21(5), 1134–1146.

Andersson, J. L. R., Skare, S., & Ashburner, J. (2003). How to correct susceptibility distortions in spin-echo echo-planar images: Application to diffusion tensor imaging. *NeuroImage*, *20*(2), 870–888. https://doi.org/10.1016/S1053-8119(03)00336-7

Andreasen, N. C., O'Leary, D. S., Cizadlo, T., Arndt, S., Rezai, K., Watkins, G. L., … Hichwa, R. D. (1995). Remembering the past: Two facets of episodic memory explored with positron emission tomography. *American Journal of Psychiatry*, *152*(11), 1576–1585. https://doi.org/10.1176/ajp.152.11.1576

Andrews-Hanna, J.R., Snyder, A.Z., Vincent, J.L., Lustig, C., Head, D., Raichle, M.E., Buckner, R.L. (2007). Disruption of large-scale brain systems in advanced aging. *Neuron,* 56, 924-935.

Anticevic, A., Cole, M. W., Murray, J. D., Corlett, P. R., Wang, X. J., & Krystal, J. H. (2012). The role of default network deactivation in cognition and disease. *Trends in Cognitive Sciences*, *16*(12), 584–592. https://doi.org/10.1016/j.tics.2012.10.008

Arbabshirani, M. R., Castro, E., Calhoun, V. (2014). Accurate classification of schizophrenia patients based on novel resting-state fMRI features resting-state fMRI features. In Proc. Conf Proc IEEE Eng Med Biol Soc., 6691–6694. https://doi.org/10.13140/2.1.1332.6723

Arne Henningsen and Jeff D. Hamann (2007). systemfit: A Package for Estimating Systems of Simultaneous Equations in R. Journal of Statistical Software 23(4), 1-40. http://www.jstatsoft.org/v23/i04/

Assaf, M., Jagannathan, K., Calhoun, V. D., Miller, L., Stevens, M. C., Sahl, R., … Pearlson, G. D. (2010). Abnormal functional connectivity of default mode sub-networks in autism spectrum disorder patients. *NeuroImage*, *53*(1), 247–256. https://doi.org/https://doi.org/10.1016/j.neuroimage.2010.05.067

Attwell, D., Iadecola, C. (2002). The neural basis of functional brain imaging signals. *Trends Neurosci*., 25, 621–625.

Bandettini, P. A., Wong, E. C., Hinks, R. S., Tikofsky, R. S., & Hyde, J. S. (1992). Time course EPI of human brain function during task activation. *Magnetic Resonance in Medicine*, *25*(2), 390–397. https://doi.org/10.1002/mrm.1910250220

Barch, D. M., Burgess, G. C., Harms, M. P., Petersen, S. E., Schlaggar, B. L., Corbetta, M., … Van Essen, D. C. (2013a). Function in the human connectome: Task-fMRI and individual differences in behavior. *NeuroImage*, *80*, 169–189. https://doi.org/10.1016/j.neuroimage.2013.05.033

Barch, D. M., Burgess, G. C., Harms, M. P., Petersen, S. E., Schlaggar, B. L., Corbetta, M., … Van Essen, D. C. (2013b). Function in the human connectome: Task-fMRI and individual differences in behavior. *NeuroImage*, *80*, 169–189. https://doi.org/10.1016/j.neuroimage.2013.05.033

Basser, P., Pajevic, S., Pierpaoli, C., Duda, J., Aldroubi, A. (2000). In vivo fiber tractography using DT-MRI data. *Magnetic Resonance Imaging in Medicine*, 44, 625-632.

Barnea-Goraly, N., Kwon, H., Menon, V., Eliez, S., Lotspeich, L., & Reiss, A. L. (2004). White matter structure in autism: Preliminary evidence from diffusion tensor imaging. *Biological Psychiatry*, *55*(3), 323–326. http://doi.org/10.1016/j.biopsych.2003.10.022

Bechara A, Damasio AR, Damasio H, Anderson SW. 1994. Insensitivity to future consequences following damage to human prefrontal cortex. *Cognition,* 50, 7–15.

Beckmann, C. F., DeLuca, M., Devlin, J. T., & Smith, S. M. (2005). Investigations into resting-state connectivity using independent component analysis. *Philosophical Transactions of the Royal Society of London. Series B, Biological Sciences*, *360*(1457), 1001–13. http://doi.org/10.1098/rstb.2005.1634

Behrens, T., Sporns, O. (2012). Human connectomics. *Curr Opin Neurobiol*., 22, 144–53.

Behrens, T. E. J., Woolrich, M. W., Smith, S. M., Boulby, P. A., Barker, G. J., Sillery, E. L., … Matthews, P. M. (2003a). Non-invasive mapping of connections between human thalamus and cortex using diffusion imaging, *Nature Neuroscience*, *6*(7), 750-757.

Behrens, T. E. J., Woolrich, M. W., Jenkinson, M., Johansen-Berg, H., Nunes, R. G., Clare, S., … Smith, S. M. (2003b). Characterization and propagation of uncertainty in diffusion-weighted MR imaging. *Magnetic Resonance in Medicine*, *50*, 1077–88. http://doi.org/10.1002/mrm.10609

Behrens, T. E. J., Berg, H. J., Jbabdi, S., Rushworth, M. F. S., & Woolrich, M. W. (2007). Probabilistic diffusion tractography with multiple fibre orientations: What can we gain? *NeuroImage*, *34*(1), 144–55. http://doi.org/10.1016/j.neuroimage.2006.09.018

Beucke, J. C., Sepulcre, J., Eldaief, M. C., Sebold, M., Kathmann, N., & Kaufmann, C. (2014). Default mode network subsystem alterations in obsessive-compulsive disorder. *British Journal of Psychiatry*, *205*(5), 376–382. https://doi.org/10.1192/bjp.bp.113.137380

Bi G, Poo M (1999) Distributed synaptic modification in neural networks induced by patterned stimulation. Nature 401:792–796.

Bird, G., Catmur, C., Silani, G., Frith, C., & Frith, U. (2006). Attention does not modulate neural responses to social stimuli in autism spectrum disorders. *Neuroimage*. 31(4),1614-24.

Birn, R.M., Saad, Z.S., Bandettini, P.A., (2001). Spatial heterogeneity of the nonlinear dynamics in the FMRI BOLD response. *NeuroImage,* 14, 817–826.

Bishop G., O'Leary. J. (1942). Factors determining the form of the potential record in the vicinity of the synapses of the dorsal nucleus of the lateral geniculate body. *J. Cell Comp. Physiol*., 19, 315–31.

Birbaumer, N. Elbert, T. Canavan, A. Rockstroh, B. (1990). Slow Potentials of the Cerebral Cortex and Behavior. *Physiological Reviews*, *70*(1), 1–41.

Biswal, B., Yetkin, Z., Haughton, V., Hyde, J. (1995). Functional Connectivity in the Motor Cortex of Resting Human Brain Using Echo-Planar MRI. *Magnetic Resonance in Medicine*, *34*(4), 537–41.

Bleuler E. (1951). Autistic thinking. In: Organization and Pathology of Thought: Selected Sources. New York: Columbia University Press, 399–437.

Bluhm, R. L., Miller, J., Lanius, R. A., Osuch, E. A., Boksman, K., Neufeld, R. W. J., … Williamson, P. (2007). Spontaneous low-frequency fluctuations in the BOLD signal in schizophrenic patients: Anomalies in the default network. *Schizophrenia Bulletin*, *33*(4), 1004–1012. https://doi.org/10.1093/schbul/sbm052

Bolam, J. P., Hanley, J. J., Booth, P. a, & Bevan, M. D. (2000). Synaptic organization of the basal ganglia. *Journal of Anatomy*, *196 (Pt 4*), 527–542. https://doi.org/10.1046/j.1469-7580.2000.19640527.x

Boly, M., Tshibanda, L., Vanhaudenhuyse, A., Noirhomme, Q., Schnakers, C., Ledoux, D., Boveroux, P., Garweg, C., Lambermont, B., Phillips, C., Luxen, A., Moonen, G., Bassetti, C., Maquet, P., Laureys, S., (2009). Functional connectivity in the default network during resting state is preserved in a vegetative but not in a brain dead patient. *Hum. BrainMapp.*, 30, 2393–2400.

Boly, M., Balteau, E., Schnakers, C., Degueldre, C., Moonen, G., Luxen, a, … Laureys, S. (2007). Baseline brain activity fluctuations predict somatosensory perception in humans. *Proceedings of the National Academy of Sciences of the United States of America*, *104*(29), 12187–12192. https://doi.org/10.1073/pnas.0611404104

Botzung, A., Denkova, E., &Manning, L. (2008). Experiencing past and future personal events: functional neuroimaging evidence on the neural bases of mental time travel. *Brain and Cognition*, 66, 202–12.

Boynton, G.M., Engel, S.A., Glover, G.H., Heeger, D.J., (1996). Linear systems analysis of functional magnetic resonance imaging in human V1. *J. Neurosci*. 16, 4207–4221.

Breshears, J.D., Roland, J.L., Sharma, M., Gaona, C.M., Freudenburg, Z.V., Tempelhoff, R., Avidan, M.S., Leuthardt, E.C. (2010). Stable and dynamic cortical electrophysiology of induction and emergence with propofol anesthesia. *Proc Natl Acad Sci USA,* 107, 21170–21175.

Broca, P. (1861). Remarques sur le siège de la faculté du langage articulé suivies d'une observation d'aphémie (perte de la parole). *Bull. Soc. Anat*., 6, 330–357.

Brodmann, K. (1909). Vergleichende Lokalisationslehre der Grosshirnrinde in ihren Prinzipien dargestellt auf Grund des Zellenbaues. Barth, Leipzig.

Brovelli, A., Ding, M., Ledberg, A. Chen, Y., Nakamura, R., Bressler, S. (2004). Beta oscillations in a large-scale sensorimotor cortical network: directional influences revealed by Granger causality. *Proc. Natl Acad. Sci. USA,* 101, 9849–9854.

Browne, M. W. (1984). Asymptotic distribution-free methods for the analysis of covariance structures. *Br. J. Math. Stat. Psychol.,* 37, 62–83. doi: 10.1111/j.2044-8317.1984.tb00789

Brune, M. (2003). Social cognition and behavior in schizophrenia. The Social Brain: Evolution and Pathology. Oxford: Wiley, 277–313.

Buckner, R. L., Andrews-Hanna, J. R., & Schacter, D. L. (2008). The brain's default network: Anatomy, function, and relevance to disease. *Annals of the New York Academy of Sciences*, *1124*, 1–38. https://doi.org/10.1196/annals.1440.011

Buckner, R. L., Carroll, D. C. (2007). Self-projection and the brain. *Trends in Cognitive Sciences*, *11*(2), 49–57. https://doi.org/10.1016/j.tics.2006.11.004

Buckner, M., Burock, M., Dale, A., Rosen, B., Woldorff, M. (1998). Randomized event-related experimental designs allow for extremely rapid presentation rates using functional MRI. *NeuroReport. 19,* 3735-3739.

Bullmore, E., Sporns, O. (2009). Complex brain networks: graph theoretical analysis of structural and functional systems. *Nat Rev Neurosci.*, 10, 186–98.

Bullock, T. (1997). Signals and signs in the nervous system: the dynamic anatomy of electrical activity is probably information-rich. *Proc. Natl. Acad. Sci. USA,* 94, 1–6.

Buxton, R. B., Wong, E. C., & Frank, L. R. (1998). Dynamics of blood flow and oxygenation changes during brain activation: the balloon model. *Magnetic Resonance in Medicine : Official Journal of the Society of Magnetic Resonance in Medicine / Society of Magnetic Resonance in Medicine*, *39*(6), 855–64.

Buxton, R. B., Uludağ, K., Dubowitz, D. J., Liu, T. T. (2004). Modeling the hemodynamic response to brain activation. *NeuroImage*, *23 Suppl 1*, S220-33. http://doi.org/10.1016/j.neuroimage.2004.07.013

Cabeza, R., Nyberg, L. (2000). Imaging cognition: An empirical review of PET studies with normal subjects. *J Cogn.Neurosci.*, *9*(1), 1–26.

Camchong, J., MacDonald, A. W., Bell, C., Mueller, B. A., & Lim, K. O. (2011). Altered functional and anatomical connectivity in schizophrenia. *Schizophrenia Bulletin*, *37*(3), 640–650. http://doi.org/10.1093/schbul/sbp131

Carmichael, S. T., Price, J. L. (1994). Architectonic subdivision of the orbital and medial prefrontal cortex in the macaque monkey. *The Journal of Comparative Neurology*, *346*(3), 366–402.

Carmichael, S. T., Price, J. L. (1996). Connectional networks within the orbital and medial prefrontal cortex of macaque monkeys. *The Journal of Comparative Neurology*, *371*(2), 179–207.

Carrington, S.J., Bailey, A.J. (2009). Are there theory of mind regions in the brain? A Review of the neuroimaging literature. *Hum Brain Mapp,* 30, 2313–2335.

Casey, B. J., Tottenham, N., Liston, C., Durston, S. (2005). Imaging the developing brain: what have we learned about cognitive development? *Trends Cogn. Sci*., *9*(3), 104-110. http://doi.org/10.1016/j.tics.2005.01.011

Castelli, F., Happé, F., Frith, U., Frith, C. (2013). Movement and mind: A functional imaging study of perception and interpretation of complex intentional movement patterns. *Social Neuroscience: Key Readings*, *325*, 155–170. https://doi.org/10.4324/9780203496190

Castro, E., Arbabshirani, M. R., Castro, E., Calhoun, V. D., & Fellow, I. (2014). Accurate classification of schizophrenia patients based on novel resting-state fMRI features resting-state fMRI features. In Proc. Conf Proc IEEE Eng Med Biol Soc., 6691–6694.

Cavada, C., Goldman- Rakic, P. S. (1989). Posterior parietal cortex in rhesus monkey: I. Parcellation of areas based on distinctive limbic and sensory corticocortical connections. *Journal of Comparative Neurology*, *287*(4), 393–421. https://doi.org/10.1002/cne.902870402

Cavada, C., Goldman-Rakic, P. S. (1989). Posterior parietal cortex in rhesus monkeys: II. Evidence for segregated corticocortical networks linking sensory and limbic\rareas with the frontal lobe. *J Comp Neurol*, *28*, 422–445.

Cavanna, A. E., Trimble, M. R. (2006). The precuneus: A review of its functional anatomy and behavioural correlates. *Brain*, *129*(3), 564–583. https://doi.org/10.1093/brain/awl004

Cecchi, G., Rish, I., Thyreau, B., Thirion, B., Plaze, M., Paillere-Martinot, M.-L., … Poline, J.-B. (2009). Discriminative Network Models of Schizophrenia. *Advances in Neural Information Processing Systems*, *22*, 1–9.

Chen, J. J., Jann, K., Wang, D. J. J. (2015). Characterizing Resting-State Brain Function Using Arterial Spin Labeling. *Brain Connectivity*, *5*(9), 527–542. https://doi.org/10.1089/brain.2015.0344

Chen, S., Ross, T. J., Zhan, W., Myers, C. S., Chuang, K.-S., Heishman, S. J., … Yang, Y. (2008). Group independent component analysis reveals consistent resting-state networks across multiple sessions. *Brain Research*, *1239*, 141–51. http://doi.org/10.1016/j.brainres.2008.08.028

Cherkassky, V., Kana, R., Keller, T., & Just, M. (2006). Functional connectivity in a baseline resting-state network in autism. *Neuroreport*, 17(16), 1687–90.

Choi, E. Y., Tanimura, Y., Vage, P. R., Yates, E. H., & Haber, S. N. (2017). Convergence of prefrontal and parietal anatomical projections in a connectional hub in the striatum. *NeuroImage*, *146*(September 2016), 821–832. https://doi.org/10.1016/j.neuroimage.2016.09.037

Choi, E. Y., Yeo, B. T., Buckner, R. L. (2012). The organization of the human striatum estimated by intrinsic functional connectivity. *Journal of Neurophysiology*, *108*(8), 2242–2263. https://doi.org/10.1152/jn.00270.2012

Chu, C. J., Kramer, M. a, Pathmanathan, J., Bianchi, M. T., Westover, M. B., Wizon, L., & Cash, S. S. (2012). Emergence of stable functional networks in long-term human electroencephalography. *The Journal of Neuroscience : The Official Journal of the Society for Neuroscience*, *32*(8), 2703–2713. https://doi.org/10.1523/JNEUROSCI.5669-11.2012

Christoff, K., Gordon, A. M., Smallwood, J., Smith, R., & Schooler, J. W. (2009). Experience sampling during fMRI reveals default network and executive system contributions to mind wandering. *Proceedings of the National Academy of Sciences*, *106*(21), 8719–8724. https://doi.org/10.1073/pnas.0900234106

Cole, M. W., Bassett, D. S., Power, J. D., Braver, T. S., & Petersen, S. E. (2014). Intrinsic and task-evoked network architectures of the human brain. *Neuron*, *83*(1), 238–251. https://doi.org/10.1016/j.neuron.2014.05.014

Corbetta M., Shulman, G.L. (2002). Control of goal-directed and stimulus-driven attention in the brain. *Nat. Rev. Neurosci.* 3, 201–15.

Cordes D., Haughton V., Carew J.D., et al., (2002) Hierarchical clustering to measure connectivity in fMRI resting-state data. *Magn Reson Imaging*. 20, 305–17.

Cordes, D., Haughton, V.M,, Arfanakis, K., Wendt, G.J., Turski, P.A., Moritz, C.H., Quigley, M.A., Meyerand, M.E. (2000). Mapping functionally related regions of brain with functional connectivity MR imaging. *Am J Neuroradiol,* 21, 1636–1644.

Crespi, B., Stead, P., Elliot, M. (2010). Comparative genomics of autism and schizophrenia. *PNAS*, 107 (suppl 1) 1736-1741.

Crittenden, B. M., Mitchell, D. J., Duncan, J. (2015). Recruitment of the default mode network during a demanding act of executive control. *ELife*, *2015*(4), 1–12. https://doi.org/10.7554/eLife.06481

Cudeck, R. Henley, S.J. (1991). Model selection in covariance structure analysis and the 'problem' of sample size: a clarification. *Psychological Bulletin*, 109, 512-519.

Cummings, J. L. (1993). Frontal-Subcortical Circuits and Human Behavior. *Neurological Review*, 50, 873–880.

Cutting, J., David, A., & Murphy, D. (1987). The nature of overinclusive thinking in schizophrenia. *Psychopathology*, 20(3-4), 213-9.

D'Argembeau, A., Xue, G., Lu, Z.-L., Van der Linden, M., & Bechara, A. (2008). Neural correlates of envisioning emotional events in the year and far future. *Neuroimage*, 40(1), 398-407.

Damasio, A.R., Van Hoesen, G.W. (1983). Emotional disturbances associated with focal lesions of the limbic frontal lobe. In Neuropsychology of Human Emotion, K.M. Heilman and P. Satz, eds. (New York: Guilford Press), pp. 85–110.

Damoiseaux, J. S., Beckmann, C. F., Arigita, E. J. S., Barkhof, F., Scheltens, P., Stam, C. J., … Rombouts, S. A. R. B. (2008). Reduced resting-state brain activity in the "default network" in normal aging. *Cerebral Cortex*, *18*(8), 1856–1864. https://doi.org/10.1093/cercor/bhm207

Damoiseaux, J. S., Rombouts, S. a R. B., Barkhof, F., Scheltens, P., Stam, C. J., Smith, S. M., & Beckmann, C. F. (2006). Consistent resting-state networks across healthy subjects. *Proceedings of the National Academy of Sciences of the United States of America*, *103*(37), 13848–53. http://doi.org/10.1073/pnas.0601417103

Daniels, J. K., McFarlane, A. C., Bluhm, R. L., Moores, K. A., Clark, C. R., Shaw, M. E., … Lanius, R. A. (2010). Switching between executive and default mode networks in posttraumatic stress disorder: Alterations in functional connectivity. *Journal of Psychiatry & Neuroscience*. 35(5), 258-266.

Davis, K. L., Stewart, D. G., Friedman, J. I., & Buchsbaum, M. (2014). White Matter Changes in *Schizophrenia*, 60, 443–456.

Davis, T. L., Kwong, K. K., Weisskoff, R. M., & Rosen, B. R. (1998). Calibrated functional MRI: Mapping the dynamics of oxidative metabolism. *Proceedings of the National Academy of Sciences*, *95*(4), 1834–1839. http://doi.org/10.1073/pnas.95.4.1834

De Havas, J. A., Parimal, S., Soon, C. S., & Chee, M. W. L. (2012). Sleep deprivation reduces default mode network connectivity and anti-correlation during rest and task performance. *NeuroImage*, *59*(2), 1745–1751. https://doi.org/10.1016/j.neuroimage.2011.08.026

de Marco, G., Fall, S., Vrignaud, P. (2007). Use of fMRI and structural equation modeling for studying inter-connected brain areas within a hypothetical network. *Current Medical Imaging Reviews*, *3* (Netherlands RF-73 LG-English PT-Journal: Review DD-20080120), 249–261. https://doi.org/10.2174/157340507782446269

Delaveau, P., Salgado-Pineda, P., Fossati, P., Witjas, T., Azulay, J.P., Blin, O. (2010). Dopaminergic modulation of the default mode network in Parkinson's disease. *Eur Neuropsychopharmacol.,* 20(11), 784-92.

Delgado, M.R., Nystrom, L.E., Fissell, C., Noll, D.C., Fiez, J.A., (2000). Tracking the hemodynamic responses to reward and punishment in the striatum. J. Neurophysiol., 84, 3072–3077.

Demirci, O. Clark, V., Manotta, V., Andreasen, N., Lauriello, J., Kiehl, K., Pearlson, G., Cahloun, V. (2008). A Review of Challenges in the use of fMRI for Disease Classification/Characterization and A Projection Pursuit application from a Multi-site fMRI Schizophrenia Study. *Brain Imaging and Behavior*, 2(3), 207-226.

Devor, A., Dunn, A.K., Andermann, M.L., Ulbert, I., Boas, D.A., Dale, A.M., (2003). Coupling of total hemoglobin concentration, oxygenation, and neural activity in rat somatosensory cortex. *Neuron,* 39, 353–359.

Dixon, M. L., De La Vega, A., Mills, C., Andrews-Hanna, J., Spreng, R. N., Cole, M. W., & Christoff, K. (2018). Heterogeneity within the frontoparietal control network and its relationship to the default and dorsal attention networks. *Proceedings of the National Academy of Sciences*, *115*(7), E1598–E1607. https://doi.org/10.1073/pnas.1715766115

Dixon, M. L., Andrews-hanna, J. R., Spreng, R. N., Irving, Z. C., Mills, C., Girn, M., & Christo, K. (2017). Interactions between the default network and dorsal attention network vary across default subsystems, time, and cognitive states. *NeuroImage*, 147, 632–649. https://doi.org/10.1016/j.neuroimage.2016.12.073

Douw, L., Wakeman, D. G., Tanaka, N., Liu, H., & Stufflebeam, S. M. (2016). State-dependent variability of dynamic functional connectivity between frontoparietal and default networks relates to cognitive flexibility. *Neuroscience*, *339*, 12–21. https://doi.org/10.1016/j.neuroscience.2016.09.034

Draganski, B., Kherif, F., Klo, S., Cook, P. A., Alexander, D. C., Parker, G. J. M., … Frackowiak, R. S. J. (2008). Evidence for Segregated and Integrative Connectivity Patterns in the Human Basal Ganglia. *J Neurosci*, *28*(28), 7143–7152. https://doi.org/10.1523/JNEUROSCI.1486-08.2008

Drayton, L. A., Santos, L. R. (2016). A decade of theory of mind research on cayo santiago: Insights into rhesus macaque social cognition. *American Journal of Primatology*, *78*(1), 106–116. https://doi.org/10.1002/ajp.22362

Du, W., Calhoun, V. D., Li, H., Ma, S., Eichele, T., Kiehl, K. a., Adali, T. (2012). High Classification Accuracy for Schizophrenia with Rest and Task fMRI Data. Frontiers in Human *Neuroscience*, 6(June), 1–12.

Ecker, C., Rocha-Rego, V., Johnston, P., Mourao-Miranda, J., Marquand, A., Daly, E. M., Murphy, D. G. (2010). Investigating the predictive value of whole-brain structural MR scans in autism: A pattern classification approach. *NeuroImage*, 49(1), 44–56. https://doi.org/10.1016/j.neuroimage.2009.08.024

Efron, B., Tibshirani, R.J. (1993). An introduction to the bootstrap. New York: Chapman & Hall.

Eickhoff, S.B., Amunts, K., Mohlberg, H., Zilles, K. (2006). The human parietal operculum. II. Stereotaxic maps and correlation with functional imaging results. *Cereb Cortex,* 16, 268–279.

Enticott, P., Kennedy, H., Rinehart, N., Tonge, B., Bradshaw, J., Taffe, J., Daskalakis, Z., Fitzgerald, P. (2012). Mirror Neuron Activity Associated with Social Impairments but not Age in Autism Spectrum Disorder. *Biological Psychiatry*, 71(5), 427-433.

Ernst, T., Hennig, J. (1994). Observation of a fast response in functional MR. *Magn. Reson. Med.*, 32(1), 146–149.

Esterman, M., Noonan, S., Rosenberg, M., Deguits, J. (2013). In the Zone or Zoning out? Tracking Behavioral and Neural Fluctuations During Sustained Attention. *Cerebral Cortex,* 23(11), 2712-2723.

Fair, D.A., Cohen, A.L., Dosenbach, N.U., Church, J.A., Miezin, F.M., Barch, D.M., Raichle, M.E., Petersen, S.E., Schlaggar, B.L. (2008). The maturing architecture of the brain's default network. *Proc Natl Acad Sci USA*. 105, 4028—4032.

Fair, D.A., Dosenbach, N.U., Church, J.A., Cohen, A.L., Brahmbhatt, S., Miezin, F.M., Barch, D.M., Raichle, M.E., Petersen, S.E., Schlaggar, B.L. (2007). Development of distinct control networks through segregation and integration. *Proc Natl Acad Sci USA,* 104, 13507–13512.

Fan, L., Li, H., Zhuo, J., Zhang, Y., Wang, J., Chen, L., … Jiang, T. (2016). The Human Brainnetome Atlas: A New Brain Atlas Based on Connectional Architecture. *Cerebral Cortex*, *26*(8), 3508–3526.

Fillard, P., Descoteaux, M., Goh, A., Gouttard, S., Jeurissen, B., Malcolm, J., … Poupon, C. (2011). Quantitative evaluation of 10 tractography algorithms on a realistic diffusion MR phantom. *NeuroImage*, 56(1), 220–34. https://doi.org/10.1016/j.neuroimage.2011.01.032

Fletcher, P. C., Happé, F., Frith, U., Baker, S. C., Dolan, R. J., Frackowiak, R. S. J., Frith, C. D. (1995). Other minds in the brain: A functional imaging study of "theory of mind" in story comprehension. *Cognition*, *57*(2), 109–128. https://doi.org/10.1016/0010-0277(95)00692-R

Fornito, A., Zalesky, A., Pantelis, C., & Bullmore, E. T. (2012). Schizophrenia, neuroimaging and connectomics. *NeuroImage*, 62(4), 2296–314.

Fox, M. D., Snyder, A. Z., Vincent, J. L., Corbetta, M., Van Essen, D. C., & Raichle, M. E. (2005). The human brain is intrinsically organized into dynamic, anticorrelated functional networks. *Proceedings of the National Academy of Sciences of the United States of America*, *102*(27), 9673–9678. https://doi.org/10.1073/pnas.0504136102

Frahm, J., Krüger, G., Merboldt, K.-D., Kleinschmidt, A., (1996). Dynamic uncoupling and recoupling of perfusion and oxidative metabolism during focal activation in man. *Magn. Reson. Med*., 35, 143–148.

Frankenstein, U., Wennerberg, a, Richter, W., Bernstein, C., Morden, D., Remy, F., & McIntyre, M. (2003). Activation and deactivation in blood oxygenation level dependent functional magnetic resonance imaging. *Concepts in Magnetic Resonance Part A*, *16A*(1), 63–70. http://doi.org/Doi 10.1002/Cmr.A.10054

Fransson, P., Kruger, G., Merboldt, K. D., Frahm, J. (1999). MRI of functional deactivation: temporal and spatial characteristics of oxygenation-sensitive responses in human visual cortex. *Neuroimage*, *9*(6 Pt 1), 611–618.

Fried, I., Mukamel, R., Kreiman, G. (2011). Internally Generated Preactivation of Single Neurons in Human Medial Frontal Cortex Predicts Volition. *Neuron*, *69*(3), 548–562. https://doi.org/10.1016/j.neuron.2010.11.045

Fries, P. (2009). Neuronal gamma-band synchronization as a fundamental process in cortical computation. *Annu. Rev. Neurosci*., 32, 209–224.

Fries, P. (2005). A mechanism for cognitive dynamics: neuronal communication through neuronal coherence. *Trends in Cognitive Sciences*, *9*, 474–480. Retrieved from http://linkinghub.elsevier.com/retrieve/pii/S1364661305002421

Friston, K. J., Harrison, L., Penny, W. (2003). Dynamic causal modeling. *Neuroimage,* 19, 1273–1302.

Friston, K., Josephs, O., Turner, R. (1997). Event-Related fMRI. *Human Brain Mapping, 5,* 243-248.

Friston, K.J., Josephs, O., Rees, G., Turner, R. (1998). Non-linear event related responses in fMRI. *Magn. Reson. Med*., 39, 41–52.

Friston, K. J., Price, C. J., Fletcher, P., Moore, C., Frackowiak, R. S., & Dolan, R. J. (1996). The trouble with cognitive subtraction. *NeuroImage*, *4*(2), 97–104. http://doi.org/10.1006/nimg.1996.0033

Friston, K. J. (1994). Functional and Effective Connectivity in Neuroimaging : A Synthesis. *Human Brain Mapping*, 2(1-2), 56-*78*.

Fromm, G., Bond, H. (1967). The relationship between neuron activity and cortical steady potentials. *Electroencephalogr. Clin.Neurophysiol*. 22,159–66.

Fromm, G.H., Bond, H.W. (1964). Slow changes in the electrocorticogram and the activity of cortical neurons. *Electroencephalogr. Clin.Neurophysiol*. 17, 520–23.

Fukunaga, M., Horovitz, S.G., van Gelderen, P., de Zwart, J.A., Jansma, J.M., Ikonomidou, V.N., Chu, R., Deckers, R.H., Leopold, D.A, Duyn, J.H. (2006). Large-amplitude, spatially correlated fluctuations in BOLD fMRI signals during extended rest and early sleep stages. *Magn. Reson.Imaging,* 24, 979–992. doi:10.1016/j.mri.2006.04.018

Gallese, V., Keyser, C., Rizzolatti, G. (2004). A unifying view of the basis of social cognition. *Trends in Cognitive Sciences*, 8(9), 396-403.
Gao, W., Zhu, H., Giovanello, K. S., Smith, J. K., Shen, D., Gilmore, J. H., & Lin, W. (2009). Evidence on the emergence of the brain s default network from 2-week-old to 2-year-old healthy pediatric subjects. *PNAS*, 106(16), 6790-6795.

Gerlach, K. D., Spreng, R. N., Gilmore, A. W., Schacter, D. L. (2011). Solving future problems: Default network and executive activity associated with goal-directed mental simulations. *NeuroImage*, *55*(4), 1816–1824. https://doi.org/10.1016/j.neuroimage.2011.01.030

Ghatan, P. H., Hsieh, J. C.,Wirsen-Meurling, A.,Wredling, R., Eriksson, L., Stone-Elander, S., Levander, S., Ingvar, M. (1995). Brain activation induced by the perceptual maze test: a PET study of cognitive performance. *Neuroimage*, 2(2), 112–24.

Gilbert, D. T., Wilson, T. D. (2007). Prospection: experiencing the future. *Science*, 317, 1351–4.

Glasser, M. F., Sotiropoulos, S. N., Wilson, J. A., Coalson, T. S., Fischl, B., Andersson, J. L., … Jenkinson, M. (2013). The minimal preprocessing pipelines for the Human Connectome Project. *NeuroImage*, *80*, 105–124. https://doi.org/10.1016/j.neuroimage.2013.04.127

Goense, J. B. M., Logothetis, N. K. (2008). Neurophysiology of the BOLD fMRI Signal in Awake Monkeys, *Curr. Biol.*, 18(9), 631–640. https://doi.org/10.1016/j.cub.2008.03.054

Goldman, R. I., Stern, J. M., Engel, J., Cohen, M. S. (2002). Simultaneous EEG and fMRI of the alpha rhythm. *Neuroreport*, *13*(18), 2487–2492. https://doi.org/10.1097/01.wnr.0000047685.08940.d0

Golland, Y., Golland, P., Bentin, S., Malach, R. (2008). Data-driven clustering reveals a fundamental subdivision of the human cortex into two global systems. *Neuropsychologia*. 46, 540–53. https://doi.org/10.1016/j.neuropsychologia.2007.10.003

Gonçalves, Ó. F., Soares, J. M., Carvalho, S., Leite, J., Ganho-Ávila, A., Fernandes-Gonçalves, A., … Sampaio, A. (2017). Patterns of Default Mode Network Deactivation in Obsessive Compulsive Disorder. *Scientific Reports*, *7*(April 2016), 44468. https://doi.org/10.1038/srep44468

Gong, G., He, Y., Concha, L., Lebel, C., Gross, D. W., Evans, A. C., & Beaulieu, C. (2009). Mapping anatomical connectivity patterns of human cerebral cortex using in vivo diffusion tensor imaging tractography. *Cerebral Cortex*, *19*(3), 524–536. http://doi.org/10.1093/cercor/bhn102

Gonzalez-Castillo, J., Saad, Z. S., Handwerker, D. a, Inati, S. J., Brenowitz, N., Bandettini, P. (2012). Whole-brain, time-locked activation with simple tasks revealed using massive averaging and model-free analysis. *Proceedings of the National Academy of Sciences of the United States of America*, 109(14), 5487–5492. https://doi.org/10.1073/pnas.1121049109

Gonzalez-Castillo, J., Hoy, C. W., Handwerker, D. a, Roopchansingh, V., Inati, S. J., Saad, Z. S., … Bandettini, P. (2014). Task Dependence, Tissue Specificity, and Spatial Distribution of Widespread Activations in Large Single-Subject Functional MRI Datasets at 7T. *Cerebral Cortex,* 25(12), 4667-4677.

Goulden, N., Khusnulina, A., Davis, N. J., Bracewell, R. M., Bokde, A. L., Mcnulty, J. P., & Mullins, P. G. (2014). The salience network is responsible for switching between the default mode network and the central executive network : Replication from DCM. *NeuroImage*, *99*, 180–190. https://doi.org/10.1016/j.neuroimage.2014.05.052

Greene, J. D., Sommerville, R. B., Nystrom, L. E., Darley, J. M., Cohen, J. D., & Runyon-walter, D. (2016). An fMRI Investigation of Emotional Engagement in Moral Judgment, *Science*, 293(5537), 2105–2108.

Greene, J., Black, K., Schlagger, B. (2016b). Considerations for MRI study design and implementation in pediatric and clinical populations. *Developmental Cognitive Neuroscience*, 18, 101-112.

Greicius, M. D., Supekar, K., Menon, V., & Dougherty, R. F. (2009). Resting-state functional connectivity reflects structural connectivity in the default mode network. *Cerebral Cortex*, *19*(1), 72–78. https://doi.org/10.1093/cercor/bhn059

Greicius, M.D., Kiviniemi, V., Tervonen, O., Vainionpaa, V., Alahuhta, S., Reiss, A.L., Menon, V. (2008). Persistent default-mode network connectivity during light sedation. *Hum. Brain Mapp*. 29, 839–847.

Greicius, M. D., Menon, V. (2004). Default-Mode Activity during a Passive Sensory Task: Uncoupled from Deactivation but Impacting Activation. *Journal of Cognitive Neuroscience*, *16*(9), 1484–1492. https://doi.org/10.1162/0898929042568532

Greicius, M. D., Krasnow, B., Reiss, A. L., Menon, V. (2003). Functional connectivity in the resting brain: a network analysis of the default mode hypothesis. *Proceedings of the National Academy of Sciences of the United States of America*, *100*(1), 253–258. https://doi.org/10.1073/pnas.0135058100

Greicius, M. D., Srivastava, G., Reiss, A. L., Menon, V. (2004). Default-mode network activity distinguishes Alzheimer's disease from healthy aging: evidence from functional MRI. *Proceedings of the National Academy of Sciences of the United States of America*, *101*(13), 4637–4642. https://doi.org/10.1073/pnas.0308627101

Greve, D.N., Fischl, B., (2009). Accurate and robust brain image alignment using boundary-based registration. *NeuroImage*, 48, 63.

Grubb, R.L., Raichle, M.E., Eichling, J.O., Ter-Pogossian, M.M., (1974). The effects of changes in PaCO2 on cerebral blood volume, blood flow, and vascular mean transit time. *Stroke,* 5, 630–639.

Gusnard, D.A., Akbudak, E., Shulman, G.L., Raichle, M.E. (2001). Medial prefrontal cortex and self-referential mental activity: relation to a default mode of brain function. *PNAS,* 98, 4259–64.

Guyon, I., Weston, J., Barnhill, S., & Vapnik, V. (2002). Gene selection for cancer classification using support vector machines. *Mach. Learn*., 46(1-3), 389-422.

Haber, S. N. (2016). Corticostriatal circuitry. *Dialogues in Clinical Neuroscience*, *18*(1), 7–21.

Haber, S., McFarland, N. R. (2001). The place of the thalamus in frontal cortical-basal ganglia circuits. *Neuroscientist*, *7*(4), 315–324. https://doi.org/10.1177/107385840100700408

Haber, S. N., Kunishio, K., Mizobuchi, M., & Lynd-Balta, E. (1995). The orbital and medial prefrontal circuit through the primate basal ganglia. *The Journal of Neuroscience : The Official Journal of the Society for Neuroscience*, *15*(7 Pt 1), 4851–4867.

Hafkemeijer, A., van der Grond, J., Rombouts, S.A. (2012). Imaging the default mode network in aging and dementia. *Biochim Bio- phys Acta*., 1822(3), 431-41.

Hagmann, P., Sporns, O., Madan, N., Cammoun, L., Pienaar, R., Wedeen, V., Meuli, R., Thiran, J., Grant, P. (2010). White matter maturation reshapes structural connectivity in the late developing human brain. *Proc. Natl. Acad. Sci. U.S.A*., 107, 19067–1907.

Hagmann, P., Cammoun, L., Gigandet, X., Meuli, R., Honey, C. J., Wedeen, V. J., Sporns, O. (2008). Mapping the structural core of human cerebral cortex. *PLoS Biology*, *6*(7), e159. https://doi.org/10.1371/journal.pbio.0060159

Hahn, A., Wadsak, W., Windischberger, C., Baldinger, P., Hö, A. S., & Losak, J. (2012). Differential modulation of the default mode network via serotonin-1A receptors. PNAS, 109(7), 2619-24. https://doi.org/10.1073/pnas.1117104109

Hahn, B., Ross, T. J., Stein, E. A. (2007). Cingulate activation increases dynamically with response speed under stimulus unpredictability. *Cerebral Cortex*, *17*(7), 1664–1671. https://doi.org/10.1093/cercor/bhl075

Hampson, M., Peterson, B., Skudlarski, P., Gatenby, J., Gore, J. (2002). Detection of functional connectivity using temporal correlations in MR images. *Hum Brain Mapp,* 15, 247–262.

Handwerker, D. A., Ollinger, J. M., D'Esposito, M. (2004). Variation of BOLD hemodynamic responses across subjects and brain regions and their effects on statistical analyses. *NeuroImage*, *21*(4), 1639–1651. http://doi.org/10.1016/j.neuroimage.2003.11.029

Hansen, E. C. a., Battaglia, D., Spiegler, A., Deco, G., Jirsa, V. K. (2014). Functional Connectivity Dynamics: Modeling the switching behavior of the resting state. *NeuroImage*, *105*, 525–535. https://doi.org/10.1016/j.neuroimage.2014.11.001

Hansen, J. (1971). Pulsed NMR study of water mobility in muscle and brain tissue. *Biochimica et Biophysica ACTA (BBA) – General Subjects,* 230(3), 482-486.

Hanson, S., Mastrovito, D., Hanson, C., Ramsey, J., Glymour, C. (2016). Scale-free exponents of resting state provide a biomarker for typical and atypical brain activity. *ArXiv*:1605.09282.

Hanson, S. J., & Halchenko, Y. O. (2008). Brain reading using full brain support vector machines for object recognition: there is no "face" identification area. *Neural Computation*, 20(2), 486–503.

Harder, D., Alkayed, N., Lange, A., Gebremedhin, D., Roman, R. (1998). Functional hyperemia in the brain: hypothesis for astrocyte-derived vasodilator metabolites. *Stroke*, 29(1), 229-34.

Harrison, B. J., Pujol, J., Contreras-Rodríguez, O., Soriano-Mas, C., López-Solà, M., Deus, J., … Menchón, J. M. (2011). Task-Induced deactivation from rest extends beyond the default mode brain network. *PLoS ONE*, *6*(7). https://doi.org/10.1371/journal.pone.0022964

Harrison, B. J., Yücel, M., Pujol, J., & Pantelis, C. (2007). Task-induced deactivation of midline cortical regions in schizophrenia assessed with fMRI. *Schizophrenia Research*, *91*(1–3), 82–86. https://doi.org/10.1016/j.schres.2006.12.027

He, B. J. (2013). Spontaneous and Task-Evoked Brain Activity Negatively Interact. *Journal of Neuroscience*, *33*(11), 4672–4682. http://doi.org/10.1523/JNEUROSCI.2922-12.2013

He, B. J., Snyder, A. Z., Zempel, J. M., Smyth, M. D., & Raichle, M. E. (2008). Electrophysiological correlates of the brain's intrinsic large-scale functional architecture. *Proceedings of the National Academy of Sciences of the United States of America*, *105*(41), 16039–44.

He, B. J., & Raichle, M. E. (2009). The fMRI signal, slow cortical potential and consciousness. *Trends in Cognitive Sciences*, *13*(7), 302–309. https://doi.org/10.1016/j.tics.2009.04.004

Hoge, R., Atkinson, J., Gill, B., Crelier, G., & Marrett, S. (1999). Investigation of BOLD signal dependence on cerebral blood flow and oxygen consumption: the deoxyhemoglobin dilution model. *Magnetic Resonance in Medicine*, 863, 849–863. https://doi.org/10.1002/(SICI)1522-2594(199911)42:5<849::AID-MRM4>3.0.CO;2-Z

Honey, C.J., Sporns, O., Cammoun, L., Gigandet, X., Thiran, J.P., Meuli, R., Hagmann, P. (2009). Predicting human resting-state functional connectivity from structural connectivity. *Proc Natl Acad Sci USA,* 106(6), 2035–2040.

Horn, A., Ostwald, D., Reisert, M., & Blankenburg, F. (2014). The structural-functional connectome and the default mode network of the human brain. *NeuroImage*, 102(P1), 142–151. http://doi.org/10.1016/j.neuroimage.2013.09.069

Horovitz, S. G., Braun, A. R., Carr, W. S., Picchioni, D., Balkin, T. J., Fukunaga, M., & Duyn, J. H. (2009). Decoupling of the brain's default mode network during deep sleep. *Proceedings of the National Academy of Sciences of the United States of America*, 106(27), 11376–11381. https://doi.org/10.1073/pnas.0901435106

Hoyle, R.H. (1995) (ed.). Structural equation modeling: concepts, issues and applications. Newbury Park, CA: Sage.

Hu, X., Le, T.H., Ugurbil, K., (1997). Evaluation of the early response in fMRI in individual subjects using short stimulus duration. *Magn. Reson. Med*., 37, 877–884.

Hutchison, R. M., Hashemi, N., Gati, J. S., Menon, R. S., & Everling, S. (2015). Electrophysiological signatures of spontaneous BOLD fluctuations in macaque prefrontal cortex. *NeuroImage*, *113*, 257–267. http://doi.org/10.1016/j.neuroimage.2015.03.062

Hutchison, R. M., Womelsdorf, T., Allen, E. a, Bandettini, P. a, Calhoun, V. D., Corbetta, M., … Chang, C. (2013a). Dynamic functional connectivity: promise, issues, and interpretations. *NeuroImage*, 80, 360–378. https://doi.org/10.1016/j.neuroimage.2013.05.079

Hutchison, R. M., Womelsdorf, T., Gati, J. S., Everling, S., & Menon, R. S. (2013b). Resting-state networks show dynamic functional connectivity in awake humans and anesthetized macaques. *Human Brain Mapping*, 34(9), 2154–2177. https://doi.org/10.1002/hbm.22058

Hutchison RM, Everling S. (2012). Monkey in the middle: why non- human primates are needed to bridge the gap in resting-state investigations. *Front Neuroanat*. 6, 29.

Hutchison, R. M., Leung, L. S., Mirsattari, S. M., Gati, J. S., Menon, R. S., & Everling, S. (2011). Resting-state networks in the macaque at 7T. *NeuroImage*, *56*(3), 1546–1555. https://doi.org/10.1016/j.neuroimage.2011.02.063

Huttenlocher, P. R. & Dabholkar, A. S. in Development of the Prefrontal Cortex: Evolution, Neurobiology, and Behavior (eds Krasnegor, N. A., Lyon, G. R. & Goldman-Rakic, P. S.) 69–84 (Paul. H. Brookes, Baltimore, 1997).

Hyder, F., Rothman, D.L., Shulman, R.G. (2002). Total neuroenergetics support localized brain activity: implications for the interpretation of fMRI. *Proc. Natl. Acad. Sci. USA,* 99, 10771–76.

Jbabdi, S., Lehman, J. F., Haber, S. N., & Behrens, T. E. (2013). Human and Monkey Ventral Prefrontal Fibers Use the Same Organizational Principles to Reach Their Targets: Tracing versus Tractography. *Journal of Neuroscience*, *33*(7), 3190–3201. https://doi.org/10.1523/JNEUROSCI.2457-12.2013

Jbabdi, S., Sotiropoulos, S. N., Savio, A. M., Graña, M., & Behrens, T. E. J. (2012). Model-based analysis of multishell diffusion MR data for tractography: how to get over fitting problems. *Magnetic Resonance in Medicine*, *68*(6), 1846–1855. https://doi.org/10.1002/mrm.24204

Jenkinson, M., Bannister, P., Brady, J. M. & Smith, S. M. (2002). Improved Optimisation for the Robust and Accurate Linear Registration and Motion Correction of Brain Images. *NeuroImage*, 17(2), 825-841.

Jenkinson, M., & Smith. M. (2001). A global optimization method for robust affine registration of brain images. *Medical Image Analysis*, 5(2), 143-156.

Jesper L. R. Andersson and Stamatios N. Sotiropoulos. (2106). An integrated approach to correction for off-resonance effects and subject movement in diffusion MR imaging. NeuroImage, 125, 1063-1078.

Joel, D., & Weiner, I. (1994). The organization of the basal ganglia-thalamocortical circuits: Open interconnected rather than closed segregated. *Neuroscience*, *63*(2), 363–379. https://doi.org/10.1016/0306-4522(94)90536-3

Jin, X., & Costa, R. M. (2015). Shaping action sequences in basal ganglia circuits. *Current Opinion in Neurobiology*, *33*, 188–196. https://doi.org/10.1016/j.conb.2015.06.011

Johnson, M. H. (2001). Functional brain development in humans. *Nature Reviews Neuroscience*, *2*(7), 475–483. https://doi.org/10.1038/35081509

Jovicich, J., Czanner, S., Greve, D., Haley, E., van der Kouwe, A., Gollub, R., Kennedy, D., Schmitt, F., Brown, G., MacFall, J. (2006). Reliability in multi-site structural MRI stud- ies: effects of gradient non-linearity correction on phantom and human data. *NeuroImage*, 30, 436-443.

Just, M.A., Cherkassky, V.L., Keller, T.A., Kana, R.K., Minshew, N.J. (2007). Functional and anatomical cortical underconnectivity in autism: Evidence from an fMRI study of an executive function task and corpus callosum morphometry. *Cereb Cortex*, 17, 951–961.

Kambeitz, J., Kambeitz-Ilankovic, L., Leucht, S., Wood, S., Davatzikos, C., Malchow, B., Falkai, P., Koutsouleris, N. (2015). Detecting Neuroimaging Biomarker for Schizophrenia: A Meta-Analysis of Multivariate Pattern Recognition Studies. *Neuropchopharmacology*, 40(7), 1742-1751.

Kastrup, A., Kruger, G., Neumann-Haefelin, T., Glover, G.H., Moseley, M.E., (2002). Changes of cerebral blood flow, oxygenation, and oxidative metabolism during graded motor activation. *NeuroImage,* 15, 74–82.

Kelly, C., Uddin, L.Q., Shehzad, Z., Margulies, D.S., Castellanos, F.X., Milham, M.P., Petrides, M. (2010). Broca's region: Linking human brain functional connectivity data and non-human primate tracing anatomy studies. *Eur J Neurosci,* 32, 383–398.

Kelly, A. M. C., Uddin, L. Q., Biswal, B. B., Castellanos, F. X., & Milham, M. P. (2008). Competition between functional brain networks mediates behavioral variability. *NeuroImage*, *39*, 527–537. https://doi.org/10.1016/j.neuroimage.2007.08.008

Kelley, W. M., Macrae, C. N., Wyland, C. L., Caglar, S., Inati, S., & Heatherton, T. F. (2002). Finding the self? An event-related fMRI study. *J. Cogn. Neurosci*., 14, 785– 94.

Kenworthy, L., Yerys, B., Gutermuth Anthony, L., Wallace, G. (2008). Understanding executive control in autism spectrum disorders in the lab and in the real world. *Neuropsychological Rev*, 18(4), 320-338.

Keuken, M. C., & Forstmann, B. U. (2015). A probabilistic atlas of the basal ganglia using 7 T MRI. *Data in Brief*, *4*, 577–582. http://doi.org/10.1016/j.dib.2015.07.028

King, M. D., Houseman, J., Roussel, S. A., Van Bruggen, N., Williams, S. R., & Gadian, D. G. (1994). q- Space imaging of the brain. *Magnetic Resonance in Medicine*, *32*(6), 707–713. https://doi.org/10.1002/mrm.1910320605

Kiviniemi, V.J., Haanpaa, H., et al., (2005). Midazolarn sedation increases fluctuation and synchrony of the resting brain BOLD signal. *Magn. Reson. Imaging,* 23 (4), 531–537.

Koch, G., Bozzali, M., Bonnì, S., Giacobbe, V., Caltagirone, C., & Cercignani, M. (2012). fMRI Resting Slow Fluctuations Correlate with the Activity of Fast Cortico-Cortical Physiological Connections. *PLoS ONE*, *7*(12), 1–8. https://doi.org/10.1371/journal.pone.0052660

Kolvin I. (1971). Studies in the childhood psychoses. I. Diagnostic criteria and classification. *British Journal of Psychiatry*, 118, 381–384.

Konstantareas, M., Hewitt T. (2001). Individuals with autism met DSM-IV diagnostic criteria for schizophrenia disorganized type. Autistic disorder and schizophrenia: diagnostic overlaps. *J Autism Dev Disord*., 31(1), 19-28.

Krantz, D.H., Luce, R.D., Suppes, P., Tversky, A. (1971). Foundations of measurement (Vol. 1). San Diego: Academic Press.

Kruger, G., Kleinschmidt, A., Frahm, J., (1996). Dynamic MRI sensitized to cerebral blood oxygenation and flow during sustained activation of human visual cortex. *Magn. Reson. Med.,* 35, 797–800.

Laird, A. R., Eickhoff, S. B., Li, K., Robin, D. A., Glahn, D. C., Fox, P. T. (2009). Investigating the Functional Heterogeneity of the Default Mode Network Using Coordinate-Based Meta-Analytic Modeling. *J. Neurosci*., *29*(46), 14496–14505. https://doi.org/10.1523/JNEUROSCI.4004-09.2009

Lanius, R. A., Bluhm, R. L., Coupland, N. J., Hegadoren, K. M., Rowe, B. , Théberge, J. , Neufeld, R. W., Williamson, P. C. and Brimson, M. (2010). Default mode network connectivity as a predictor of post- traumatic stress disorder symptom severity in acutely traumatized subjects. *Acta Psychiatrica Scandinavica*, 121, 33-40. doi:10.1111/j.1600-0447.2009.01391.x

Larson-Prior, L.J., Zempel, J.M., Nolan, T.S., Prior, F.W., Snyder, A.Z., Raichle, M.E. (2009). Cortical network functional connectivity in the descent to sleep. *Proc. Natl Acad. Sci. USA,* 106, 4489–4494.

Lauritzen, M. (2005). Reading vascular changes in brain imaging: is dendritic calcium the key? N*at. Rev. Neurosci*., 6, 77–85.

Lauritzen, M., Gold, L. (2003). Brain function and neurophysiological correlates of signals used in functional neuroimaging. *J. Neurosci.,* 23,3972–80.

Lauritzen, M. (2001). Relationship of spikes, synaptic activity, and local changes of cerebral blood flow. *J. Cereb. Blood Flow Metab*. 21, 1367–83.

Lee, J. H., Durand, R., Gradinaru, V., Zhang, F., Goshen, I., Kim, D.-S., … Deisseroth, K. (2010). Global and local fMRI signals driven by neurons defined optogenetically by type and wiring. *Nature*, *465*(7299), 788–92. http://doi.org/10.1038/nature09108

Lee, M., Hacker, C., Snyder, A., et al., (2012). Clustering of resting state networks. PLoS One, 7, e40370.

Leech, R., Braga, R., & Sharp, D. J. (2012). Echoes of the brain within the posterior cingulate cortex. *The Journal of Neuroscience : The Official Journal of the Society for Neuroscience*, *32*(1), 215–222. https://doi.org/10.1523/JNEUROSCI.3689-11.2012

Leech, R., Kamourieh, S., Beckmann, C. F., & Sharp, D. J. (2011). Fractionating the default mode network: distinct contributions of the ventral and dorsal posterior cingulate cortex to cognitive control. *The Journal of Neuroscience : The Official Journal of the Society for Neuroscience*, *31*(9), 3217–3224.

Leichnetz, G. R. (2001). Connections of the medial posterior parietal cortex (area 7m) in the monkey. *Anatomical Record*, *263*(2), 215–236. https://doi.org/10.1002/ar.1082

Leopold, D. a, Murayama, Y., & Logothetis, N. K. (2003). Very slow activity fluctuations in monkey visual cortex: implications for functional brain imaging. *Cerebral Cortex (New York, N.Y. : 1991)*, *13*(4), 422–433. Retrieved from http://www.ncbi.nlm.nih.gov/pubmed/12631571

Lewis, C.M., Baldassarre, A., Committeri, G., Romani, G.L., Corbetta, M. (2009). Learning sculpts the spontaneous activity of the resting human brain. *Proc Natl Acad Sci USA,* 106,17558–17563.

Liang, X., Zou, Q., He, Y., & Yang, Y. (2016). Topologically Reorganized Connectivity Architecture of Default-Mode, Executive-Control, and Salience Networks across Working Memory Task Loads. *Cerebral Cortex*, 26(4), 1501–1511.

Liddle, E. B., Hollis, C., Batty, M. J., Groom, M. J., Totman, J. J., Liotti, M., … Liddle, P. F. (2011). Task-related default mode network modulation and inhibitory control in ADHD: Effects of motivation and methylphenidate. *Journal of Child Psychology and Psychiatry and Allied Disciplines*, *52*(7), 761–771. https://doi.org/10.1111/j.1469-7610.2010.02333.x

Lindquist, M., Loh, J., Atlas, L., Wagner, T. (2009). Modeling the Hemodynamics Response Function in fMRI: Efficiency, Bias and Mis-modeling. *NeuroImage*, *45*, S187–S198.

Liu, X., Yanagawa, T., Leopold, D. a, Fujii, N., & Duyn, J. H. (2015). Robust Long-Range Coordination of Spontaneous Neural Activity in Waking, Sleep and Anesthesia. *Cerebral Cortex*, 25(9), 2929-38. https://doi.org/10.1093/cercor/bhu089

Liu, C.-H., Ma, X., Li, F., Wang, Y.-J., Tie, C.-L., Li, S.-F., … Wang, C.-Y. (2012). Regional Homogeneity within the Default Mode Network in Bipolar Depression: A Resting-State Functional Magnetic Resonance Imaging Study. *PLOS ONE*, *7*(11), e48181. Retrieved from https://doi.org/10.1371/journal.pone.0048181

Liu, Y., Shen, H., Zhou, Z., & Hu, D. (2011). Sustained negative BOLD response in human fMRI finger tapping task. *PLoS ONE*, *6*(8), 1–7. https://doi.org/10.1371/journal.pone.0023839

Logothetis, N. K., Pauls, J., Augath, M., Trinath, T., & Oeltermann, A. (2001). Neurophysiological investigation of the basis of the fMRI signal. *Nature*, *412*, 150–157.

Logothetis, N. K. (2002). The neural basis of the blood-oxygen-level-dependent functional magnetic resonance imaging signal. *Philosophical Transactions of the Royal Society of London. Series B, Biological Sciences*, *357*(1424), 1003–37. http://doi.org/10.1098/rstb.2002.1114

Lorente de N´ o R. (1947). Action potentials of the motor neurones of the hypoglossus nucleus. *J. Cell Comp. Physiol*., 29, 207– 88.

Lord, C., Risi, S., Lambrecht, L., Cook, E. H., Jr, Leventhal, B. L., DiLavore, P. C., Pickles, A., Rutter M. (2000). The autism diagnostic observation schedule–generic: A standard measure of social and communication deficits associated with the spectrum of autism. *Journal of Autism and Developmental Disorders*, 30, 205–223.

Lorenzi, M., Beltramello, A., Mercuri, N.B., Canu, E., Zoccatelli, G., Pizzini, F.B., et al., (2011). Effect of memantine on resting state default mode network activity in Alzheimer's disease. *Drugs Aging,* 28(3), 205-17.

Lowe, M., Mock, B., Sorenson, J. (1998). Functional connectivity in single and multislice echoplanar imaging using resting-state fluctuations. *Neuroimage,* 7, 119–132.

Lu, H., Zou, Q., Gu, H., Raichle, M.E., Stein, E.A., Yang, Y. (2012). Rat brains also have a default mode network. *Proc. Natl Acad. Sci. USA*, 109, 3979–3984. (doi:10. 1073/pnas.1200506109)

Luczak, A., Bartho´, P., Harris, K.D. (2009). Spontaneous events outline the realm of possible sensory responses in neocortical populations. *Neuron,* 62, 413– 425.

Magaud. E., Kebir, O., Gut, A., Willard, D., Chauchot, F., Olie, J., Kazes, M., & Krebs, M. (2010). Altered semantic but not phonological verbal fluency in young help-seeking individuals with ultra high risk of psychosis. *Schizophr Res*., 123(1), 53-8.

Mahy, C. E. V., Moses, L. J., Pfeifer, J. H. (2014). How and where: Theory-of-mind in the brain. *Developmental Cognitive Neuroscience*, *9*, 68–81. https://doi.org/10.1016/j.dcn.2014.01.002

Mandeville, J.B., Marota, J.J.A., Ayata, C., Zaharchuk, G., Moskowitz, M.A., Rosen, B.R., Weisskoff, R.M. (1999). Evidence of a cerebrovascular post-arteriole Windkessel with delayed compliance. *J. Cereb. Blood Flow Metab*., 19, 679–689.

Mantini, D., Gerits, A., Nelissen, K., Durand, J.-B., Joly, O., Simone, L., … Vanduffel, W. (2011). Default Mode of Brain Function in Monkeys. *Journal of Neuroscience*, *31*(36), 12954–12962. https://doi.org/10.1523/JNEUROSCI.2318-11.2011

Margulies, D.S., Vincent, J.L., Kelly, C., Lohmann, G., Uddin, L.Q., Biswal, B.B., Villringer, A., Castellanos, F.X., Milham, M.P., Petrides, M. (2009). Precuneus shares intrinsic functional architecture in humans and monkeys. *Proc Natl Acad Sci USA,* 106, 20069–20074.

Marrett, S., Gjedde, A. (1997). Changes of blood flow and oxygen consumption in visual cortex of living humans. *Adv Exp Med Biol*, 413, 205–208.

Mastrovito, D., Hanson, C., & Hanson, S. J. (2018). Differences in atypical resting-state effective connectivity distinguish autism from schizophrenia. *NeuroImage: Clinical*, 18(February), 367–376. http://doi.org/10.1016/j.nicl.2018.01.014

Mastrovito, D. (2013). Interactions between Resting-State and Task-Evoked Brain Activity Suggest a Different Approach to fMRI Analysis. *J. Neuroscience*, 33(32), 12912-1214.

Maus, B., van Breukelen, G.J., Goebel, R., Berger, M.P. (2012). Optimal design for nonlinear estimation of the hemodynamic response function. *Human Brain Mapp*., 33, 1253–1267.

Mayberg, H., Lozano A.,Voon, V.,McNeely, H., Seminowicz, D., Hamani C., et al., (2005). Deep brain stimulation for treatment-resistant depression. *Neuron,* 45, 651–660.

Mazoyer, B., Zago, L., Mellet, E., Bricogne, S., Etard, O., et al., (2001), Cortical networks for working memory and executive functions sustain the conscious resting state in man. *Brain Res Bull,* 54, 287–298.
Mazziotta, J., Toga, A., Evans, A., Fox, P., Lancaster, J. (1995). A Probabilistic Atlas of the Human Brain: Theory and Rationale for Its Development, *NeuroImage*, 2, 89-101.

McCarthy, S., Gillis, J., Kramar, M, Lihm, J., Yoon, S. , Berstein, Y., Mistry M., Pavlidis, P., Solomon, R., Ghiban, E., Antoniou, E., et al., (2014). De novo mutations in schizophrenia implicate chromatin remodeling and support a genetic overlap with autism and intellectual disability. *Molecular Psychiatry*, 19, 652-658.

McRobbie, D., Moore, E., Graves, M., & Prince, M. (2017). Seeing is Believing: Introduction to Image Contrast. *MRI from Picture to Proton*. Cambridge: Cambridge University Press.

Mechelli, A., Henson, R. N. A., Price, C. J., & Friston, K. J. (2003). Comparing event-related and epoch analysis in blocked design fMRI. *NeuroImage*, *18*(3), 806–810. https://doi.org/10.1016/S1053-8119(02)00027-7

Mega, S., & Cummings, L. (1994). Frontal-subcortical circuits and neuropsychiatric disorders. *The Journal of Neuropsychiatry and Clinical Neurosciences*, *6*(4), 358–370. https://doi.org/10.1176/jnp.6.4.358

Mehta, U., Thirthalli, J., Basavaraju, R., Gangadhar, B., & Pascual-Leone, A. (2013). Reduced Mirror Neuron Activity in Schizophrenia and Its Association With Theory of Mind Deficits: Evidence From a Transcranial Magnetic Stimulation Study. *Schizophrenia Bulletin*, 40(5), 1083-1094.

Meier, J., Tewarie, P., Hillebrand, A., Douw, L., van Dijk, B. W., Stufflebeam, S. M., Van Mieghem, P. (2016). A Mapping Between Structural and Functional Brain Networks. *Brain Connectivity*, *6*(4), 298–311. http://doi.org/10.1089/brain.2015.0408

Mennes, M., Kelly, C., Zuo, X., Di Martino A., Biswal, B., Castellanos, F., Milham, M. (2010). Inter- individual differences in resting-state functional connectivity predict task-induced BOLD activity. *Neuroimage,* 50, 1690–1701.

Menon, V. (2011). Large-scale brain networks and psychopathology : a unifying triple network model. *Trends in Cognitive Sciences*, *15*(10), 483–506. https://doi.org/10.1016/j.tics.2011.08.003

Menon, V., Uddin, L. Q. (2010). Saliency, switching, attention and control: a network model of insula function. *Brain Structure & Function*, *214*(5–6), 655–667. https://doi.org/10.1007/s00429-010-0262-0.Saliency

Menon, R.S., Ogawa, S., Strupp, J.P., Anderson, P., Ugurbil, K. (1995). BOLD based functional MRI at 4 tesla includes a capillary bed contribution: echo-planar imaging correlates with previous optical imaging using intrinsic signals. *Magn. Reson. Med*., 33, 453–459.

Messé, A., Rudrauf, D., Benali, H., & Marrelec, G. (2014). Relating Structure and Function in the Human Brain: Relative Contributions of Anatomy, Stationary Dynamics, and Non-stationarities. *PLoS Computational Biology*, *10*(3). http://doi.org/10.1371/journal.pcbi.1003530

Mesulam, M. M. (2000). Principles of Behavioral and Cognitive Neurology.New York:Oxford University Press.

Mesulam, M. M., Van Hoesen, G. W., Pandya, D. N., & Geschwind, N. (1977). Limbic and sensory connections of the inferior parietal lobule (area PG) in the rhesus monkey: A study with a new method for horseradish peroxidase histochemistry. *Brain Research*, *136*(3), 393–414. https://doi.org/10.1016/0006-8993(77)90066-X

Metzger, C. D., Van der Werf, Y. D., & Walter, M. (2013). Functional mapping of thalamic nuclei and their integration into cortico-striatal-thalamo-cortical loops via ultra-high resolution imaging-from animal anatomy to in vivo imaging in humans. *Frontiers in Neuroscience*, *7*(7 MAY), 1–14. https://doi.org/10.3389/fnins.2013.00024

Miezin, F. M., Maccotta, L., Ollinger, J. M., Petersen, S. E., & Buckner, R. L. (2000). Characterizing the hemodynamic response: Effects of presentation rate, sampling procedure, and the possibility of ordering brain activity based on relative timing. *NeuroImage*, *11*(6 I), 735–759. http://doi.org/10.1006/nimg.2000.0568

Minzengerg, M., Yoon, J., Carter, C. S. (2011). Modafinil modulation of the default mode network. *Psychopharmacology*, 215(1), 23–31. https://doi.org/10.1007/s00213-010-2111-5

Mishra, A. M., Ellens, D. J., Schridde, U., Motelow, J. E., Purcaro, M. J., DeSalvo, M. N., … Blumenfeld, H. (2011). Where fMRI and Electrophysiology Agree to Disagree: Corticothalamic and Striatal Activity Patterns in the WAG/Rij Rat. *Journal of Neuroscience*, *31*(42), 15053–15064. http://doi.org/10.1523/JNEUROSCI.0101-11.2011

Mitchell, J. P., Macrae, C.N., Banaji, M. R. (2006). Dissociable medial prefrontal contributions to judgments of similar and dissimilar others. *Neuron*, 50, 655–63.

Möhring, N., Shen, C., Hahn, E., Ta, T., Dettling, M., Neuhaus, A. (2015). Mirror neuron deficit in schizophrenia: Evidence from repetition suppression. *Schizophrenia Res.*, 168(1-2), 174-9.

Mori, S., Crain, B. J., Chacko, V. P., van Zijl, P. C. (1999). Three-dimensional tracking of axonal projections in the brain by magnetic resonance imaging. *Annals of Neurology*, *45*(2), 265–269.

Morrison, R., Bellack, A., & Mueser, K. (1998). Deficits in facial-affect recognition and schizophrenia. *Schizophr Bull.*, 14(1), 67-83.

Nagai, Y., Critchley, H. D., Featherstone, E., Fenwick, P. B. C., Trimble, M. R., & Dolan, R. J. (2004). Brain activity relating to the contingent negative variation: an fMRI investigation. *NeuroImage*, *21*(4), 1232–1241. https://doi.org/10.1016/j.neuroimage.2003.10.036

Nagy, Z., Westerberg, H., Klingberg, T. (2004). Maturation of White Matter is Associated with the Development of Cognitive Functions during Childhood. *Journal of Cognitive Neuroscience*, *16*(7), 1227–1233. http://doi.org/10.1162/0898929041920441

Nakahara, K., Adachi, Y., Osada, T., Miyashita, Y. (2007). Exploring the neural basis of cognition: multi- modal links between human fMRI and macaque neurophysiology. *Trends Cogn. Sci*. 11, 84–92.

Nielsen, J. a, Zielinski, B. a, Fletcher, P. T., Alexander, A. L., Lange, N., Bigler, E. D., … Anderson, J. S. (2013). Multisite functional connectivity MRI classification of autism: ABIDE results. *Frontiers in Human Neuroscience*, *7*(September), 599. http://doi.org/10.3389/fnhum.2013.00599

Niendam, T. A., Laird, A. R., Ray, K. L., Dean, Y. M., Glahn, D. C., Carter, C. S. (2012). Meta-analytic evidence for a superordinate cognitive control network subserving diverse executive functions. *Cognitive, Affective and Behavioral Neuroscience*, 12(2), 241–268. https://doi.org/10.3758/s13415-011-0083-5

Niendorf T, Dijkhuizen RM, Norris DG, van Lookeren Campagne M, Nicolay K. (1996). Biexponential diffusion attenuation in various states of brain tissue: implications for diffusion-weighted imaging. *Magn Reson Med*,. 36, 847–857.

Niessing, J., Ebisch, B., Schmidt, K., Niessing, M., Singer, W., Galuske, R. (2005). Hemodynamic Signals Correlate Tightly with Synchronized Gamma Oscillations. *Science*, 309(5736), 948–951. https://doi.org/10.1126/science.1115233

Nijhuis, E. H. J., van Cappellen van Walsum, A. M., Norris, D. G. (2013). Topographic Hub Maps of the Human Structural Neocortical Network. *PLoS ONE*, 8(6).

Nir, Y. et al., (2008) Interhemispheric correlations of slow spontaneous neuronal fluctuations revealed in human sensory cortex. *Nat.Neurosci.* 11, 1100–1108.

Nir, Y., Fisch, L., Mukamel, R., Gelbard-Sagiv, H., Arieli, A., Fried, I., & Malach, R. (2007). Coupling between neuronal firing rate, gamma LFP, and BOLD fMRI is related to interneuronal correlations. *Current Biology : CB*, *17*(15), 1275–85. http://doi.org/10.1016/j.cub.2007.06.066

Northoff, G., Qin, P., Nakao, T. (2010). Rest-stimulus interaction in the brain: a review. *Trends in Neurosciences*, *33*(6), 277–284. https://doi.org/10.1016/j.tins.2010.02.006

Oberman, L., Pineda, J., Ramachandran, V. (2007). The human mirror neuron system: A link between action observation and social skills. *Soc Cogn Affect Neurosci.*, 2(1), 62-66.

Oberman, L., Hubbard, E.,McCleery, J., Altschuler, E., Ramachandran, V., & Pineda, J. (2005). EEG evidence for mirror neuron dysfunction in autism spectrum disorders. *Cognitive Brain Research*, 24(2), 190-198.

Okuda, J., Fujii, T., Ohtake, H., Tsukiura, T., Tanji, K., Suzuki, K., … Yamadori, A. (2003). Thinking of the future and past: The roles of the frontal pole and the medial temporal lobes. *NeuroImage*, *19*(4), 1369–1380. https://doi.org/10.1016/S1053-8119(03)00179-4

Olesen, P. J., Nagy, Z., Westerberg, H., & Klingberg, T. (2003). Combined analysis of DTI and fMRI data reveals a joint maturation of white and grey matter in a fronto-parietal network. *Cognitive Brain Research*, *18*(1), 48–57. http://doi.org/10.1016/j.cogbrainres.2003.09.003

Ongür, D., Price, J. L. (2000). The organization of networks within the orbital and medial prefrontal cortex of rats, monkeys and humans. *Cerebral Cortex*, *10*(3), 206–219. http://doi.org/10.1093/cercor/10.3.206

Orellana, G., Slachevsky, A. (2013). Executive Functioning in Schizophrenia. *Frontiers in Psychiatry*, 4, 35.

Palaniyappan, L., Liddle, P. F. (2012). Does the salience network play a cardinal role in psychosis? An emerging hypothesis of insular dysfunction. *Journal of Psychiatry & Neuroscience*, 37, 17–27.

Pandya, D. N., Seltzer, B. (1982). Intrinsic connections and architectonics of posterior parietal cortex in the rhesus monkey. *J Comp Neurol*, *204*(2), 196–210. https://doi.org/10.1002/cne.902040208

Pandya, D., Van Hoesen, G., Mesulam, M. (1981). Efferent Connections of the Cingulate Gyrus in the Rhesus Monkey. *Experimental Brain Research*, *42*, 319–330.

Parvizi, J., Van Hoesen, G. W., Buckwalter, J., & Damasio, A. (2006). Neural connections of the posteromedial cortex in the macaque. *PNAS*, *103*(5), 1563–1568. https://doi.org/10.1073/pnas.0507729103

Pearl, J. (2000). Causality: Models, Reasoning, and Inference.New York,NY: Cambridge University Press.

Pellerin, L., Magistretti, L. (2004). Neuroenergetics: Calling Upon Astrocytes to Satisfy Hungry Neurons. *The Neuroscientist*, 10(1),53-62.

Persico, A., Bourgeron, T. (2006). Searching for ways out of the autism maze: genetic, epigenetic and environmental clues. *TRENDS in Neurosciences*, 29(7), 349-358.

Petrides, M., Pandya, D. N. (2007). Efferent association pathways from the rostral prefrontal cortex in the macaque monkey. *The Journal of Neuroscience : The Official Journal of the Society for Neuroscience*, *27*(43), 11573–86. http://doi.org/10.1523/JNEUROSCI.2419-07.2007

Petrides,M., Pandya, D. N. (1999). Dorsolateral prefrontal cortex: comparative cytoarchitectonic analysis in the human and the macaque brain and corticocortical connection patterns. *Eur. J. Neurosci.*, 11, 1011–1036.

Petrides, M., Pandya, D. (1984). Projections to the frontal lobe from the posterior-parietal region in the rhesus monkey. *The Journal of Comparative Neurology*, *228*, 105–116.

Pfefferbaum, A., Chanraud, S., Pitel, A. L., Muller-Oehring, E., Shankaranarayanan, A., Alsop, D. C., … Sullivan, E. V. (2011). Cerebral blood flow in posterior cortical nodes of the default mode network decreases with task engagement but remains higher than in most brain regions. *Cerebral Cortex*, *21*(1), 233–244. http://doi.org/10.1093/cercor/bhq090

Pilowsky, T., Yirmiya, N., Arbelle, S., Mozes, T. (2000). Theory of mind abilities of children with schizophrenia, children with autism, and normally developing children. *Schizophr Res.*, 42(2), 145-55.

Plitt, M., Barnes, K. A., & Martin, A. (2015). Functional connectivity classification of autism identifies highly predictive brain features but falls short of biomarker standards. *NeuroImage: Clinical*, 7, 359–366.

Plum, E, Posner, J. B., Troy, B. (1968). Cerebral metabolic and circulatory responses to induced convulsions in animals. *Archives of Neurology*, 18, 1-13.

Popa, D., Popescu, A.T., Pare, D. (2009). Contrasting activity profile of two distributed cortical networks as a function of attentional demands. *J. Neurosci.,* 29, 1191–201.

Posner, J., Cha, J., Wang, Z., Talati, A., Warner, V., Gerber, A., … Weissman, M. (2016). Increased Default Mode Network Connectivity in Individuals at High Familial Risk for Depression. *Neuropsychopharmacology*, *41*(7), 1759–1767. https://doi.org/10.1038/npp.2015.342

Posner, J. B., Plum, E, Van Poznak, A. (1969). Cerebral metabolism during electrically induced seizures in man. *Archives of Neurology*, 20, 388-395.

Power, J. D., Barnes, K. A., Snyder, A. Z., Schlaggar, B. L., Petersen, S. E. (2012). Spurious but systematic correlations in functional connectivity MRI networks arise from subject motion. *NeuroImage*, *59*(3), 2142–2154. http://doi.org/10.1016/j.neuroimage.2011.10.018

Power, J. D., Cohen, A. L., Nelson, S. M., Wig, G. S., Barnes, K. A., Church, J., … Petersen, S. E. (2011). Functional network organization of the human brain. *Neuron*, *72*(4), 665–78.

Price, J. L., Drevets, W. C. (2009). Neurocircuitry of Mood Disorders. *Neuropsychopharmacology*, *35*(1), 192–216. http://doi.org/10.1038/npp.2009.104

Pulvermüller F., Lutzenberger, W., Preil, H., Birbaumer, N. (1995) Spectral responses in the gamma-band: physiological signs of higher cognitive processes? *NeuroReport*, 6, 2059-2064.

Raichle, M. E., Mintun, M. A. (2006). Brain Work and Brain Imaging. *Annual Review of Neuroscience*, *29*(1), 449–476.http://doi.org/10.1146/annurev.neuro.29.051605.112819

Raichle, M. E. (2015). The Brain ' s Default Mode Network. *Annual Review of Neuroscience*, *38*, 433–447. https://doi.org/10.1146/annurev-neuro-071013-014030

Ramsey, J. D., Hanson, S. J., Glymour, C. (2011). Multi-subject search correctly identifies causal connections and most causal directions in the DCM models of the Smith et al., simulation study. *NeuroImage*, *58*(3), 838–48.

Reivich, M. (1964). Arterial Pco_2 and cerebral hemodynamics. *American Journal of Physiology*, 206, 25-35.

Reveley, C., Seth, A. K., Pierpaoli, C., Silva, A. C., Yu, D., Saunders, R. C., … Ye, F. Q. (2015). Superficial white matter fiber systems impede detection of long-range cortical connections in diffusion MR tractography. *Proceedings of the National Academy of Sciences*, *112*(21), E2820–E2828. https://doi.org/10.1073/pnas.1418198112

Richiardi, J., & Altmann, A. (2015). Correlated gene expression supports synchronous activity in brain networks. *Science*, *348*(6240), 11–14. https://doi.org/10.1126/science.1255905

Rilling, J. K., Sanfey, A. G., Aronson, J. A., Nystrom, L. E., Cohen, J. D. (2004). The neural correlates of theory of mind within interpersonal interactions. *NeuroImage*, *22*(4), 1694–1703. https://doi.org/10.1016/j.neuroimage.2004.04.015

Ripley, B. D. (1996). Pattern Recognition and Neural Networks. Cambridge University Press.

Rizzolatti, G. Fadiga, L., Gallese, V., Fogassi, L. (1996). Premotor cortex and the recognition of motor actions. *Cognitive Brain Research*, 3(2), 131-141.

Roberto, A. J., Mohan, A., Jones, K., Carney, M. J., Liogier-weyback, L., Hwang, S., … Link, C. (2016). The Significance of the Default Mode Network (DMN) in Neurological and Neuropsychiatric Disorders : A Review. *Yale Journal of Biology and Medicine*, *89*, 49–57.

Rodriguez, E., George, N., Lachaux, J.-P., Martinerie, J., Renault, B., & Varela, F. J. (1999). Perception's shadow : long- distance synchronization of human brain activity. *Nature*, 397(February), 430–433. https://doi.org/10.1038/17120

Rokem, A., Yeatman, J. D., Pestilli, F., Kay, K. N., Mezer, A., van der Walt, S., Wandell, B. (2015). Evaluating the accuracy of diffusion MRI models in white matter. *PloS One*, *10*(4), e0123272. http://doi.org/10.1371/journal.pone.0123272

Roth, T., Lubin, F., Sodhi, M., Kleinman, J. (2009). Epigenetic mechanisms in schizophrenia. *Biochimica et Biophysica Acta*, 1790, 869-877.

Rutter M. (1972). Childhood schizophrenia reconsidered. Journal of Autism and Childhood *Schizophrenia*, 2, 315–337.

Sämann, P. G., Wehrle, R., Hoehn, D., Spoormaker, V. I., Peters, H., Tully, C., … Czisch, M. (2011). Development of the brain's default mode network from wakefulness to slow wave sleep. *Cerebral Cortex*, *21*(9), 2082–2093. https://doi.org/10.1093/cercor/bhq295

Sämann,PG, Tully C, Spoormaker VI, Wetter TC, Holsboer F, Wehrle R, Czisch M. (2010). Increased sleep pressure reduces resting state functional connectivity. *MAGMA,* 23, 375—389.

Sala-Llonch, R., Peña-Gómez, C., Arenaza-Urquijo, E. M., Vidal-Piñeiro, D., Bargalló, N., Junqué, C., & Bartrés-Faz, D. (2012). Brain connectivity during resting state and subsequent working memory task predicts behavioural performance. *Cortex; a Journal Devoted to the Study of the Nervous System and Behavior*, 48(9), 1187–1196. https://doi.org/10.1016/j.cortex.2011.07.006

Salomon, R., Levy, D. R., & Malach, R. (2014). Deconstructing the default: Cortical subdivision of the default mode/intrinsic system during self-related processing. *Human Brain Mapping*, *35*(4), 1491–1502. https://doi.org/10.1002/hbm.22268

Sasson, N., Pinkham, A., Carpenter, K., Belger, A. (2011). The benefit of directly comparing autism and schizophrenia for revealing mechanisms of social cognitive impairment. *J Neurodevelopment Disord.*, 3, 87–100.

Scheeringa, R., Mazaheri, A., Bojak, I., Norris, D.G., Kleinschmidt, A. (2011). Modulation of visually evoked cortical FMRI responses by phase of ongoing occipital alpha oscillations. *J Neurosci,* 31,3813–3820.

Scheeringa, R., Fries, P., Petersson, K. M., Oostenveld, R., Grothe, I., Norris, D. G., … Bastiaansen, M. C. M. (2011). Neuronal Dynamics Underlying High and Low-Frequency EEG Oscillations Contribute Independently to the Human BOLD Signal. *Neuron*, *69*(3), 572–583. http://doi.org/10.1016/j.neuron.2010.11.044

Scheltens, P., Barkhof, F., Valk, J., Algra, P., van der Hoop, R., Nauta, J., Wolters, E. (1992). White Matter Lesions on Magnetic Resonance Imaging in Clinically Diagnosed Alzheimer'S Disease: Evidence for Heterogeneity. *Brain*, *115*(3), 735–748. http://doi.org/10.1093/brain/115.3.735

Schultz, R. T. (2005). Developmental deficits in social perception in autism: The role of the amygdala and fusiform face area. *International Journal of Developmental Neuroscience*, 23(2–3 SPEC. ISS.), 125–141.

Scoville, W. B. Milner, B. (1957). Loss of recent memory after bilateral hippocampal lesions. *J. Neurol. Neurosurg. Psychiatry,* 20, 11–21.

Segall, J. M., Allen, E. A., Jung, R. E., Erhardt, E. B., Arja, S. K., Kiehl, K., Calhoun, V. D. (2012). Correspondence between structure and function in the human brain at rest. *Frontiers in Neuroinformatics*, *6*(March), 1–17. https://doi.org/10.3389/fninf.2012.00010

Seitz,, R.J., Roland, P.E., (1992).Vibratory stimulation increases and decreases the regional cerebral blood flow and oxidative metabolism: a positron emission tomography (PET) study. *Acta Neurol. Scand*. 86, 60–67.

Selemon, L. D., Goldman-Rakic, P. S. (1985). Longitudinal topography and interdigitation of cortico-striatal projections in the rhesus monkey. *J. Neurosci*. 5, 776—94.

Semendeferi, K., Armstrong, E., Schleicher, A., Zilles, K., & Van Hoesen, G. W. (2001). Prefrontal cortex in humans, apes and monkey: A Comparative Study of area 10. *American Journal of Physical Anthropology*, *114*, 1224–241.

Shannon, B.J., Dosenbach, R.A., Su, Y., Vlassenko, A.G., Larson-Prior, L.J., et al., (2013). Morning-evening variation in human brain metabolism and memory circuits. *J. Neurophysiol*. ,109,1444–56.

Shehzad, Z., Kelly, A. M. C., Reiss, P. T., Gee, D. G., Gotimer, K., Uddin, L. Q., … Milham, M. P. (2009). The resting brain: Unconstrained yet reliable. *Cerebral Cortex*,

19(10), 2209–2229. http://doi.org/10.1093/cercor/bhn256

Sheline, Y. I., Barch, D. M., Price, J. L., Rundle, M. M., Vaishnavi, S. N., Snyder, A. Z., … Raichle, M. E. (2009). The default mode network and self-referential processes in depression. *Proceedings of the National Academy of Sciences*, *106*(6), 1942–1947.

Shen, H., Wang, L., Liu, Y., Hu, D. (2010). Discriminative analysis of resting-state functional connectivity patterns of schizophrenia using low dimensional embedding of fMRI. *NeuroImage*, 49(4), 3110–3121.

Sherman, L. E., Rudie, J. D., Pfeifer, J. H., Masten, C. L., McNealy, K., & Dapretto, M. (2014). Development of the Default Mode and Central Executive Networks across early adolescence: A longitudinal study. *Developmental Cognitive Neuroscience*, *10*, 148–159. https://doi.org/10.1016/j.dcn.2014.08.002

Sherman, S. (2001). Vision: From Neurons to Cognition Chapter 4 Thalamic relay functions. *Progress in Brain Research*, *134*, 51–69. https://doi.org/https://doi.org/10.1016/S0079-6123(01)34005-0

Shirer, W. R., Ryali, S., Rykhlevskaia, E., Menon, V., & Greicius, M. D. (2012). Decoding subject-driven cognitive states with whole-brain connectivity patterns. *Cerebral Cortex*, *22*(1), 158–65. http://doi.org/10.1093/cercor/bhr099

Shmuel, A., Augath, M., Oeltermann, A., & Logothetis, N. K. (2006). Negative functional MRI response correlates with decreases in neuronal activity in monkey visual area V1. Nature Neuroscience, 9(4), 569–577. https://doi.org/10.1038/nn1675

Shulman RG, Rothman DL, Behar KL, Hyder F. (2004). Energetic basis of brain activity: Implications for neuroimaging. *Trends in Neuroscience*s, 27, 489–95.

Shulman, R.G., Hyder, F., Rothman, D.L. (2001). Cerebral energetics and the glycogen shunt: neurochemical basis of functional imaging. *Proc Natl Acad Sci U S A.,* 98(11):6417–22.

Shulman, G. L., Corbetta, M., Buckner, R. L., Fiez, J. a, Miezin, F. M., Raichle, M. E., Petersen, S. E. (1997a). Common Blood Flow Changes across Visual Tasks: I. Increases in Subcortical Structures and Cerebellum but Not in Nonvisual Cortex. *Journal of Cognitive Neuroscience*, 9(5), 624–647. https://doi.org/10.1162/jocn.1997.9.5.624

Shulman, G. L., Fiez, J. A., Corbetta, M., Buckner, R. L., Miezin, F. M., Raichle, M. E., Petersen, S. E. (1997b). Common Blood Flow Changes across Visual Tasks : II . Decreases in Cerebral Cortex. *Journal of Cog*, 9(5), 648–663.

Sidtis, J. J., Strother, S. C., Anderson, J. R., & Rottenberg, D. (1999). Are brain functions really additive? *NeuroImage*, 9(5), 490–6. http://doi.org/10.1006/nimg.1999.0423

Siegel, M., Buschman, T. J., Miller, E. K. (2015). Cortical information flow during flexible sensorimotor decisions. *Science*, 348(6241), 1352–1356.

Singe,r W. (2001). Consciousness and the binding problem. *Ann NY Acad Sci,* 929,123–146.

Simpson, J. R., Drevets, W. C., Snyder, A. Z., Gusnard, D. A., & Raichle, M. E. (2001). Emotion-induced changes in human medial prefrontal cortex: II. During anticipatory anxiety. *Proceedings of the National Academy of Sciences of the United States of America*, *98*(2), 688–693. https://doi.org/10.1073/pnas.98.2.688

Smith, S. M., Miller, K. L., Moeller, S., Xu, J., Auerbach, E. J., Woolrich, M. W., … Ugurbil, K. (2012). Temporally-independent functional modes of spontaneous brain activity. *Proceedings of the National Academy of Sciences of the United States of America*, 109(8), 3131–6. http://doi.org/10.1073/pnas.1121329109

Smith, R., Keramatian, K., Christoff, K. (2007). Localizing the rostrolateral prefrontal cortex at the individual level. *NeuroImage* 36, 1387–1396.

Smith, S., Jenkinson, M., Woolrich, M., Beckmann, C., Behrens, T., Johansen-Berg, H., Bannister, P., De Luca, M., Drobnjak, I., Flitney, D., Niazy, R., Saunders, J., Vickers, J., Zhang, Y., De Stefano, N., Brady, J., Matthews, P. (2004) Advances in functional and structural MR image analysis and implementation as FSL. *NeuroImage*, 23(S1):208-219.

Smith, A.J., Blumenfeld, H., Behar, K.L., Rothman, D.L., Shulman, R.G., Hyder, F. (2002a). Cerebral energetics and spiking frequency: The neurophysiological basis of fMRI. *Proc. Natl. Acad. Sci. USA,* 99, 10765–70.

Smith, S. (2002b). Fast robust automated brain extraction. *Human Brain Mapping*, 17(3),

143-15.

Sokoloff, L., Mangold, R., Wechsler, R.L., Kenney, C,, Kety, S.S. (1955). The effect of mental arithmetic on cerebral circulation and metabolism. *J. Clin. Invest*. 34, 1101–1108. (doi:10.1172/JCI103159)

Solomon, M., Olsen, E., Niendam, T., Ragland, J., Yoon J., Minzenberg M., & Carter C. (2011). From lumping to splitting and back again: atypical social and language development in individuals with clinical-high-risk for psychosis, first episode schizophrenia, and autism spectrum disorders. *Schizophr Res.*, 131(1-3), 146-51.

Sotiropoulos, S. N., Jbabdi, S., Xu, J., Andersson, J. L., Moeller, S., Auerbach, E. J., … Behrens, T. E. J. (2013). Advances in diffusion MRI acquisition and processing in the Human Connectome Project. *NeuroImage*, *80*, 125–43. http://doi.org/10.1016/j.neuroimage.2013.05.057

Sowell, E. R., Thompson, P. M., Leonard, C. M.,Welcome, S. E., Kan, E. & Toga, A.W. 2004 Longitudinal mapping of cortical thickness and brain growth in normal children. J. Neurosci. 24, 8223–8231. (doi:10.1523/JNEUROSCI. 1798-04.2004)

Spirtes, P., Glymour, C., Scheines, R. (2000). Causation, Prediction and Search. Cambridge, MA. MIT Press.

Spreng, R. N., Stevens, W. D., Chamberlain, J. P., Gilmore, A. W., Schacter, D. L. (2010). Default network activity, coupled with the frontoparietal control network, supports goal-directed cognition. *NeuroImage*, *53*(1), 303–317. https://doi.org/10.1016/j.neuroimage.2010.06.016

Spreng, R. N., Mar, R. A., Kim, A. (2009). The Common Neural Basis of Autobiographical Memory, Prospection, Navigation, Theory of Mind, and the Default Mode: A Quantitative Meta-analysis. *Journal of Cognitive Neuroscience*, *21*(3), 489–510. https://doi.org/10.1162/jocn.2008.21029

Sridharan, D., Levitin, D. J., Menon, V. (2008). A critical role for the right fronto-insular cortex in switching between central-executive and default-mode networks. *Networks*, *105*(34), 12569–12574. https://doi.org/10.1073/pnas.0800005105

Stafford, J.M., Jarrett, B.R., Mirnada-Dominguez, O., Mills, B.D, Cain, N., Mihala, S., Lahvis, G.P., Lattal, K. M, Mitchell, S, H., David, S.V, Fryer, J.D, Nigg, J.T, Fair, D.A. (2014) Large-scale topology and the default mode network in the mouse connectome.

Proc. Natl Acad. Sci. USA, 111, 18745–18750. (doi:10.1073/pnas.1404346111)

Stevenson, J. L., Kellett, K. A. (2010). Can magnetic resonance imaging aid diagnosis of the autism spectrum? *J Neuroscience*, 30(50), 16763–16765.

Sun, L., Cao, Q., Long, X., Sui, M., Cao, X., Zhu, C., … Wang, Y. (2012). Abnormal functional connectivity between the anterior cingulate and the default mode network in drug-naïve boys with attention deficit hyperactivity disorder. *Psychiatry Research - Neuroimaging*, *201*(2), 120–127. https://doi.org/10.1016/j.pscychresns.2011.07.001

Supekar, K., Musen, M., Menon, V. (2009). Development of large-scale functional brain networks in children. *PLoS Biology*, *7*(7). https://doi.org/10.1371/journal.pbio.1000157

Szpunar, K. K., Watson, J. M., McDermott, K. B. (2007). Neural substrates of envisioning the future. *Proc.Natl. Acad. Sci. U.S.A*., 104, 642–7.

Tatti, R., Haley, M. S., Swanson, O. K., Tselha, T., & Maffei, A. (2017). Neurophysiology and Regulation of the Balance Between Excitation and Inhibition in Neocortical Circuits. *Biological Psychiatry*, *81*(10), 821–831. https://doi.org/10.1016/j.biopsych.2016.09.017

Tekin, S., Cummings, J. L. (2002). Frontal-subcortical neuronal circuits and clinical neuropsychiatry: An update. *Journal of Psychosomatic Research*, *53*(2), 647–654. http://doi.org/10.1016/S0022-3999(02)00428-2

Titone D., Ditman T., Holzman P., Eichenbaum H., Levy D. (2004). Transitive inference in schizophrenia: impairments in relational memory organization. *Schizophr Res.*, 68(2-3), 235-47.

Tu, P., Lee, Y., Chen, Y., Li, C., Su, T. (2013). Schizophrenia and the brain's control network: aberrant within-and between-network connectivity of the frontoparietal network in schizophrenia. *Schizophrenia Research*, 147(2-3), 339-47.

Ugurbil, K., Xu, J., Auerbach, E. J., Vi, A., Van de Moortele, P. F., Strupp, J., … Yacoub, E. (2013). Pushing spatial and temporal resolution for functional and diffusion MRI in the Human Connectome Project. *NeuroImage*, *80*, 80–104.

https://doi.org/10.1016/j.neuroimage.2013.05.012

Uddin, L. Q., Supekar, K. S., Ryali, S., & Menon, V. (2011). Dynamic Reconfiguration of Structural and Functional Connectivity Across Core Neurocognitive Brain Networks with Development. *Journal of Neuroscience*, *31*(50), 18578–18589. https://doi.org/10.1523/JNEUROSCI.4465-11.2011

Uddin, L. Q., Kelly, a M., Biswal, B. B., Xavier Castellanos, F., & Milham, M. P. (2009). Functional connectivity of default mode network components: correlation, anticorrelation, and causality. *Human Brain Mapping*, *30*(2), 625–637. https://doi.org/10.1002/hbm.20531

Uludag, K., Dubowitz, D.J., Yoder, E.J., Restom, K., Liu, T.T., Buxton, R.B. (2004). Coupling of cerebral blood flow and oxygen consumption during physiological activation and deactivation measured with fMRI. *NeuroImage,* 23, 148–155.

Upadhyay, J., Baker, S. J., Chandran, P., Miller, L., Lee, Y., Marek, G. J., … Day, M. (2011). Default-Mode-Like Network Activation in Awake Rodents. *PLoS ONE*, *6*(11), e27839. https://doi.org/10.1371/journal.pone.0027839

van den Heuvel, M. P., & Sporns, O. (2013). Network hubs in the human brain. *Trends in Cognitive Sciences*, 17(12), 683–696.

Van Eimeren, T., Monchi, O., Ballanger, B., & Strafella, A. P. (2009). Dysfunction of the Default Mode Network in Parkinson Disease: A Functional Magnetic Resonance Imaging Study. *Archives of Neurology*, *66*(7), 877–883. http://doi.org/10.1001/archneurol.2009.97

Vatansever, D., Menon, D. K., Manktelow, A. E., Sahakian, B. J., & Stamatakis, E. A. (2015). Default mode network connectivity during task execution. *NeuroImage*, *122*, 96–104. https://doi.org/10.1016/j.neuroimage.2015.07.053

Venables, W. N, Ripley, B. D. (2002). Modern Applied Statistics with S. Fourth edition. Springer.

Venkataraman, A., Whitford, T., Westin, C., Golland, P., & Kubicki, M. (2012). Whole brain resting state functional connectivity abnormalities in schizophrenia. *Schizophrenia Research*, 139, 7-12.

Verstynen, T. D. (2014). The organization and dynamics of corticostriatal pathways link

the medial orbitofrontal cortex to future behavioral responses. *Journal of Neurophysiology*, *112*(10), 2457–2469. https://doi.org/10.1152/jn.00221.2014

Vincent, J.L., Patel, G.H., Fox, M.D., Snyder, A.Z., Baker, J.T., Van Essen, D.C., Zempel, J.M., Snyder, L.H., Corbetta, M., Raichle, M.E. (2007). Intrinsic functional architecture in the anaesthetized monkey brain. *Nature,* 447, 83–86.
Vincent, J. L., Snyder, A. Z., Fox, M. D., Shannon, B. J., Andrews, J. R., Raichle, M. E., & Buckner, R. L. (2006). Coherent Spontaneous Activity Identifies a Hippocampal-Parietal Memory Network. *Journal of Neurophysiology*, *96*(6), 3517–3531. https://doi.org/10.1152/jn.00048.2006

Vincent, J.L., Patel, G.H., Fox, M.D. Synder, A.Z, Baker, J.T., van Essen, D.C., Zempel, J.M., Snyder, L.H., Corbetta, M., Raichle, M.E. (2007). Intrinsic functional architecture in the anaesthetized monkey brain. *Nature,* 447, 83–86. (doi:10.1038/ nature05758)

Vogt, B. a, Vogt, L., Laureys, S. (2006). Cytology and Functionally Correlated Circuits of Human Posterior Cingulate Areas. *Neuroimage*, *29*(2), 452–466. https://doi.org/10.1016/j.neuroimage.2005.07.048.Cytology

Vogt, B. A., Pandya, D. N. (1987). Cingulate cortex of the rhesus monkey: II. Cortical afferents. *J Comp Neurol*, *262*(2), 271–289. https://doi.org/10.1002/cne.902620208

Vogt, B. A., Pandya, D. N., Rosene, D. L. (1987). Cingulate cortex of the rhesus monkey: I. Cytoarchitecture and thalamic afferents. *Journal of Comparative Neurology*, *262*(2), 256–270. https://doi.org/10.1002/cne.902620207

Vogt, B., Rosene, D., Pandya, D. (1979). Thalamic and Cortical Afferents Differentiate Anterior from Posterior Cingulate Cortex in the Monkey. *Science*, *204*(4389), 205–207.

Volkmar, F (2005). Handbook of autism and pervasive developmental disorders. Hoboken, NJ: John Wiley & Sons.

von Bonin, G. (1950). Essay on the cerebral cortex. Springfield, IL: Charles C. Thomas.

Von Economo, C. (1929). The cytoarchitectonics of the human cerebral cortex. Oxford University Press, London.

Von Economo, C., Koskinas, G. N. (1925). Die Cytoarchitecktonik der Grosshirnrinde des erwachsenen Menschen. J. Springer, Berlin.

Walker, A.E. (1940). A cytoarchitectural study of the prefrontal area of the macaque monkey. J. Comp. Neurol. 73:59-86.

Wall, N. R., Parra, M. D. La, Callaway, E. M., Kreitzer, A. C. (2013). Differential Innervation of Direct- and Indirect-Pathway Striatal Projection Neurons. *Neuron*, *79*(2), 347–360. https://doi.org/10.1016/j.neuron.2013.05.014

Wallace, G., Case, L., Harms, M., Silvers, J., Kenworthy, L., Martin, A. (2011). D**i**minished sensitivity to sad facial expressions in high functioning autism spectrum disorders is associated with symptomatology and adaptive functioning. *J Autism Dev Disord*., 41(11), 475-86.

Wang, K., Liang, M., Wang, L., Tian, L., Zhang, X., Li, K., Jiang, T. (2007a). Altered functional connectivity in early Alzheimer's disease: A resting-state fMRI study. *Human Brain Mapping*, *28*(10), 967–978. https://doi.org/10.1002/hbm.20324

Wang, R., Benner, T., Sorensen, A., Wedeen, V. (2007b). Diffusion Toolkit: A Software Package for Diffusion Imaging Data Processing and Tractograpy. *Proc. Intl. Soc. Mag. Reson. Med*., 15 3720. TrackVis.org

Wang,Y., Zhong,S., Jia, Y., Sun,Y., Wang, B.,Liu,T., Pan, J., Huang, L. (2016). Disrupted Resting-State Functional Connectivity in Nonmedicated Bipolar Disorder. *Radiology*, 280(2), 529-536.

Washington, S. D., Gordon, E. M., Brar, J. , Warburton, S. , Sawyer, A. T., Wolfe, A. , Mease- Ference, E. R., Girton, L. , Hailu, A. , Mbwana, J. , Gaillard, W. D., Kalbfleisch, M. L. and VanMeter, J. W. (2014), Dysmaturation of the default mode network in autism. *Hum. Brain Mapp.*, 35, 1284-1296.

Wedeen, V. J., Wang, R. P., Schmahmann, J. D., Benner, T., Tseng, W. Y. I., Dai, G., … de Crespigny, A. J. (2008). Diffusion spectrum magnetic resonance imaging (DSI) tractography of crossing fibers. *NeuroImage*, *41*(4), 1267–1277. http://doi.org/10.1016/j.neuroimage.2008.03.036

Wedeen, V. J., Hagmann, P., Tseng, W. Y. I., Reese, T. G., Weisskoff, R. M. (2005). Mapping complex tissue architecture with diffusion spectrum magnetic resonance imaging. *Magnetic Resonance in Medicine*, *54*(6), 1377–1386.

http://doi.org/10.1002/mrm.20642

Weiner, J. (1997). The connections of the primate subthalamic nucleus: indirect pathways and the open-inter- connected scheme of basal ganglia-thalamocortical circuitry. *Brain Research Reviews,* 23, 62–78.

Weiner, J. (1994). The organization of the basal ganglia- thalamocortical circuits: open interconnected rather than closed segregated. *Neuroscience,* 63, 363–379.

Wernicke, C. (1874). Der Aphasische Symptomencomplex Cohn and Weigert, Breslau.

Weissman, D. H., Roberts, K. C., Visscher, K. M., Woldorff, M. G. (2006). The neural bases of momentary lapses in attention. *Nature Neuroscience*, *9*(7), 971–978. https://doi.org/10.1038/nn1727

Wey, H.-Y., Phillips, K. A., McKay, D. R., Laird, A. R., Kochunov, P., Davis, M. D., … Fox, P. T. (2014). Multi-region hemispheric specialization differentiates human from nonhuman primate brain function. *Brain Structure and Function*, *219*(6), 2187–2194. https://doi.org/10.1007/s00429-013-0620-9

Wheatley, T., Milleville, S. C., & Martin, A. (2007). Distinct Roles for the Social Network and Mirror System. *Psychological Science*, *18*(6), 469–474. https://doi.org/10.1111/j.1467-9280.2007.01923.x

Wolff, J. J., Gu, H., Gerig, G., Elison, J. T., Styner, M., Gouttard, S., … Piven, J. (2012). Differences in White Matter Fiber Tract Development Present From 6 to 24 Months in Infants with Autism. *American Journal of Psychiatry*, *169*(16), 589–600. http://doi.org/10.1176/appi.ajp.2011.11091447

Woolrich, M. W., Behrens, T. E. J., Beckmann, C. F., Smith, S. M. (2005). Mixture models with adaptive spatial regularization for segmentation with an application to FMRI data. *Medical Imaging, IEEE Transactions on*, *24*(1), 1–11. http://doi.org/10.1109/TMI.2004.836545(410) 24

Worsley, K.J., Evans, A.C., Marrett, S., Neelin, P. (1992). A three- dimensional statistical analysis for CBF activation studies in human brain. *J. Cereb. Blood Flow Metab*., 12, 900–918.

Xia, M., Wang, J., He, Y. (2013). BrainNet Viewer: A Network Visualization Tool for Human Brain Connectomics. *PLOS ONE,* 8(7), e68910. https://doi.org/10.1371/journal.pone.0068910

Yahata, N., Morimoto, J., Hashimoto, R., Lisi, G., Shibata, K., Kawakubo, Y., Kuwabara, H., Kuroda, M., Yamada, T., Megumi, F., Imamizu, H., Nanez, J., Takahashi, H., Okamoto, Y., Kasai, K., Kato, N., Sasaki, Y., Watanabe, T., Kawata, M. (2016). A small number of abnormal brain connections predicts adult autism spectrum disorder. *Nature Communications*, 7, 11254.

Yeh, F. C., Verstynen, T. D., Wang, Y., Fernández-Miranda, J. C., Tseng, W. Y. I. (2013). Deterministic diffusion fiber tracking improved by quantitative anisotropy. *PLoS ONE*, *8*(11), 1–16. https://doi.org/10.1371/journal.pone.0080713

Yeo, B.T., Krienen, F.M., Sepulcre, J., Sabuncu, M.R., Lashkari, D., Hollinshead, M., Roffman, J.L., Smoller, J.W., Zollei, L., Polimeni, J.R., Fischl, B., Liu, H., Buckner, R.L. (2011). The organization of the human cerebral cortex estimated by intrinsic functional connectivity. *J. Neurophysiol.,* 106, 1125–1165.

Yeterian, E. H., Pandya, D. N. (1985). Corticothalamic connections of the posterior parietal cortex in the rhesus monkey. *The Journal of Comparative Neurology*, *237*(3), 408–426. https://doi.org/10.1002/cne.902370309

Yeterian, E. H., VanHoesen, G. W. (1978). Cortico-striate projections in the rhesus monkey : The organization of certain cortico-caudate connections. *Brain Res*. 139, 43-63.

Yin, H., Liu, Y., Li, M., Hu, D. (2011). Hemodynamic observation and spike recording explain the neuronal deactivation origin of negative response in rat. *Brain Research Bulletin*, 84(2), 157–162. https://doi.org/10.1016/j.brainresbull.2010.12.004

Yizhar, O., Fenno, L. E., Prigge, M., Schneider, F., Davidson, T. J., Ogshea, D. J., … Deisseroth, K. (2011). Neocortical excitation/inhibition balance in information processing and social dysfunction. *Nature*, 477(7363), 171–178. https://doi.org/10.1038/nature10360

Yu, C., Zhou, Y., Liu, Y., Jiang, T., Dong, H., Zhang, Y., Walter, M. (2011). Functional

segregation of the human cingulate cortex is confirmed by functional connectivity based neuroanatomical parcellation. *NeuroImage*, *54*(4), 2571–2581. https://doi.org/10.1016/j.neuroimage.2010.11.018

Zhang, J., Wei, L., Hu, X., Xie, B., Zhang, Y., Wu, G. R., Wang, J. (2015). Akinetic-rigid and tremor-dominant Parkinson's disease patients show different patterns of intrinsic brain activity. *Parkinsonism and Related Disorders*, *21*(1), 23–30. https://doi.org/10.1016/j.parkreldis.2014.10.017

Zhong, X., Shi, H., Ming, Q., Dong, D., Zhang, X., Zeng, L., Yaou, S. (2017). Whole-brain resting-state functional connectivity identified major depressive disorder: A multivariate pattern analysis in two independent samples. *J Affect Disord.,* 15(218), 346-352.

Zou, Q., Wu, C. W., Stein, E. A., Zang, Y., & Yang, Y. (2009). Static and dynamic characteristics of cerebral blood flow during the resting state. *NeuroImage*, *48*(3), 515–524. http://doi.org/10.1016/j.neuroimage.2009.07.006

Appendix A

Table A1. Regions of Interest

Gyrus	ROI	Description	Left MNI	Right MNI
Superior Frontal	A8m	medial area 8	-5 ,15, 54	7, 16, 54
	A8dl	dorsolateral area 8	-18, 24, 53	22, 26, 51
	A9l	lateral area 9	-11, 49, 40	13, 48, 40
	A6dl	dorsolateral area 6	-18, -1, 65	20, 4, 64
	A6m	medial area 6	-6, -5, 58	7, -4, 60
	A9m	medial area 9	-5, 36, 38	6, 38, 35
	A10m	medial area 10	-8, 56, 15	8, 58, 13
Middle Frontal	A9/46d	dorsal area 9/46	-27, 43, 31	30, 37, 36
	IFJ	inferior frontal junction	-42, 13, 36	42, 11, 39
	A46	area 46	-28, 56, 12	28, 55, 17
	A9/46v	ventral area 9/46	-41, 41, 16	42, 44, 14
	A8vl	ventrolateral area 8	-33, 23, 45	42, 27, 39
	A6vl	ventrolateral area 6	-32, 4, 55	34, 8, 54
	A10l	lateral area10	-26, 60, -6	25, 61, -4
Inferior Frontal	A44d	dorsal area 44	-46, 13, 24	45, 16, 25
	IFS	inferior frontal sulcus	-47, 32, 14	48, 35, 13
	A45c	caudal area 45	-53, 23, 11	54, 24, 12
	A45r	rostral area 45	-49, 36, -3	51, 36, -1
	A44op	opercular area 44	-39, 23, 4	42, 22, 3
	A44v	ventral area 44	-52, 13, 6	54, 14, 11
Orbital	A14m	medial area 14	-7, 54, -7	6, 47, -7
	A12/47o	orbital area 12/47	-36, 33, -16	40, 39, -14
	A11l	lateral area 11	-23, 38, -18	23, 36, -18
	A11m	medial area 11	-6, 52, -19	6, 57, -16
	A13	area 13	-10, 18, -19	9, 20, -19
	A12/47l	lateral area 12/47	-41, 32, -9	42, 31, -9
Precentral	A4hf	area 4(head and face region)	-49, -8, 39	55, -2, 33
	A6cdl	caudal dorsolateral area 6	-32, -9, 58	33, -7, 57
	A4ul	area 4(upper limb region)	-26, -25, 63	34, -19, 59
	A4t	area 4(trunk region)	-13, -20, 73	15, -22, 71
	A4tl	area 4(tongue and larynx region)	-52, 0, 8	54, 4, 9
	A6cvl	caudal ventrolateral area 6	-49, 5, 30	51, 7, 30
Paracentral Lobule	A1/2/3ll	area1/2/3 (lower limb region)	-8, -38, 58	10, -34, 54
	A4ll	Area 4 lower limb	-4, -23, 61	5, -21, 61
Superior Temporal	A38m	medial area 38	-32, 14, -34	31, 15, -34
	A41/42	area 41/42	-54, -32, 12	54, -24, 11
	TE1.0 TE1.2		-50, -11, 1	51, -4, -1
	A22c	caudal area 22	-62, -33, 7	66, -20, 6
	A38l	lateral area 38	-45, 11, -20	47, 12, -20
	A22r	rostral area 22	-55, -3, -10	56, -12, -5
Middle Temporal	A21c	caudal area 21	-65, -30, -12	65, -29, -13
	A21r	rostral area 21	-53, 2, -30	51, 6, -32
	A37dl	dorsolateral area37	-59, -58, 4	60, -53, 3
	aSTS	anterior superior temporal sulcus	-58, -20, -9	58, -16, -10
Inferior Temporal	A20iv	intermediate ventral area 20	-45, -26, -27	46, -14, -33
	A37elv	extreme lateroventral area37	-51, -57, -15	53, -52, -18
	A20r	rostral area 20	-43, -2, -41	40, 0, -43
	A20il	intermediate lateral area 20	-56, -16, -28	55, -11, -32
	A37vl	ventrolateral area 37	-55, -60, -6	54, -57, -8
	A20cl	caudolateral of area 20	-59, -42, -16	61, -40, -17
	A20cv	caudoventral of area 20	-55, -31, -27	54, -31, -26

Fusiform	A20rv	rostroventral area 20	-33, -16, -32	33, -15, -34
	A37mv	medioventral area37	-31, -64, -14	31, -62, -14
	A37lv	lateroventral area37	-42, -51, -17	43, -49, -19
Para-hippocampal posterior	A35/36r	rostral area 35/36	-27, -7, -34	28, -8, -33
	A35/36c	caudal area 35/36	-25, -25, -26	26, -23, -27
	TL	area TL lateral posterior parahippocampal gyrus	-28, -32, -18	30, -30, -18
	A28/34	area 28/34 entorhinal cortex	-19, -12, -30	19, -10, -30
	TI	TI(temporal agranular insular cortex)	-23, 2, -32	22, 1, -36
	TH	area TH (medial PPHC)	-17, -39, -10	19, -36, -11
Superior Temporal	rpSTS	rostroposterior superior temporal sulcus	-54, -40, 4	53, -37, 3
	cpSTS	caudoposterior superior temporal sulcus	-52, -50, 11	57, -40, 12
Sulcus Superior Parietal Lobule	A7r	rostral area 7	-16, -60, 63	19, -57, 65
	A7c	caudal area 7	-15, -71, 52	19, -69, 54
	A5l	lateral area 5	-33, -47, 50	35, -42, 54
	A7pc	postcentral area 7	-22, -47, 65	23, -43, 67
	A7ip	intraparietal area 7(hIP3)	-27, -59, 54	31, -54, 53
Inferior Parietal Lobule	A39c	caudal area 39(PGp)	-34, -80, 29	45, -71, 20
	A39rd	rostrodorsal area 39(Hip3)	-38, -61, 46	39, -65, 44
	A40rd	rostrodorsal area 40(PFt)	-51, -33, 42	47, -35, 45
	A40c	caudal area 40(PFm)	-56, -49, 38	57, -44, 38
	A39rv	rostroventral area 39(PGa)	-47, -65, 26	53, -54, 25
	A40rv	rostroventral area 40(PFop)	-53, -31, 23	55, -26, 26
Precuneus	A7m	medial area 7(PEp)	-5, -63, 51	6, -65, 51
	A5m	medial area 5(PEm)	-8, -47, 57	7, -47, 58
	dmPOS	dorsomedial parietooccipital sulcus(PEr)	-12, -67, 25	16, -64, 25
	A31	area 31 (Lc1)	-6, -55, 34	6, -54, 35
Postcentral	A1/2/3ulhf	area 1/2/3(upper limb head and face	-50, -16, 34	50, -14, 44
	A1/2/3tonla	area 1/2/3(tongue and larynx region)	-56, -14, 16	56, -10, 15
	A2	area 2	-46, -30, 50	48, -24, 48
	A1/2/3tru	area1/2/3(trunk region)	-21, -35, 68	20, -33, 69
Insular	G	hypergranular insula	-36, -20, 10	37, -18, 8
	vla	ventral agranular insula	-32, 14, -13	33, 14, -13
	dla	dorsal agranular insula	-34, 18, 1	36, 18, 1
	vld/vlg	ventral dysgranular and granular insula	-38, -4, -9	39, -2, -9
	dlg	dorsal granular insula	-38, -8, 8	39, -7, 8
	dld	dorsal dysgranular insula	-38, 5, 5	38, 5, 5
Cingulate	A23d	dorsal area 23	-4, -39, 31	4, -37, 32
	A24rv	rostroventral area 24	-3, 8, 25	5, 22, 12
	A32p	pregenual area 32	-6, 34, 21	5, 28, 27
	A23v	ventral area 23	-8, -47, 10	9, -44, 11
	A24cd	caudodorsal area 24	-5, 7, 37	4, 6, 38
	A23c	caudal area 23	-7, -23, 41	6, -20, 40
	A32sg	subgenual area 32	-4, 39, -2	5, 41, 6
Medio-Ventral Occipital	cLinG	caudal lingual gyrus	-11, -82, -11	10, -85, -9
	rCunG	rostral cuneus gyrus	-5, -81, 10	7, -76, 11
	cCunG	caudal cuneus gyrus	-6, -94, 1	8, -90, 12
	rLinG	rostral lingual gyrus	-17, -60, -6	18, -60, -7
	vmPOS	ventromedial parietooccipital sulcus	-13, -68, 12	15, -63, 12

lateral Occipital	mOccG	middle occipital gyrus	-31, -89, 11	34, -86, 11
	V5/MT+	area V5/MT+	-46, -74, 3	48, -70, -1
	OPC	occipital polar cortex	-18, -99, 2	22, -97, 4
	iOccG	inferior occipital gyrus	-30, -88, -12	32, -85, -12
	msOccG	medial superior occipital gyrus	-11, -88, 31	16, -85, 34
	lsOccG	lateral superior occipital gyrus	-22, -77, 36	29, -75, 36
Amygdala	mAmyg	medial amygdala	-19, -2, -20	19, -2, -19
	lAmyg	lateral amygdala	-27, -4, -20	28, -3, -20
Hippocampus	rHipp	rostral hippocampus	-22, -14, -19	22, -12, -20
	cHipp	caudal hippocampus	-28, -30, -10	29, -27, -10
Basal Ganglia	vCa	ventral caudate	-12, 14, 0	15, 14, -2
	GPe	globus pallidus external	-20, 0, 4	20, 0, 4
	GPi	globus pallidus internal	-20,-6,-2	20,-4,-2
	SN	substantia nigra	-8,-14,-14	10,-14,-14
	STN	subthalamic nucleus	-10,-12,-8	12,-12,-6
	NAC	nucleus accumbens	-17, 3, -9	15, 8, -9
	vmPu	ventromedial putamen	-23, 7, -4	22, 8, -1
	dCa	dorsal caudate	-14, 2, 16	14, 5, 14
	dlPu	dorsolateral putamen	-28, -5, 2	29, -3, 1
Thalamus	mPFtha	medial pre-frontal thalamus	-7, -12, 5	7, -11, 6
	mPMtha	pre-motor thalamus	-18, -13, 3	12, -14, 1
	Stha	sensory thalamus	-18, -23, 4	18, -22, 3
	rTtha	rostral temporal thalamus	-7, -14, 7	3, -13, 5
	PPtha	posterior parietal thalamus	-16, -24, 6	15, -25, 6
	Otha	occipital thalamus	-15, -28, 4	13, -27, 8
	cTtha	caudal temporal thalamus	-12, -22, 13	10, -14, 14
	lPFtha	lateral pre-frontal thalamus	-11, -14, 2	13, -16, 7

Appendix B DMN Diffusion Imaging Regional Connections

Regions	Description	Regions	Description
BA 9m	medial area 9	PPtha	posterior parietal thalamus
BA 32sg	subgenual area 32	BA 12_47l	lateral area 12/47
BA 32p	pregenual area 32	BA 7m	medial area 7(PEp)
BA 14m	medial area 14	BA 1_2_3ll	area1/2/3 (lower limb region)
BA 9l	lateral area 9	cHipp	caudal hippocampus
BA 10l	lateral area10	SN	substantia nigra
BA 11m	medial area 11	rHipp	rostral hippocampus
BA 10m	medial area 10	TH	area TH (medial PPHC)
BA 24rv	rostroventral area 24	vId_vIg	ventral dysgranular and granular insula
BA 46	area 46	vmPOS	ventromedial parietooccipital sulcus
dCa	dorsal caudate	vIa	ventral agranular insula
BA 8m	medial area 8	BA 12_47o	orbital area 12/47
vmPu	ventromedial putamen	BA 35_36c	caudal area 35/36
vCa	ventral caudate	BA 28_34	area 28/34 (EC entorhinal cortex)
BA 23c	caudal area 23	BA 4ll	area 4 (lower limb region)
mPFtha	medial pre–frontal thalamus	V5_MT	area V5/MT+
BA 24cd	caudodorsal area 24		
BA 31	area 31 (Lc1)		
BA 23d	dorsal area 23		
BA 23v	ventral area 23		
GPe	globus pallidus external		
lPFtha	lateral pre–frontal thalamus		
dlPu	dorsolateral putamen		
cTtha	caudal temporal thalamus		
NAC	nucleus accumbens		
rTtha	rostral temporal thalamus		
BA 13	area 13		
BA 5m	medial area 5(PEm)		
Otha	occipital thalamus		
dmPOS	dorsomedial parietooccipital sulcus(PEr)		
BA 6m	medial area 6		
BA 8dl	dorsolateral area 8		
BA 9_46d	dorsal area 9/46		
BA 9_46v	ventral area 9/46		
mPMtha	pre–motor thalamus		

Table B1. Structural Connections of BA 10 medial

Regions	Description
BA 9m	medial area 9
BA 32sg	subgenual area 32
BA 10m	medial area 10
BA 24rv	rostroventral area 24
BA 24cd	caudodorsal area 24
BA 8m	medial area 8
BA 32p	pregenual area 32
BA 23c	caudal area 23
BA 23d	dorsal area 23
BA 31	area 31 (Lc1)
BA 14m	medial area 14
NAC	nucleus accumbens
BA 13	area 13
BA 23v	ventral area 23
BA 9l	lateral area 9
dmPOS	dorsomedial parietooccipital sulcus(PEr)
BA 6m	medial area 6
BA 5m	medial area 5(PEm)
BA 7m	medial area 7(PEp)
BA 1_2_3ll	area1/2/3 (lower limb region)
mPFtha	medial pre–frontal thalamus
BA 11m	medial area 11
rCunG	rostral cuneus gyrus
vmPOS	ventromedial parietooccipital sulcus
BA 8vl	ventrolateral area 8
BA 10l	lateral area10
BA 9_46d	dorsal area 9/46
BA 8dl	dorsolateral area 8

Table B2. Structural Connections of BA 32 pregenual

Regions	Description	Regions	Description
BA 31	area 31 (Lc1)	BA 13	area 13
BA 23c	caudal area 23	dlPu	dorsolateral putamen
BA 23v	ventral area 23	TE1_0_TE1_2	TE1.0 and TE1.2
BA 23d	dorsal area 23	BA 35_36c	caudal area 35/36
BA 24rv	rostroventral area 24	BA 8m	medial area 8
BA 5m	medial area 5(PEm)	rTtha	rostral temporal thalamus
BA 24cd	caudodorsal area 24	BA 40rd	rostrodorsal area 40(PFt)
BA 1_2_3ll	area1/2/3 (lower limb region)	mPFtha	medial pre−frontal thalamus
BA 7m	medial area 7(PEp)	mPMtha	pre−motor thalamus
BA 7pc	postcentral area 7	rpSTS	rostroposterior superior temporal sulcus
BA 32sg	subgenual area 32	cpSTS	caudoposterior superior temporal sulcus
dmPOS	dorsomedial parietooccipital sulcus(PEr)	BA 22r	rostral area 22
cHipp	caudal hippocampus	aSTS	anterior superior temporal sulcus
BA 32p	pregenual area 32	BA 4ul	area 4(upper limb region)
PPtha	posterior parietal thalamus	BA 35_36r	rostral area 35/36
BA 7r	rostral area 7	BA 20rv	rostroventral area 20
BA 1_2_3tru	area1/2/3(trunk region)	BA 28_34	area 28/34 (EC entorhinal cortex)
dCa	dorsal caudate	vId_vIg	ventral dysgranular and granular insula
cTtha	caudal temporal thalamus	TL	area TL (lateral PPHC posterior parahippocampal gyru
BA 10m	medial area 10	BA 39rv	rostroventral area 39(PGa)
rHipp	rostral hippocampus	BA 7c	caudal area 7
Stha	sensory thalamus	BA 39rd	rostrodorsal area 39(Hip3)
TH	area TH (medial PPHC)	BA 1_2_3tonIa	area 1/2/3(tongue and larynx region)
NAC	nucleus accumbens	BA 21c	caudal area 21
Otha	occipital thalamus		
BA 9m	medial area 9		
BA 14m	medial area 14		
vmPOS	ventromedial parietooccipital sulcus		
lPFtha	lateral pre−frontal thalamus		
rCunG	rostral cuneus gyrus		
BA 22c	caudal area 22		
BA 41_42	area 41/42		
BA 40c	caudal area 40(PFm)		
BA 4ll	area 4 (lower limb region)		
BA 40rv	rostroventral area 40(PFop)		

Table B3. Structural Connections of BA 23 dorsal

Regions	Description	Regions	Description
BA 23d	dorsal area 23	BA 9l	lateral area 9
BA 5m	medial area 5(PEm)	GPe	globus pallidus external
BA 7m	medial area 7(PEp)	BA 13	area 13
dmPOS	dorsomedial parietooccipital sulcus(PEr)	Stha	sensory thalamus
rCunG	rostral cuneus gyrus		
BA 23v	ventral area 23		
vmPOS	ventromedial parietooccipital sulcus		
BA 31	area 31 (Lc1)		
BA 23c	caudal area 23		
BA 24rv	rostroventral area 24		
BA 24cd	caudodorsal area 24		
BA 9m	medial area 9		
BA 32p	pregenual area 32		
BA 10m	medial area 10		
BA 32sg	subgenual area 32		
BA 1_2_3ll	area1/2/3 (lower limb region)		
BA 8m	medial area 8		
PPtha	posterior parietal thalamus		
cHipp	caudal hippocampus		
BA 7c	caudal area 7		
BA 6m	medial area 6		
BA 14m	medial area 14		
NAC	nucleus accumbens		
cTtha	caudal temporal thalamus		
BA 7r	rostral area 7		
Otha	occipital thalamus		
dlPu	dorsolateral putamen		
BA 7pc	postcentral area 7		
TH	area TH (medial PPHC)		
lPFtha	lateral pre−frontal thalamus		
msOccG	medial superior occipital gyrus		
dCa	dorsal caudate		
BA 1_2_3tru	area1/2/3(trunk region)		
BA 4ll	area 4 (lower limb region)		
mPFtha	medial pre−frontal thalamus		

Table B4. Structural Connections of BA 31

Regions	Description	Regions	Description
BA 5m	medial area 5(PEm)	BA 4ll	area 4 (lower limb region)
BA 31	area 31 (Lc1)	BA 40c	caudal area 40(PFm)
BA 7r	rostral area 7	vmPu	ventromedial putamen
dmPOS	dorsomedial parietooccipital sulcus(PEr)	mPMtha	pre−motor thalamus
BA 7c	caudal area 7	BA 39c	caudal area 39(PGp)
BA 7m	medial area 7(PEp)	TE1_0_TE1_2	TE1.0 and TE1.2
rCunG	rostral cuneus gyrus	BA 37lv	lateroventral area37
msOccG	medial superior occipital gyrus	BA 39rd	rostrodorsal area 39(Hip3)
BA 23d	dorsal area 23	BA 39rv	rostroventral area 39(PGa)
BA 23v	ventral area 23	vId_vIg	ventral dysgranular and granular insula
vmPOS	ventromedial parietooccipital sulcus	BA 20cl	caudolateral of area 20
BA 23c	caudal area 23	rHipp	rostral hippocampus
PPtha	posterior parietal thalamus	BA 20iv	intermediate ventral area 20
cHipp	caudal hippocampus	BA 20cv	caudoventral of area 20
BA 7pc	postcentral area 7	BA 20rv	rostroventral area 20
BA 24cd	caudodorsal area 24	BA 9l	lateral area 9
Otha	occipital thalamus		
BA 6m	medial area 6		
cTtha	caudal temporal thalamus		
BA 32p	pregenual area 32		
BA 8m	medial area 8		
BA 9m	medial area 9		
lsOccG	lateral superior occipital gyrus		
NAC	nucleus accumbens		
BA 1_2_3ll	area1/2/3 (lower limb region)		
lPFtha	lateral pre−frontal thalamus		
BA 24rv	rostroventral area 24		
dlPu	dorsolateral putamen		
BA 10m	medial area 10		
Stha	sensory thalamus		
BA 32sg	subgenual area 32		
BA 7ip	intraparietal area 7(hIP3)		
dCa	dorsal caudate		
BA 6dl	dorsolateral area 6		
GPe	globus pallidus external		

Table B5. Structural Connections of BA 7 medial

Regions	Description	Regions	Description
BA 40c	caudal area 40(PFm)	BA 6cvl	caudal ventrolateral area 6
cpSTS	caudoposterior superior temporal sulcus	BA 20r	rostral area 20
BA 39c	caudal area 39(PGp)	BA 38l	lateral area 38
BA 39rd	rostrodorsal area 39(Hip3)	PPtha	posterior parietal thalamus
BA 37dl	dorsolateral area37	BA 8vl	ventrolateral area 8
V5_MT	area V5/MT+	vmPu	ventromedial putamen
rpSTS	rostroposterior superior temporal sulcus	BA 5l	lateral area 5
BA 37vl	ventrolateral area 37	BA 21r	rostral area 21
BA 22c	caudal area 22	BA 1_2_3ulhf	area 1/2/3(upper limb head and face region)
aSTS	anterior superior temporal sulcus	BA 44d	dorsal area 44
BA 21c	caudal area 21	BA 7r	rostral area 7
BA 40rv	rostroventral area 40(PFop)	BA 6cdl	caudal dorsolateral area 6
BA 40rd	rostrodorsal area 40(PFt)	BA 23v	ventral area 23
IFJ	inferior frontal junction	cHipp	caudal hippocampus
BA 41_42	area 41/42	BA 7pc	postcentral area 7
BA 20cl	caudolateral of area 20	BA 37mv	medioventral area37
BA 37elv	extreme lateroventral area37	Otha	occipital thalamus
BA 7ip	intraparietal area 7(hIP3)	cTtha	caudal temporal thalamus
BA 22r	rostral area 22	BA 4tl	area 4(tongue and larynx region)
mOccG	middle occipital gyrus	msOccG	medial superior occipital gyrus
BA 37lv	lateroventral area37	BA 45r	rostral area 45
dlPu	dorsolateral putamen	BA 1_2_3tonla	area 1/2/3(tongue and larynx region)
TE1_0_TE1_2	TE1.0 and TE1.2	BA 7m	medial area 7(PEp)
BA 6vl	ventrolateral area 6	BA 44op	opercular area 44
BA 4hf	area 4(head and face region)	BA 5m	medial area 5(PEm)
BA 20il	intermediate lateral area 20	IFS	inferior frontal sulcus
BA 20cv	caudoventral of area 20	BA 23d	dorsal area 23
lsOccG	lateral superior occipital gyrus	dId	dorsal dysgranular insula
vId_vIg	ventral dysgranular and granular insula	Stha	sensory thalamus
BA 20iv	intermediate ventral area 20	BA 10l	lateral area10
BA 7c	caudal area 7		
BA 20rv	rostroventral area 20		
BA 2	caudal area 22		
NAC	nucleus accumbens		
BA 9_46v	ventral area 9/46		

Table B6. Structural Connections of BA 39 rostroventral